Příloha 1

Geophysical evidence of the Eastern Marginal Fault of the Cheb Basin (Czech Republic)

Studia Geophysica et Geodaetica

Blecha et al. 2018

Blecha V., Fischer T., Táborík P., Vilhem J., Klanica R., Valenta J., Štěpančíková P. (2018): Geophysical evidence of the eastern marginal fault of the Cheb basin (Czech republic). Stud. Geophys. Geod. 62/4, 660–680. DOI: 10.1007/s11200-017-0452-9.

Geophysical evidence of the Eastern Marginal Fault of the Cheb Basin (Czech Republic)

VRATISLAV BLECHA[1], TOMÁŠ FISCHER[1,2], PETR TÁBOŘÍK[1,3], JAN VILHEM[1], RADEK KLANICA[1,2], JAN VALENTA[1,3] AND PETRA ŠTĚPANČÍKOVÁ[3]

1 Institute of Hydrogeology, Engineering Geology and Applied Geophysics, Faculty of Science, Charles University, Albertov 6, 128 43 Prague 2, Czech Republic (vblecha@natur.cuni.cz)

2 Institute of Geophysics, The Czech Academy of Sciences, Boční II/1401, 141 31 Prague 4, Czech Republic

3 Institute of Rock Structure and Mechanics, The Czech Academy of Sciences, V Holešovičkách 94/41, 182 09 Prague 8, Czech Republic

Received: August 4, 2017; Revised: November 15, 2017; Accepted: April 15, 2018

ABSTRACT

The western part of the Bohemian Massif hosts an intersection of two regional fault zones, the SW-NE trending Ohře/Eger Graben and the NNW-SSE trending Mariánské Lázně Fault, which has been reactivated several times in the geological history and controlled the formation of the Tertiary Cheb Basin. The broader area of the Cheb Basin is also related to permanent seismic activity of M_L 3+ earthquake swarms. The Eastern Marginal Fault of the Cheb Basin (northern segment of the Mariánské Lázně Fault) separates the basin sediments and underlying granites in the SW from the Krušné Hory/Erzgebirge Mts. crystalline unit in the NE. We describe a detailed geophysical survey targeted to locating the Eastern Marginal Fault and determining its geometry in the depth. The survey was conducted at the Kopanina site near the Nový Kostel focal zone, which shows the strongest seismic activity of the whole Western Bohemia earthquake swarm region. Complex geophysical survey included gravimetry, electrical resistivity tomography, audiomagnetotellurics and seismic refraction. We found that the rocks within the Eastern Marginal Fault show low resistivity, low seismic velocity and density, which indicates their deep fracturing, weathering and higher water content. The dip of the fault in shallow depths is about 60° towards SW. At greater depths, the slope turns to subvertical with dip angle of about 80°. Results of geoelectrical methods show blocky fabric of the Cheb Basin and deep weathering of the granite bedrock, which is consistent with geologic models based on borehole surveys.

Keywords: fault tectonics, geophysical survey, gravimetry, electrical resistivity tomography, audiomagnetotellurics, seismic refraction

Stud. Geophys. Geod., 62 (2018), 660–680, DOI: 10.1007/s11200-017-0452-9

© 2018 Inst. Geophys. CAS, Prague

1. INTRODUCTION

The Cheb Basin in Western Bohemia is a shallow Cenozoic depositional center developed at the intersection of two tectonic structures: NE striking Ohře/Eger Graben and NW trending Cheb-Domažlice Graben (Figs 1 and 2). The Cheb Basin developed jointly with other Krušné hory/Erzgebirge Mts. (KEM) basins as a part of the NE striking Ohře/Eger Graben from late Oligocene to mid-Miocene. Since early Pliocene the NW-SE striking faults were preferentially activated and the basin gradually developed as a part of an asymmetrical Cheb-Domažlice graben that was controlled by the Mariánské Lázně Fault (MLF) on the east, superimposed on the Ohře/Eger graben (*Malkovský, 1987*; *Špičáková et al., 2000*). The Cheb Basin is a center of recent geodynamic activity represented by repeating earthquake swarms with the largest earthquakes of magnitudes up to 4.6, not related to MLF and massive degassing of CO_2 of upper mantle origin (*Bräuer et al., 2005*; *Fischer et al., 2014*).

On the east, the Cheb Basin is controlled by the Eastern Marginal Fault (EMF), which is a northern segment of the Mariánské Lázně Fault (MLF) zone, an important NW-SE tectonic line, which was reactivated several times during the geological history of the Western Bohemia region (*Švancara et al., 2008*). This fault probably served as magma feeding channel for Variscan granites of Smrčiny/Fichtelgebirge massif (Figs 1, 3 and 4) before 320 Ma (*Hecht et al., 1997*; *Blecha et al., 2009*).

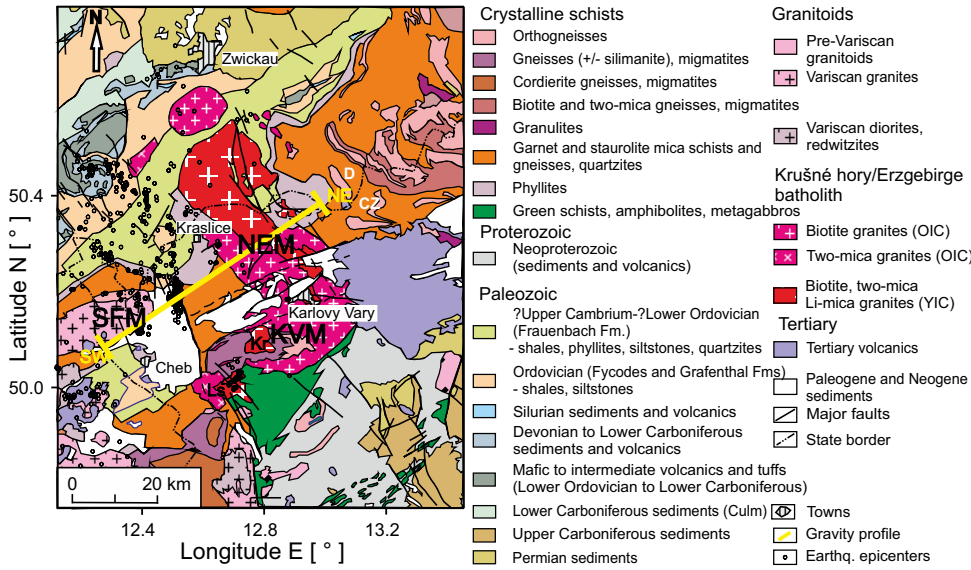


Fig. 1. Simplified geology and geography of the Western Bohemia (after *Cháb et al., 2007* and *Blecha et al., 2009*, © Inst. Geophys. AS CR, Prague) with location of gravity profile and epicenters of $M_L > 0.5$ earthquakes in the period 1991–2007. KVM: Karlovy Vary Massif, NEM: Nejdek/Eibenstock Massif, SFM: Smrčiny/Fichtelgebirge Massif, Kr: Krudum Massif, Ls: Lesný-Lysina Massif.

In the present study we investigate in detail the geometry of the shallow parts of the EMF of the Cheb Basin at Kopanina site near the Nový Kostel focal zone, which shows the strongest seismic activity in the whole West Bohemia/Vogtland seismoactive region (*Fischer et al., 2014*). This site has already been a subject of our previous studies. Paleoseismological study of *Štěpančíková et al. (2015)* revealed pre-historic Holocene coseismic displacements in the deformed Quaternary sediments. *Fischer et al. (2012)* further investigated the near-surface structures in 3-D using geophysical techniques.

Here we extend the depth range of the survey using additional geophysical methods to trace the EMF to depth and learn about geometry to the eastern delimitation of the basin infill. In the place of the anticipated position of the fault line we used gravity, geoelectric, electromagnetic and seismic methods in order to locate the fault trace in the subsurface, determine its slope and establish the physical properties of rocks in the vicinity of the fault plane.

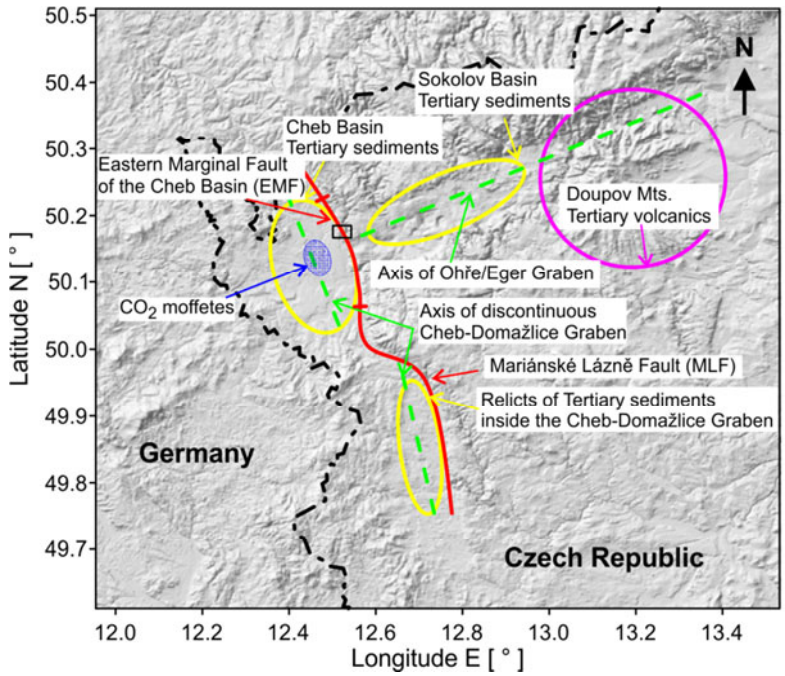


Fig. 2. Tectonic overview. Eastern Marginal Fault of the Cheb Basin (EMF) is part of the Mariánské Lázně Fault (MLF) on the eastern margin of the Cheb Basin. Black rectangle on EMF marks the study area.

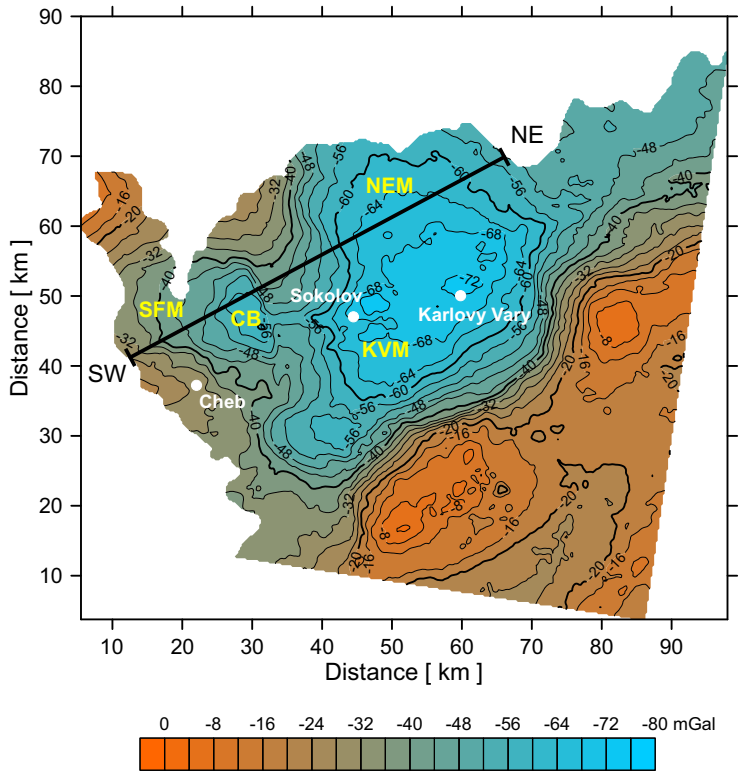


Fig. 3. Bouguer anomaly map of NW Bohemia (*Blecha et al., 2009*, © Inst. Geophys. AS CR, Prague). Position of interpreted SW–NE gravity profile is marked. Gravity minima caused by granite massifs: KVM - Karlovy Vary Massif, NEM - Nejdek/Eibenstock Massif, SFM - Smrčiny/Fichtelgebirge Massif, CB - gravity low partly caused by Cheb Basin sediments.

2. GEOLOGY AND TECTONICS

The Cheb Basin has evolved from late Eocene controlled by differently striking faults under a changing stress field (*Malkovský, 1987*; *Špičáková et al. 2000*). *Špičáková et al. (2000)* divided and simplified the stratigraphic units into three main intervals. The first one, Pre-Cypris strata (Late Oligocene to Early Miocene, c. 26–21 Ma) includes volcanics and volcanoclastics, coal seam formation, and alluvial/fluvial deposits related to depositional centers governed by E-W trending faults. The second interval, Cypris Formation (Early to Middle Miocene, c. 21–17 Ma), is characterized by widespread lacustrine conditions with NNW-oriented depocenter adjacent to the EMF and with termination of the deposition by partial uplift and erosion. The third one, Vildštejn Formation (Late Pliocene, c. 4.5–1.5 Ma), was deposited discordantly after a hiatus of 12 My duration. It consists of fluvio-lacustrine kaolinic clays, sands and gravels. Since this period the NW trending EMF became a master fault and controlled the shape of the basin depocenters with an eastward thickening sedimentary wedge, as well as of the

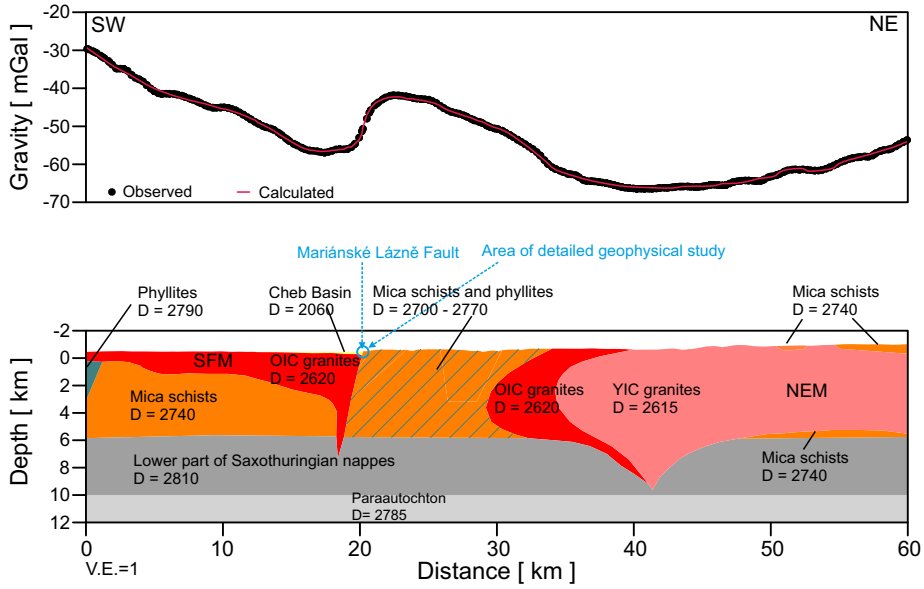


Fig. 4. Geological model (**bottom**) along SW-NE gravity profile (**top**). Rock densities *D* are in kg m^{-3}. SFM: Smrčiny/Fichtelgebirge Massif, NEM: Nejdek/Eibenstock Massif, OIC: old igneous complex, YIC: young igneous complex.

present-day morphology of uplifted KEM well-expressed by about 200-m high escarpment to the east (*Peterek et al., 2011*).

The Cheb Basin is typified by a blocky structural fabric due to a network of faults of different strike. Besides the NNW and NW marginal faults *Špičáková et al. (2000)* identified also faults striking NE, E-W and N-S. *Bankwitz et al. (2003)* underlined the present-day significance of the N-S faults and pointed out that the roughly N-S striking Počátky-Plesná Fault Zone (PPZ) delineated by the valley of the Plesná river is parallel to the elongation of cluster of epicenters, which strike about 170° in the Nový Kostel area (*Fischer at al., 2014*). *Peterek et al. (2011)* documented neotectonic activity of the Cheb Basin area where the MLF branches in four individual segments and interpret the PPZ as a sinistral wrench zone.

The Paleozoic basement of the Cheb Basin is formed by phyllites in the south and granites of the Smrčiny pluton in the north with a small area of phyllites at the northern tip (*Kolářová, 1965*; *Mlčoch et al., 2008*). Deep weathering of the basement, which resulted in unconsolidated rock material composed of kaolin, clays and relicts of quartz and mica is documented by a dense network of boreholes realized in the 2-nd half of 20-th century with the aim of surveying for coal deposits. In Fig. 5 and Table 1 we show three boreholes in the close vicinity of the survey area and other three in broader area, which penetrated the granite basement. According to Table 1, the thickness of weathered zone or local alterations reaches dozens of meters; some of the boreholes do not reach intact granite even after 30 to 50 m of drilling through the basement.

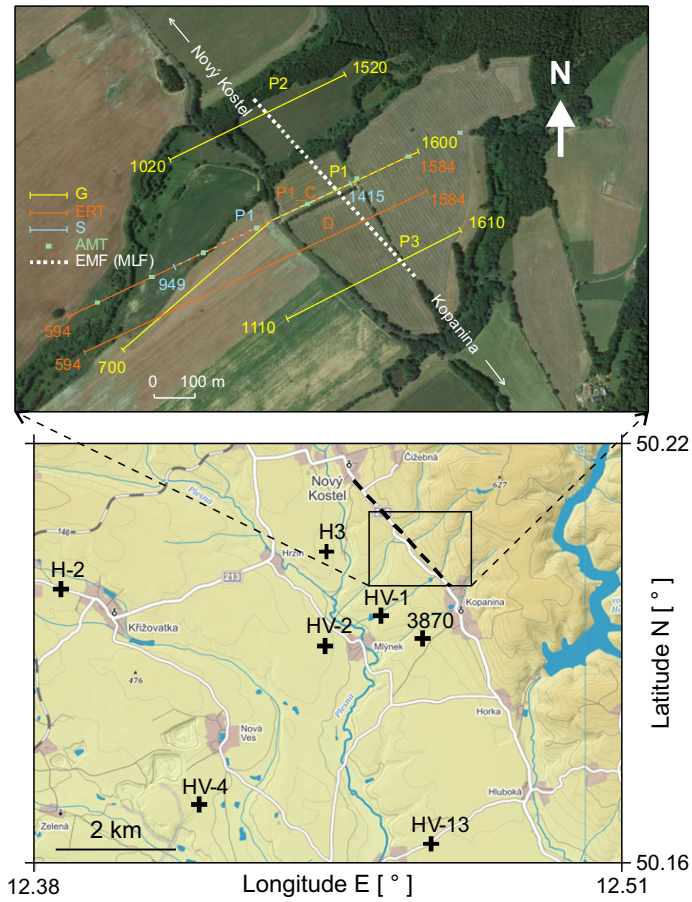


Fig. 5. **Top:** Situation of profiles. G: gravity profiles (P1, P2, P3), ERT: electrical resisitivity tomography profiles (C, D), S: seismic refraction profile, AMT: audiomagnetotelluric stations, EMF (MLF): trace of the Eastern Marginal Fault of the Cheb Basin (part of the Mariánské Lázně Fault) according to geophysical results. **Bottom:** Topographic map indication the study area (rectangle) and boreholes (crosses) listed in Table 1. The bold dashed line shows the trace of EMF (MLF) according to geophysical results.

Table 1. Selected exploration boreholes penetrating the granite basement. Positions of boreholes are marked in Fig. 5.

	Borehole						
	H-2	HV-4	HV-13	3870	HV-1	H-3	HV-2
Depth of granite basement [m]	64	114	225	267	196	207	136
Depth of basement weathered zone [m]	96	---	226	---	---	---	---
Depth of borehole [m]	142	166	281	297	230	241	163
Thickness od basement weathering [m]	32	>52	1	>30	>34	>34	>27

The geophysical studies focused to the area of the Cheb Basin involve both the analyses of present seismic activity (see *Fischer et al., 2014* for review), Quaternary volcanic activity, e.g., *Mrlina et al. (2009)*, and structural studies. Based on dipole geoelectric measurements *Flechsig et al. (2010)* derived a block faulted-fabric for the resistivity model of the wider Cheb Basin area. *Halpaap et al. (2018)* carried out a high resolution reflection seismic survey in order to image shallow structural features of the Cheb Basin.

3. REGIONAL GRAVITY PROFILE

With the aim of obtaining broader context for the analyzed geophysical data sets we first analyze a regional SW-NE trending gravity profile whose position is shown in Fig. 1 in the geological map, and in Fig. 3, where the Bouguer gravity map of NW Bohemia is presented.

We used the GM-SYS computer program for profile modelling of gravity data (*GM-SYS Modelling, 2017*). In this program, the geological units are visualized as tabular prisms with axes in their strike direction. These prisms may be truncated along the strike at some distance. Beyond the ends of the prisms there are new prisms of the same cross section, but with different densities. The two ends of the prisms may be asymmetrically positioned relative to the line of profile or, if needed, both may be on the same side of the profile plane. This concept is termed 2.75D modelling (*Blecha and Štemprok, 2012*). Our model, depending on the position of each body in the geological map, consists of 2D, 2.5D and 2.75D bodies.

Gravity data along profile were extracted from a digital Bouguer gravity map of the Czech Republic (grid 0.25 × 0.25 km; reduction density 2670 kg m^{-3}; theoretical gravity World Geodetic System 1984; terrain corrections calculated to 166.7-km distance from measured stations). Original gravity data in the area of study are derived from the gravity mapping at a scale of 1:25 000. Average spacing of gravity stations was 5 stations/km^2 and mean square error of measurements did not exceed 0.05 mGal. Digital (non-public) gravity data were provided by the Czech Geological Survey.

Values of densities used for modelling of outcroping rocks are taken from laboratory measurements of rock samples (*Blížkovský et al., 1981*; *Hrouda and Chlupáčová, 1993*; *Sedlák et al., 2009*). Densities of the deep geological units are based on velocity-density relations (*Behr et al., 1994*).

Near-surface rocks along the profile line consist of Upper Proterozoic and Paleozoic phyllites and mica schists (density 2700–2790 kg m^{-3}), Variscan granites (2615–2620 kg m^{-3}) and Tertiary/Quaternary sediments of Cheb Basin modeled with average density of 2060 kg m^{-3}.

In the SW the gravity profile starts in the Variscan granites of the Smrčiny/Fichtelgebirge massif and the source of the negative anomaly with center at km 18 (Fig. 4) is the root zone of a granitic intrusion (*Štemprok and Blecha, 2015*; *Hecht et al., 1997*); MLF is supposed to serve here as feeding channel for granite magma. Other bodies of Variscan granites along the MLF south of the area of study are documented. The country rocks of granites are predominantly phyllites and mica schists. Between km 13 and 20 of the profile Tertiary sediments of the Cheb basin occur at the surface. The

thickness of sediments increases towards the east and in the vicinity of the MLF (Eastern Marginal Fault of the Cheb Basin) the maximal thickness of sediments is about 300 m. Shallow basin sediments only partly contribute to the regional gravity image with about −6 mGal (1 mGal = 10^{-5} m s^{-2}) in the deepest parts of the basin (*Blížkovský et al., 1981*), and −4 mGal on our profile.

The MLF separates granites of the Smrčiny/Fichtelgebirge massif from the Upper Proterozoic and Paleozoic Krušné hory/Erzgebirge Mts. crystalline complex formed mainly by phyllites (north of profile) and mica schists (south of profile) - Fig. 1. The Paleozoic crystalline complex manifests itself by relatively positive gravity anomaly (Fig. 4). Towards NE the gravity field descends to extensive negative anomaly which is caused by Variscan granites of the Nejdek/Eibenstock massif. Two major granite intrusive complexes are distinguished in the KEM area: the old igneous complex (OIC) and the young igneous complex (YIC) (*Štemprok, 1986*; *Breiter, 2012*). The YIC granites show slightly lower densities (2615 kg m^{-3}) in comparison with the OIC granites (2620 kg m^{-3}; *Blecha et al., 2009*).

For modelling of the deeper parts we accepted the concept of boundaries between Saxothuringicum and Bohemicum postulated by *Tomek et al. (1997)*. The Saxothuringicum is divided into a lower part of high-density equivalent of oceanic crust (2810 kg m^{-3}) and an upper part consisting of various crustal metamorphic rocks. The existence of a high velocity/density layer with a lower boundary in depths of about 10 km in the area of study is interpreted from seismic measurements by *Krawczyk et al. (2000)* and used in gravity modelling in the area of study by *Hofmann et al. (2003)* and *Guy et al. (2011)*. The Allochtonous Saxothuringicum rests on the middle and lower crust of the European para-autochton with a density of 2785 kg m^{-3} (*Hofmann et al., 2003*; *Blecha et al., 2009*).

4. DATA ACQUISITION AND PROCESSING

A combination of geophysical methods was applied at the Kopanina site in order to reveal the EMF fault geometry down to a depth of the first hundreds of meters.

4.1. Gravity

Field measurements of gravity were conducted using the gravity meter Scintrex CG-3M with a resolution of 0.001 mGal on profiles P1, P2 and P3 (Fig. 5). The profile P1 was measured first, parallel profiles P2 and P3 were measured later after evaluation of the P1 data in order to verify the obtained results.

The distance between gravity stations was 5 m on profile P1 and 10 m on profiles P2 and P3. Tidal effects and the long-term linear drift were removed by internal software of the gravimeter. The residual drift was recorded by repeated measurement on the base station in a time interval of about 1 hour. 20% of field gravity stations were measured repeatedly at different times and after correction for a residual drift the measurement error was calculated. The root mean square error of measurements was 0.003 mGal. From the measured gravity data on all three profiles relative Bouguer anomalies for reduction density of 2700 kg m^{-3} have been calculated and these were separated into regional and

residual parts. Bouguer anomalies on the longest profile P1 have been interpreted quantitatively using the GM-SYS modelling program (*GM-SYS Modelling, 2017*).

4.2. Electromagnetic and geoelectric measurements

Audiomagnetotelluric measurements (AMT) were conducted along a 1050 m long profile with eight stations and in-line spacing of 150 m. Only high frequency data were recorded, with periods between 0.0001 and 0.3 s, by the Metronix GMS06 system (Metronix Geophysics) to image the resistivity section down to a depth of about 1 km with sufficiently high resolution. Data were processed by the standard software Mapros (*Friedrichs, 2004*) using the methods of robust processing, which removes influence of the outliers in data by iteratively weighted least square type algorithm (*Simpson and Bahr, 2005*). The resulting sounding data (example in Fig. 6) show acceptable quality, only data at the shortest periods ($T < 0.001$ s) are scattered excessively at several stations, probably

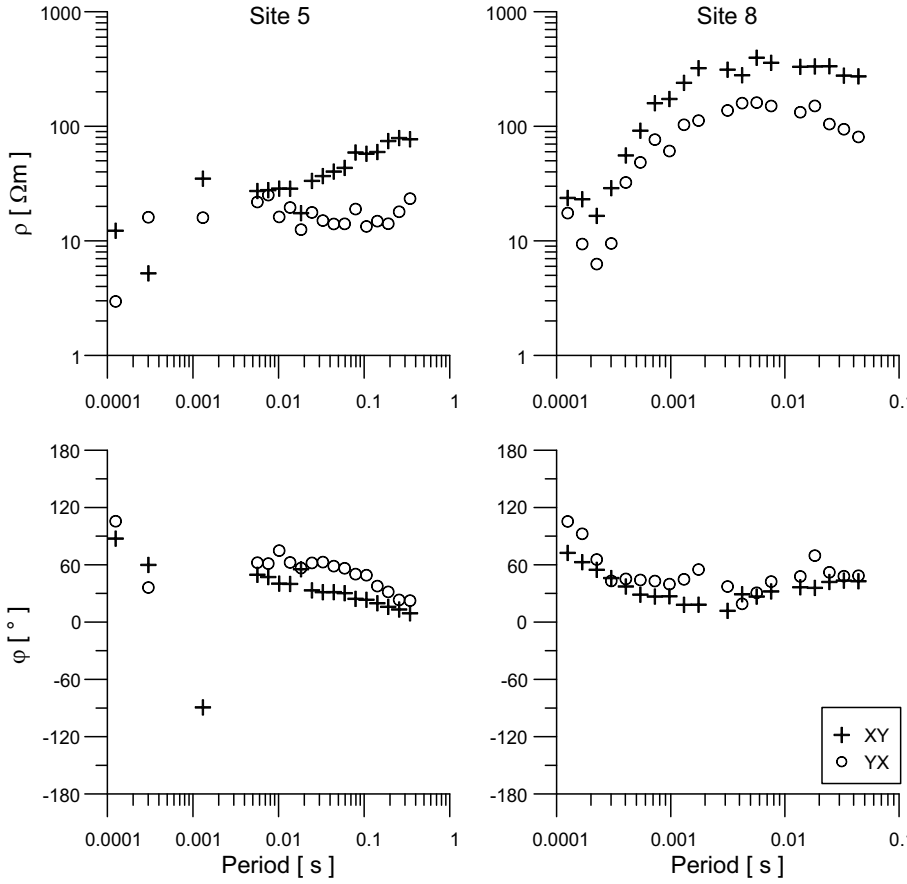


Fig. 6. Sample resistivity and phase data for both polarizations from AMT site 5 (Cheb Basin) and site 8 (Krušné Hory/Erzgebirge Mts. crystalline).

due to the close vicinity of electric power lines, and were not considered for the subsequent analysis.

To verify the 2D structural hypothesis for the subsequent 2D modelling, we performed a dimensionality and directionality analysis of the AMT data. The resulting Swift's skew (*Swift, 1967*) is small and allows subsequent 2D modelling. Swift's principal direction ranges from −40° to −20° and we chose −28° for modelling according to the trend of the MLF. We further conducted a series of 2D resistivity inversions with the AMT data. The regularization weight for the smoothness function was selected after several inversion runs using the L-curve approach (*Hansen and O'Leary, 1993*). We applied the non-linear conjugate gradient routine by *Pek et al. (2012)* as a minimization procedure. All resulting models show three main resistivity zones, only their extent slightly changed through different inversion runs.

Geoelectrical survey using the electrical resistivity tomography (ERT) was performed to image the shallow depth section in more detail. Two parallel ERT profiles with length of 990 m and 10-m electrode spacing were measured in order to gain maximum possible depth of penetration (up to 200 m). We used the ARES I device (GF Instruments) with 25 multi-electrode cable sections with 100 simultaneously connected electrodes. The Wenner-Schlumberger electrode array (*Pazdírek and Bláha, 1992*) was chosen for its high depth range and robustness to a geoelectrical noise. Measurements of each of the resistivity points were repeated four or eight times (depending on the standard deviation of measured apparent resistivity values). The median of standard deviations of repeated measurements for individual points was 0.2% for the profile C and 0.1% for the profile D. The C and D profiles with mutual distance 100 m were situated perpendicularly to the assumed fault line and with expected position of the fault in the centre of the array; the first part of the profile C being identical to the gravity profile P1 (Fig. 5). The measured apparent resistivity data (Fig. 7) were processed using two different inversion algorithms: (i) Res2Dinv software (*Loke, 1997*) and (ii) the BERT inversion code (*Günther et al., 2006*; *Rücker et al., 2016*). First, outliers from data were removed. Next, damping factors for the inversion procedure were adjusted to be large enough for the first few iterations to achieve reliable smooth model and then to decrease in final iterations to let the fine structures evolve. Results were more or less the same from both inversion codes and

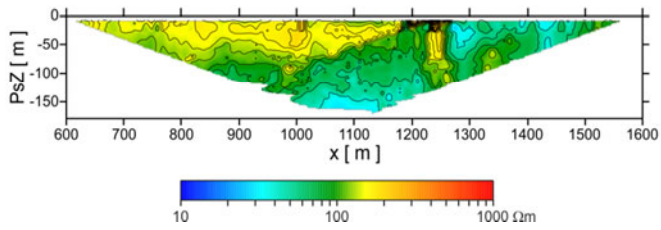


Fig. 7. An example of apparent electrical resistivity (ρ) from the profile C measured using the multi-electrode method. The vertical axis shows pseudo-depth in accordance with *Edwards (1977)*. Both profiles C and D were measured using the Wenner-Schlumberger electrode configuration.

therefore we have chosen just the BERT results for further interpretations. The final results are depicted as inverted resistivity models representing a distribution of modelled resistivities in sections along the profiles. Elevation corrections were introduced to the inversion process.

4.3. Seismic refraction

The seismic refraction measurement was made using three 24-channel Geode seismographs (Geometrics) and vertical 10-Hz geophones (Sensor). Two different impulsive sources were used: a 6-kg sledge-hammer and a Seismic Impulse Source System (SISSY, Geosym GmbH). The former source was used to generate high-frequency signals for shallow survey in one part of the seismic profile, while the latter was used for deeper survey along the whole length of the seismic profile. Receiver spacing was 2 and 4 m for sledge-hammer source measurement and 5-m spacing was used with SISSY seismic source. By using totally 40 hammer shots and 5 explosions approximately 1300 first-break time-readings were obtained. The tomographic inversion by Plotrefa software (OYO) was used for inverting the data into a velocity model. The comparison of measured arrival times and model data is available in Fig. 8. The quality of velocity model obtained by seismic tomography is demonstrated by the global root mean square (*RMS*) error of 1.83 ms. The higher data density near the fault position ensures better ray coverage and higher reliability of this part of velocity section.

5. RESULTS AND INTERPRETATION OF THE FIELD MEASUREMENTS

5.1. Gravity

Bouguer anomalies on the three parallel gravity profiles show similar general course of gravity (Fig. 9). Towards SW gravity decreases with the increasing thickness of the Cheb basin sediments; the decrease can be generally expressed using a quadratic polynomial. However, towards NE, at specific station on each profile, the general trend

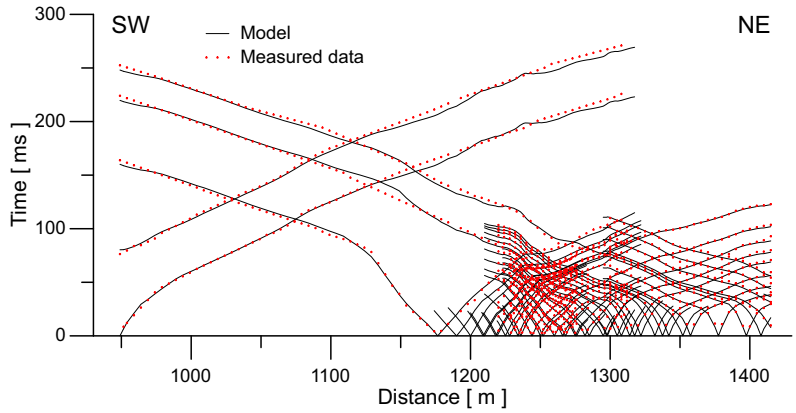


Fig. 8. Comparison of measured and modeled seismic arrival times.

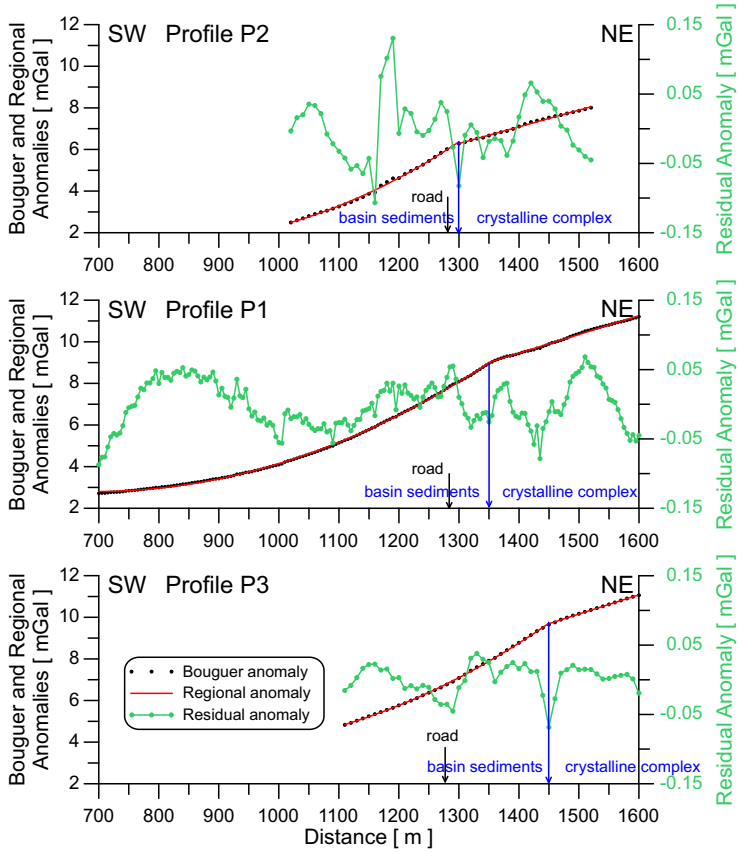


Fig. 9. Bouguer, regional and residual gravity anomalies on profiles P1, P2 and P3.

(regional anomaly) is changing to linear. The respective stations are P2/1300 m, P1/1350 m, and P3/1450 m (Fig. 9). According to our interpretation these positions delineate the boundary between the Tertiary basin sediments and the older crystalline complex, which appears identical with the near surface course of the Eastern Marginal Fault of the Cheb Basin. Local minima of residual gravity anomalies in the vicinity of the predicted fault course show increased thickness of overburden and/or occurrence of fractured and weathered rocks in the near surface parts of the profile.

The optimal gravity model for the profile P1 (Fig. 10a) shows the observed and calculated Bouguer gravity values (top) and the vertical geological section (bottom) based on an optimal fit between the observed and calculated gravity data. This model is based on the regional gravity profile (Fig. 4) in the proximity of km 20. In addition to the geological units of the regional gravity profile a Quaternary overburden (density of 1950 kg m^{-3}) and disrupted and weathered rocks in the vicinity of the MLF zone (density of 2200 kg m^{-3}) are added to this detailed model. Existence of the Quaternary overburden

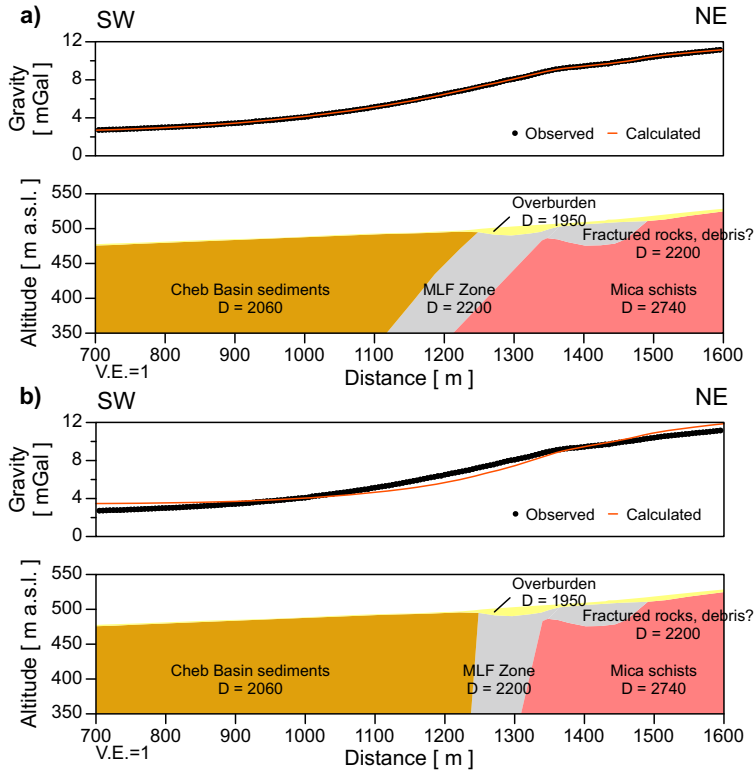


Fig. 10. **a)** Optimal geological model along the gravity profile P1. Rock densities *D* are in kg m^{-3}. Root mean square (*RMS*) error of modeling is 0.025 mGal. **b)** Alternative geological model (subvertical dip of the MLF zone) along the gravity profile P1. *RMS* error of modeling is 0.516 mGal. Upper panels in both models a) and b) show comparison of the observed and modeled gravity data, bottom panels show geological models.

in the near-surface part of the profile is documented by trenching and geoelectrical surveys in the immediate vicinity of our profile (*Fischer et al., 2012*). Overburden is formed by loamy sandy gravelly colluvium, sand, sandy gravel, gravelly sand and clayey sand. Density used in our model is estimated average for these rocks.

The width of fractured rocks zone around the MLF fault in gravity model is inferred from ERT measurements (Fig. 11) and roughly coincides with the zone of low resistivities at this part of profile. The same holds (zone of low resistivities) for fractured rocks and/or debris modeled in the footwall of the fault.

According to our modelling the MLF zone is dipping towards the SW with an approximate dip angle of 60° in the first 120-m depth range.

5.2. Electromagnetic and geoelectric measurements

The results of ERT were displayed as the resistivity sections along the profile (Fig. 11). The inversion processing in both programs (Res2Dinv and BERT) delivered

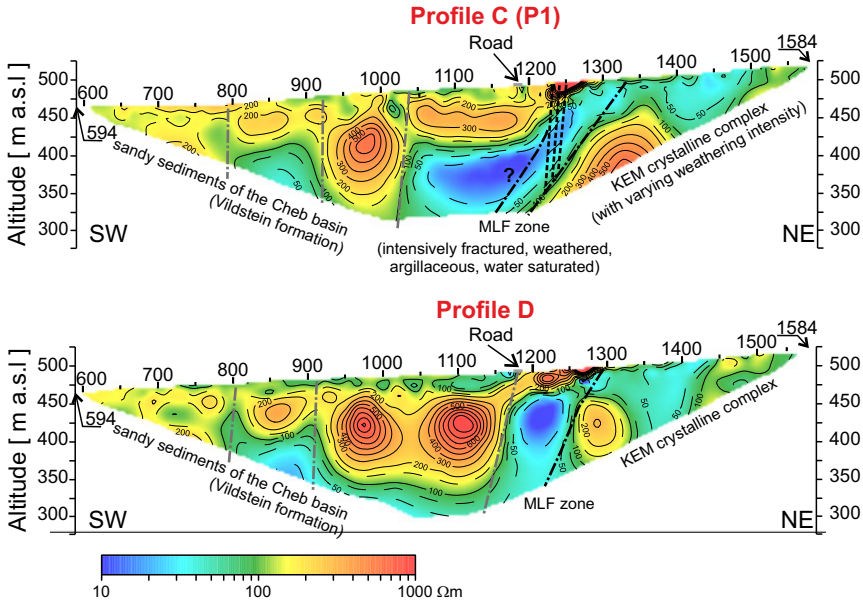


Fig 11. Electrical resistivity tomography (ERT) profiles C and D. Dark grey dashed and dotted lines represent possible faults in agreement with hypotheses of blocky structure of the Cheb Basin with differential subsidence/thrusting of individual blocks (e.g., *Špičáková et al., 2000*); the black lines represent MLF zone, probably fractured and/or intensively weathered and water saturated. The dotted lines represent a splay of faults revealed by trenching and ERT by *Fischer et al. (2012)*. KEM: Krušné hory/Erzgebirge Mts.

very similar models, thus we can consider the results convincing. Both profiles show vertically inclined zone of low resistivity values (< 50 Ωm) at *x* coordinates 1200–1300 on Profile C and 1150–1300 on Profile D.

The basin sediments are represented mostly with mid resistivity values, ranging from 50 to ca. 700 Ωm, except for the near-surface (approx. 10 m thick) high resistivity sedimentary body in stationing of 1220–1260 m (profile C) with values about 1000 Ωm.. This body is, according to the paleoseismological trenching (*Štěpančíková et al., 2015*) and detailed geoelectrical surveying (*Fischer et al., 2012*), formed of heterogeneous coarse gravely sandy sediment with scattered boulders. The resistivity response of the KEM crystalline rocks is slightly more complicated. Since the crystalline bedrock complex is intensively weathered, the resistivity values are ranging from about 25 to 600 Ωm. Actual resistivity value then depends on a particular rock type (mica-schist, phyllites) and local intensity of its weathering and/or fracturing. Both sections (C and D) differ in some small details, but generally they show very similar image, suggesting a blocky structure of the Cheb basin with possible vertical differentiation of individual blocks (Fig. 11).

The results of the AMT 2D resistivity modelling show the resistivity section along the profile to the depth of 1 km (Fig. 12). The accuracy of the near-surface part of the model is limited by the fact that the shallowest depths represented by the AMT data are about 100–150 m. The discrepancy between resistivities obtained by AMT and ERT is caused by different principles of both methods, scale of measurements (number and size of details) and different inversion procedures. The sedimentary basin located on the west shows resistivity values between 1 and 50 Ωm to a depth of about 300 m, where it meets with the basement granites. The maximum depth of the basin sediments was estimated on the basis of the lithological logs of the nearest boreholes HV-1 and 3870 (see Fig. 5 and Table 1), because the AMT method is rather insensitive to bottom boundaries of the

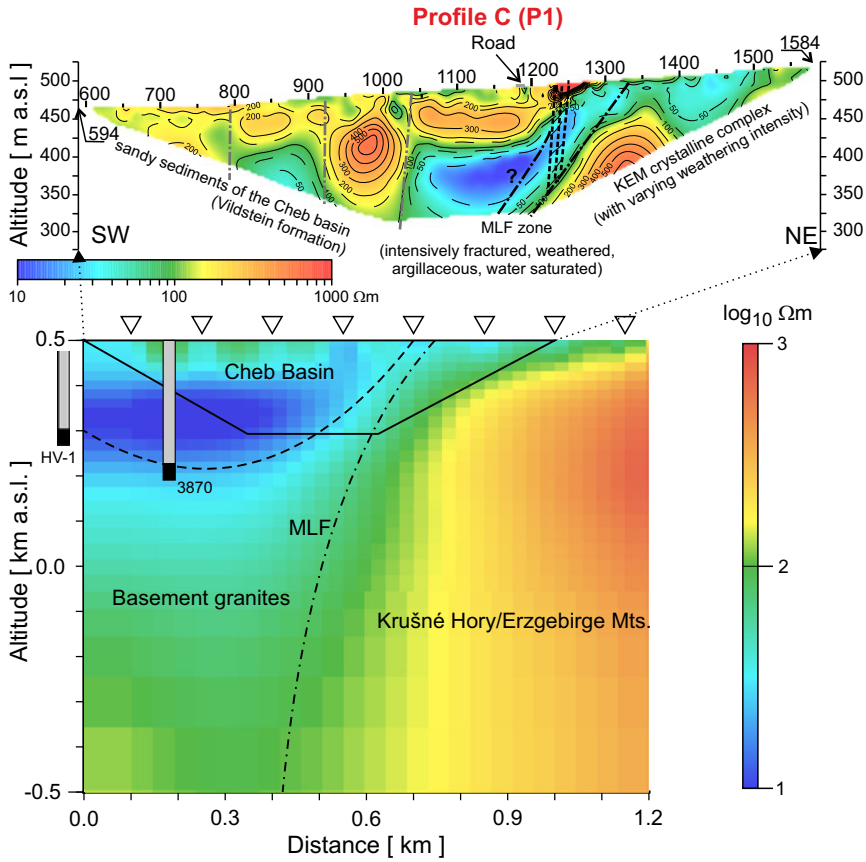


Fig. 12. Audiomagnetotellurics (AMT) on profile C (P1). Triangles on horizontal axis mark positions of AMT stations in Fig. 5. Zero on the horizontal axis corresponds to stationing 600. Depth of weathered granite basement in the boreholes HV-1 and 3870 is marked (black). Black trapezoid marks extent of electrical resistivity tomography (ERT) measurements; dashed curve indicates the estimated position of the Cheb Basin basement and dashed and dotted represents position of MLF. Upper panel is the ERT measurement in the scale of AMT profile.

resistivity anomalies. The higher resistivity of the near surface part of the basin (< 100 m) is probably caused by missing data as discussed previously. A gradual increase of resistivity with depth from 80 to > 100 Ωm is observed in the basement granites, which probably corresponds to the decreased grade of weathering in deeper parts. In the east, the KEM crystalline unit with higher resistivities between 300 and 700 Ωm is located. The near surface part of the crystalline unit seems to be more conductive, with a resistivity below 100 Ωm. The weathering at shallow depths is similar to that one of the granite basement in the west. The resistivity zone of about 70–80 Ωm between the sedimentary basin and granites in the west and the crystalline unit in the east most probably corresponds to the sub-vertically dipping MLF. Below the depths of about 150 m the dip angle of the MLF zone is nearly 80°.

5.3. Seismic refraction

The obtained velocity distribution (Fig. 13) provides limited depth range compared to the other methods used. It shows a detailed information about the near-surface, namely in the NE part of the profile, where a high-resolution measurement was performed. The P wave velocities range between 0.4 and 2.7 km s^{-1}. The areas with velocities higher than approx. 2.0 km s^{-1} in the NE part of the profile correspond to the KEM crystalline unit characterized by a strong decrease of weathering with increasing depth. In the SW part of the refraction profile the seismic velocities are generally lower than 2.0 km s^{-1}, which correspond to the Cheb basin sediments. The near-surface manifestation of the MLF zone is indicated by the highly heterogeneous character of the velocity distribution between stations 1200 and 1300 m, and low-velocity zone between 1230 and 1270 m. The horizontal velocity gradient and the nearly vertical velocity isolines near the stations 1250 and 1300 can be caused by a block structure of weathered crystalline rocks within the fault zone. The velocity distribution is in a good agreement with the ERT resistivity distribution and with the gravity model.

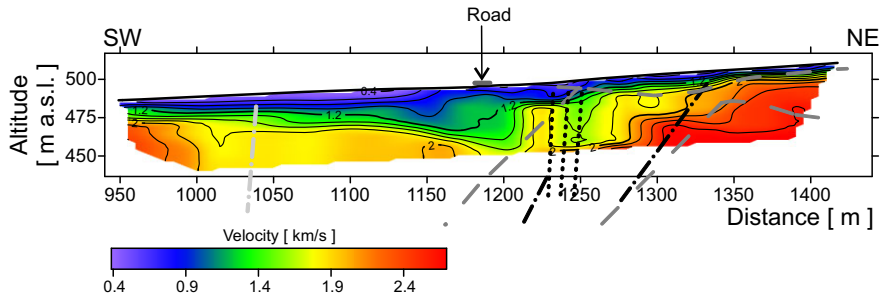


Fig. 13. Velocity model determined from seismic refraction on profile P1. Boundaries of low density zone according to gravity modeling (dashed lines), possible faults according to electrical resistivity tomography (ERT, dashed and dotted lines) and splay of faults revealed by trenching and ERT (dotted lines, by *Fischer et al. 2012*) are marked.

6. DISCUSSION

The distinct gravity gradient increasing from the sediments of the Cheb Basin in the SW towards the Krušné hory/Erzgebirge Mts. crystalline complex in the NE (Figs 3 and 4) signifies the eastern tectonic margin of the Cheb Basin. The negative gravity anomaly in the area of the Cheb Basin is only partly caused by the shallow basin sediments; the main source of the negative anomaly is the root zone of the Smrčiny/Fichtelgebirge granite massif. This inference follows both from the results of our modelling on the regional profile (Fig. 4) and from the results of previous works in this area (*Blížkovský et al., 1981*; *Hecht et al., 1997*; *Blecha et al., 2009*).

To examine the sensitivity of gravity modelling to the model geometry we show in Fig. 10b an alternative model where the MLF zone is represented by an almost vertical wedge. The fit between the observed and calculated gravity curves has decreased significantly, which is also characterized by the increased root mean square (*RMS*) error (0.516 mGal compared to 0.025 mGal in the optimal model).

The MLF zone is represented in the regional gravity model by a subvertical contact of granites on the west and mica schists on the east down to a depth of 8 km. In the detailed scale it is modelled by a low density wedge of weathered crystalline dipping 60° towards SW. Being aware of the ambiguity of gravity modelling we note that the optimal fit is rather sensitive to the dip of the MLF zone in shallow depths (Fig. 10), which indicates that the MLF zone dip increases with depth to an almost vertical one. The change of the dip with depth agrees with the results of the resistivity inversion; the moderate MLF dip in the ERT section changes to the steep MLF indicated in the AMT section in depths from 200 m to 1 km (Fig. 12).

The integrated interpretation of the geophysical data sets gained from different geophysical techniques was found successful. Gravity modelling is naturally ambiguous and we can create many different models whose gravity effect will match the observed data. Gravity modelling begins with the creation of a simple starting model with basic geological units and elements that are further modified. To overcome the inherent ambiguity of gravity modelling it is convenient to use results of other geophysical methods. We adjusted the starting gravity model in compliance with the ERT section (a wide fault zone had been added to the starting model). A final gravity model shows a good match between the observed and modelled gravity values. It confirms the importance of integrated interpretation of different geophysical data sets.

The AMT survey shows higher resistivities of the crystalline complex of the KEM (up to 700 Ωm) on the east compared to the lower resistivities of granites (up to 100 Ωm) on the west. This agrees well with the blocky-fabric resistivity model of *Flechsig et al. (2010)* who found a high resistive block in the east in contrast to lower resisitive block in the basement of the Cheb Basin. The application of AMT measurements in the Cheb Basin proved that even in an industrial area like the West Bohemia deep electromagnetic methods can be successfully used to image the deeper part of the section in a short time at small costs.

The ERT survey revealed a 100 m wide steeply dipping low-resistivity zone (Fig. 11), which coincides with the position of the MLF indicated by the gravity model (Fig. 10) and with the basin infill limit identified by the trenching survey (*Štěpančíková et al., 2015*).

This zone is indicated also in seismic section showing large horizontal velocity gradient (Fig. 13). The low-resistivity zone could be explained by different mechanisms and/or their combinations: (i) intensively fractured water-saturated rocks with a certain clay content, which was formed by the faulting activity along MLF; (ii) deeply weathered crystalline rocks of the KEM unit, possibly also due to hydrothermal processes; (iii) colluvial wedges with clayey matrix originating from the uplifted weathered KEM crystalline unit, which were covered by basin sediments.

Both ERT sections (C and D in Fig. 11) suggest a "step-like" structure of the Cheb basin with possible vertical differentiation of individual blocks and their subsidence along the fault planes. This is in accordance with findings of other authors (*Špičáková et al., 2000*; *Peterek et al., 2011*).

It should be noted that we identify the fault zone in the depth by geophysical methods only indirectly. In the gravity model the fault is identified as a contact of granite and crystalline complex down to 8-km depth and as a wedge of low density rocks in shallow depth. In the resistivity model it corresponds to the margin between the lower resistivity of the granite massif and the higher resistivity of the crystalline unit in depths below 200 m and to the low resistive weathered crystalline in shallower depths. The MLF position identified in this study matches the eastern edge of the Cheb Basin, which is traditionally considered as MLF also in geological models (*Špičáková et al., 2000*; *Peterek et al., 2011*). It also agrees with the recent seismic reflection study of *Halpaap et al. (2018)*, which found dipping reflectors at the eastern edge of the Cheb Basin.

7. CONCLUSIONS

The EMF of the Cheb Basin separates the basin sediments overlying granites of the Smrčiny/Fichtelgebirge massif on the west from the KEM crystalline unit on the east. The EMF is a northern segment of the MLF zone, an important NW-SE tectonic line, which has been reactivated several times in geological history. A detailed geophysical survey of the EMF at the Kopanina site resulted in the following findings:

- The area of expected EMF position is characterized by up to 100 m wide zone of low resistivity, low density and low seismic velocity. This could indicate a zone of intensively fractured and weathered rocks along the fault zone.
- The EMF generally steeply dips towards SW; the angle increases from about 60° near the surface to 80° in the deeper parts.
- The ERT sections suggest a block-like structure of the Cheb basin with possible differential subsidence of individual blocks along the fault planes.
- The low resistivity of granites forming the basement rocks of the northern part of the Cheb Basin points to their alteration by intensive and deep weathering.

The integrated geophysical survey benefited from complementary character of the various geophysical results, enabled optimized data processing, and provided solid data for geological interpretation.

Acknowledgements: The research was supported by the Czech Science Foundation by grant No. 16-10116J and by the Institutional Research Plan RVO 67985891 of the Institute of Rock Structure and Mechanics CAS, v.v.i.

References

Bankwitz P., Schneider G., Kämpf H. and Bankwitz E., 2003. Structural characteristics of epicentral areas in Central Europe: study case Cheb Basin (Czech Republic). *J. Geodyn.*, **35**, 5–32, DOI: 10.1016/S0264-3707(02)00051-0.

Behr H.-J., Dürbaum H.-J. and Bankwitz P., 1994. Crustal structure of the Saxothuringian Zone: results of the deep seismic profile MVE-90 (East). *Z. Geol. Wiss.*, **22**, 647–770.

Blecha V. and Štemprok M., 2012. Petrophysical and geochemical characteristics of late Variscan granites in the Karlovy Vary Massif (Czech Republic) - implications for gravity and magnetic interpretation at shallow depths. *J. Geosci*., **57**, 65–85.

Blecha V., Štemprok M. and Fischer T., 2009. Geological interpretation of gravity profiles through the Karlovy Vary Granite Massif (Czech Republic). *Stud. Geophys. Geod*., **53**, 295–314.

Blížkovský M., Čejchanová B., Friáková O., Hanák J., Kadlec E., Mitrenga P., Novák M., Novotný A., Ondra P. and Švancara J., 1981. *Construction of the Stripped Gravity Map of the Bohemian Massif on the Basis of Revision of Density Data, Part II. Density Data on the Bohemian Massif on the Territory of ČSR*. Geofyzika n.p., Brno; Czech Geological Survey - Geofond, Prague, Czech Republic (in Czech).

Bräuer K., Kämpf H., Niedermann S. and Strauch G., 2005. Evidence for ascending upper mantle-derived melt beneath the Cheb Basin, central Europe. *Geophys. Res. Lett.*, **32**, L08303, DOI: 10.1929/2004GL022205.

Breiter K., 2012. Nearly contemporaneous evolution of the A- and S-type fractionated granites in the Krušné hory/Erzgebirge Mts, Central Europe. *Lithos*, **151**, 105–121.

Edwards L.S., 1977. A modified pseudosection for resistivity and IP. *Geophysics*, **42**, 1020–1046.

Fischer T., Štěpančíková P., Karousová M., Tábořík P., Flechsig C. and Gaballah M., 2012. Imaging the Mariánské Lázně Fault (Czech Republic) by 3-D ground-penetrating radar and electric resistivity tomography. *Stud. Geophys. Geod.*, **56**, 1019–1036, DOI: 10.1007/s11200-012-0825-z.

Fischer T., Horálek J., Hrubcová P., Vavryčuk V., Bräuer K. and Kämpf H., 2014. Intra-continental earthquake swarms in West-Bohemia and Vogtland: a review. *Tectonophysics*, **611**, 1–27, DOI: 10.1016/j.tecto.2013.11.001.

Flechsig C., Fabig T., Rücker C. and Schütze C., 2010. Geoelectrical investigations in the Cheb Basin/W-Bohemia: an approach to evaluate the near-surface conductivity structure. *Stud. Geophys. Geod.*, **54**, 443–463.

Friedrichs B., 2004, *Mapros*, Ver. 0.87b freeware, https://www.geo-metronix.de/mtxgeo/images /wiki/Software/mapros_07/Setup.zip.

GM-SYS Modelling, 2017. *http://www.geosoft.com/products/gm-sys*.

Günther T., Rücker C. and Spitzer K., 2006. Three-dimensional modelling and inversion of dc resistivity data incorporating topography - II. Inversion. *Geophys. J. Int.*, **166**, 506-517.

Guy A., Edel J.B., Schulmann K., Tomek Č. and Lexa O., 2011. A geophysical model of the Variscan orogenic root (Bohemian Massif): implications for modern collisional orogens. *Lithos*, **124**, 144–157.

Halpaap F., Paschke M. and Bleibinhaus F., 2018. Shallow Reflection Seismic Evidence of Tectonic Activity in the Cheb Basin, NW Bohemia. *Stud. Geophys. Geod.*, **62**, 80–101, DOI: 10.1007/s11200-016-0386-7.

Hansen P.Ch. and O'Leary D., 1993. The use of the L-curve in the regularization of discrete ill-posed problems. *SIAM J. Sci. Comput.*, **14**, 1487–1503.

Hecht L., Vigneresse J.-L. and Morteani G., 1997. Constraints on the origin of zonation of the granite complexes in the Fichtelgebirge (Germany and Czech Republic): evidence from a gravity and geochemical study. *Geol. Rundsch.*, **86**, S93–S109.

Hofmann I., Jahr T. and Jentzsch G., 2003. Three-dimensional gravimetric modelling to detect deep structure of the region Vogtland/NW-Bohemia. *J. Geodyn.*, **35**, 209–220.

Hrouda F. and Chlupáčová M., 1993. A petrophysical study, part II: densities, magnetic properties, elasticity and radioactivity. In: Vrána S. and Štědrá V. (Eds), *Geological Model of Western Bohemia in Relation to the Deep Borehole (KTB-1) in FRG*. Czech Geological Survey - Geofond, Prague, Czech Republic.

Kolářová M., 1965. Hydrogeology of the Cheb Basin. *J. Geol. Sci. (Hydrogeol.)*, **3**, 7–101 (in Czech with English abstract).

Krawczyk C.M., Stein E., Choi S., Oetinger G., Schuster K., Götze H.-J., Haak V., Oncken O., Prodehl C. and Schulze, A., 2000. Geophysical constraints on exhumations mechanism of high-pressure rocks: the Saxo-Thuringian case between the Franconian Line and Elbe Zone. In: Franke W., Haak V., Oncken O. and Tanner, D. (Eds), *Orogenic Processes: Quantification and Modelling in the Variscan Belt*. *Geol. Soc. London Spec. Publ.*, **179**, 303–322.

Loke M.H., 1997. Electrical imaging surveys for environmental and engineering studies. A practical guide to 2-D and 3-D surveys. http:// www.geotomosoft.com/.

Malkovský M., 1987. The Mesozoic and Tertiary basins of the Bohemian Massif and their evolution. *Tectonophysics*, **137**, 31–42.

Mlčoch B., Bezděková Š, Breiter K., Čápová D., Fifernová M., Holub F.V., Jelenová M., Jeřábek P., Rapprich V., Sedláček J. and Skácelová Z., 2008. *3D Modeling of the Bedrock Relief of the Cheb and Sokolov Basins*. Czech Geological Survey - Geofond, Prague, Czech Republic (in Czech).

Mrlina J., Kämpf H., Kroner C., Mingram J., Stebich M., Bräuer A., Geissler W.H., Kallmeyer J., Matthes H. and Seidl M., 2009. Discovery of the first Quaternary maar in the Bohemian Massif, Central Europe, based on combined geophysical and geological surveys. *J. Volcanol. Geotherm. Res.*, **182**, 97–112, DOI: 10.1016/j.jvolgeores.2009.01.027.

Pazdírek O. and Bláha V., 1996. Examples of resistivity imaging using ME-100 resistivity field acquisition system. Extended Abstract. *58th EAGE Conference and Exhibition*, DOI: 10.3997/2214-4609.201408817.

Pek J., Santos F. A. M. and Li Y., 2012. Non-linear conjugate gradient magnetotelluric inversion for 2-D anisotropic conductivities. In: Börner R.-U. and Schwalenberg K. (Eds), *Proceedings of the 24-th Schmucker-Weidelt Colloqium "Electromagnetic Depth Investigations"*, Neustadt an der Weinstraße, 19.–23. September 2011. Deutsche Geophysikalische Gesellschaft, Hamburg, Germany, 187–206.

Peterek A., Reuther C.D. and Schunk R., 2011. Neotectonic evolution of the Cheb Basin (Northwestern Bohemia, Czech Republic) and its implications for the late Pliocene to Recent crustal deformation in the western part of the Eger Rift. *Z. Geol. Wiss*., **39**, 335–365.

Rücker C., Günther T. and Spitzer K., 2006. Three-dimensional modelling and inversion of dc resistivity data incorporating topography - I. Modelling. *Geophys. J. Int.*, **166**, 495–505.

Sedlák J., Gnojek I., Scheibe R. and Zabadal S., 2009. Gravity response of igneous rocks in the northwestern part of the Bohemian Massif. *J. Geosci*., **54**, 325–342.

Simpson F. and Bahr K., 2005. *Practical Magnetotellurics*. Cambridge University Press, Cambridge, U.K., 272 pp.

Špičáková L., Uličný D. and Koudelková G., 2000. Tectonosedimentary evolution of the Cheb Basin (NW Bohemia, Czech Republic) between Late Oligocene and Pliocene: a preliminary note. *Stud. Geophys. Geod*., **44**, 556–580.

Štemprok M., 1986. Petrology and geochemistry of the Czechoslovak part of the Krušné Hory Mts. granite pluton. *Sbor. Geol. Věd Lož. Geol. Mineral.*, **27**, 111–156.

Štemprok M. and Blecha V., 2015. Variscan Sn-W-Mo metallogeny in the gravity picture of the Krušné Hory/Erzgebirge granite batholith (Central Europe). *Ore Geol. Rev*., **69**, 285–300.

Štěpančíková P., Tábořík P., Fischer T., Hartvich F., Karousová M., Stemberk J. and Nováková L., 2015. Holocene activity of the Mariánské Lázně Fault (Cheb basin, Bohemian Massif): youngest proved surface faulting in central Europe? In: Blumetti A.M., Cinti F.R., De Martini P.M., Galadini F., Guerrieri L., Michetti A.M., Pantosti D. and Vittori E. (Eds), *6th International INQUA Meeting on Paleoseismology, Active Tectonics and Archaeoseismology, 19-24 April 2015, Pescina, Fucino Basin, Italy*. *Miscellanea INGV*, **27** 478–480.

Švancara J., Havíř J. and Conrad W., 2008. Derived gravity field of the seismogenic upper crust of SE Germany and West Bohemia and its comparison with seismicity. *Stud. Geophys. Geod.*, **52**, 567–588.

Swift C.M., 1967. *A Magnetotelluric Investigation of an Electrical Conductivity Anomaly in the South Western United States*. Ph.D. Thesis. Massachusetts Institute of Technology, Cambridge, MA

Tomek Č., Dvořáková V. and Vrána, S., 1997. Geological interpretation of the 9HR and 503M seismic profiles in Western Bohemia. In: Vrána S. and Štědrá V. (Eds.), *Geological Model of Western Bohemia Related to the KTB Borehole in Germany*. *J. Geol. Sci.*, **47**, 43–50.

Příloha 2

Geophysical evidence of the Mariánské Lázně Fault (Cheb Basin, Czech Republic)

7TH INTERNATIONAL GEOSCIENCES STUDENT CONFERENCE

Tábořík et al. 2016

Tábořík P., Fischer T., Vilhelm J., Blecha V., Štěpančíková P., Jirků J., Vlček J., Hartvich F. (2016): Geophysical evidence of the Mariánské Lázně Fault (Cheb Basin, Czech Republic). In Drwiła M., Kotlarek P., Kubalski J. P. (eds.): Conference Proceedings of 7th International Geosciences Student Conference. 145–147. ISBN 978-83-945593-0-4

Geophysical evidence of the Mariánské Lázně Fault (Cheb Basin, Czech Republic)

Petr Tábořík[1, 2], Tomáš Fischer[1], Jan Vilhem[1], Vratislav Blecha[1], Petra Štěpančíková[2], Jaroslav Jirků[1], Josef Vlček[1, 2] and Filip Hartvich[2]

email: petr.taborik@natur.cuni.cz

[1] Charles University in Prague, Institute of Hydrogeology, Engineering Geology and Applied Geophysics

[2] Czech Academy of Sciences, Institute of Rock Structure and Mechanics

Summary

A subsurface manifestation of the Mariánské Lázně Fault was investigated by means of combined geophysical surveying and integrated interpretations of measured data sets. The integrated results of the electrical resistivity tomography, shallow refraction seismics and gravity survey indicate a wide steeply inclined fault zone, likely formed of intensively disrupted and weathered crystalline rocks, and delimiting the sedimentary infill of the Cheb basin from the crystalline rocks of the Krušné hory Mts. Importance of employing more than a single geophysical technique and subsequent integrated interpretation of the various geophysical data sets was confirmed.

Introduction

In order to depict subsurface manifestation of the Mariánské Lázně Fault (MLF), a complex geophysical surveying was performed during years 2010-2014 at the Kopanina site. The study site is situated in the Cenozoic Cheb basin (western part of the Bohemian Massif), bordered by the NW-trending Mariánské Lázně Fault in the northeast. The Cheb basin is a part of the Cheb-Domažlice graben on its intersection with NE-trending Eger rift. The area belongs to most active seismic zones in central Europe. The Kopanina site is located in immediate proximity of the Nový Kostel zone, which is known for the frequent earthquake swarms and also for the CO_2 emanations. Besides the detailed shallow investigation of the near-surface fault manifestation by means of integrated interpretation of the geoelectrical and trenching survey, which has been published in Fischer et al. (2012) and Štěpančíková et al. (2015), we focused on the detection and tracking the MLF into the depth.

Methods

For the deep geophysical survey we used the ERT survey complemented with shallow seismic refraction method and, earlier performed gravity survey. Two ERT profiles with length of 1 km and with 10 m electrode spacing were measured in order to gain maximum possible depth of penetration (up to 200 m). We employed ARES I device (GF Instruments, Czech Rep.) with 25 multi-electrode cable sections with maximum possible number of 200 simultaneously connected electrodes. We measured with the Wenner-Schlumberger electrode array. The profiles (C and D) were parallel with mutual distance 100 m, perpendicularly to the assumed fault line and with expected position of the fault in the centre of the array. Measured data sets were processed by Res2Dinv (Geotomo Software) and depicted as inverted resistivity models representing a distribution of modelled real resistivity in section along the profiles. Shallow seismic refraction measurements were carried out in the same trace as ERT profile C with total length of 465m and geophone distance 5 m. Three Geode seismographs (Geometrics, USA) with 72 geophones connected simultaneously were combined. Total profile length was reached by using roll-along

measurement system. As a seismic signal source we combined seismic sledge-hammer (triggered by accelerometer) and Seismic Impulse Source System – SISSY (Geosym, Germany), using blank shotgun shells. Data were processed using seismic tomography approach based on the first arrivals of the P-waves. The SeisImager – PickWin software was used for the arrival times picking. The tomographic inversion was performed in the SeisImager – Plotrefa (OYO Corp.). The final results were depicted as a P-wave velocity distribution model. Gravity survey was performed on three profiles – P1 with length 900 m and measurement step of 5 m, and two parallel profiles P2 a P3 of 500 m length with step of 10 m. Measurements were carried out using Scintrex CG-3M Autograv gravimeter and gravity stations were levelled (using levelling device and levelling rod). Bouguer anomalies were calculated from the measured gravity values and GM-SYS program (Geosoft Inc., 2015) for forward 2.5-D modelling was used. The P1 profile was situated in the trace of the geoelectric and seismic profile.

Results

The deep ERT survey confirmed a steeply inclined low resistivity fault zone of MLF with values of < 70 Ω.m on both parallel profiles (profiles C and D). Sandy sedimentary infill of the Cheb Basin is clearly distinguishable south-westwards of the fault zone with resistivity values between 70 – 500 Ω.m, typical for the sands and sand-dominated sediments. Situation north-eastwards of the fault zone is slightly more complicated. Resistivity values of the crystalline rocks ranging from ca. 20 Ω.m to 950 Ω.m, where the highest values probably represent rigid and non-weathered bedrock, whereas lower values stand for a weathered crystalline. The resistivity values further decrease (to first tens of Ω.m) with increasing intensity of weathering (Figure 1). The 2.5-dimensional gravity model revealed a possible transition zone with medium values of density (2200 kg/m^3) is wedged between basin sedimentary infill (2065 kg/m^3) and crystalline rocks represented by mica-schists (2740 kg/m^3). Similarly, the shallow seismic refraction survey with limited depth of penetration (< 50 m) shows a rapid velocity drop at the position of the interpreted fault.

Conclusions

The vertically inclined zone of low resistivity values likely does not represent a sedimentary body, but a tectonically disrupted margin of the crystalline rock steeply dipping along the MLF. High intensity of disruption and intensive argillaceous-type weathering, together with probable higher content of water causes the low resistivity of this zone. This hypothesis was also confirmed by gravity model which supposes the fault zone of medium density wedged between basin sediments and crystalline. Considering the density values of ~ 2200 kg/m^3, it confirms the assumption of tectonically weakened zone of the crystalline rock. The drop in velocity of seismic waves is, also, in agreement with other two methods. Determination of the inclination/slant of the MLF is, however, very disputable due to the very wide disrupted fault zone. Nevertheless, the integrated interpretation of the geophysical data sets gained from different geophysical techniques brought one more positive result – the original gravity model was adjusted in compliance with ERT model and the above mentioned wide disrupted fault zone had been added to the model. A new gravity model gains even better match between observed and modelled (calculated) curves of the gravity values. It confirms the importance of integrated interpretation of different geophysical data sets. The integrated interpretation brings (i) a cross-validation of the various geophysical results, (ii) a reinterpretation and possible processing optimisation of the data, and last but not least (iii) an improvement of final geological interpretations.

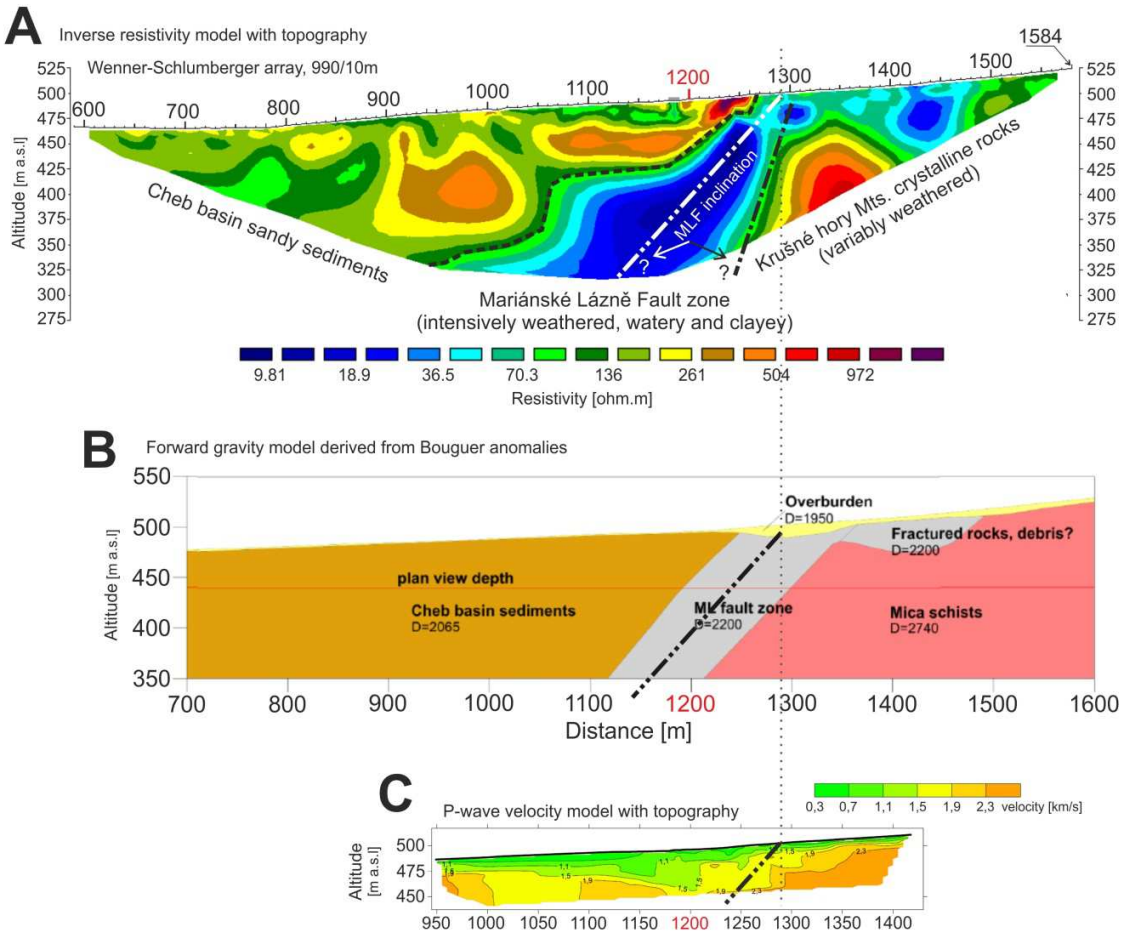


Figure 1 *Integrated interpretation of measured geophysical data sets: (A) Inverse resistivity model with topography and geological interpretation of main subsurface structures, (B) Gravity model derived from Bouguer anomalies (Profile P1), (C) P-wave velocity model with topography*

Acknowledgements

The research was supported by Grant Agency of Czech Academy of Sciences, project No. IAA300120905 and Czech Science Foundation No.16-10116J.

References

Fischer, T., Štěpančíková, P., Karousová, M., Tábořík, P., Flechsig, C., Gaballah, M. (2012). Imaging the Mariánské Lázně Fault (Czech Republic) by 3-D ground-penetrating radar and electric resistivity tomography. Stud. Geophys. Geod. 56: 1019-1036.

Štěpančíková, P., Tábořík, P., Fischer, T., Hartvich, F., Karousová, M., Stemberk, J., Nováková, L. (2015): Holocene activity of the Mariánské Lázně Fault (Cheb basin, Bohemian Massif): youngest proved surface faulting in central Europe? In: Blumetti AM et al. (eds): Abstracts Volume 6th International INQUA Meeting on Paleoseismology, Active Tectonics and Archaeoseismology 19-24 April 2015, Pescina, Fucino Basin, Italy. Miscellanea INGV, n. 27, 478-480

Conference Proceedings of 7th International Geosciences Student Conference

Editors: Małgorzata Drwiła, Paulina Kotlarek, Jacek Piotr Kubalski

Student Technical Oral Session Chairmen:

GEOLOGY: Andrew Robinson *(Statoil)* and Jan Król *(AMU Poznań)*

GEOPHYSICS I: Norbert Smalera *(PGNiG)* and Grzegorz Lizurek *(Institute of Geophysics PAS)*

GEOPHYSICS II: Koya Suto *(Australian Society of Exploration Geophysicists)* and Maciej Mendecki *(University of Silesia)*

OIL & GAS: Klaus Fischer *(Wintershall)* and Elżbieta Wójcik *(MAX Solutions)*

Publisher: Studenckie Koło Naukowe Geofizyków PREM Uniwersytetu Śląskiego

ISBN: 978-83-945593-0-4

Katowice, July 2016





Příloha 3

Late Quaternary Activity of Central European Fault Driven by Ice Loading as revealed by geological data and modeling

Earth Surface Processes and Landforms

Štěpančíková et al. under review

Štěpančíková P., Rockwell T. K., Stemberk J. jr., Hartvich F., Hók J., Luttrell K., Myers M., Nývlt D., Ortuño M., Rhodes E. J., Rood D. H., Tábořík P., Wechsler N. (2022, under review): Late Quaternary Activity of Central European Fault Driven by Ice Loading as revealed by geological data and modeling. Earth Surface Processes and Landforms.

Late Quaternary Activity of Central European Fault Driven by Ice Loading as revealed by geological data and modeling

Petra Štěpančíková [1)*], Thomas K. Rockwell [1,2)], Jakub Stemberk [1,3)], Filip Hartvich [1,3)], Jozef Hók [4)], Karen Luttrell [5)], Madeline Myers [5,6)], Daniel Nývlt [7)], María Ortuño [8)], Edward J. Rhodes [9,10)], Dylan H. Rood [11)], Petr Tábořík [1,3)], Neta Wechsler [12)]

[1)] *Inst. of Rock Structure and Mechanics, Czech Acad. of Sci., Prague, Czech Rep.*
[2)] *Dept. of Geol. Sci., San Diego State Univ., California*
[3)] *Faculty of Science, Charles Univ., Prague, Czech Rep.*
[4)] *Faculty of Science, Comenius Univ., Bratislava, Slovakia*
[5)] *Dept. of Geology and Geophysics, Louisiana State Univ., Baton Rouge, Louisiana*
[6)] *Dept. of Geography and Planning, Queen's University, Kingston, Ontario, Canada*
[7)] *Faculty of Science, Masaryk Univ., Brno, Czech Rep.*
[8)] *Risknat-Institute Geomodels, Dept. of Earth and Ocean Dynamics, University of Barcelona, Spain*
[9)] *Dept. of Geography, Univ. of Sheffield, S10 2TN UK*
[10)] *Dept. of Earth, Planetary and Space and Sciences, University of California Los Angeles, CA, USA*
[11)] *Dept. of Earth Science and Engineering, Royal School of Mines, Imperial College London, UK*
[12)] *Neev Center for Geoinfomatics, Fredy & Nadine Herrmann Institute of Earth Sciences, The Hebrew University of Jerusalem, Israel*

Abstract

We studied the NW-SE trending Sudetic Marginal Fault (SMF), situated at the northeastern limit of the Bohemian Massif in central Europe, to assess its potential seismic hazard to the region. Eighteen trenches and twenty-nine electric resistivity profiles were performed at Bílá Voda to study the 3-dimensional distribution of a beheaded alluvial fan on the NE side of the fault. We interpret a small drainage, located about 29-45 m to the SE of the fan apex, as the only plausible source channel implying a similar amount of left-lateral offset. The alluvial fan deposits yielded radiometric ages that ranged between about 24 and 63 ka, but post glacial deposits as old as 11 ka are not displaced, indicating that all motion occurred in the late Pleistocene. The site lies ~150 km south of the late Pleistocene Weichselian maximum (~20 ka) ice sheet front. We model the effects of the ice load on lithospheric flexure and stress orientation and show that slip on the SMF was promoted by the presence of the ice sheet, resulting in a late Pleistocene slip rate of ~$1.1^{+2.3}/_{-0.6}$ mm/yr. As the most favorable time for glacial loading-induced slip would be during the glacial maximum between about 24 and 12 ka, it is doubtful that the slip rate remained constant during the entire period of activity, and if most slip occurred during this period, the rate may have been as high as 2.5 ± 0.5 mm/yr. Our observations also indicate that the likelihood of continued motion and earthquake production is low in the absence of an ice sheet when considering that the modern maximum principal stress ($\sigma 1$) is oriented nearly parallel to the Sudetic Marginal fault (NNW-SSE) and is thus unfavorable for fault motion.

1. Introduction

The Sudetic Marginal Fault (SMF) is a major NW striking structural element situated at the northeastern limit of the Bohemian Massif that exhibits a pronounced morphological escarpment which indicates that the fault has been active in the Quaternary (Fig. 1). It is a part of the regional-scale WNW-striking Elbe Fault System, which has had variable kinematics since the Late Carboniferous Variscan orogeny (Scheck et al., 2002). The fault likely initiated with a predominantly

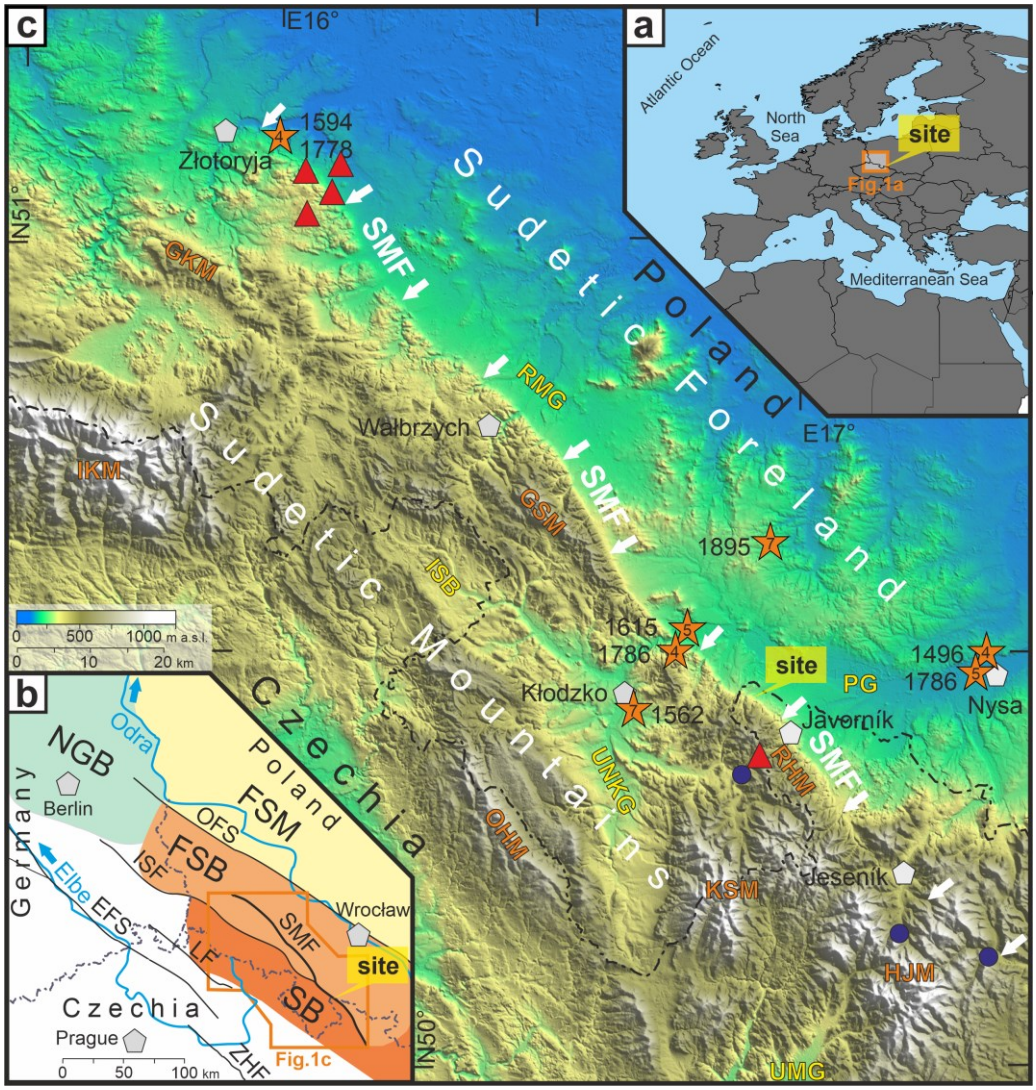


Fig. 1 a) Site localization on the Europe map; b) Simplified geological map modified after Scheck et al. (2002). Main faults and fault zones: EFS – Elbe fault system zone, ISF – Intra-Sudetic main fault, LF – Lužický fault, OFS – Odra fault zone, SMF – Sudetic Marginal Fault, ZHF – Železné hory fault; Main geological units: FSB – Fore-Sudetic block, FSM – Fore-Sudetic Monocline, NGB – North German basin, SB – Sudetic block; c) Relief map of the Sudetes using SRTM (resolution 30m; Farr (Eds.), 2007). The Sudetic Marginal fault (SMF) forms a border between Sudetic Mts. on the SW side and Sudetic Foreland on the NE side. Orange stars: epicenters of historical earthquakes with intensity (I_0) and year; Rectangles: Tertiary volcanoes; Blue dots – thermal and mineral springs; Basins: ISB – Intra-Sudetic Basin, PG – Paczków Graben, RMG – Roztoki–Mokrzeszow graben, UMG – Upper Moravia Graben, UNKG – Upper Nysa Kłodzka Graben. Mountains: GKM – Góry Kaczawskie Mts., GSM – Góry Sowie Mts., HJM – Hrubý Jeseník Mts., OHM – Orlické hory Mts., IKM – Izera - Krkonoše Mts., KSM – Kralický Sněžník Mts., RHM – Rychlebské hory Mts./Góry Złote Mts.

dextral sense of slip (Oberc, 1991) but then acted as a normal fault during a period of early Late Cretaceous basin formation. The sense of slip was reversed in the Late Cretaceous (Danišík et al., 2012) during transpressional deformation induced by far-field stress from Europe-Iberia-Africa convergence, which resulted in basin inversion in much of central Europe (Scheck et al., 2002; Kley and Vogt, 2008). The fault was reactivated in the Miocene as a transtensional oblique-slip structure that cuts Oligocene intrusions (Birkenmajer et al., 1977), and its normal component of motion resulted in the accumulation of 300-600 m of fluvial and lacustrine sediments in several sub-basins in northeastern Czech Republic and southwestern Poland (Oberc and Dyjor, 1969; Dyjor, 1983; Badura et al., 2004). The uplift of the footwall of the SMF, which is responsible for the current mountainous topography, is considered to have started in Miocene/Pliocene time (Dyjor, 1983; Krzyszkowski et al., 2000). The question is whether the Sudetic Marginal fault remains active today in the modern tectonic regime and is therefore a potential seismic hazard to central Europe.

Identification of active faults is important to correctly assess seismic hazard to societies, especially in light of recent nuclear power plant (NPP) disasters such as in Japan in 2011 (Fukushima). However, intraplate Europe is generally known as a region of low seismicity, nevertheless there are several cases where Late Quaternary faulting has been identified. A fundamental question is whether these faults are capable of producing earthquakes in the near future or whether motion on these faults is a consequence of conditions that no longer exist.

Evidence for Quaternary reactivation of the SMF is found in the geomorphology of the landscape along the fault, including a relatively linear 130 km-long mountain front that expresses triangular or trapezoidal facets, hanging wine-glass valleys and deep incision of the Sudetic Mountains with consequent deposition of alluvial fans along the range margin (Fig. 1; Badura et al., 2007; Krzyszkowski and Pijet, 1993; Krzyszkowski et al., 2000). Along the Polish portion of the fault, middle Pleistocene fluvial terraces are truncated by the SMF and show scarp heights of 15-25 m, whereas Late Pleistocene terraces have scarp heights of 10-15 m (Krzyszkowski et al., 2000). There is also sparse microseismicity and rare historical moderate earthquakes (I_0=VII° MSK-64) that suggest that this fault is still a potential seismic threat to the region (Guterch and Lewandowska-Marciniak, 2002; Fig. 1c).

The activity on seismogenic faults, while mostly driven by far-field plate tectonics forces, can also be affected by near-field changes in the crustal stresses, which may either promote or inhibit seismic activity. Sources of significant stress change can result from activity on near-by faults (King et al., 1994), which predominates over one or several seismic cycles, and vertical load changes caused by climate driven mass fluctuations, which include volumetric variations in ocean basins, ice caps, glaciers and lakes and associated erosion-deposition processes (Stewart et al., 2000; Luttrell et al., 2007; Luttrell and Sandwell, 2010; Hampel et al., 2010) that act over longer time scales. Related fluid pressure effects also play a part in changing seismicity patterns and earthquake nucleation processes (Byerlee, 1993). Moreover, it was demonstrated that seismic activity can ensue after deglaciation in otherwise seismically quiescent continental shields and cause faulting in previously inactive areas, such as the northern Europe (Stewart et al., 2000; Brandes et al., 2015; Steffen et al., 2021). The effect of mass loading and unloading on crustal deformation can extend to several hundred kilometers beyond the limits of the loading mass (James and Bent, 1994).

We present here the results of a field paleoseismic study where geological and geophysical data show that the Sudetic Marginal Fault in northeastern Bohemian Massif (Czech Republic) in central Europe sustained major displacement in latest Pleistocene time, yet no displacement in the Holocene. Modeling demonstrates that the presence of the northern European ice-sheet during the last glacial maximum caused sufficient driving stress to promote fault motion, followed by at least 11 thousand years of inactivity after removal of the ice. There may be many such faults in Europe that were activated by ice-loading and may not represent a current seismic hazard. Identification of which faults are currently active versus those that sustained motion due to ice-loading is critical in the correct assessment of seismic hazard in Europe and worldwide.

2. Methods

2.1. Trenching

The study region currently experiences a temperate climate, resulting in complete coverage of dense vegetation, and has an erosion rate that is higher than rates of tectonic processes resulting in few natural exposures. Consequently, the excavation of trenches was necessary to study the late Quaternary activity of the SMF. We excavated 9 trenches across and 9 trenches parallel to the fault near the village of Bílá Voda in northeastern Czech Republic with a backhoe (Fig. 2). The faces of the one-meter-wide trenches were cleaned with metal scrappers, gridded with string at half-meter intervals, and then photographed, from which we constructed photomosaics of each trench face. The trenches were logged in the field, and sample locations were recorded on the logs. The locations of all trenches were surveyed with a total station tied to geodetic benchmarks.

2.2. Dating

Chronological control for the sediments displaced by the fault, as well as the sediment that caps the fault, was provided by several different techniques, including ^{14}C, Cosmogenic Radionuclide (CRN) dating, Optically Stimulated Luminescence (OSL) and Infra-Red Stimulated Luminescence (IRSL). Results from these techniques provide a framework for development of the site chronology (Table 1). There is broad concordance in age within and between the different techniques, though with some complexity in places (see Supplementary section S2 Chronology).

2.2.1. ^{14}C Dating

We applied ^{14}C dating to samples of detrital charcoal and bulk soil samples collected from the various stratigraphic units. The majority of the charcoal was cleaned in D.I. water at the SDSU (San Diego State University) Quaternary Laboratory, hand-picked with a steel needle under a microscope, and sent to the CAMS facility at UCI (University of California in Irvine) for dating using standard protocol. The other charcoal samples were dated at facilities in GADAM center in Gliwice (Poland), Poznań Radiocarbon Laboratory (Poland), and Kyiv Radiocarbon Laboratory (Ukraine). The samples were processed using the standard published protocols of the individual dating laboratories (e.g. Brock et al., 2010). Calibrated ages of radiocarbon dates (Table 1), reported at 2σ uncertainty, were calculated

using the on-line program OxCal v4.3.1 (Bronk Ramsey, 2009) and applying the IntCal13 atmospheric curves (Reimer et al., 2013).

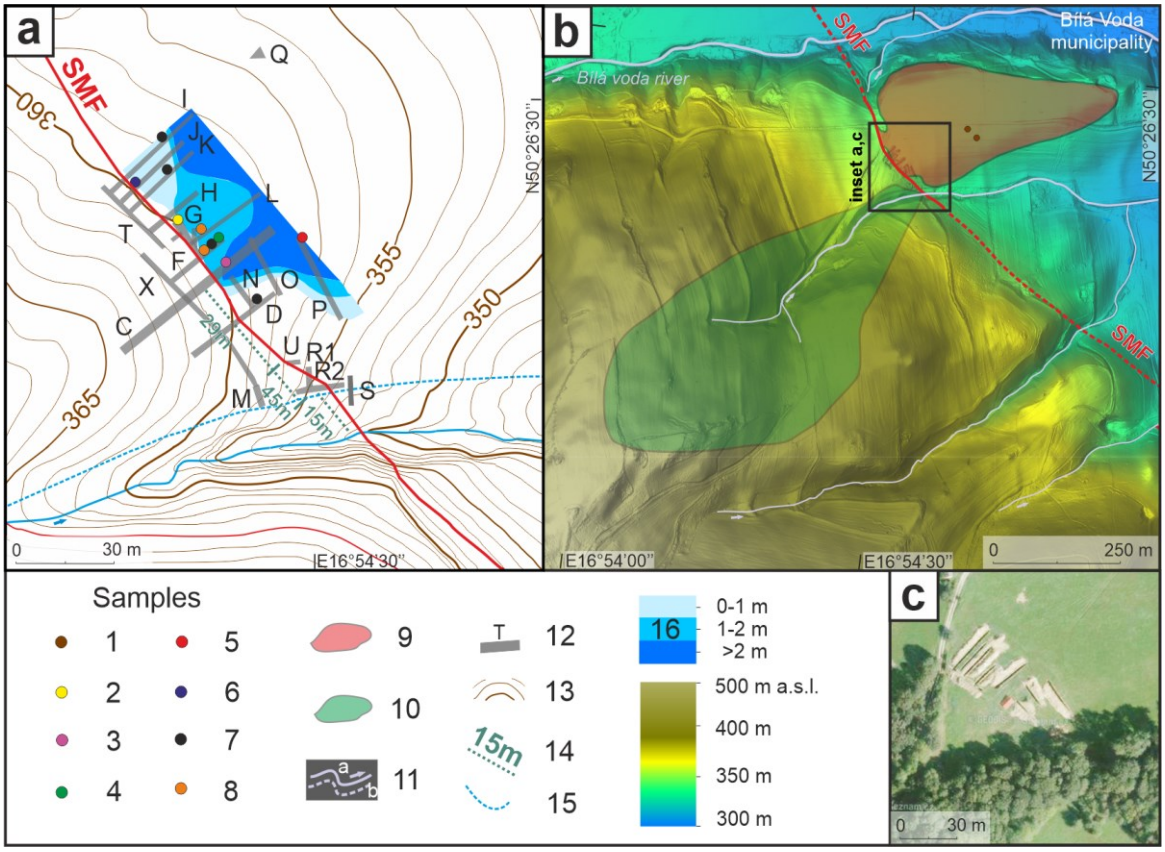


Fig. 2. a) Contour lines map of the trenching site. Sample positions and results of all dating methods on the isopach map of the alluvial fan deposits derived from the trenches, for results see Tab. 1; b) Relief map of the trenching site based on LIDAR data DEM. Note the alluvial fan and its probable source valley; c) Aerial photo of the site from 2012 (source: www.mapy.cz; accessed 03 Jun 2020). 1 – reddish soil, 2 – OSL dated sediments, 3 – $IRSL_{225}$ alluvial fan deposits + geliflucted deposits + Holocene deposits, 4 – ^{10}Be dating in alluvial fan deposits, 5 – ^{14}C dated charcoals/bulk, 6 – alluvial fan deposits derived from geophysical survey, 7 – source area of the alluvial fan deposits, 8a – current channel, 8b – inferred feeder channel, 9 – trench, 10 – contour line interval 1 m, 11 – approximate offset measurements, 12 – isopach map of the alluvial fan deposits based on trenches.

2.2.2. Luminescence Dating

We applied two luminescence techniques to date sandy sediments in the various trenches: OSL and IRSL. The OSL samples were collected by driving opaque tubes into the trench wall, extracted, and wrapped in foil to preclude light damage. The samples were taken to the luminescence dating laboratory at GADAM Centre in Gliwice, Poland and processed using their standard published protocols. Quartz was separated under controlled light conditions in the lab, and the single aliquot regenerative method was applied to multi-grain aliquots of quartz grains. Dose rate samples were taken from the ends of the tubes. Ages were calculated using the Central Age Model (CAM) which calculates the weighted average including all equivalent doses (Galbraith et al., 1999).

IRSL samples were collected in aluminum tubes hammered into cleaned vertical walls of Trench F. Twelve samples were collected in a sequence from one wall of the Trench F (Fig. S1.1), and one sample from the opposite wall. For each of the 2015 IRSL sample locations (BV15 codes) a measurement of the in-situ gamma dose rate was made with a Rainbow calibrated portable NaI gamma spectrometer. Samples were prepared and measured at the University of Sheffield, UK, following the approach developed for active tectonic contexts described in detail in Rhodes (2015).

In the laboratory, sample tubes were opened under controlled lighting conditions, and unexposed sediment from the central part of each tube used for the dating sample. This material was treated with HCl and H_2O_2 to remove carbonate and organic matter, respectively, and sieved to isolate the 180-212µm fraction. Potassium feldspar grains were separated using a sodium polytungstate heavy liquid with a density of 2.565 gcm^{-3} ("Super-K" separation) and the light fraction was subsequently treated in 10% HF for 10 minutes to clean and etch grains. After rinsing and drying, grains smaller than 180µm were removed by sieving, the remaining material forming the K-feldspar dating fraction. Two angular cobbles of local metamorphic bedrock were collected in the small stream that lies immediately to the west of the site, and K-feldspar grains were also separated from the central unexposed parts of these after crushing using the same procedure. These bedrock samples were used as an additional means to assess anomalous fading of the post-IR IRSL dating signal as performed by Brown et al. (2015).

Single grains of potassium feldspar separated using a "Super-K" (<2.565 gcm^{-3}) approach were dated applying a post-IR IRSL SAR protocol at 225°C, incorporating a pre-heat at 250°C for 60s and a hot bleach for 40s IRSL at 290°C (Rhodes, 2015 and references therein). Fading was assessed directly for each grain and by the measurement of additional bedrock cobble samples, and found to be negligible for the 225°C signal.

Individual grains were mounted in Risø single grain holders under a binocular microscope with dim amber lighting, and measurements made in a Risø TL-DA-20CD DASH automated luminescence reader fitted with a single grain XY dual laser unit. IRSL stimulation used a 150 mW 830 nm IR laser at 90% power for 2.5s passed through a single RG-780 filter to reduce resonance emission at 415 nm, and was detected with an Electron Tube 1" EMD-9107 PMT fitted with a BG3 and BG39 filter combination, transmitting at around 340 - 470 nm. The hot bleach treatment at 290 C incorporated a 40s IRSL exposure using Vishay TSFF 5210 870nm IR diodes at 90% power. Full individual laser exposures (2.5s) to each grain were used for the IRSL stimulation at 50ºC to overcome problems of optical shading of grains.

	SAR step	Measurement parameters
1	Beta irradiation	0 (Nat), 23, 7.4, 74, 230, 740, 0, 23 Gy in turn
2	Preheat	60s at 250°C
3	IRSL 1	2.5s IR laser 90% power at 50°C
4	IRSL 2	2.5s IR laser 90% power at 225°C
5	Beta test dose	8 Gy
6	Preheat	60s at 250°C
7	IRSL S1 Sensitivity measurement	2.5s IR laser 90% power at 50°C
8	IRSL S1 Sensitivity measurement	2.5s IR laser 90% power at 225°C
9	Hot bleach – then return to step 1	40s IRSL (diodes) at 290°C

Table 2. Parameters used in post-IR IRSL dating measurements.

Table 2 details the steps used in post-IR IRSL dating measurements. IRSL data from steps 4 and 8 measured at 225°C were used for age estimation. Following the final 23Gy SAR (Single Aliquot Regenerative-Dose) cycle, each grain was irradiated, preheated and stored for between 2 days to 4 weeks, and subsequently remeasured to assess anomalous fading.

Age estimation was performed in the manner described in Grützner et al. (2017), developed using samples from active tectonic contexts, and which has been shown to provide ages in good agreement with independent age control (Rhodes, 2015). Gamma dose rates were based on in-situ NaI measurements, beta dose rates were calculated based on ICP-MS determinations of U and Th in the sediment, and ICP-OES for K content, an internal K content of 12.5 ± 2.5% was assumed (Huntley and Baril, 1997), cosmic dose rates were based on overburden thickness, and a water content of 15 ± 5% was used. An overdispersion value of 15% was used, based on experience from single grain measurements of quartz (Rhodes et al., 2010).

2.2.3. Cosmogenic Radionuclide Dating

A depth profile was collected to 2.5 m for cosmogenic exposure dating from a well-preserved part of the alluvial fan (Trench P, Fig. 2a). Samples were transferred to the CRN lab at the Scottish Universities Environmental Research Centre (SUERC) and processed using standard quartz purification (Kohl and Nishiizumi, 1992) and chemistry protocols (Corbett et al., 2016). Beryllium isotope analyses were conducted at the accelerator mass spectrometry (AMS) laboratory at SUERC (Xu et al., 2015) and normalized to the NIST standard with assumed ratio of 2.79×10^{-11}, which is consistent with the revised standard value and ^{10}Be half-life (Nishiizumi et al., 2007). Samples were background corrected by propagating the AMS uncertainties for the samples and blanks in quadrature (Table S2.2).

2.3. Geophysical survey

An extensive electric resistivity tomography (ERT) survey was conducted to study the subsurface geology surrounding the Sudetic Marginal fault zone at Bílá Voda. Altogether 34 profiles were measured for various purposes: several measurements preceded the trenching to specify the planned trench positions as the detailed profile series enabled the tracing of the exact fault location due to favorable lithological contrasts. Additional ERT profiles were measured during trenching, either to test a hypothesis or to help in deciding the placement of additional trenches, a practice that is being applied in a growing number of cases, especially in environments that lack natural fault exposures (Štěpančíková et al., 2011; Carbonel et al., 2013). Finally, a series of long profiles, systematically covering the plateau above Bílá Voda village, was measured in order to map the extent of the faulted alluvial fan (Fig. 3).

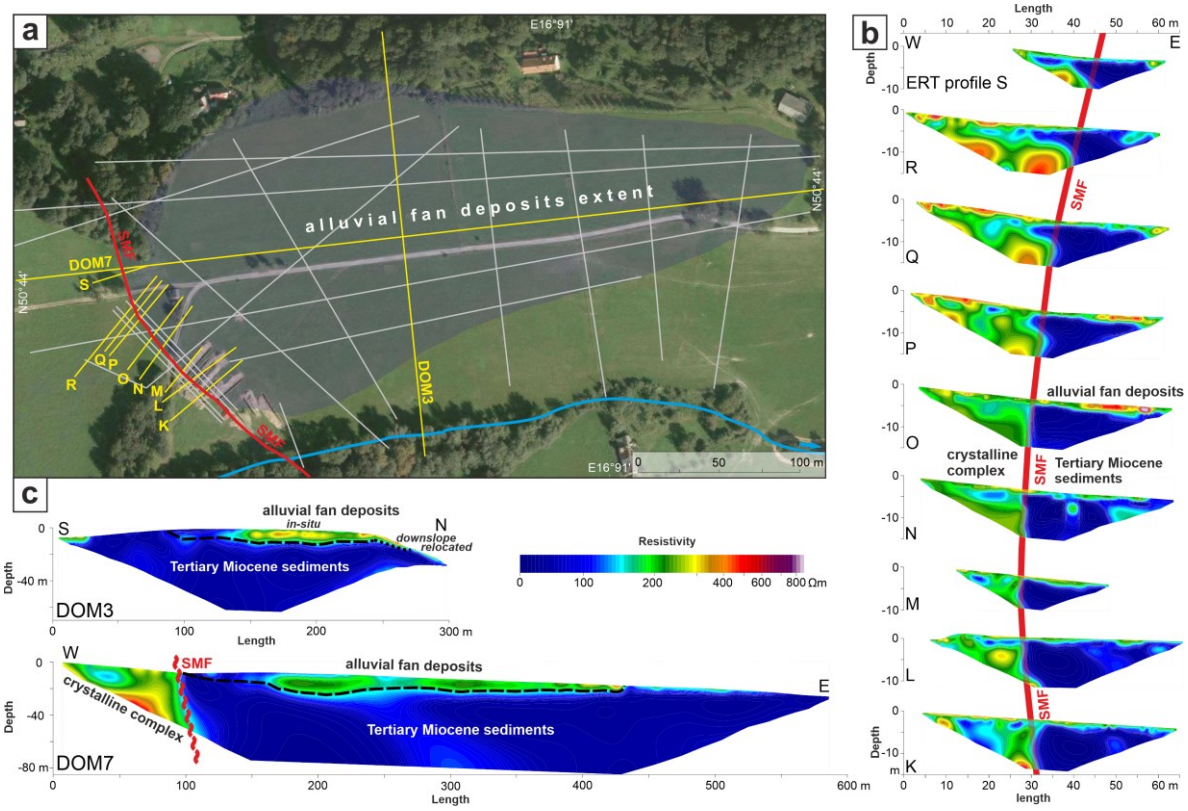


Fig. 3. a) Position of the ERT profiles across the SMF and the alluvial fan on the aerial map; b) ERT profiles K-S crossing the SMF. Notice sharp borderline between Miocene clays (NE of the fault) and weathered crystalline rock (SW of the fault), with very significant resistivity difference; c) ERT profiles DOM3 (N-S) and DOM7 (W-E), clearly showing both horizontal and vertical extent of the alluvial fan. Note: All the ERT profiles share the same resistivity scale.

All ERT measurements were performed using ERT device ARES, manufactured by GF Instruments Ltd., with a varying number of multi-electrode cable sections employed. The Wenner – Schlumberger array was used for all profiles as it is considered universal and can detect both vertical and horizontal structures (Loke, 2014).

The measured data were inverted using by Res2DInv64 by Geotomo Software (Loke, 2014). After cleaning the data from the points with excessively high RMS error, the inversion with standard constraints and the 5th iteration were used. Topographic profiles derived from the 5th generation of the LiDAR-based DEM (DMR 5G by the Czech Office for Surveying, Mapping and Cadastre) was introduced to the resistivity models during the inversion process. The processed data were visualized in Surfer (Golden software) and adjusted to display unified resistivity and size scales.

The properties of individual ERT profiles were based on their purpose. The short profiles, in the 1st phase aimed at mapping the subsurface fault trace, position of lithological units or the position of new trenches, were much more detailed, with electrode spacing as close as 0.8 m and profile length between 39 and 108 m. Consequently, the final interpretations of these profiles were calibrated according to the geological profiles derived from the findings in the trenches (profiles G to S) (Fig. 3b). Secondly, there was the set of long profiles, as shown in Fig. 3a, the purpose of which was

to estimate the alluvial fan extent and thickness. These profiles were measured using electrode spacing of 5 m, and their length varied between 165 and 588 m.

2.4. Ice-loading modelling

The load shape over time is derived from models of northern hemisphere ice sheet geometry (Zweck and Huybrechts, 2005) interpolated at 1000 yr timesteps. We numerically calculate the stress changes due to this load within a flexing elastic lithosphere overlying a viscoelastic asthenosphere by convolving the analytically derived 3-D deformation due to a surface point load with the actual load shape as it varies over time (Luttrell and Sandwell, 2010). The resulting 4-D stress tensor represents the stress changes induced by ice sheet loading relative to ice free conditions. This stress field can then be resolved into the changes in normal ($\Delta\tau_n$) and shear ($\Delta\tau_s$) stress components acting on a hypothetical fault plane within the lithosphere with a specified strike, dip, and sense of slip (rake). The change in Coulomb failure stress on the fault plane ($\Delta\tau_c$) is calculated as

$$\Delta\tau_c = \Delta\tau_s + \mu_f \Delta\tau_n, \quad (1)$$

where μ_f represents the coefficient of friction and a positive change in coulomb stress promotes failure on the specified fault plane in the specified sense of slip (e.g., King and Cocco, 2001; King et al., 1994).

Results of testing various lithosphere thickness, relaxation time and slip directions are described in Supplementary material S3 and Fig. S3.1.

3. Results

3.1. Geology exposed by trenches

The trenches exposed Paleozoic metamorphic rocks (phyllitic mica schists) in the footwall juxtaposed against Quaternary alluvium and underlying Miocene fluvio-lacustrine strata in the hanging wall (Fig. 4, Fig. S1.1, S2.2., Supplementary Section S1), both units of which are folded down into the fault zone (Štěpančíková et al., 2011). The Miocene strata consist of strongly kaolinized clayey silty sand, with the downwarped footwall sediments more strongly folded as they approach the fault zone. The upper part of the Miocene unit is geliflucted, and very often the gelifluction “lobes” interfinger with the Quaternary alluvial fan deposits, which indicates that the gelifluction acted after their deposition (see Fig. S1.1). In several trenches (TC, TJ, TK, TL), pieces of tectonic breccia within dark grey fault gouge were also geliflucted and now rest on the geliflucted Miocene surface at a distance of several meters from the fault (Fig. S1.1). The fault zone, with the youngest strand exhibiting a strike of 135° and dipping ~75° to the NE, comprises a flower structure (especially pronounced in trenches TC and TD) within the 4-m wide zone of tectonic breccia and fault strands outlined by dark gouge. The fault gouge is composed of at least three generations, as exhibited by various colors and consistencies (massive or schistous clay), which shows repeated and alternating periods of faulting (Fig. S2.2a).

Classic features indicative of significant strike-slip motion include rotation of clasts into the plane of the fault and the complete mismatch of units across the fault.

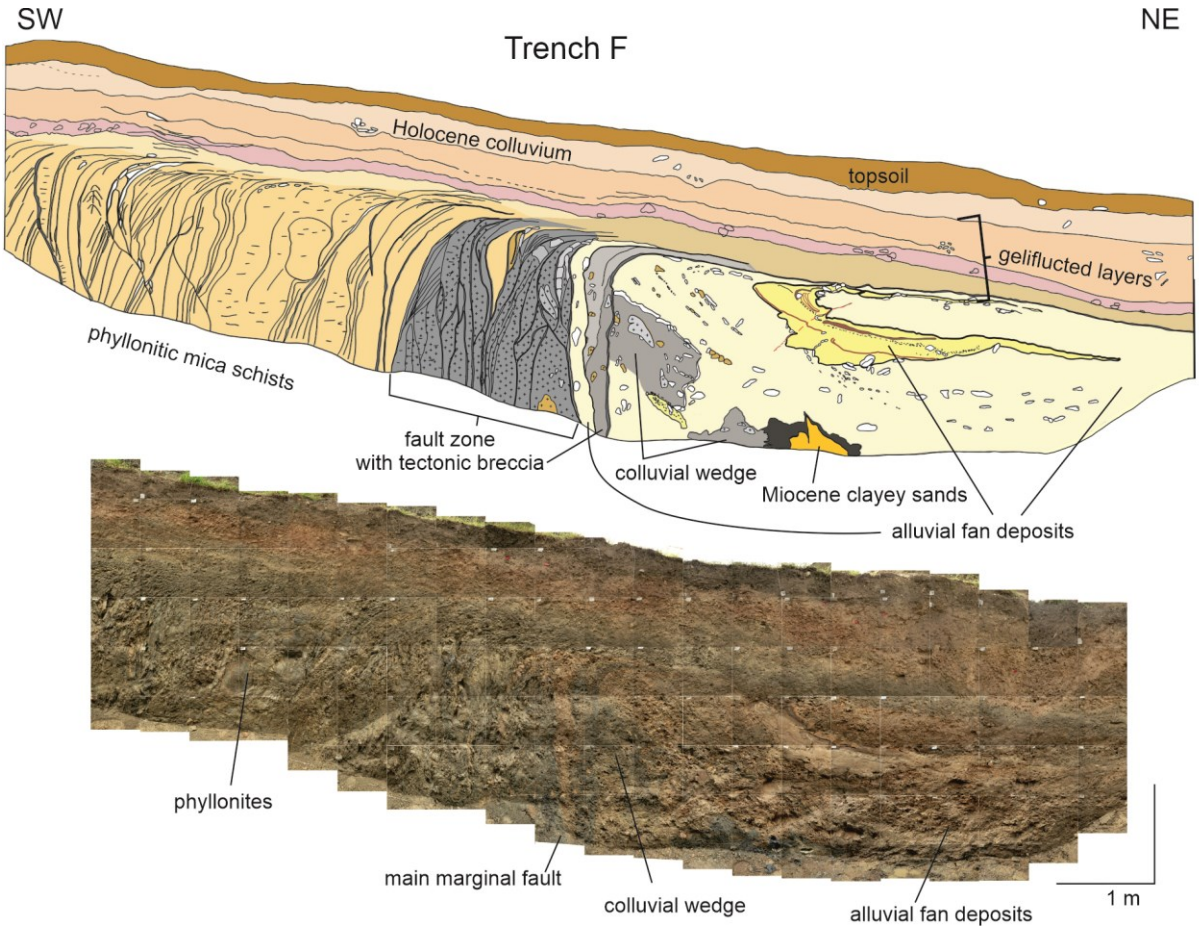


Fig. 4. Log of the SE-facing wall of Trench F and the respective photomosaic. Note the non-mixed geliflucted layers. Colluvial wedge includes pieces of tectonic breccia and fault gouge (black clay) from the fault zone, which gives the dark color to the deposit.

The Quaternary alluvium displays some bedding and channelization with an otherwise relatively massive matrix, indicating an alluvial fan origin, which is consistent with the surface fan morphology. We distinguished several distinct units within the alluvial fan deposits, which could be correlated throughout the trenches (Tab S1.1, Fig. S1.1). Most of them (Units 150, 170, 185, 210, 217) might be best described as matrix-supported intermediate to sandy diamictons with gravel clast content between 5 and 25% and sandy to silty matrix. The average size of the clasts is 57 cm and the largest ones are up to 30 cm. The clasts are composed of angular to subangular gneiss, granodiorite and quartz. There are also rare clasts of erratic material that has been brought to the area by an ice-sheet when the last continental glacier reached the study area during the Elsterian 2 glacial epoch, about 400-460 ka BP.

In the upper part of the alluvial fan deposits near the fault, there are finely laminated lenses of beige to grey clayey silt, sand and pebbles (unit 160) that are up to 3 m long and 35–40 cm thick. The upper parts of the lens are dominated by bands of Mn and Fe oxides, which percolate through fine to medium sand with some granule clasts. The general orientation and dimension of this distinctive sedimentary body was studied in parallel (TG) and perpendicular trenches (TC, TF) trying to resolve the horizontal offset from its source canyon. However, no source was found on the footwall.

The sedimentary body was exposed in trenches C, F, G, and L, demonstrating that it is >15 m long and 2 m wide oriented parallel to the fault. A plausible interpretation for this unit is a channel that was deflected along the fault due to horizontal displacement, which also implies that lateral displacement was occurring during fan deposition. After its deposition the lens was tilted and folded and its uphill part was affected by most probably horizontal and reverse faulting as exposed in trench F (Fig. 4, Fig. S1.1, S2.2b).

Within the alluvial fan deposits adjacent to the fault, there are several wedge-shaped deposits made of matrix-supported, median-grained diamicton with clasts of tectonic breccia clasts and fault gouge (units 143, 147, 165, 180, 200, and 220). These wedge-shaped deposits are interpreted as colluvial wedges that fell or were eroded from the fault plane that was exposed during surface rupturing events. The largest boulder of tectonic breccia that was incorporated into a colluvial wedge measured up to 0.75 m in diameter and was found in the trench D (Fig. S1.1, S1.2), suggesting that this is an indication of the height of the exposed fault plane due to a single earthquake. Gravel clasts are also derived from the hanging wall (upslope) bedrock lithologies (phyllonite, schist, granodiorite). Several colluvial wedges appear to be superimposed, which we interpret represent recurring earthquakes: they were successively deformed by subsequent earthquake events, as well as by the periglacial surface processes.

Upslope from the fault, the bedrock exhibits steeply dipping foliation that is impacted by gelifluction near the ground surface. In the upper 1-1.5 m, there are individual bands of unmixed material 3 to 50 cm thick (typically 10-20 cm) that continue >7 m downslope, and each of the distinct bands could be traced back to the bedrock stratum from which it originated (Fig. 4, Fig. S1.1). The geliflucted layers cross the fault and have flowed over the alluvial deposits. The thickness of bands is similar to what was described in other trenches studied along the Sudetic Marginal Fault at the Vlčice site (Štěpančíková et al., 2010), where layers up to 20 cm thick were interpreted to be deposited by sheet gelifluction and dated to the Late Glacial period based on radiocarbon dating. Thus, gelifluction in this part of Bohemian was limited to the periglacial climate of the late Pleistocene (c.f. Sauer and Felix-Henningsen, 2006), indicating that the alluvial fan, which is overlain by geliflucted material, predates the full glacial conditions of the Last Glacial Maximum (LGM - Marine Isotope Stage (MIS) 2) (Supplementary material S2 Chronology). All the banded soliflucted/geliflucted layers are overlain by late Holocene colluvial deposits into which the modern topsoil has developed.

3.2. Age determination of the sediments

Direct dating of the alluvial fan deposits near to the eastern limit of the fan using optically stimulated luminescence (OSL) techniques yielded an age of 25.8±1.6 ka for the alluvial fan deposits in trench C (Fig. S1.1, S2.2, Table 1). A sample of detrital charcoal from a fault-related colluvial wedge overlying the base of the alluvial fan deposits in trench J yielded a calibrated ^{14}C age of $44.2^{+5.5}/_{-2.1}$ ka (Fig. S1.1, S2.1, Table 1). Infrared stimulated luminescence (IRSL) dating of feldspars from the same deposits indicates that the basal alluvium overlying the Miocene strata date to 63±6 ka, grading up to between 24±3 and 31±4 ka for the top of the fan deposits, all of which show that deposition occurred during MIS 3 and early MIS 2 time (Fig. 4, S1.1; see thorough discussion of dating results presented in the Supplementary Section S2). Strata of silt-rich deposits that locally overlie the geliflucted layers in Trench R yielded calibrated radiocarbon ages as old as 11.15±0.05 ka and confirm the inference for the late Pleistocene age of the gelifluction process. This is consistent with cosmogenic ^{10}Be surface

exposure dating that supports an end of gelifluction and surface stability since about ~12 ka (Fig. S2.1, Supplementary section S2, Tab. S2.1). Applying a simple model to the observed ^{10}Be results, i.e., best fit to data of an exponential profile with density = 2.13 g/cm^3 and attenuation length = 160 g/cm^2, that accounts for pre-depositional exposure (best fit inheritance = 46,211 atoms/g) and assuming no surface erosion, ^{10}Be concentrations are well-fit with an apparent exposure age, corrected for topographic shielding, of ~12 ka (Fig. 5, Table S2.1). However, this is a minimum limiting age if the surface was eroded by gelifluction in the late Pleistocene. Notably, the ~11 ka strata cap the fault, demonstrating the lack of Holocene motion on the SMF at this location. Younger Holocene colluvium in other trenches, which was dated by radiocarbon dating method and yielded 0.3 to 5.3 ka ages, was also unfaulted.

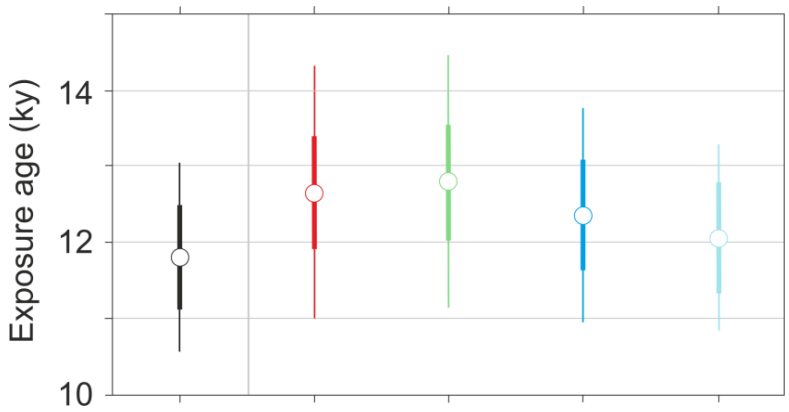


Fig. 5. Comparison of Be-10 exposure ages generated from the CRONUS online calculator (wrapper version 2.2, main calculator version 2.1, constants version 2.2.1, muons version 1.1, with global production rate calibration; Balco et al. 2008) using various scaling schemes. Leftmost, constant production rate: Lal (1991)/Stone (2000) scaling scheme (black). Others, time-dependent production: red, Desilets et al. (2003, 2006); green, Dunai (2001); blue, Lifton et al. (2006); cyan, time-dependent adaptation of Lal (1991)/Stone (2000). 1 sigma internal uncertainties shown are 6%, which is the average AMS uncertainty of all the samples in the profile. The tick line – 1-sigma internal uncertainty, the thin line – 1-sigma external uncertainty.

3.3. Alluvial fan offset and slip-rate determination

The 3-dimensional distribution of the alluvial fan deposits was explored through a network of trenches (Fig. 2). The thickness of the fan deposits varies systematically throughout the site, with the greatest thickness at the inferred apex of the paleo-fan and thinning with distance from the apex. The apex thickness of the youngest part of the fan as exposed in the trenches ranges between 2 and 3 m, with the majority of the fan deposit less than 1.5 m near the fault (Fig. S1.1). Altogether, the well-defined apex, along with the distribution of fan deposits, can be used to assess the sense and rate of slip of this fault.

Fault-parallel trenches excavated southwest of the fault (Trench T and Trench X, Fig. 2) exposed only Paleozoic schist across the entire site. The top of the schist is remarkably smooth and is capped by the gelifluction layers that originated a few meters upslope (Fig. 4, Fig. S1.1), so any paleo-channel cut into the schist would be readily apparent unless the footwall was considerably eroded by at least 2 m more than the hanging wall, which we consider unlikely.

We searched for a possible “feeder channel” as the source of the alluvial fan deposits based on fault-parallel trenches and geoelectric profiles (electrical resistivity tomography – ERT)(Fig. 2, Fig. 3), but no such channel exists on the southwest side of the fault northwest of the fan apex for at least 100 m. In contrast, a small drainage of the appropriate size for the fan deposit is present about 45-60 m to the southeast of the fan. Based on these observations, the most plausible interpretation is that the alluvial fan is left-laterally displaced by a few tens of meters (Fig. 2), which is consistent with geomorphic observations of left-laterally offset valley walls on the SMF (Štěpančíková and Stemberk, 2016).

To estimate the amount of late Quaternary left-lateral motion, we reconstructed the apex to the small channel to the southeast (Fig. 2). Using a straight-line projection of the average channel trend results in about 45 m of reconstructed slip. Taking the apex to the center of the currently incised drainage adds another 10-15 m, although it is likely that this is an overestimate because the drainage curves to the southeast, whereas the alluvial fan appears to have spilled along the same trend as the upslope portion of the channel. For an estimate of the minimum displacement, we take the elevation of the base of the alluvium at the apex and reconstruct it horizontally to the same elevation contour in the modern topography at the source drainage, and allowing for as much as a half-meter of vertical slip, results in 29 m of estimated slip (Fig. 2).

Based on these reconstructions, we estimate that the fan apex is left-laterally offset by 29 to 45 m, with a maximum possible displacement of about 60 m if the apex is reconstructed to the center of the modern drainage. As the actual value could fall anywhere in between these values, and because we consider the maximum value to be an overestimate, we use a best estimate of 37±8 m of left-lateral slip for the ~24-63 ka alluvial fan. Thus, we calculate the best estimate of the average long-term strike-slip rate is about $0.85^{+1.0}/_{-0.4}$ mm/yr.

We excavated several trenches on the northern side of the modern drainage to both search for remnants of the alluvial fan and also to search for younger faulted deposits. Trench R1 (Fig. 2, Fig. S2.1) exposed faulted alluvium sealed by unfaulted fine silt-rich strata that yielded calibrated radiocarbon ages on charcoal of about 11 ka, indicating that the last period of motion was greater than 11,000 years ago. This is consistent with observations in all trench exposures, which showed a pattern of geliflucted layers capping the fault (Fig. S1.1): this consistent pattern is surprising when the amount of late Pleistocene displacement is considered. In fact, this implies that the 37±8 m of left lateral displacement occurred in the period between about 11 ka BP and 24-63 ka. If correct, this indicates that the slip rate was $1.1^{+2.3}/_{-0.6}$ mm/yr during the latest Pleistocene, and has been essentially zero during the Holocene.

4. Modeling of ice-loading as a possible cause of surprisingly fast intraplate slip

Bílá Voda lies about 150-170 km south from the late Pleistocene Weichselian culmination (~20 ka) ice front (Ehlers et al., 2011). At face value, it appears that most or all of the activity on the Sudetic Marginal fault occurred during the time when ice was locked up on the European continent or was receding, with the ice-margin not too far from the fault. Based on our data, after the end of Pleistocene time, surface movement on the fault ceased and has been zero through the Holocene, at least until the present. These observations suggest a cause and effect between ice loading and fault motion.

The modern maximum principal stress ($\sigma 1$) is oriented nearly parallel to the Sudetic Marginal fault (NNW-SSE) (Havíř, 2004), which is currently unfavorable for fault motion. We hypothesize that the forebulge from the ice load may have caused a change in the local stress field, which would have rotated $\sigma 1$ and induced left-lateral motion of the Sudetic Marginal fault, or at least caused an acceleration in the rate of fault motion. This phenomenon has been reported from other regions and attributed to the effects of ice-loading and/or deglaciation (Arvidsson, 1996; Houtgast et al., 2005). If that was the case, then removal of the ice would have caused relaxation of the stress field and locking of the fault in the Holocene, which would explain the lack of Holocene motion.

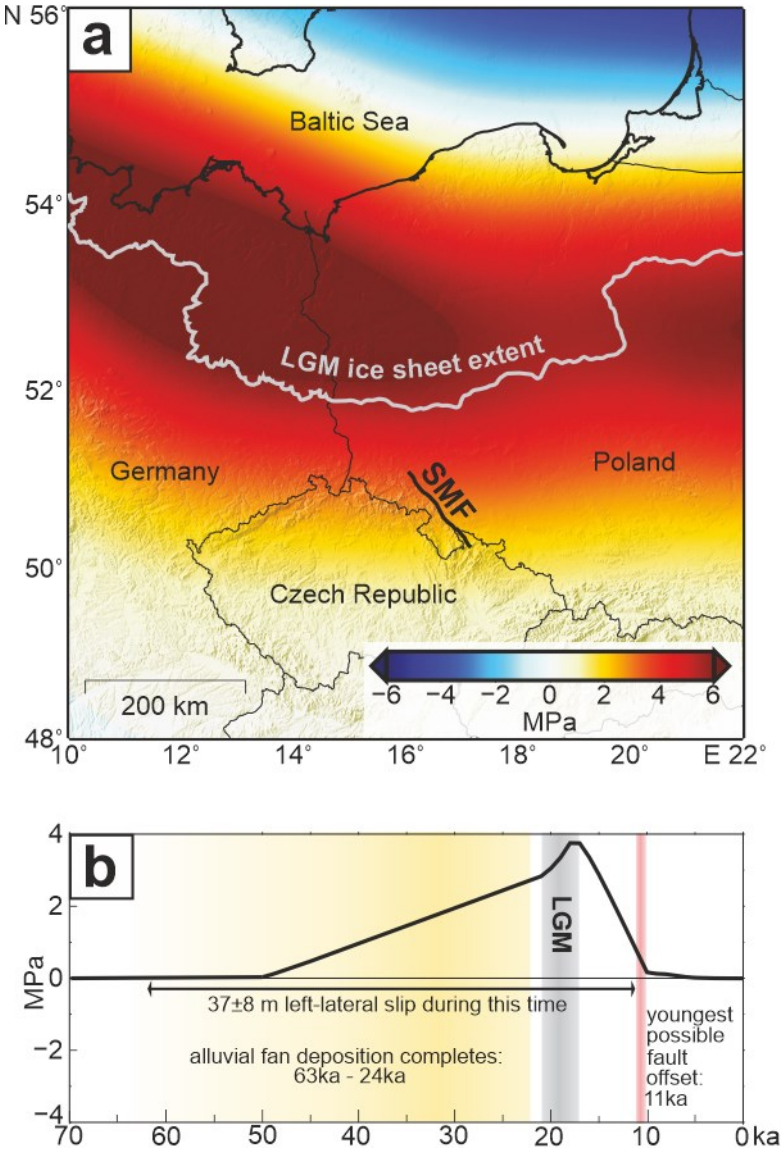


Fig. 6. a) Predicted change in Coulomb failure stress at LGM (18 ka), relative to ice-free conditions, on a left-lateral fault plane with same orientation as SMF. Positive (negative) change in Coulomb failure stress promotes (inhibits) failure. b) Coulomb failure stress change over time at northern end of SMF. Note both the highest Coulomb failure stress and the highest rate of Coulomb failure stress accumulation occur during LGM. Ice sheet extent is adopted from Ehlers et al. (2011). Timing of the offset alluvial fan deposition and its offset is from this study.

To test this hypothesis, we modeled changes in stress due to glacial loading and unloading on a bending lithosphere as a flexing elastic plate overlying a viscoelastic halfspace (Luttrell et al., 2007; Luttrell and Sandwell, 2010). A changing glacial load was added and removed from the plate in time intervals coinciding with the history of glaciation (Ehlers et al., 2011; Zweck and Hybrechts, 2005). The resulting 3-D spatially varying stress tensor is resolved into normal, shear, and Coulomb failure stress on hypothetical fault planes with the same orientation as the SMF (see Supplementary material S3 for detailed description, Fig. S3.1). For most of the episode of last glaciation, the SMF lies along the edge of the flexural bulge associated with the continental ice sheet, which tends to promote slip on the SMF. As the ice sheet advances, the flexural bulge shifts southward and more strongly affects the SMF. As the ice sheet retreats, the flexural bulge shifts northward, which reduces the Coulomb stress on the SMF (Fig. 6).

Coulomb stress on the SMF increased by ~1 MPa during the time leading up to the LGM, and then rapidly decreased as the ice sheet retreated. Our modeling suggests that the most likely time for rapid left-lateral SMF reactivation over the last 50 ka is between ~21 ka – 17 ka, although it is likely that motion began when a threshold stress level was exceeded, and then motion ceased when it dropped below another threshold level. For the purposes of estimating a plausible slip rate for this period, we use the timing of the beginning of rapid ice growth at about 28 ka for the initiation of fault motion during and after fan growth. Similarly, we use the end of the Younger Dryas at about 12 ka as the likely end of the period of ice-driven fault slip because the ice-shield retreated rapidly after this time. These inferred dates closely match the age control of the offset alluvial fan and sediments that post-date fault motion but also implies that the slip rate during this time interval was at the high end of our slip rate estimates.

5. Conclusion

We studied late Quaternary activity of the Sudetic Marginal fault (SMF) by extensive paleoseismic trenching (9 fault-crossing and 9 fault-parallel trenches), geophysical surveys (34 ERT profiles), and radiometric dating in the study site near the town of Bílá Voda in northeastern Bohemian Massif (Czech Republic). The SMF has experienced alternating kinematics since the Paleozoic, but in this study, we exposed the SMF as a subvertical fault zone striking 135° – 150°/75° NE with a left-lateral sense of slip. The strike-slip kinematics is suggested by a flower structure within the 4-m wide zone of tectonic breccia and fault gouge, and by the juxtaposition of Paleozoic crystalline rocks (phyllites, schists, granitic aplite) against Miocene strata and late Pleistocene alluvial fan deposits across the fault. We dated the alluvial fan by ^{14}C, OSL, IRSL, and ^{10}Be methods, which indicate that the alluvium accumulated between 63 and 24 ka. We estimate displacement by reconstructing the fan apex to its probable (and only plausible) source drainage, resulting in 37±8 m of left lateral offset. As there has been no Holocene motion, we assume this all of this displacement occurred during and after deposition of the alluvial fan deposits, resulting in a late Pleistocene slip rate of $1.1^{+2.3}/_{-0.6}$ mm/yr, dropping to zero in the Holocene.

As the site lies ~150 km south from the Late Pleistocene Weichselian maximum (~20 ka) ice-sheet front, we hypothesized that the slip rate acceleration was due to ice-loading, which we then modeled. The models of related lithosphere flexure suggest failure on the SMF was promoted by the presence of the ice sheet, relative to an ice-free state, while Coulomb stress on the SMF increased by ~1 MPa during the time leading up to the LGM, and then rapidly decreased as the ice sheet

retreated. Thus, the most favorable time for a glacially-loaded lithosphere to induce rapid left-lateral reactivation on the SMF over the last 50 ka would be during the glacial maximum ~21-17 ka, with most or all displacement likely occurring between about 28 and 12 ka; the resulting slip rate in that period may have been as high as 2.3±0.5 mm/yr. The implications of our work are that there are likely many late Quaternary faults in Europe that were affected by the phenomenon of near-field ice loading and its attendant changes in stress, which resulted in a pronounced increase in late Pleistocene seismicity and higher slip rates than are now active in the Holocene. We note that this is a different effect from the direct removal of ice load (Brandes et al., 2015; Steffen et al., 2021), which occurs north of the ice front during glacial retreat (glacial isostatic adjustment). Finally, unless the current stress regime is actively stressing a fault based on its orientation, these late Pleistocene active faults will not likely move in the foreseeable future until they are again stressed by some mechanism, making them a far smaller seismic hazard than most conventional models would imply.

Acknowledgements: The research was supported by the Czech Science Foundation projects No. 205/08/P521, No. P210/12/0573, and by the Czech Ministry of Education, Youth and Sports project No. LH12078. We thank the staff of the AMS Laboratory at the Scottish Universities Environmental Research Centre (SUERC) for support during beryllium isotope analyses. Věra Primasová, Monika Hladká, Petra Bestajovská, and Jana Šreinová are acknowledged for technical and graphical support. We thank Miroslav Kocián, the mayor of Bílá Voda municipality in the study site, for all-embracing support during several field campaigns.

References

Arvidsson, R., 1996. Fennoscandian earthquakes: Whole crustal rupturing related to postglacial rebound. Science, 274, 1, 744-746. https://doi.org/10.1126/science.274.5288.744.

Badura, J., Przybylski, B., Zuchiewicz, W., 2004. Cainozoic evolution of Lower Silesia, SW Poland: a new interpretation in the light of sub-Cainozoic and sub-Quaternary topography. Acta Geodyn. Geomater., 1(3), 7-29.

Badura, J., Zuchiewicz, W., Štěpančíková, P., Przybylski, B. Kontny, B., Cacoń, S., 2007. The Sudetic Marginal Fault: A young morphotectonic feature at the NE margin of the Bohemian Massif, central Europe. Acta Geodyn. Geomater., 4(4), 7-29.

Balco, G., Stone, J., Lifton, N., Dunai, T., 2008. A complete and easily accessible means of calculating surface exposure ages or erosion rates from ^{10}Be and ^{26}Al measurements. Quaternary Geochronology, 3, 174-195. https://doi.org/10.1016/j.quageo.2007.12.001.

Birkenmajer, K., Jeleńska, M., Kądziałko-Hofmokl, M., Kruczyk, J., 1977. Age of deep-seated fractures zones in Lower Silesia (Poland), based on K-Ar and paleomagnetic dating of Tertiary basalts. Rocznik Polskiego Towarzystwa Geologicznego - Annales de la Société Géologique de Pologne, Kraków, XLVII, 4, 545-552.

Brandes, C., Steffen, H., Steffen, R., Wu, P., 2015. Intraplate seismicity in northern Central Europe is induced by the last glaciation. Geology, 43(7), 611-614. https://doi.org/10.1130/G36710.1.

Brock, F., Higham, T., Ditchfield, P., Ramsey, C.B., 2010. Current pretreatment methods for AMS radiocarbon dating at the Oxford Radiocarbon Accelerator Unit (ORAU). Radiocarbon, 52(1), 103-112. https://doi.org/10.1017/S0033822200045069.

Ramsey, C.B., 2009. Bayesian analysis of radiocarbon dates. *Radiocarbon, 51*(1), 337-360. https://doi.org/10.1017/S0033822200033865.

Brown, N.D., Rhodes, E.J., Antinao, J.L., McDonald, E.V., 2015. Single-grain post-IR IRSL signals of K-feldspars from alluvial fan deposits in Baja California Sur, Mexico. Quaternary International, 362, 132-138. https://doi.org/10.1016/j.quaint.2014.10.024.

Carbonel, D., Gutiérrez, F., Linares, R., Roqué, C., McCalpin, J., Guerrero, J., Rodríguez, V., 2013. Differentiating between gravitational and tectonic faults by means of geomorphological mapping, trenching and geophysical surveys. The case of the Zenzano Fault (Iberian Chain, N Spain). Geomorphology, 189, 93-108. https://doi.org/10.1016/j.geomorph.2013.01.020.

Corbett, L.B., Bierman, P.R., Rood, D.H., 2016. An approach for optimizing in situ cosmogenic ^{10}Be sample preparation. Quaternary Geochronology, 33, 24-34. https://doi.org/10.1016/j.quageo.2016.02.001.

Danišík, M., Štěpančíková, P., Evans, N., 2012. Constraining long-term denudation and faulting history in intraplate regions by multi-system thermochronology - an example of the Sudetic Marginal Fault (Bohemian Massif, Central Europe). Tectonics, 31, Tc2003, 19pp. https://doi.org/10.1029/2011TC003012.

Desilets, D., Zreda, M., Prabu, T., 2006. Extended scaling factors for in situ cosmogenic nuclides: New measurements at low latitude. Earth Planet. Sci. Lett., 246, 265-276. https://doi.org/10.1016/j.epsl.2006.03.051.

Desilets, D., Zreda, M, 2003. Spatial and temporal distribution of secondary cosmic-ray nucleon intensities and applications to in situ cosmogenic dating. Earth Planet. Sci. Lett., 206, 21-42. https://doi.org/10.1016/S0012-821X(02)01088-9.

Dunai, T., 2001. Influence of secular variation of the geomagnetic field on production rates of in situ produced cosmogenic nuclides. Earth Planet. Sci. Lett., 193, 197-212. https://doi.org/10.1016/s0012-821x(01)00503-9.

Dyjor, S., 1983. Ewolucja trzeciorzędowych przedgórskich rowów tektonicznych centralnych i wschodnich Sudetów, III. Sympozjum. Współczesne i neotektoniczne ruchy skorupy ziemskiej w Polsce, Wrocław, 155-181.

Ehlers, J., Gibbard, P. L., Hughes, P. D., eds., 2001. Quaternary Glaciations – Extent and Chronology, A closer look. Developments in Quaternary Science, Elsevier, 15, 37-46.

Farr, T. G., eds., 2007. The Shuttle Radar Topography Mission. Rev. Geophys., 45, RG2004. https://www2.jpl.nasa.gov/srtm, Accessed date: 12 Nov 2018. https://doi.org/10.1029/2005RG000183.

Galbraith, R.F., Roberts, R.G., Laslett, G.M., Yoshida, H., Olley, J.M., 1999. Optical dating of single and multiple grains of quartz from Jinmium rock shelter, northern Australia: Part I, experimental design and statistical models. Archaeometry, 41(2), 339-364. https://doi.org/10.1111/j.1475-4754.1999.tb00987.x.

Grützner, C., Carson, E., Walker, R.T., Rhodes, E.J., Mukambayev, A., Mackenzie, D., Elliott, J.R., Campbell, G., Abdrakhmatov, K., 2017. Assessing the activity of faults in continental interiors: palaeoseismic insights from SE Kazakhstan. Earth Planet. Sci. Lett., 459, 93-104. https://doi.org/10.1016/j.epsl.2016.11.025.

Guterch, B., Lewandowska-Marciniak, H., 2002. Seismicity and seismic hazard in Poland. Folia Quaternaria 73, 85-99.

James, T. S., Bent, A. L., 1994. A comparison of eastern North American seismic strain-rates to glacial rebound strain-rates. Geophysical Research Letters, 21(19), 2127-2130. https://doi.org/10.1029/94GL01854.

Hampel, A., Hetzel, R., Maniatis, G., 2010. Response of faults to climate-driven changes in ice and water volumes on Earth's surface. Philosophical Transactions of the Royal Society A: Mathematical, Physical and Engineering Sciences, 368(1919), 2501-2517. https://doi.org/10.1098/rsta.2010.0031.

Havíř, J., 2004. Orientations of recent principal stress axes in the Jeseníky region. Acta Geodynamica et Geomaterialia, 1, 3(135), 49-57.

Houtgast, R.F., Van Balen, R.T., Kasse, C., 2005. Late Quaternary evolution of the Feldbiss Fault (Roer Valley Rift System, the Netherlands) based on trenching, and its potential relation to glacial unloading. Quaternary Science Reviews 24, 489-508. https://doi.org/10.1016/j.quascirev.2004.01.012.

Huntley, D. J., Baril, M., 1997. The K content of the K-feldspar being measured in optical dating or in thermoluminescence dating. Ancient TL, 15, 11-13.

King, G. C. P., Stein, R. S., Lin, J., 1994. Static stress changes and the triggering of earthquakes, Bull. Seismol. Soc Am., 84(3), 935-953.

King, G.C.P., Cocco, M., 2001. Fault interaction by elastic stress changes: New clues from earthquake sequences. Advances in Geophysics, 44, pp. 1-38. https://doi.org/10.1016/S0065-2687(00)80006-0.

Kley, J., Voigt, T., 2008. Late Cretaceous intraplate thrusting in central Europe: Effect of Africa-Iberia-Europe convergence, not Alpine collision. Geology, 36(11), 839-842. https://doi.org/10.1130/G24930A.1.

Kohl, C., Nishiizumi, K., 1992. Chemical isolation of quartz for measurement of in-situ-produced cosmogenic nuclides. Geochim. Cosmochim. Acta, 56, 3583-3587. https://doi.org/10.1016/0016-7037(92)90401-4.

Krzyszkowski, D., Pijet, E., 1993. Morphological effects of Pleistocene fault activity in the Sowie Mts., southwestern Poland, Zeitschr. Geomorph., 4, 243-259.

570 Krzyszkowski, D., Przybylski, B., Badura, J., 2000. The role of neotectonics and glaciation on terrace
571 formation along the Nysa Kłodzka River in the Sudeten Mountains (southwestern Poland),
572 Geomorphology, 33, 149-166. https://doi.org/10.1016/S0169-555X(99)00123-3.

573 Lal, D., 1991. Cosmic ray labeling of erosion surfaces: in situ nuclide production rates and erosion
574 models. Earth Planet. Sci. Lett., 104, 424-439. https://doi.org/10.1016/0012-821X(91)90220-C.

575 Lifton, N., Bieber, J., Clem, J., Duldig, M., Evenson, P., Humble, J., Pyle, R., 2005. Addressing solar
576 modulation and long-term uncertainties in scaling secondary cosmic rays for in situ cosmogenic
577 nuclide applications. Earth Planet. Sci. Lett., 239, 140-161.
578 https://doi.org/10.1016/j.epsl.2005.07.001.

579 Loke, M.H., 2014. Tutorial: 2-D and 3-D electrical imaging surveys. Geotomo Software, Malaysia.
580 www.geotomosoft.com.

581 Luttrell, K., Sandwell, D., 2010. Ocean loading effects on stress at near shore plate boundary fault
582 systems. J. Geophys. Res., 115, B08411. https://doi.org/10.1029/2009JB006541.

583 Luttrell, K., Sandwell, D., Smith-Konter, B., Bills, B., Bock, Y., 2007. Modulation of the earthquake
584 cycle at the southern San Andreas fault by lake loading. J. Geophys. Res., 112, B08411.
585 https://doi.rog/10.1029/2006JB004752.

586 Nishiizumi, K., Imamura, M., Caffee, M., Southon, J., Finkel, R., McAninch, J., 2007. Absolute
587 calibration of ^{10}Be AMS standards. Nucl. Instrum. Methods Phys. Res. B Beam Interact. Mater. At.,
588 258, 403-413. https://doi.org/10.1016/j.nimb.2007.01.297.

589 Oberc, J., Dyjor, S., 1969. Uskok sudecki brzeżny, Biul. Inst. Geol, 236, 41-142.

590 Oberc, J., 1991. Systems of main longitudinal strike-slip faults in the vicinity of the Gory Sowie Block
591 (Sudetes), Kwart. Geol., 35, 403-420.

592 Reimer, P.J., Bard, E., Bayliss, A., Beck, J.W., Blackwell, P.G., Ramsey, C.B., Buck, C.E., Cheng, H.,
593 Edwards, R.L., Friedrich, M., Grootes, P.M., Guilderson, T.P., Haflidason, H., Hajdas, I., Hatte, C.,
594 Heaton, T.J., Hoffmann, D.L., Hogg, A.G., Hughen, K.A., Kaiser, K.F., Kromer, B., Manning, S.W., Niu,
595 M., Reimer, R.W., Richards, D.A., Scott, E.M., Southon, J.R., Staff, R.A., Turney, C.S.M., Van der Plicht,
596 J., 2013. Intcal13 and Marine13 Radiocarbon Age Calibration Curves 0-50,000 Years Cal BP.
597 Radiocarbon, 55, 1869-1887. https://doi.org/10.2458/azu_js_rc.55.16947.

598 Rhodes, E.J., 2005. Dating sediments using potassium feldspar single-grain IRSL: initial methodological
599 considerations. Quaternary International, 362, 14-22. https://doi.org/10.1016/j.quaint.2014. 12.012.

600 Rhodes, E.J., Fanning, P.C., Holdaway, S.J., 2010. Developments in optically stimulated luminescence
601 age control for geoarchaeological sediments and hearths in western New South Wales, Australia.
602 Quaternary Geochronology, 5, 348-352. https://doi.org/10.1016/j.quageo.2009.04.001.

603 Scheck, M., Ulf, B., Otto, V., Lamarche, J., Banka, D., Pharaoh, T., 2002. The Elbe Fault System in
604 North Central Europe – a basement controlled zone of crustal weakness. Tectonophysics, 360, 281-
605 299. https://doi.org/10.1016/S0040-1951(02)00357-8.

606 Steffen, H., Olesen, O., Sutinen, red., 2021. *Glacially-Triggered Faulting*. Cambridge University Press,
607 *in press.* https://doi.org/10.1017/9781108779906.

608 Štěpančíková, P., Stemberk, J. jr., 2016. Region of the Rychlebské hory Mountains – tectonically
609 controlled landforms and unique landscape of granite inselbergs (Sudetic Mountains). In: Pánek, T.,
610 Hradecký, J., eds., 2016. Landscapes and Landforms of the Czech Republic, Series World
611 Geomorphological Landscapes. Springer, 263-276. https://doi.org/10.1007/978-3-319-27537-6_21.

612 Štěpančíková, P., Dohnal, J., Pánek, T., Łój, M., Smolková, V., Šilhán, K., 2011. The application of
613 electrical resistivity tomography and gravimetric survey as useful tools in an active tectonics study of
614 the Sudetic Marginal Fault (Bohemian Massif, central Europe). Journal of Applied Geophysics, 74, 69-
615 80. https://doi.org/10.1016/j.jappgeo.2011.03.007.

616 Štěpančíková, P., Hók, J., Nývlt, D., Dohnal, J., Sýkorová, I., Stemberk, J., 2010. Active tectonics
617 research using trenching technique on the south-eastern section of the Sudetic Marginal Fault (NE
618 Bohemian Massif, central Europe). Tectonophysics, 485, 269-282.
619 https://doi.org/10.1016/j.tecto.2010.01.004.

620 Stewart, I. S., Sauber, J. y Rose, J., 2000. Glacio-seismotectonics: ice sheets, crustal deformation and
621 seismicity. Quaternary Science Reviews, 19, 1367-1389. https://doi.org/10.1016/S0277-
622 3791(00)00094-9.

623 Stone, J.O., 2000. Air pressure and cosmogenic isotope production. Journal of Geophysical Research,
624 105, 23753-23759. https://doi.org/10.1029/2000JB900181.

625 Xu, S., Freeman, S.P.H.T., Rood, D.H., Shanks, R.M., 2015. Decadal ^{10}Be, ^{26}Al and ^{36}Cl QA
626 measurements on the SUERC accelerator mass spectrometer. Nuclear Instruments and Methods B:
627 Beam Interactions with Materials and Atoms, 361, 39-42.
628 https://doi.org/10.1016/j.nimb.2015.03.064.

629 Zweck, C., Hybrechts, P., 2005. Modeling of the northern hemisphere ice sheets during the last glacial
630 cycle and glaciological sensitivity. J. Geophys. Res., 110, (D07103).
631 https://doi.org/10.1029/2004JD005489.

632

633 *Table 1 (on the next page). Dating results from Bílá Voda trenching site. Calibrated ages of radiocarbon*
634 *dating (^{14}C) were obtained using OxCal v4.3.1 programme (Bronk Ramsey 2009), 2σ uncertainty and*
635 *the IntCal13 atmospheric curves (Reimer et al., 2013). Optically Stimulated Luminescence (OSL) on*
636 *quartz dated by GADAM Centre at Silesian University of Technology using OSL-SAR single aliquot*
637 *regenerative method; CAM (Central Age Model). Infra-Red Stimulated Luminescence (IRSL) post-IR*
638 *$IRSL_{225}$ dating on feldspar. For details see Supplementary material S2 – Chronology. For units position*
639 *see Fig. S1.*
640 *italics – samples non-used due to discrepancy*
641 * *probably the age of gelifluction process not the layer accumulation, see S.2 section*
642 ■ *sample of mud, but all the other samples for radiocarbon dating are charcoals*
643 *Note: e.g. trench wall NW = facing to the NW*
644

Stratigraphy		Dating method	Sample	Trench wall facing to	Age (BP) Calibrated ^{14}C	Comment
Unit	**Material**					
50-60 Holocene colluvium	polymict material	^{14}C	Ti 18	TI SE	326-502	
			Ti 16	TI SE	683-730	
			Bila Voda F 50	TC NW	689-893	
			Bila Voda F 13, C 11	TF SE	937-1 280	
			Bila Voda DJV 4	TD SE	1 063-1 178	
			Bila Voda FJV 16	TF SE	2 006-2 296	
			Bila Voda DSZ 7	TD NW	3 353-3 556	
		$IRSL_{225}$	BV15-13	TF NW	0.77 ± 0.12 ka	
		^{14}C	BV Ti 1	TI SE	4 416-4 515	
			BV Ti 5	TI SE	4 441-4 798	
			Ti 3	TI SE	5 054-5 312	
			BV Tk 1	TK SE	2 003-2 125	
fluvial/colluvial layer in recent valley	silty layers	^{14}C	TR 2 1	TR2 W	9 032-9 264	fault sealing layers
			TR 1 V	TR1 SE	10 871-11 186	
			TR 1 VII	TR1 SE	10 776-11 103	
			TR 1 VIII	TR1 SE	10 907-11 197	
100-140 – geliflucted/ soliflucted layers	monomict material	^{14}C	*BV Ti 20*	*TI SE*	*1 827-1 926*	
			Ti 8	*TI SE*	*1 736-1 866*	
			Bila Voda F 18, E19	*TF NW*	*981-1 268*	burnt root
			Bila Voda F 19, E20	*TF NW*	*694-1 296*	burnt root
			Bila Voda D 12, F25	*TD NW*	*804-1 271*	bioturbation, charcoal in a fault fissure
			Bila Voda D1/0.75m	*TD SE*	*2 489-2 740*	burnt root
		$IRSL_{225}$	BV15-12	TF NW	30.6 ± 4.2 ka	
150 – alluvial fan deposits	gravels, sometimes with silty layers	^{10}Be	SMF-P1	TP SW	~11.8 ka *	best fit
		$IRSL_{225}$	BV15-11	TF NW	24.1 ± 3.7 ka	
			BV15-10	TF NW	30.8 ± 4.1 ka	
160 – alluvial fan deposits	silty layer	^{14}C	*BV L-F6/RES* ■	*TL NW*	*5 324-5 584*	? translocation of Holocene organic acids
			BV L-F6/NaOHsol ■	*TL NW*	*6 324-6 503*	
			BV F F31/1.5m ■	*TF SE*	*7 952-8 152*	
		OSL	*Bila Voda 5 (J63)*	*TC SE*	*2.6 ± 1.2ka*	
			Bila Voda 4 (J60)	TC NW	20.1 ± 5.5ka	combined age of 06, 07, 08, 09
		$IRSL_{225}$	BV15-09	TF NW	53.2 ± 3.0 ka	
			BV15-08	TF NW	53.2 ± 3.0 ka	
			BV15-07	TF NW	53.2 ± 3.0 ka	
			BV15-06	TF NW	53.2 ± 3.0 ka	
170 – alluvial fan deposits	gravels	$IRSL_{225}$	BV15-05	TF NW	37.1 ± 3.1 ka	
175 – alluvial fan deposits	silty-sandy layer	OSL	Bila Voda 3 (K58)	TC NW	23.2 ± 1.3ka	
190 – alluvial fan deposits	silty layer	^{14}C	*BV F H18/2.5m* ■	*TF NW*	*6 350-6 494*	? translocation of Holocene organic acids
		$IRSL_{225}$	BV15-04	TF NW	54.6 ± 5.8 ka	combined age 03, 04
			BV15-03	TF NW	54.6 ± 5.8 ka	
203 – colluvial wedge	silty-sandy layer	^{14}C	BV Tj 1	TJ SE	42 070-49 751	the larger uncertainties are due to the small sample size
215 – within colluvial wedge	silty-sandy layer	OSL	Bila Voda 2 (L56)	TC NW	26.5 ± 1.3 ka	
		$IRSL_{225}$	*BV15-01*	*TF SE*	*14.1 ± 2.4 ka*	
210 – base of alluvial fan	gravels	$IRSL_{225}$	BV15-02	TF NW	62.9 ± 6.1 ka	
a layer incorporated into fault zone vertically dragged	silty layer		Bila Voda G1	TG	56.4 ± 2.6ka	trench bottom sampled, position of the layer at TL
			Bila Voda G2	TG	76.6 ± 6.6ka	

645

Supplementary Section S1 - Stratigraphy

To study the late Quaternary activity of the Sudetic Marginal fault (SMF), we first excavated a trench across the fault (2008) on a gentle scarp at Bílá Voda site that exposed Paleozoic metamorphosed rocks (phyllonites, mica schists) on the southwestern footwall juxtaposed against Quaternary alluvial sediments overlying Miocene fluvial to -limnic sediments on the northeastern hanging-wall both folded down into the fault zone (Fig. S1.1). The alluvial sediments, which itself show signs of gelifluction, are overlain by distinct layers of geliflucted material, each of which could be traced back to the bedrock stratum from which it originated. All the Pleistocene layers are overlain by polymict Holocene colluvial sediments and topsoil. Later, 2009, 2012-2013 we excavated another 9 fault-crossing and 9 fault-parallel trenches on the both sides of the fault to delimit the alluvial fan deposits displaced by the fault and to look for the source valley (Fig. 2). The following lithology/stratigraphy is captured in detail in Fig. S1.1 with description of individual units in Table S1.1.

Pre-Cenozoic basement

The crystalline bedrock exposed in the trenches in the southwestern footwall comprises highly deformed so called Bílá Voda phyllonites (derived from mica-schists) of Neoproterozoic to early Paleozoic age. They alternate with less deformed amphibolites, and gneisses. The multiple deformation and metamorphism of these rocks took place during the Paleozoic times. Higher parts of the slopes are made of Variscan Javorník granodiorite, which is also an important source for Quaternary clastic material found in studied trenches.

Miocene

The Miocene basement situated on the northeastern block comprises of homogenous, strongly kaolinized clayey silty sand with a small pebble admixture (mostly made of granitoid and quartz clasts up 6 cm large). Clay originated by chemical weathering of feldspars and granite groundmass. These sediments may be correlated with Member C described in the trenches performed 16 km to the SE (Vlčice site) by Štěpančíková et al. (2010) and interpreted as to be deposited in the fluvial to limnic environment by rivers flowing towards several lakes in the marginal part of the Vidnava Basin during the Karpatian and lower Badenian (i.e., early to mid-Miocene, ~18–15 Ma). In the Trench D at the Bílá Voda site (Fig. S1.1, S1.2), which lacks the alluvial fan deposits and where the Miocene deposits are overlain directly by thin, probably eroded, geliflucted layers and by Holocene colluvium, prismatic subvertical jointing with cracks up to 0.4 m deep may be seen in the upper part of Miocene clayey sand showing the thermal cracking during glacial exposure of the surface. On the other hand, in this trench, the uppermost ~15 cm of the Miocene subvertically cracked surface bear traces of pedogenesis. However, it could not be described as *in situ* developed palaeosoil, but more probably as soil sediments of some gleyic soil type, as fining upwards from coarse sand to granule leg towards sandy silts could be seen here.

Pleistocene alluvial fan

The alluvial fan is laterally continuous for hundreds of meters, which is exposed throughout the trenches and varies in its thickness. It is thickest in the proximal part close to the fault (up to 3m) and fades out laterally. The alluvial fan is generally made of debris-flow dominated facies, which are

represented by matrix-supported diamictons, as well as by sheet-flow dominated facies represented by laminated silt to sand. Sieve alluvial facies are less common, but better sorted clast-supported sandy diamictons to conglomerates prove occasional channelization of alluvial fan surface. The paleochannel exposed in the Trenches I, J, and K (Units 230 – 250) and documented also by shallow geophysics (electric resistivity profiles, see Fig. 4) show slightly different general slope of the fan from the present-day topography. Alluvial fan has sharp erosional base and has been deposited upon the Miocene clayey sand, which had been superficially geliflucted, which is evidenced by geliflucted dark fault gouge resting upon the Miocene surface (Trench C, K, L; Fig. S1.1).

Unit	Description	Depositional environment
10	homogenized A-horizon with ploughed erosional base	topsoil
50	matrix-supported clast-poor intermediate diamicton with clasts ø 1 cm	colluvium
60	matrix-supported intermediate diamicton	colluvium
100-140	monomict unmixed 3–50 cm thick layers of frost-shattered clasts (1–2 cm) of solid rocks (phyllonite, schist, granodiorite) cropping upslope	soliflucted layers/horizon
143	tectonized matrix-supported clast-poor intermediate diamicton with pebbles < 1 cm	colluvial wedge
145	matrix-supported intermediate diamicton with gravel clast < 6 cm, soliflucted	debris-flow alluvial fan deposits
147	matrix-supported sandy gravel with clasts of tectonic breccia	colluvial wedge
150	matrix-supported intermediate diamicton with gravel clasts < 5 cm	debris-flow alluvial fan deposits
155	matrix-supported clast-poor intermediate diamicton with gravel clasts < 5 cm	debris-flow alluvial fan deposits
160	finely laminated clayey silt to granule	sheet-flow alluvial fan deposits
165	tectonized matrix- to clast-supported clast-rich intermediate diamicton with gravel < 8 cm	colluvial wedge
170	matrix-supported intermediate diamicton with gravel clasts < 5 cm	debris-flow alluvial fan deposits
175	laminated clayey silt to sand	sheet-flow alluvial fan deposits
180	tectonized matrix-supported intermediate diamicton with tectonic breccia clasts < 20 cm	colluvial wedge
185	matrix-supported intermediate diamicton with gravel clasts < 5 cm	debris-flow alluvial fan deposits
190	clayey silt to sand	sheet-flow alluvial fan deposits
195	matrix-supported intermediate diamicton with gravel clasts < 1 cm	debris-flow alluvial fan deposits
200	tectonized matrix-supported intermediate diamicton with tectonic breccia clasts < 15 cm	colluvial wedge
203	silt with charcoal	sheet-flow alluvial fan deposits
210	matrix- to clast-supported clast-rich intermediate diamicton with gravel clasts < 15 cm	debris-flow alluvial fan deposits
215	sandy silt	sheet-flow alluvial fan deposits
217	matrix-supported clast-rich intermediate diamicton with gravel clasts < 15 cm	debris-flow alluvial fan deposits
220	tectonized matrix-supported intermediate diamicton with tectonic breccia clasts < 15 cm	colluvial wedge
230	matrix- to clast-supported clast-rich sandy diamicton with gravel clasts < 15 cm	sieve alluvial fan deposits
240	matrix-supported clast-rich intermediate diamicton with gravel clasts < 5 cm	debris-flow alluvial fan deposits
250	clast-supported sandy conglomerate with gravel clasts < 25 cm	sieve alluvial fan deposits

Table S1.1. Description and interpretation of depositional environment for individual units in the trenches (see Fig. S1.1).

Holocene colluvium and topsoil

Holocene (0.3 to 5.3 ka) colluvial deposits, which overlaid the geliflucted layers, are usually 0.5 to 1.5 m thick (units 50 and 60). They are matrix-supported, with the matrix composed predominantly of sandy fraction originating from the weathering of local Javorník granodiorite, which is mixed with silt (weathered micas and feldspars from Javorník granodiorite) and mostly pebble to fine cobble clasts. Gravel clast typically first cm large are mostly subangular to less subrounded and are made of Javorník granodiorite, quartz, (ortho)gneiss and schist, rather rare are clast of Nordics (originating from tills and glaciofluvial deposits left here by Pleistocene ice sheets; Nývlt et al., 2011). Largest blocks are up to 25–30 cm large in a-axis. Highest gravels amount up to >30% is located close to the fault zone, further down this amount decreases to 5–10%. The age of the deposits is discussed in the Supplementary material S2 Chronology. On the top of the colluvia, a recent cambisol is developed with 25–30 cm thick, light grey-brown homogenized A-horizon with ploughed erosional base.

References

Nývlt, D., Engel, Z., Tyráček, J., 2011. Pleistocene Glaciations of Czechia. In: Ehlers, J., Gibbard, P. L., Hughes, P. D., eds: Quaternary Glaciations – Extent and Chronology, A closer look. Developments in Quaternary Science, 15, 37–46. https://doi.org/10.1016/B978-0-444-53447-7.00004-0

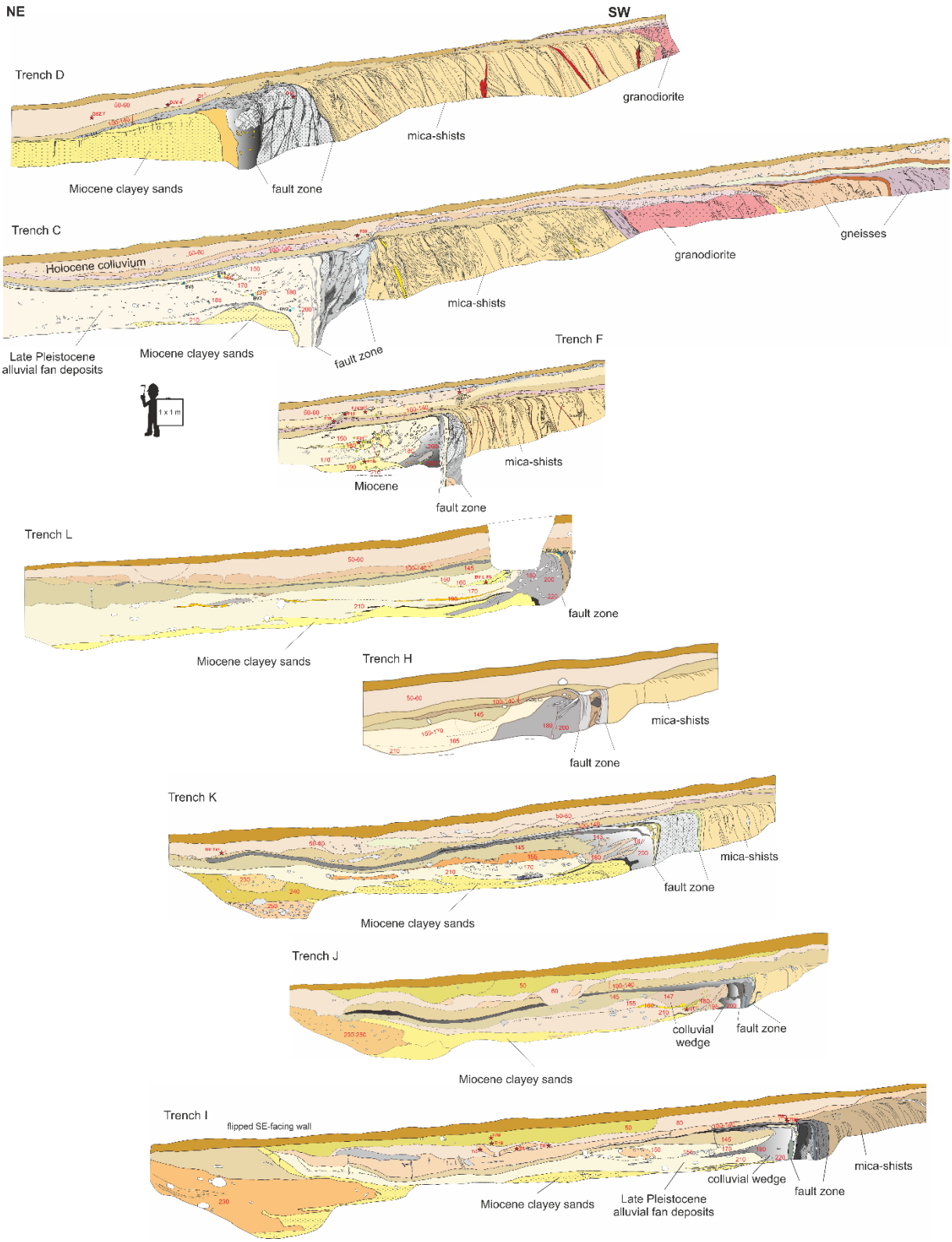
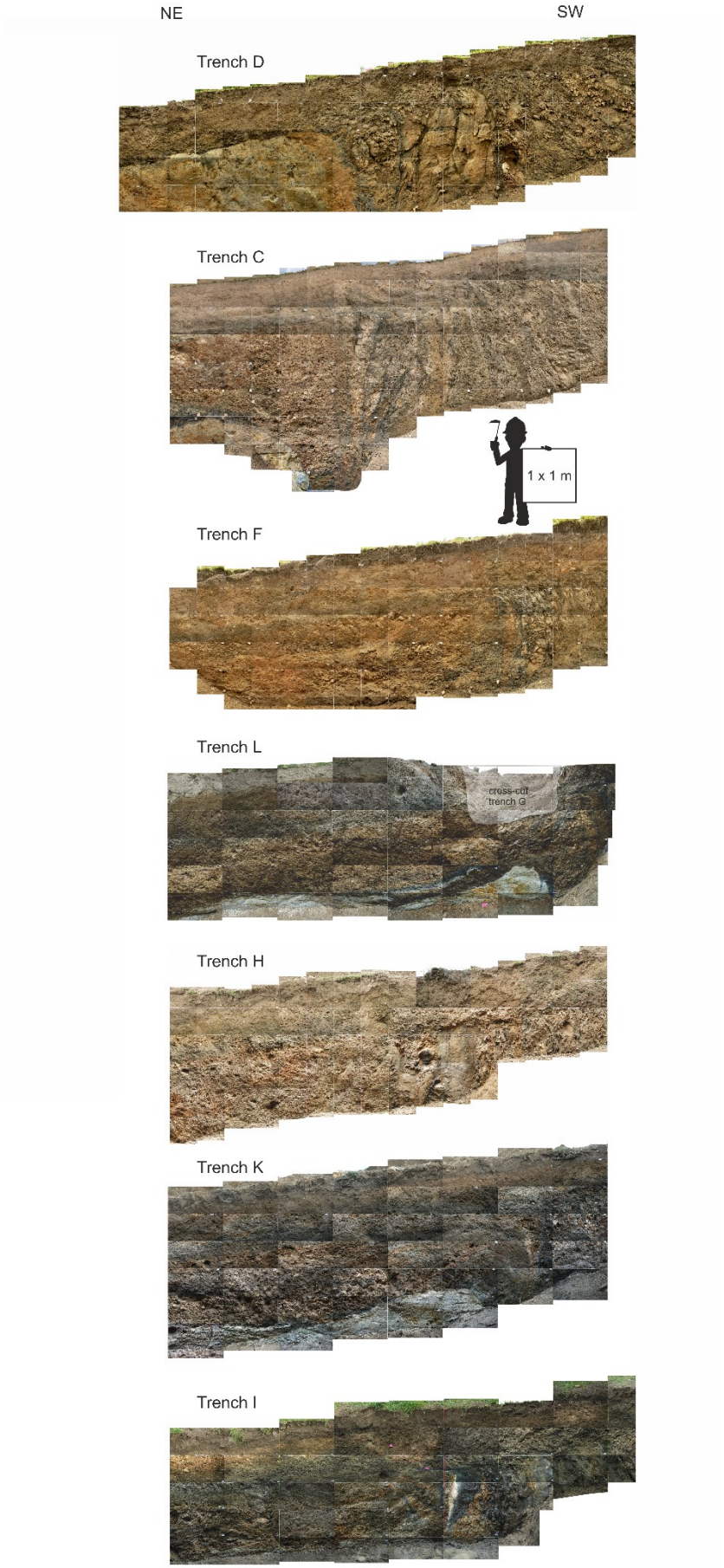


Fig. S1.1. Geological logs of the fault-crossing trenches at the Bílá Voda site with the dated samples position. Numbers express individual lithological units, for their description see Table S1.1. For the trenches position see Fig. 2a

Fig. S1.2 (on the next page). Photomosaics of selected trenches. They were produced from manually rectified photographs of individual grid fields of 0.5 x 0.5 m or 0.5 x 1.0 m size.

Figure S1.2.


NE
SW
Trench D
Trench C
1 x 1 m
Trench F
Trench L
cross-cut trench G
Trench H
Trench K
Trench I

Supplementary Section S2 - Chronology

The chronology of alluvial and colluvial deposits at Bílá Voda is somewhat problematic for a variety of reasons, but the best estimate using a combination of techniques argue for a late Pleistocene age that ranges from 24±4 ka to 63±6 ka. We used radiocarbon dating on detrital charcoal and bulk soil carbon, along with optically stimulated luminescence (OSL) and infrared-stimulated luminescence (IRSL) dating of the sediments and ^{10}Be dating of the sediment column to provide age control on the offset alluvial fan complex (Fig. 2; Table 1). There is broad concordance in age within and between the different techniques, though with some complexity in places. Each method has its strengths and weaknesses, as discussed below, and from these data, we derive a best estimated age along with the likely uncertainty range of the fan age.

Radiocarbon dating

We conducted radiocarbon dating on detrital charcoal and bulk soil samples. The radiocarbon results on detrital charcoal are relatively straight forward, but are mostly limited to the Holocene deposits. We collected charcoal from the upper colluvial deposits in trenches C, D, F, I, and K, and from a silt-rich stratum near a stream cut in Trench R, both of which overlie the geliflucted layers (Table 1, Fig. S1.1). The upper colluvium yielded charcoal that dated to the middle to late Holocene, with ages ranging from about 5 ka to nearly modern times. The charcoal within the silt-rich stratum in trench R, which also caps the fault and overlies displaced fluvial layers, yielded early Holocene ages that range from 9 to 11.2 ka BP (calibrated) (Fig. S2.1). We also collected charcoal-like material from the geliflucted layers in trenches D, F and I, but we now interpret this charcoal as burned root because the samples yielded ages from about 0.7 to 2.7 ka (calibrated). We suggest that the burned root represents the initial burning of the forest when people moved into the area and established agriculture. The precise timing of this event is not known historically but must have occurred prior to the 13th century AD, as the local town of Javorník is mentioned in 1290 as having a church and castle. The youngest ages from the inferred burned roots date to about the 8th-9th century AD, so this is reasonable. As these dates overlap with some from the upper colluvium, it is plausible that some of the upper colluvial dates are also burned roots. Finally, a single sample of charcoal was recovered from a fissure fill in the fault zone, and which dated to about 1 ka. We also consider that this sample is likely a burned root fragment because the fissure fill itself is affected by gelifluction and must date to the late Pleistocene.

The only detrital charcoal sample that we found in the Pleistocene deposits was recovered from a colluvial wedge (unit 203 in Trench J; Fig. S1.1, S2.1) that appears to interfinger with the sediments near the base of the offset alluvial fan complex deposits and yielded an apparent age of about 42-49.7 ka calibrated years BP. As this is very close to the maximum age of radiocarbon dating, we consider this a reliable minimum age for the basal fan deposits. That said, this date falls in the middle of the age range indicated by the Post IR-IRSL results presented below, so it may be a reliable date.

Finally, we sampled the offset alluvial fan deposits for bulk carbon to attempt to directly date them with radiocarbon. All four samples yielded mid-Holocene ages, and as these samples were recovered from below the late Pleistocene gelifluction layers, we discount these ages as representing the age of the deposits. Rather, we interpret that the humic dates represent the translocation of Holocene

organic acids and humus downward through the sediments, and they probably represent the average time of accumulation of post-gelifluction humus.

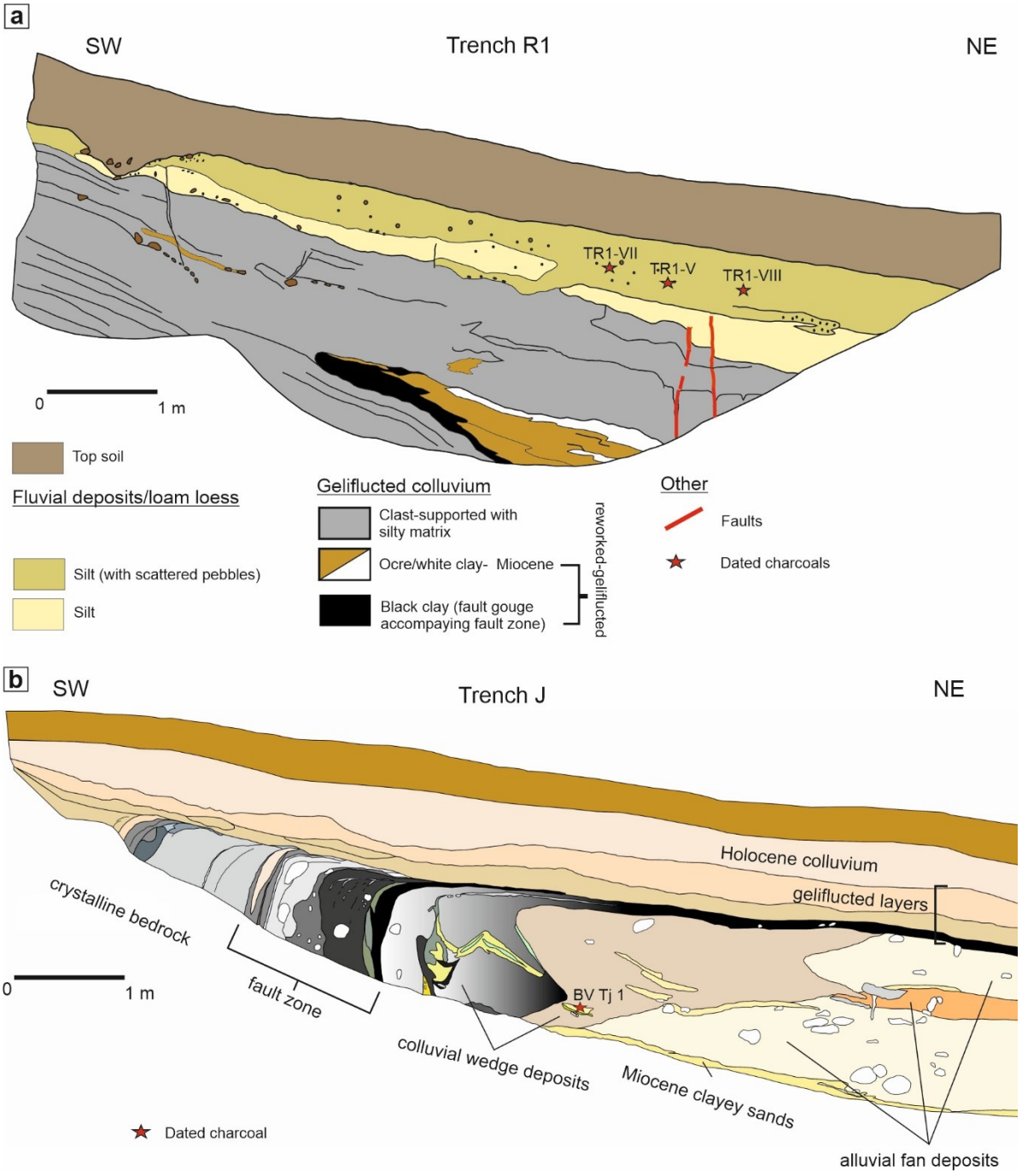
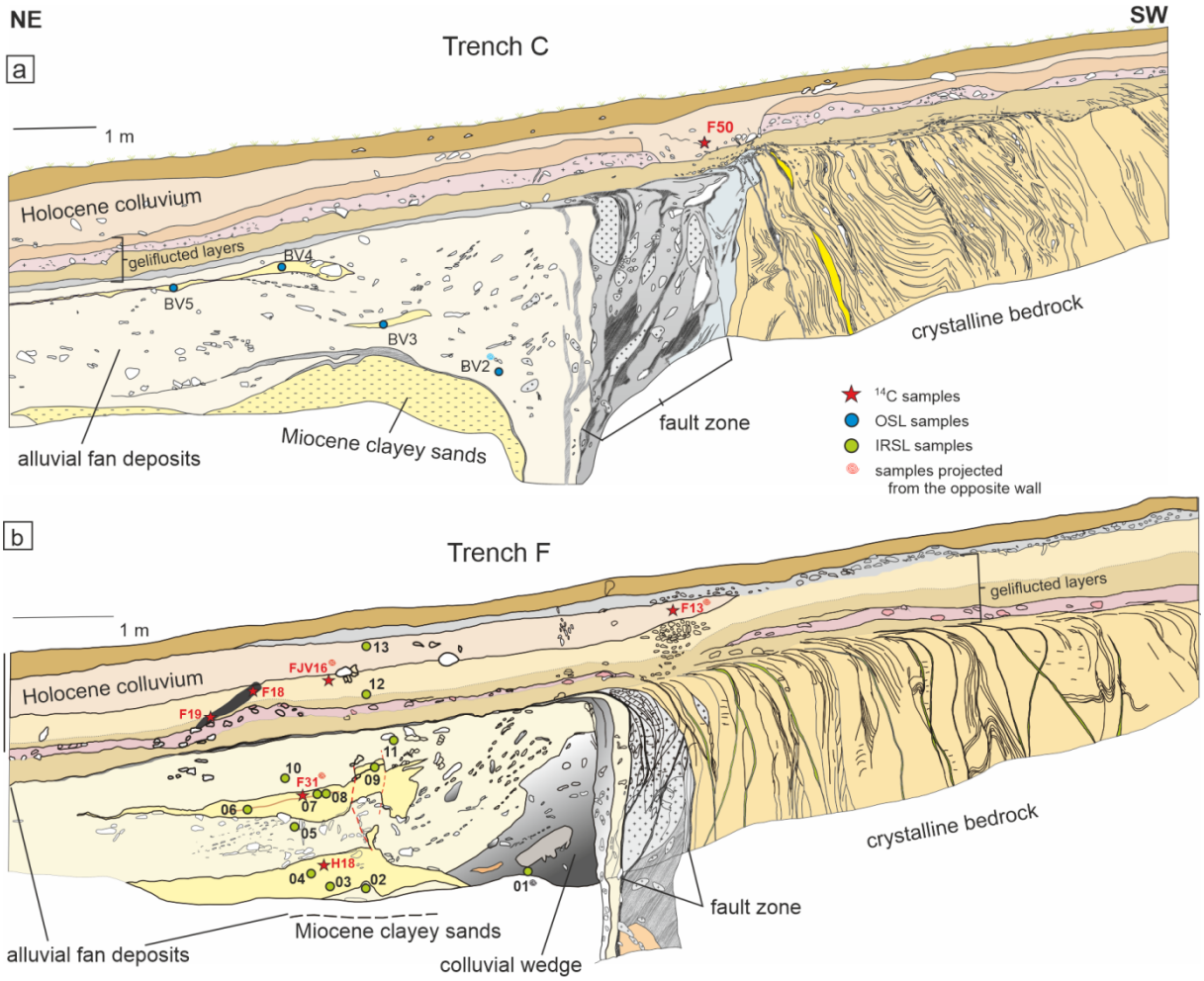


Fig. S2.1. a) Trench R1 log of SE-facing wall with position of radiocarbon dated samples. The dated silty layer of 9-11.2 ka calibrated ages caps the fault; b) Trench J log of SE-facing wall around the fault zone. Radiocarbon dated sample of calibrated age 42-49.7 ka recovered from colluvial wedge close to the base of alluvial fan deposits.

OSL Dating

The ages determined with OSL techniques were analyzed from sediments that comprise the offset alluvial fan complex. The OSL dates (average age of multi-grain, single aliquots) that were determined for the offset alluvial fan deposits ranged from 2.6 to 25.8 ka in age (BV5 2.6 ka, BV4 20.1 ka, BV3 9.46 ka, and BV2 25.8 ka in stratigraphic order) (Fig. S2.2a), which is very problematic in that the alluvial fan sediments must pre-date the period of gelifluction. Because the gelifluction is associated with frozen ground permafrost conditions and seasonal thawing (Matsuoka, 2001), the latest time that these processes could have occurred was before the dramatic warming at the transition between the Younger Dryas and Preboreal period at the beginning of the Holocene (Štěpančíková et al., 2010). Three Late-Glacial gelifluction phases that relate to cold-humid stadials of the Oldest, Older and Youngest Dryas were reported in Germany (see Völkel and Mahr, 1997; Kösel, 1996; Semmel, 1965; Sauer and Felix-Henningsen, 2006). Interestingly, geliflucted layers were observed with constant thickness, typically about 50 cm, in different regions (Kleber and Terhorst eds., 2013), which is also the case of the youngest pre-Holocene geliflucted layers overlying the alluvial fan complex deposits at the Bílá Voda site. In any case, gelifluction occurs over frozen ground, so part of the history of luminescence dose accumulation occurred while the sediments were encased in ice.



142

143 *Fig. S2.2. a) Log of NW-facing wall of the Trench C with the position of OSL and 14C samples; b) Log of*
144 *NW-facing wall of the Trench F with position of IRSL and 14C samples.*

145 If we assume that the lower two samples, which show a strong grouping of aliquots, are affected
146 only to a low degree by grains which give underestimates in age, possibly due to the gelifluction, we
147 recalculate the ages based on the grouping and infer that samples BV2 and BV3 are 26.5±1.3 ka and
148 23.2±1.3 ka, respectively. We take these as minimum ages because it appears that younger grains
149 have been able to penetrate vertically downward and contaminate the OSL signal. Similarly, the
150 upper two samples (BV4 and BV5) yield minimum ages in the range of 20 to 14 ka when only the
151 older aliquots are considered, but BV5 (2.6 ka average age) must have suffered significant intrusion
152 of grains from above because it appears to have many aliquots that greatly underestimate the true
153 age. Alternatively, there may be aspects of gelifluctedsoils that affect OSL age estimates that we do
154 not understand, as the sediments below the active layer were frozen for much of the period
155 between 23 and 12 ka. In any case, we consider all of the OSL ages as minimum age estimates that
156 require further work.
157

Samples BV G1 and G2 were collected from a silty layer dragged along and within the fault zone, and yielded ages of 56.4±2.6 ka and 76.6±6.6 ka (Fig. S1.1 - projected to Trench L). Although these dates are in the range of those determined by Post IR-IRSL (below), considering the issues with other OSL samples from these trenches, we are not certain of their reliability. Nevertheless, they were collected from trenches near the northwestern margin of the fan complex, which is expected to be older due to lateral slip, so they may read true.

^{10}Be Cosmogenic Radionuclide (CRN) Dating

With the apparent discrepancy in ages from the ^{14}C and OSL results, we attempted to apply ^{10}Be cosmogenic radionuclide (CRN) dating by sampling a depth profile in the fan deposits in the Trench P (see Fig. 2a for position). The resulting data (Table S2.1 and S2.2) and depth profile (Fig. S2.3) yielded a consistent exponential decrease in ^{10}Be with depth, albeit with a large inherited component, but suggested that the surface age is only about 11.8 ka in age (see Fig. 5). This is particularly problematic because the timing when gelifluction was active concludes at about 12 ka, which implies that the actual age of the alluvium must be older than the period of gelifluction (~23-12 ka).

One explanation is that a few meters of material has been removed, probably by gelifluction (?), resulting in an apparently young ^{10}Be age (i.e., the ~11.8 ka exposure age represents the age of fan stabilization after erosion by gelifluction, rather than the age of original fan sediment deposition). Evidence for an extensive period of erosion during the onset of the last glaciation (Weichselian) was discussed by Rohdenburg (1965), Schönhals et al. (1964), and Semmel (1968). Studies in eastern Germany suggest as much as 10 to 20 m of periglacial lowering of the land surface occurred through the processes of gelifraction, gelifluction and slopewash erosion during the Elsterian and penultimate Saalian glaciations (5–10 m for each cold period) (Eissmann, 2002).

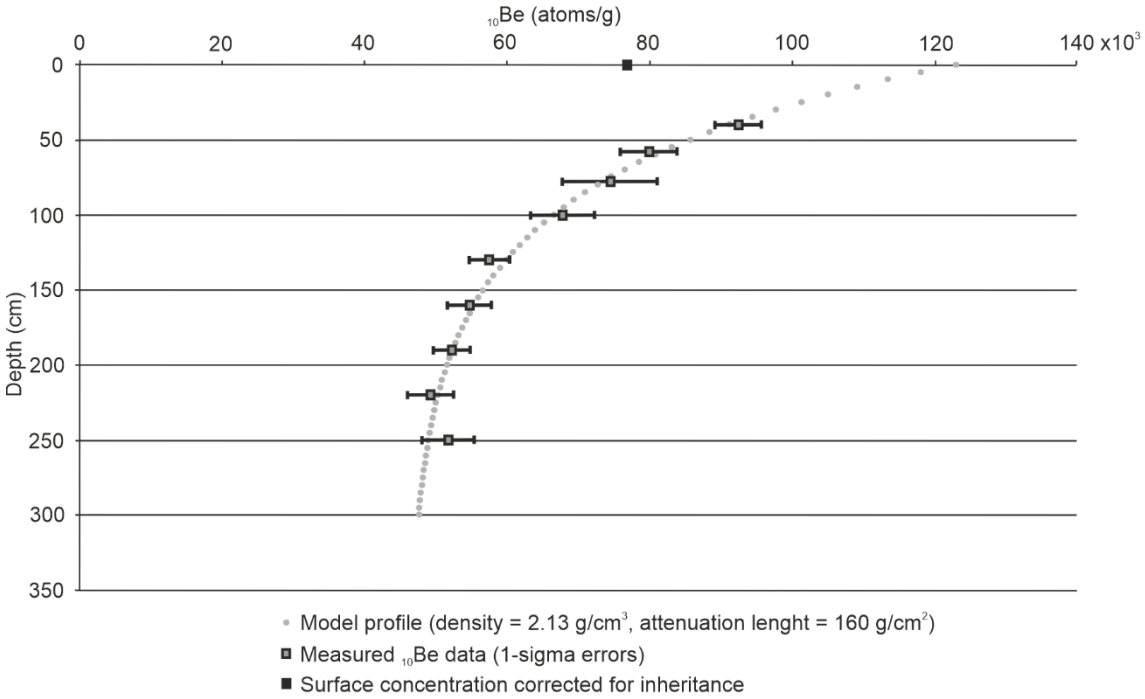


Fig. S2.3. Depth profile showing results of CRN dating of fan surface

CRONUS-Earth ^{10}Be – ^{26}Al exposure age calculator - results							
Version information			Wrapper script			v2.2	
			Main calculator			v2.1	
			Constants			v2.2.1	
			Muons			v1.1	
Production rate calibration information			Using default calibration data set				
^{10}Be Results							
Results not dependent on spallogenic production rate model:				**Exposure ages – constant production rate model:**			
Scaling scheme for spallation			Lal (1991) / Stone (2000)				
Sample name	Thickness scaling factor	Schielding factor	Production rate (muons) (atoms/g/yr)	Internal uncertainty (yr)	Exposure age (yr)	External uncertainty (yr)	Production rate (spallation) (atoms/g/yr)
SMF-P1	0.9994	0.9996	0.203	696	11797	1241	8.33
					Exposure ages – time varying production model:		
Scaling scheme for spallation	Desilets and others (2003, 2008)		Dunai (2001)		Lifton and others (2005)		Time-dependent Lal (1991) / Stone (2000)
Sample name	Exposure age (yr)	External uncert. (yr)	Exposure age (yr)	External uncert. (yr)	Exposure age (yr)	External uncert. (yr)	Exposure age (yr)	External uncert. (yr)
SMF-P1	12652	1673	12800	1686	12358	1423	12058	1243

Table S2.1. CRONUS age calculator results (see Methods section for details). Scaling scheme for spallation: Lal (1991) / Stone (2000).

However, the presence of a significant soil, which includes a reddened and relatively thick argillic horizon with strong clay film development in the downslope position of the fan (Fig. 2 for location), argues against several meters of surface removal, assuming that the amount of removal due to gelifluction is similar across the fan surface. Nevertheless, we estimate that to completely remove previous CRN inventory accumulated prior to ~12 ka would likely require at least 2 m of removal. Two meters of removal would also imply that the original fan apex was likely thicker than 6 m.

SUERC ID	Sample name	Normalized			Background corrected		
		Ratio	Uncertainty	Uncertainty	Ratio	Uncertainty	Uncertainty
b7522	SSMF40	1.09×10^{-13}	3.52×10^{-15}	3.2%	1.06×10^{-13}	3.71×10^{-15}	3.5%
b7523	SSMF60	6.14×10^{-14}	2.71×10^{-15}	4.4%	5.87×10^{-14}	2.95×10^{-15}	5.0%
b7524	SSMF80	4.21×10^{-14}	3.35×10^{-15}	7.9%	3.95×10^{-14}	3.55×10^{-15}	9.0%
b7525	SSMF100	5.41×10^{-14}	3.24×10^{-15}	6.0%	5.15×10^{-14}	3.45×10^{-15}	6.7%
b7529	SSMF130	6.78×10^{-14}	2.93×10^{-15}	4.3%	6.52×10^{-14}	3.16×10^{-15}	4.8%
b7530	SSMF160	6.39×10^{-14}	3.21×10^{-15}	5.0%	6.12×10^{-14}	3.42×10^{-15}	5.6%
b7531	SSMF190	7.42×10^{-14}	3.35×10^{-15}	4.5%	7.16×10^{-14}	3.55×10^{-15}	5.0%
b7532	SSMF220	4.41×10^{-14}	2.45×10^{-15}	5.6%	4.14×10^{-14}	2.72×10^{-15}	6.6%
b7533	SSMF250	5.08×10^{-14}	3.04×10^{-15}	6.0%	4.81×10^{-14}	3.26×10^{-15}	6.8%
b7519	SCFG1315	2.64×10^{-15}	1.18×10^{-15}	44.7%	-	-	-

Table S2.2. The calculation of ^{10}Be concentration for each sample based on AMS ^{10}Be/^{9}Be ratios measured at SUERC and normalized to the NIST standard with assumed ratio of 2.79 x 10^{-11}.

$IRSL_{225}$ Age Determinations

Finally, we re-opened Trench F and sampled the alluvial fan deposits for post-IR IRSL dating. Trench F was adjacent to Trench C where the OSL samples were collected (approx. 5m apart) and from the same sedimentary units (for position see Fig. S2.2b). A sequence of 13 IRSL tubes was collected from the NW facing wall of Trench F.

Many grains provided intense $IRSL_{225}$ decays, and displayed regular growth with applied dose that were well-fitted with an exponential or exponential plus linear function. Saturation doses for most grains were in the region of many hundreds of Gy. Equivalent dose values showed significant variation for most samples, interpreted as primarily caused by incomplete signal zeroing by light exposure prior to deposition under relatively high energy conditions. Most samples show a minimum value shared by a group of grains within the expected over-dispersion (15%), interpreted as their depositional age (Rhodes, 2015).

In broad terms, the age estimates are internally and externally consistent and suggest that the main Pleistocene gravelly fan unit comprises grains that were originally deposited around 100-150 ka under medium to low energy conditions, and subsequently reworked and redeposited during Marine Isotope Stage (MIS) 3 without significant light exposure, as represented by the minimum age grouping, highlighted in red, with red dashed lines (Fig. S2.4, a through g). The lowest deposits sampled provide post-IR $IRSL_{225}$ age estimates of 63±6 ka (BV15-02), higher gravels of the fan deposit give age estimates of 37±3 (BV15-05), 31±4 (BV15-10) and 24±4 ka (BV15-11). Two sand lenses within the gravel were sampled with two and four tubes, respectively. Some of these sand lens samples showed very poor bleaching, with few grains that were well-bleached. To overcome this limitation, the individual age estimates for each lens have been combined giving 55±6 ka for the lower lens and 53±3 ka for the upper lens.

Field code	Lab code	Depth (m)	Stratigraphic notes	De (Gy)	Dose rate (mGy/a)	p-IR $IRSL_{225}$ age (ka)
BV15-13	Shfd15153	0.36	Holocene colluvium	3.13 ± 0.47	4.06 ± 0.19	0.77 ± 0.12
BV15-12	Shfd15152	0.38	Gravelly gelifluctate	123 ± 16	4.01 ± 0.18	30.6 ± 4.2
BV15-11	Shfd15151	1.32	Gravel	120 ± 17	4.99 ± 0.25	24.1 ± 3.7
BV15-10	Shfd15150	1.66	Gravel	137 ± 17	4.43 ± 0.21	30.8 ± 4.1
BV15-09	Shfd15149	1.65	Sand lens	343 ± 22	5.43 ± 0.21	53.2 ± 3.0 *
BV15-08	Shfd15148	1.93	Sand lens	222 ± 19	4.85 ± 0.19	53.2 ± 3.0 *
BV15-07	Shfd15147	1.99	Sand lens	257 ± 22	5.04 ± 0.21	53.2 ± 3.0 *
BV15-06	Shfd15146	2.09	Sand lens	250 ± 29	4.63 ± 0.20	53.2 ± 3.0 *
BV15-05	Shfd15145	2.32	Gravel	190 ± 13	5.12 ± 0.24	37.1 ± 3.1
BV15-04	Shfd15144	2.65	Sandy silt	223 ± 23	4.34 ± 0.17	54.6 ± 5.8 **
BV15-03	Shfd15143	2.78	Sandy silt	433 ± 22	4.23 ± 0.18	54.6 ± 5.8 **
BV15-02	Shfd15142	2.82	Gravel	273 ± 23	4.33 ± 0.19	62.9 ± 6.1
BV15-01	Shfd15141	3.00	Sandy silt	74.4 ± 12.1	5.28 ± 0.23	14.1 ± 2.4

*Table S2.3. Parameters and age estimates for post-IR $IRSL_{225}$ dating. * Combined age 06, 07, 08, 09; ** Combined age 03, 04*

There is some apparent age inversion between gravel sample BV15-05 and the upper lens (samples BV15-06, 07, 08 and 09 combined age), and it is possible that this body of sediment was transported as a frozen block. The fan gravel deposits are overlain by a gravel-rich gelifluctate that moved downhill during periglacial conditions. It contains grains exposed to light at 31±4 ka, and may have moved into position without light exposure of the constituent grains.

A sample from the upper Holocene colluvium gives an age estimate of 770±120 years, consistent with the range of ^{14}C dates from this layer. A sample collected from the opposite wall of Trench F in a small silty sand lens provides an age estimate of 14±2 ka, but it is difficult to relate the stratigraphy of that deposit to the deposits dated by other 12 post-IR $IRSL_{225}$ samples, and the significance of this age estimate remains uncertain.

We note that in many cases, the apparent age distributions of these single grain populations retain information about previous light exposure events suggesting that low energy conditions prevailed in MIS 5. Dating results and parameters used in age calculations are presented in Table S2.3, including combined ages for the two sand lenses within the fan gravels. The single grain apparent age distributions from individual samples, or groups for the two sand lenses where samples have been combined, are presented in Fig. S2.4, showing individual age estimates for each single grain of K-feldspar, plotted in decreasing order of sensitivity, with the most sensitive grain plotted on the left. This is a useful way to show these data as grains with same apparent age lie on a horizontal line.

In order to assess the possibility that these age estimates were affected by anomalous fading, we determined the stored dose for each grain using a delayed measurement following storage. Results for sample BV15-04 are shown in Fig. S2.4. After 3 weeks of storage, only a very small reduction is observed suggesting that anomalous fading of this signal is not a significant concern. This is consistent with similar observations from other samples, and no fading correction has been applied. The response of K-feldspar grains separated from two cobbles collected from the drainage to the south of the site were also measured. The natural signal was effectively in saturation for the majority of grains measured and for the summed post-IR $IRSL_{225}$ signal, consistent with the conclusion that this signal in this location is not adversely affected by anomalous fading, as observed elsewhere (Thomsen et al., 2011).

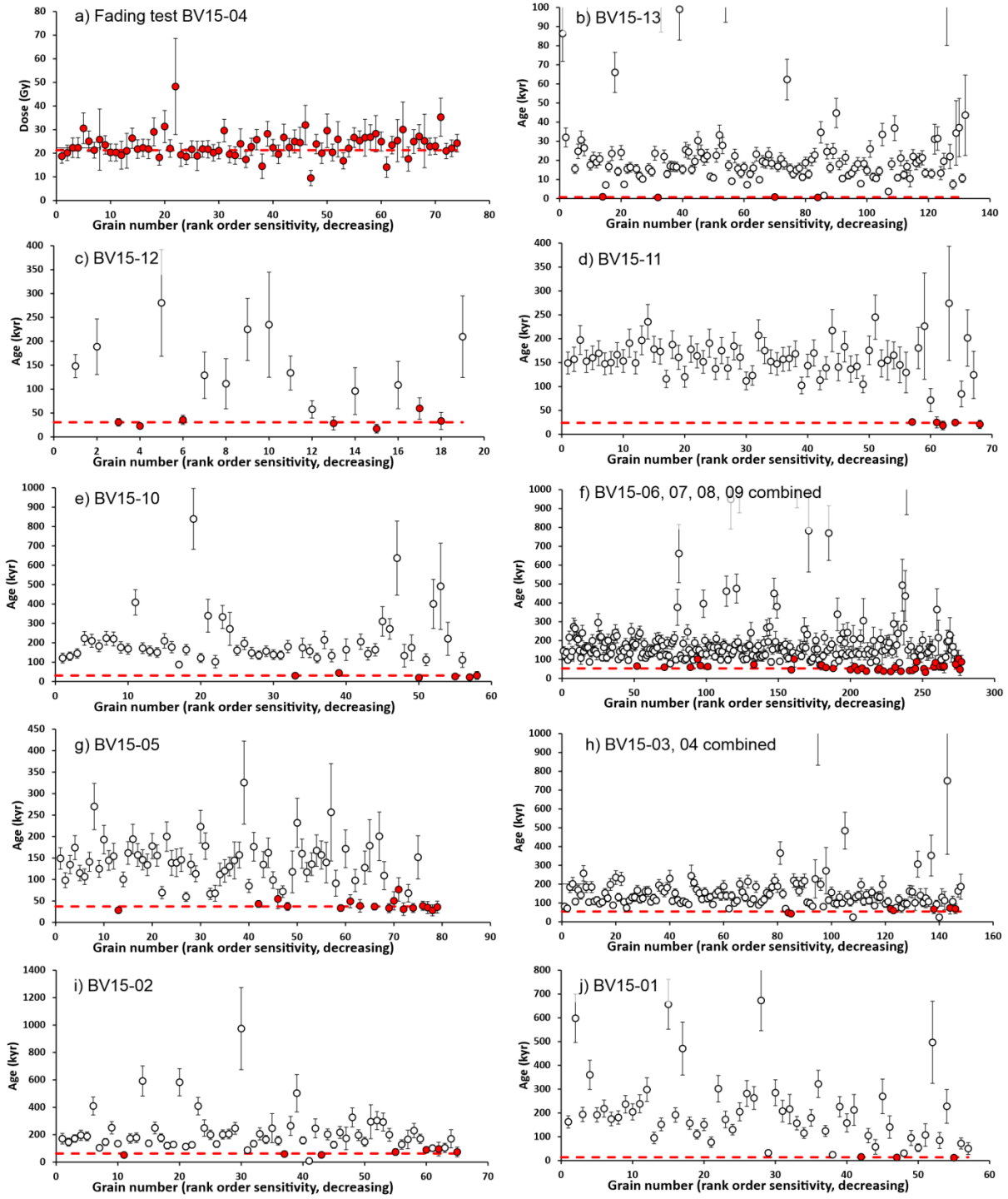


Fig. S2.4. Single grain post-IR IRSL$_{225}$ results for Bílá Voda samples from Trench F. BV15 codes represent field codes for each sample, for corresponding laboratory codes see in Table S2.3; a) single grain fading test data for sample BV15-04 measured three weeks after a dose of 21.15 Gy was administered; the red dashed line is the dose determined using a central age model, providing an estimate of 21.26 ±0.47 Gy, demonstrating no measurable fading, b) – j) single grain post-IR IRSL$_{225}$ dating results for the samples indicated in approximate stratigraphic order; data points in red = included in age calculation, open symbols = excluded; see Table S2.3 for age estimates and associated 1 sigma uncertainties; the distribution of apparent ages suggests that this gravel unit from the fan

(samples BV15-02 to 11) comprises grains that were originally deposited around 100-150 ka under medium low energy conditions, and subsequently reworked between 63±7 ka and 24±4 with only very limited light exposure; grains exposed during the final depositional event are represented by the minimum age groupings highlighted in red for each sample set, with age estimates indicated by the red dashed line. Note for samples BV15-03 & 04 (plot h) collected within a single sand lens, the plot shows the combined data; this is also the case for samples BV15-06, 07, 08, and 09 (plot f).

In summary, the large body of evidence represented by the post-IR $IRSL_{225}$ age estimates clearly indicate a MIS 3 to MIS 2 (63 to 24 ka) age range for the fan deposits truncated and deformed by fault movement.

References

Desilets, D., Zreda, M., 2003. Spatial and temporal distribution of secondary cosmic-ray nucleon intensities and applications to in situ cosmogenic dating. Earth Planet. Sci. Lett., 206, 21-42. https://doi.org/10.1016/S0012-821X(02)01088-9.

Desilets, D., Zreda, M., Prabu, T, 2006. Extended scaling factors for in situ cosmogenic nuclides: New measurements at low latitude. Earth Planet. Sci. Lett., 246, 265-276. https://doi.org/10.1016/j.epsl.2006.03.051.

Dunai, T., 2001. Influence of secular variation of the geomagnetic field on production rates of in situ produced cosmogenic nuclides. Earth Planet. Sci. Lett., 193, 197-212. https://doi.org/10.1016/s0012-821x(01)00503-9.

Eissmann, L., 2002. Quaternary geology of eastern Germany (Saxony, Saxon–Anhalt, South Brandenburg, Thuringia), type area of the Elsterian and Saalian Stages in Europe. Quaternary Science Reviews, 21, 1275-1346. https://doi.org/10.1016/S0277-3791(01)00075-0.

Kleber, A., Terhorst, B. (eds.), 2013. Mid-latitude Slope Deposits (Cover beds), Developments in Sedimentology, 66, Elsevier.

Kösel, M., 1996. Der Einfluss von Relief und periglazialen Deckschichten auf die Bodenaus-bildung im mittleren Rheingletschergebiet von Oberschwaben. Tübinger geowissenschaft Arbeiter, Reihe D, 1, pp. 147.

Lal, D., 1991. Cosmic ray labeling of erosion surfaces: in situ nuclide production rates and erosion models. Earth Planet. Sci. Lett., 104, 424-439. https://doi.org/10.1016/0012-821X(91)90220-C.

Lifton, N., Bieber, J., Clem, J., Duldig, M., Evenson, P, Humble, J., Pyle, R., 2005. Addressing solar modulation and long-term uncertainties in scaling secondary cosmic rays for in situ cosmogenic nuclide applications. Earth Planet. Sci. Lett., 239, 140-161. https://doi.org/10.1016/j.epsl.2005.07.001.

Matsuoka, N., 2001. Solifluction rates, processes and landforms: a global review. Earth Science Reviews, 55, 107-134. https://doi.org/10.1016/S0012-8252(01)00057-5.

Rhodes, E.J., 2015. Dating sediments using potassium feldspar single-grain IRSL: initial methodological considerations. Quaternary International, 362, 14-22. https://doi.org/10.1016/j.quaint.2014. 12.012.

Sauer D., Felix-Henningsen P., 2006. Saprolite, soils, and sediments in the Rhenish Massif as records of climate and landscape history. Quaternary International, 156-157, 4-12. https://doi.org/10.1016/j.quaint.2006.05.001.

Semmel, A., 1965. Überein Vorkommen von allerödzeitlichem Bimstuff bei Odersbach (Bl. 5515 Weilburg). Notizbl. hess. L.-Amt Bodenforschung, 93, 346-347.

Štěpančíková, P., Hók, J., Nývlt, D., Dohnal, J., Sýkorová, I., Stemberk, J., 2010. Active tectonics research using trenching technique on the south-eastern section of the Sudetic Marginal Fault (NE Bohemian Massif, central Europe). Tectonophysics, 485, 1-4, 269-282. https://doi.org/10.1016/j.tecto.2010.01.004.

Stone, J.O., 2000. Air pressure and cosmogenic isotope production. Journal of Geophysical Research, 105, 23753-23759. https://doi.org/10.1029/2000JB900181.

Thomsen, K.J., Murray, A.S., Jain, M., 2011. Stability of IRSL signals from sedimentary K-feldspar samples. Geochronometria, 38, 1-13. https://doi.org/10.2478/s13386-011-0003-z.

Völkel, J., Mahr, A., 1997. Neue Befunde zum Alter der periglazialen Deckschichten im Vorderen Bayerischen Wald. Zeitschrift fur Geomorphologie, Neue Folge, 41, 131-137.

Supplementary Section S3 – Ice-loading

We calculate stresses assuming a lithosphere 100 km thick with a Young's modulus of 70 GPa and a Poisson's ratio of 0.25, typical values for continental lithosphere. The asthenosphere is modeled as a Maxwell viscoelastic halfspace with the same elastic bulk modulus as the lithosphere and with a viscous relaxation time of 1130 years, corresponding to a viscosity of 5×10^{20} Pa s. The resulting stress tensor is sampled at a mean seismogenic depth of 10 km and resolved onto a plane striking 320ºE of N and dipping 70º to the northeast, assuming a left-lateral slip sense and using a coefficient of friction of 0.6. We tested a range of possible lithospheric thicknesses from 75 – 200 km (Conrad and Lithgow-Bertelloni, 2006) and asthenosphere relaxation times from 680 – 2260 yrs (Steffen and Kaufmann, 2005; Harig et al., 2010; Schmidt et al., 2014) (Fig. S3.1a). A thicker lithosphere causes the flexural bulge associated with ice sheet loading to shift further south, causing much higher Coulomb stress values along the SMF. Results are much less sensitive to the asthenosphere relaxation time, with peak stress values varying by < 10%. We conservatively use the lowest reasonable lithospheric thickness for the region, and note that the absolute stress changes could reasonably be higher by up to a factor of 2.

Fig. S3.1b shows the change in Coulomb stress expected along the SMF for different possible slip directions. We find that right lateral slip would be inhibited by ice sheet growth. Normal and reverse slip would both be promoted, but with stress accumulation rates and absolute stress changes much lower than expected for left-lateral slip.

The 130 km long SMF experiences a range of Coulomb stress change magnitudes along strike due to varying proximity to the Weichselian Ice Sheet (Fig. S3.1c). Stress accumulation rate during gradual ice sheet build up prior to 22 ka varies from 0.05 – 0.1 kPa/yr, while stress accumulation rate during the rapid buildup to LGM is more consistent at 0.28 – 0.31 kPa/yr. While the field observations reported here were taken at Bílá Voda, we have no information about where along strike fault slip may have initiated. Consequently, we show in Fig. 5 the stress changes at the northern end of the SMF, which is the area most likely to have been affected by ice sheet changes. Overall, the uncertainty in stress perturbation magnitude associated with ice sheet unloading is most sensitive to choice of lithosphere thickness, with all other factors having second-order influence.

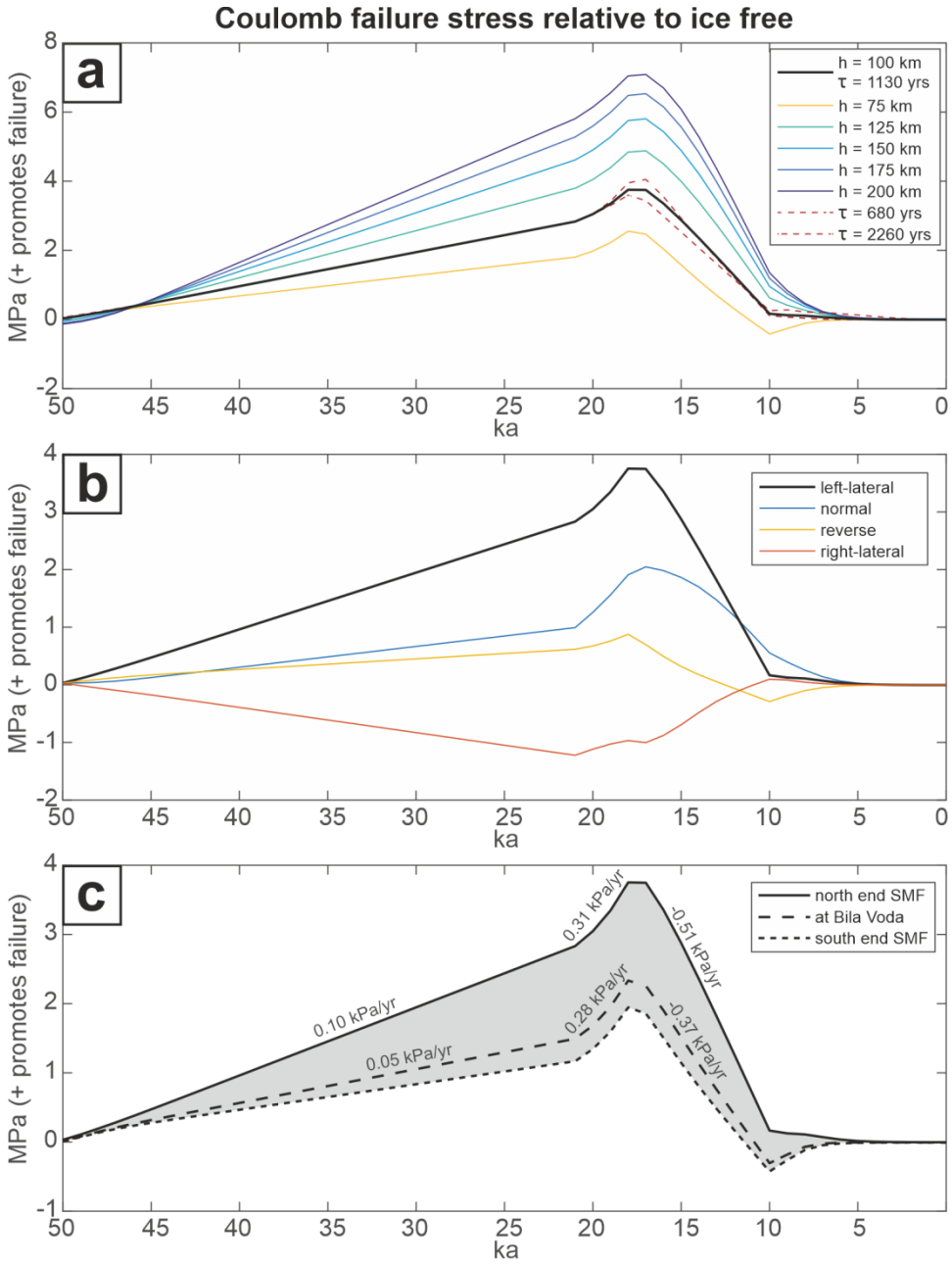


Figure S3.1: Changes in Coulomb failure stress resolved on the SMF relative to ice free conditions for different possible model parameter; a) varying lithosphere thickness (solid lines) and asthenosphere relaxation time (dashed lines); b) varying fault slip sense; c) varying location along the SFM, with gray shaded region indicating range of possible values along strike, and stress accumulation rates indicated. In all cases, thick black line represents the solution shown in Fig. 5.

References

Conrad, C.P., Lithgow-Bertelloni, C., 2006. Influence of continental roots and asthenosphere on plate-mantle coupling. Geophys. Res. Lett., 33 (L05312). https://doi.org/10.1029/2005GL025621.

Harig, C., Zhong, A., Simons, F.J., 2010. Constraints on upper mantle viscosity from the flow-induced pressure gradients across the Australian continental keel, Geochem. Geophys. Geosys., 11(6), Q06004, https://doi.org/10.1029/2010GC003038.

Schmidt, P., B. Lund, J.O., 2014. Näslund, and J. Fastook Comparing a thermo-mechanical Weichselian Ice Sheet reconstruction to reconstructions based on the sea level equation: aspects of ice configurations and glacial isostatic adjustment. Solid Earth, 5, 371-388. https://doi.org/10.5194/se-5-371-2014.

Steffen, H., Kaufmann, G., 2005. Glacial isostatic adjustment of Scandinavia and northwestern Europe and the radial viscosity structure of Earth's mantle, Geophys. J. Int., 163, 801-812. https://doi.org/10.111/j.1365-246X.2005.02740.x.

Příloha 4

Hypogenic Versus Epigenic Origin of Deep Underwater Caves Illustrated by the Hranice Abyss (Czech Republic) – The World's Deepest Freshwater Cave

Journal of Geophysical Research: Earth Surface

Klanica et al. 2020

Klanica R., Kadlec J., Táborík P., Mrlina J., Valenta J., Kováčiková S., Hill G. J. (2020): Hypogenic versus epigenic origin of deep underwater caves illustrated on the Hranice Abyss (Czech Republic) – the world's deepest freshwater cave. Journal of Geophysical Research: Earth Surface 125(9), e2020JF005663. https://doi.org/10.1029/2020JF005663

JGR Earth Surface

RESEARCH ARTICLE
10.1029/2020JF005663

Key Points:
- Hypogenic and epigenic evolution is considered for deep underwater caves
- Geophysical models show geometry and extent of the Hranice Abyss
- A new formation model of the Hranice Abyss based on epigenic formation is presented

Correspondence to:
R. Klanica,
rk@ig.cas.cz

Citation:
Klanica, R., Kadlec, J., Táborík, P., Mrlina, J., Valenta, J., & Kováčiková, S., et al. (2020). Hypogenic versus epigenic origin of deep underwater caves illustrated by the Hranice Abyss (Czech Republic)—The world's deepest freshwater cave. *Journal of Geophysical Research: Earth Surface*, *125*, e2020JF005663. https://doi.org/10.1029/2020JF005663

Received 17 APR 2020
Accepted 10 AUG 2020
Accepted article online 15 JUL 2020

©2020. American Geophysical Union. All Rights Reserved.

Hypogenic Versus Epigenic Origin of Deep Underwater Caves Illustrated by the Hranice Abyss (Czech Republic)—The World's Deepest Freshwater Cave

Radek Klanica[1], Jaroslav Kadlec[1], Petr Táborík[2,3], Jan Mrlina[1], Jan Valenta[2], Světlana Kováčiková[1], and Graham J. Hill[1]

[1]Institute of Geophysics, Czech Academy of Sciences, Prague, Czech Republic, [2]Faculty of Science, Institute of Hydrogeology, Engineering Geology and Applied Geophysics, Charles University, Prague, Czech Republic, [3]Institute of Rock Structure and Mechanics, Czech Academy of Sciences, Prague, Czech Republic

Abstract Extremely deep freshwater filled cave systems are common in karst systems globally. The origin and evolution of such caves are usually attributed to hypogenic (bottom-up) processes, in which acidic groundwater dissolves limestone from below. However, these deep cave systems can form by epigenic (top-down) processes, with meteoric waters descending from the surface underground. The Hranice Abyss (Czech Republic), with a reached depth of 473.5 m, is the deepest mapped extent of such a system globally, although its maximum depth is unknown. Multiple geophysical data sets (gravity, electrical resistivity tomography, audiomagnetotellurics, and seismic refraction and reflection) are used to investigate the extent and formation of the Hranice Abyss. The geophysical results suggest the Hranice Abyss extends to depths of ~1 km. Further, we identify structures within the karst, including buried cockpit karst towers with several NW-SE-oriented valleys. The new geophysical results from the Hranice Abyss, considered in combination with geological constraints of the region (tectonic evolution and morphology of karst structure), suggest an epigenic formation process, rather than the traditionally invoked hypogenic origin. Formation by epigenic rather than hypogenic processes has implications for local and regional karst history associated with areas hosting deep karst systems.

1. Introduction

Whether large cave systems formed via epigenic or hypogenic processes is a fundamental question for understanding the regional and local karst processes of the cave area. Epigenic caves form by top-down dissolution of meteoric water enriched with soil CO_2 infiltrating from the surface and may be the dominant formation processes for as many as 80–90% of known caves (Audra & Palmer, 2015). On the other hand, hypogenic cave systems form from a bottom-up migration of deep-sourced thermally elevated CO_2-H_2S bearing fluids, often typically related to volcanic/mantle structures (Klimchouk et al., 2017) or more rarely to petroleum generating processes (DuChene et al., 2017). Hypogenic fluids in the upper crust result in groundwater enriched with strong acids (e.g., CO_2, H_2S, or HCl) that can upwell via artesian aquifers or interformational flow in/from the zone of fluid-geodynamic influence along faults or fractured zones (Klimchouk et al., 2017).

Determining the evolution dominant process and formation history of deep-flooded cave systems is complicated by the difficulty of completing detailed exploration beneath the water table. Flooded deep karst cave systems are found globally (Vysoká et al., 2019) for example, in Italy (Pozzo del Merro, 392 m), Mexico (Zacatón, 335 m), Brazil (Lagoa Misteriosa, 220 m), and South Africa (Boesmangsat, 283 m). The commonly invoked mechanism of formation of these vertical caves is hypogenic (Klimchouk et al., 2017), largely based on present-day observations such as groundwater filling the Pozzo del Merro and El Zacatón abysses being enriched by CO_2 and H_2S from nearby volcanic centers (Gary, 2017; Gary et al., 2003).

The local structure of karstified regions is a controlling factor in the formation of horizontal or vertical cave morphologies. Further, the surficial geomorphic evolution (e.g., variations in the erosional base elevation) of the surrounding landscape also plays a fundamental role in the evolution of epigenic cave systems (Ford & Williams, 2007). Deep epigenic water-filled caves have developed in southern France (Fountaine de Vaucluse, 308 m; Audra et al., 2004) and in Croatia (Red Lake, 350 m; Andrić & Bonacci, 2014). The

formation of Fountaine de Vaucluse was triggered by a dramatic regional erosional base elevation decrease during the Messinian period (5.96–5.32 Ma) when the Mediterranean Sea was almost dry. The erosional base drop quickly led to river valley deepening, followed by the formation of a deep cave system. Marine transgression caused the end of the Messinian lowstand, which led the deep canyon-like valleys in the karst regions to be infilled with clastic sequences. The pre-Messinian freshwater springs flowing at the base of the canyon system did not experience a corresponding rise in base level associated with the canyon filling sedimentation; rather, they became "buried," leading to bottom-up flooding of the karst cave systems (Audra et al., 2004).

The Hranice Abyss (HA) currently represents the deepest flooded freshwater cave in the world, with a maximum depth 473.5 m below surface estimated using a ROV (remote-operated vehicle). The depth the submersible reached was limited by the length of the fiber-optic communication cable and, as such, does not represent the full extent of the cave system (Guba, 2016; Zajíček, 2020). The HA is filled with Ca-HCO_3 mineral water enriched by CO_2 with temperature varying from 14.5–18.8°C depending on seasonal variations and the depth below the water table level (Vysoká et al., 2019). Stable isotopic CO_2 compositions, together with a ratio of $^3He/^4He$ dissolved in the water, indicate an origin of the gasses close to the Earth's mantle/crust transition (e.g., Meyberg & Rinne, 1995; Šmejkal et al., 1976; Sracek et al., 2019), evoking the possibility of the extreme depth of the HA (Meyberg & Rinne, 1995) and suggesting a hypogene (hydrothermal) origin of the HA (e.g., Sracek et al., 2019; Zajíček, 2020), following an early accepted view on the Hranice Karst area evolution (Hynie & Kodym, 1936).

Geophysical methods have been frequently used to image subsurface karst structure (e.g., Carvalho et al., 2005; Zhou et al., 2002). Geophysical imaging of these regions can provide valuable information needed for reconstruction of the tectonic and morphological evolution of these areas. In the case of cave formation features, such as a well-developed and deep-seated fault network, and alteration zones resulting from large-scale fluxing of heated waters and mantle-derived gasses are indicative of hypogenic formation, while a complex shallow drainage pattern morphology, including sinkholes and dolines, suggests epigenic formation.

We use the results from geophysical surveys of the HA area to reveal the local geological and morphological structures within the HA. The new geophysical results are then integrated with regional tectonic history and period of formation of the HA in a reassessment of its formation mechanism. A similar approach may be applied to other deep-flooded karst cave systems globally to identify the key karst structures associated with each of the formation mechanisms.

2. Geological Settings and Karst Evolution

The HA is a part of the Hranice Karst (HK) located in the eastern part of the Czech Republic, ~35 km east of Olomouc City. The HK covers an ~15 km^2 area and formed at a contact between the Bohemian Massif and Outer Western Carpathians within the Carpathian orogenic belt. The carbonate rocks, susceptible to karst processes, were deposited on carbonate platforms and reef slopes in a tropical ocean during the Middle Devonian and Early Carboniferous (Macocha and Líšeň Fms.) (Otava, 2010). The estimated thickness of carbonates reaches 1.2 km based on a coring conducted about 11 km SE of the HK area (Sracek et al., 2019). Deposition of overlying Carboniferous turbidite flysch sequences, up to 6 km thick, indicate deepening of the sedimentary basin (Bubík et al., 2018). Both carbonate and clastic sequences were folded and thrusted during the Variscan Orogeny in the Late Carboniferous (Kalvoda et al., 2008). In the Carpathian domain, marine silicic-clastic and flysch sediments were deposited within the Cretaceous and Paleogene periods. These sequences were folded and thrusted over the eastern margin of the Bohemian Massif during the Alpine Orogeny since the Oligocene/Miocene transition to the mid-Miocene (early Langhian). The frontal thrust terminations are found very close to the HK area (Figure 1). Parallel with the Carpathian deformation front, the Carpathian Foredeep (CF) basin originated during the early Miocene (Burdigalian) and subsequently was filled with shallow-water carbonates and marine clastic deposits (e.g., Sracek et al., 2019). The CF segment passing along the HK area was opened later—in the early Langhian (Otava et al., 2016) by sinistral strike-slip horizontal fault movements (Havíř et al., 2004) forming a canyon-like graben up to 1 km deep (Bubík et al., 2018). The CF, together with the surrounding areas, was subsequently filled and covered with conglomerates, sandstones, and mudstones during the short early Langhian marine transgression

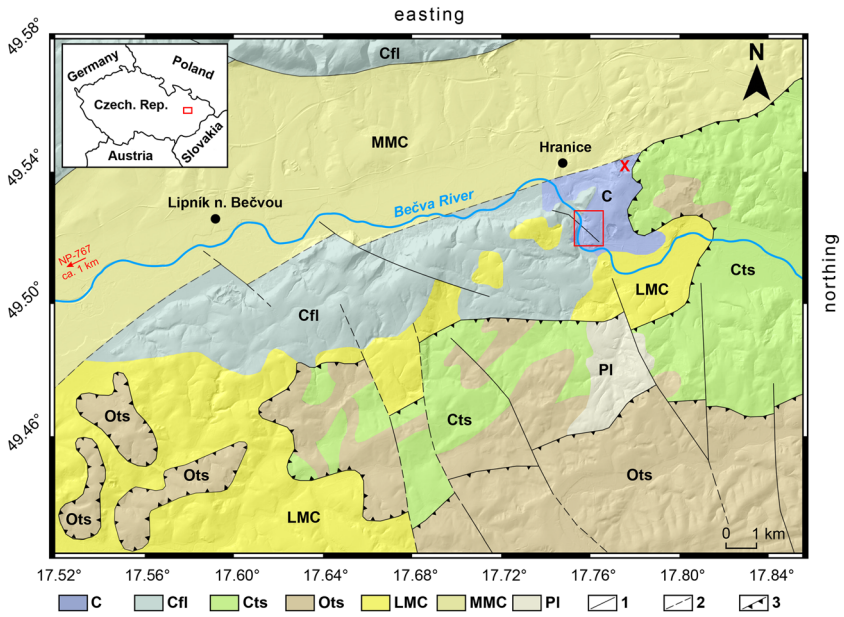


Figure 1. Simplified geological map (compiled after CGS [Czech Geological Survey], 2014, and Otava et al., 2016) with the location of the study area (red rectangle), Skalka limestone quarry (red X), and NP-767 borehole. C, Devonian carbonates; Cfl, Carboniferous flysch deposits; Cts, Cretaceous thrust sheet of the Carpathians; Ots, Oligocene thrust sheet of the Carpathians; LMC, Lower Miocene of the Carpathian Foredeep; MMC, Middle Miocene of the Carpathian Foredeep; Pl, Pliocene; 1, faults; 2, suspected faults; 3, thrust terminations.

(e.g., Holcová et al., 2015). These youngest marine sediments were slightly deformed during the final stages of the Alpine Orogeny thrusting (Sracek et al., 2019). Fluvial and lacustrine depositions dominate in following Pliocene and Quaternary periods in the HK and surrounding areas.

The Devonian carbonate sequences within the HK are disrupted by a Variscan deformation foliation (cleavage in 315/40 direction) and NW-SE faults following the prominent regional Elbe Fault Zone direction (Špaček et al., 2015). The younger Alpine Orogeny compression was partly reactivated the Paleozoic NW-SE faults, which opened them to more intense groundwater circulation.

The HK has undergone several periods of limestone dissolution and karst feature formation. The first time carbonates were exposed to a karstification event was during a 3.7 Ma long marine regression at the Frasnian/Famennian transition (Bábek & Novotný, 1999), after which the HK area was exposed to weathering, denudation, and karstification from the early Permian through the early Late Cretaceous (Otava et al., 2009). The karstification stage took place under tropical conditions. The karst weathering formed cavities filled with Cretaceous fluvial clastics of the Rudice Fm. found in cavities exposed in the Skalka limestone quarry (Figure 1; Otava, 2010). The third stage of the karst formation underwent in Cenozoic until the early Miocene when cockpit-like karst morphology was formed at the limestone surface (e.g., Tyráček, 1962). The early Miocene karstification was terminated by a mid-Miocene marine transgression, which covered the whole area with predominantly clastic deposits. The last karstification stage began during the mid-Miocene regression following partial denudation of the marine deposit from the HK surface and continues through to the present. The flooded cave passages are filled with CO_2-enriched water. The high CO_2 content was detected on several groundwater upwelling points concentrated along the SE tectonic border of the CF, both SW and NE of the HK area (Květ & Kačura, 1978).

3. The HA

The dry opening of the HA covers an area of approximately 104 × 34 m with an inclined vertical cavity shape 69.5 m deep with a small lake at the bottom of the chamber. The underwater portion of the HA is an irregular cylinder-like shape with a diameter varying from ~10 to 30 m (Figure 2b). The uppermost 200 m (below water level) of the HA is relatively well documented, compared to the greater depths, which remain poorly

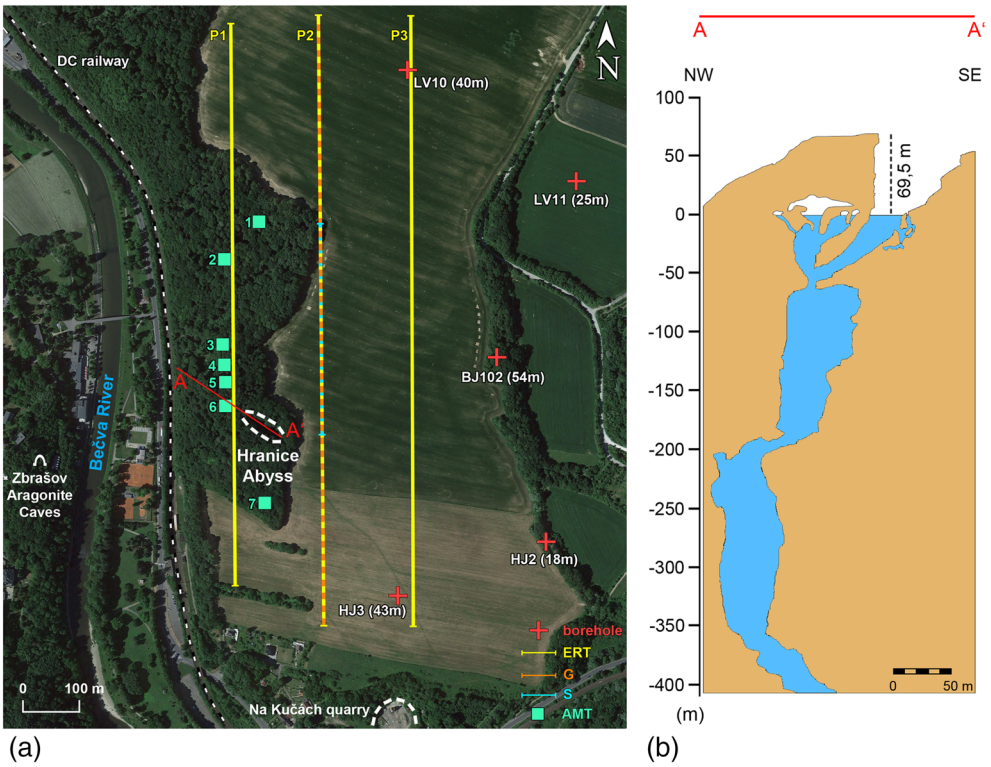


Figure 2. (a) Location of geophysical data collection: ERT, electrical resistivity tomography profiles (P1, P2, P3); AMT, audiomagnetotellurics stations; G, gravity profile; S, seismic measurements; crosses, boreholes with known depth of buried limestone surface. (b) Cross section of the Hranice Abyss along A-A′ (see panel (a)). Groundwater table is placed at 0 m and used as reference point (simplified and redrawn after Lukeš, 2018).

understood with limited understanding from ROV and only a few diver's visits by Krzysztof Starnawski (maximum depth −265 m reached 2015) (Zajíček, 2020).

4. Data Acquisition and Processing

Geophysical methods are widely used as a noninvasive tool for imaging the subsurface morphology of karst structures and identification of the thickness and extent of the overlying sedimentary cover. A combination of geophysical techniques including electrical resistivity tomography (ERT), gravity, and seismic methods (e.g., Válois et al., 2011) can be beneficial for characterization of the near-surface structure of karst regions. Information about the deeper structure and morphology requires the use of deeper penetrating techniques such as magnetotellurics (e.g., Hill et al., 2015; Wunderman et al., 2018) and/or using deep-reaching audio-magnetotellurics (AMT) in combination with expanded investigation scales of geophysical methods (resistivity, gravity, and seismic) typically used for near-surface investigations (Blecha et al., 2018).

4.1. Gravity

Gravity measurements were completed using a Scintrex CG-6 gravimeter, with a sensitivity of 0.0001 mGal. The quality of gravity measurements was normally high, with an rms error of 0.005 mGal and repeatability of 0.008 mGal for sites occupied multiple times. The weather during data collection was cold (2–5°C), with winds up to 5 m/s and some snowfall. Locations of all gravity points were measured with a GNSS Trimble R10 GPS receiver with a vertical accuracy of 2 cm. A profile of 51 locations with a 20-m measurement spacing was collected along ERT profile P2 and corrected using a local reference base station.

Gravity data were corrected for instrumental drift, tidal effects, and point elevation. In addition, terrain corrections for distances 0–1,000 m from measured points were calculated using a 0.50-m (vertical) LiDAR DEM (Digital Elevation Model; CUZK [State Administration of Land Surveying and Cadastre], 2017), while the distal corrections from 1,000 m to 166.7 km were calculated from the SRTM90 DEM (Jarvis et al., 2008).

Table 1
Density and Porosity Values From Lab Measurements for Two Rock Types —Limestone (Ls) and Siltstone (Ss)

Rock	Bulk density (kg/m^3)	Grain density (kg/m^3)	Porosity (%)	Wet density (kg/m^3)
Ls 1	2,698	2,712	0.54	2,703
Ls 2	2,702	2,712	0.39	2,706
Ls 3	2,704	2,712	0.27	2,707
Ls 4	2,700	2,711	0.40	2,704
average Ls	**2,701**	**2,712**	**0.401**	**2,705**
Ss 1	2,496	2,676	6.72	2,564
Ss 2	2,542	2,698	5.76	2,600
Ss 3	2,566	2,695	4.80	2,614
Ss 4	2,600	2,734	4.92	2,649
Ss 5	2,535	2,697	6.01	2,595
Ss 6	2,571	2,683	4.17	2,612
Ss 7	2,563	2,708	5.36	2,616
average Ss	**2,553**	**2,699**	**5.391**	**2.607**

Note. The difference is large enough to provide significant contrast for gravity modeling of the limestone topography under siltstone cover.

For the Bouguer correction, a bulk density of 2,670 kg/m^3 was used for the near-surface layer of the Earth crust to determine the complete Bouguer gravity anomaly (CBA).

To estimate representative densities for the underlying rock, we collected four samples from a limestone outcrop located ~80 m west of profile P2. The near-surface density was estimated from debris samples (seven samples) along the central part of the profile; these samples are (probably Miocene) siltstone with a medium to fine-grained texture.

Bulk and grain densities of all samples were measured along with porosity and with the wet (fully saturated or "natural") density calculated from these values. Three weighting methods were used when a sample was measured: (1) dry in the air; (2) in saturation liquid (water); and (3) saturated in the air (details in Carmichael, 1984). The accuracy of the technique is 0.003 kg/m^3, and porosity determination is 0.02%. The measured values are presented in Table 1. There is a clear difference between the two rock types (limestones and near-surface rocks) in all parameters except grain density. The most important quantities for the gravity modeling are the wet and bulk density, which, as seen by the laboratory results, have a significant difference between the rock types (e.g., for bulk [dry] density 146 kg/m^3 and 98 kg/m^3 for wet density).

4.2. Electrical Resistivity Tomography

Three parallel ~1 km north-south ERT profiles were collected using the ARES II resistivity system (GF Instruments, Czechia) with a Wenner-Schlumberger electrode array roughly centered on the HA. Profile P1 has a length of 955 m with an electrode spacing of 5 m, while P2 and P3 both are of length 995 m with a 5-m electrode spacing. The east-west offset between profiles was 150 m (Figure 2a).

4.3. AMT

Seven AMT measurements were collected on a 0.5 km long segment of ERT profile P1. Station spacing for the central portion of the short AMT profile was 30 m with a larger spacing of 150 m for the distal stations. The station layout was based on forward modeling of the expected geometry and extent of the HA. A Metronix ADU06 coil magnetometer system with nonpolarizable electrodes was used for the data acquisition to collect the horizontal components of both the **E** and **H** field; the vertical magnetic field data H_z were not collected. Data quality was hampered by the presence of the nearby DC rail line (130 m from the profile) as well as residential and industrial infrastructure in the area.

The collected data were processed by standard robust techniques (Gamble et al., 1979) using the Mapros implementation (Friedrichs, 2004) with additional notch filtering of noisy frequencies (MathWorks, 2018). The TM mode of the resulting sounding curves are adequate for simple 1-D modeling; unfortunately, the TE mode was heavily affected by the DC noise related to the electric train line and has not been used further in modeling the AMT data set (Pádua et al., 2002).

4.4. Seismic Measurements

Seismic measurements were carried out along the middle portion (~360 m) of profile P2 (Figure 2a). Five 24-channel Geometrics Geode seismographs forming a 120-channel system were coupled with 10- and 20-Hz geophones at 3 m spacing to establish a 357 m long seismic line. A Seismic Impulse Source System (SISSY) was used (GEOSYM GmbH). The SISSY is essentially a buffalo gun with an electrical trigger. The seismic energy provided by its shots is sufficient in typical conditions for investigations of up to ~200 m depth. The seismic wave source spacing along the profile was 12 m (i.e., a four geophone spacing) and included additional offset shots. The length of the seismic record was 2 s, with a sampling period of 125 μs (Figure 3). Obtained seismic data were subsequently processed by seismic tomography and seismic reflection techniques.

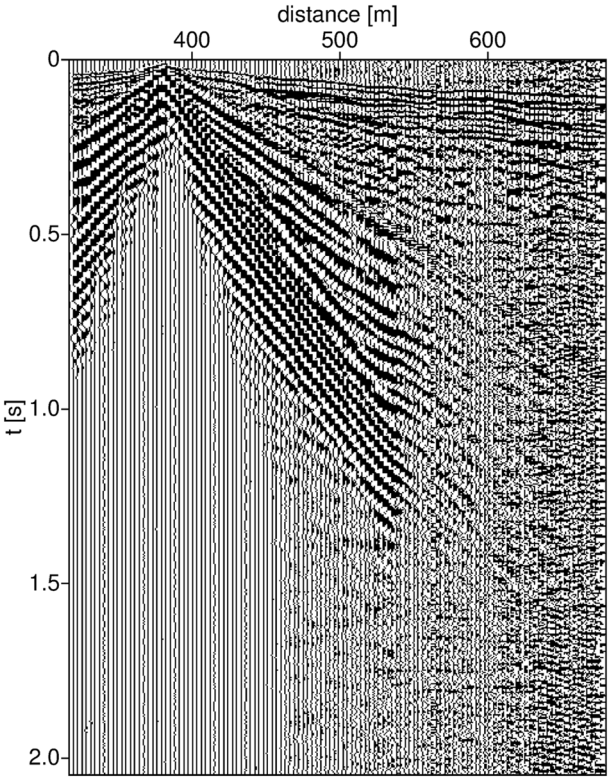


Figure 3. A sample raw shot record (normalized). The first onsets are clearly defined for the distal offsets.

5. Results

5.1. Gravity

The calculated gravity (CBA) curve in Figure 4 rises steeply from the south and then shows two well-distinguished maxima with a minimum between them. The gravity changes along the profile by more than 0.4 mGal, which implies significant changes in density. 2-D modeling of the gravity measurements was undertaken using GM-SYS (GM-SYS Modelling, 2017), incorporating the bulk density values determined from samples collected in this study (bulk density of 2,700 kg/m^3 for limestone; 2,500 kg/m^3 for sediment overburden; 2,540–2,690 kg/m^3 for karstified and weathered zones). Modeling revealed sharp high density "towers" accompanied by less dense blocks forming significant dolines, underlying the low-density surface cover.

5.2. ERT

Data were inverted using the Res2Dinv algorithm (Loke & Barker, 1996), with a topographic correction applied based on the LiDAR DEM (CUZK [State Administration of Land Surveying and Cadastre], 2017; Figure 5). Resistivity values depicted on all three ERT inverted sections (Wenner-Schlumberger array) can be divided into three main features: (i) the low-resistivity (< ~50 Ωm) near-surface layers, (ii) resistivity from 50 to ~400 Ωm with varying thicknesses covering the lowermost layer, and (iii) high to extreme resistivity values (from 400 to thousands of Ωm) in the lowermost layer. All profiles reveal a high-resistivity basement overlain by low-resistivity layers. Profile P1, the closest to the HA, images high-resistivity structures (>1,000 Ωm) above the groundwater level (GWL) parts and lower-resistivity values (<300 Ωm) below the GWL. The low-resistivity features below GWL are accompanied by a "channel" of lower resistivities (A), which is connected to a significantly lower resistivity zone (<50 Ωm) under the substantial depression in topography (at 450–600 m). Profile P2 shows two resistive units (B and C; >1,000 Ωm) prograding to the surface, which are interrupted by a low-resistivity zone (D; <500 Ωm), while the near-surface layers exhibit low-resistivity values (≤50 Ωm). Profile P3 images a low-resistivity layer (<100 Ωm) covering the high-resistivity structure (>1,000 Ωm) along the whole profile.

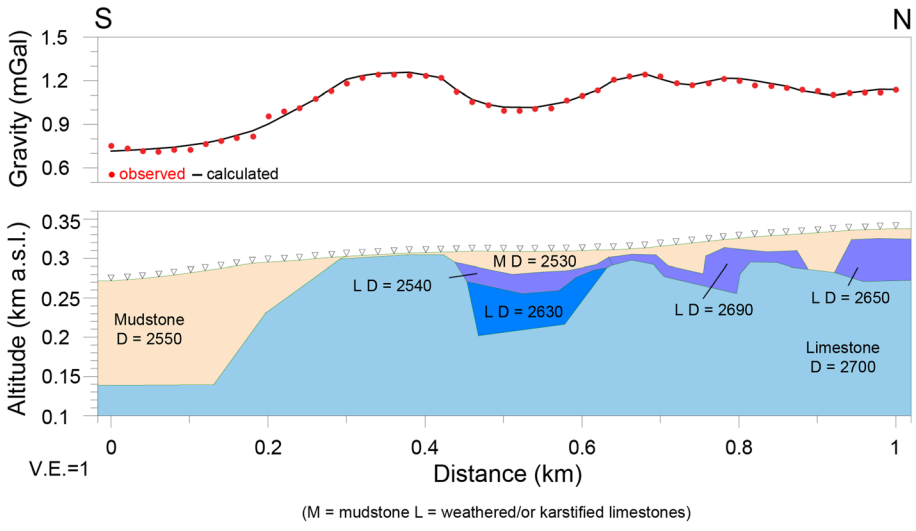


Figure 4. Geological model along the gravity profile with complete Bouguer gravity anomaly. Rock bulk densities are in kg/m^3. The root mean square (RMS) error of modeling is 0.017 mGal.

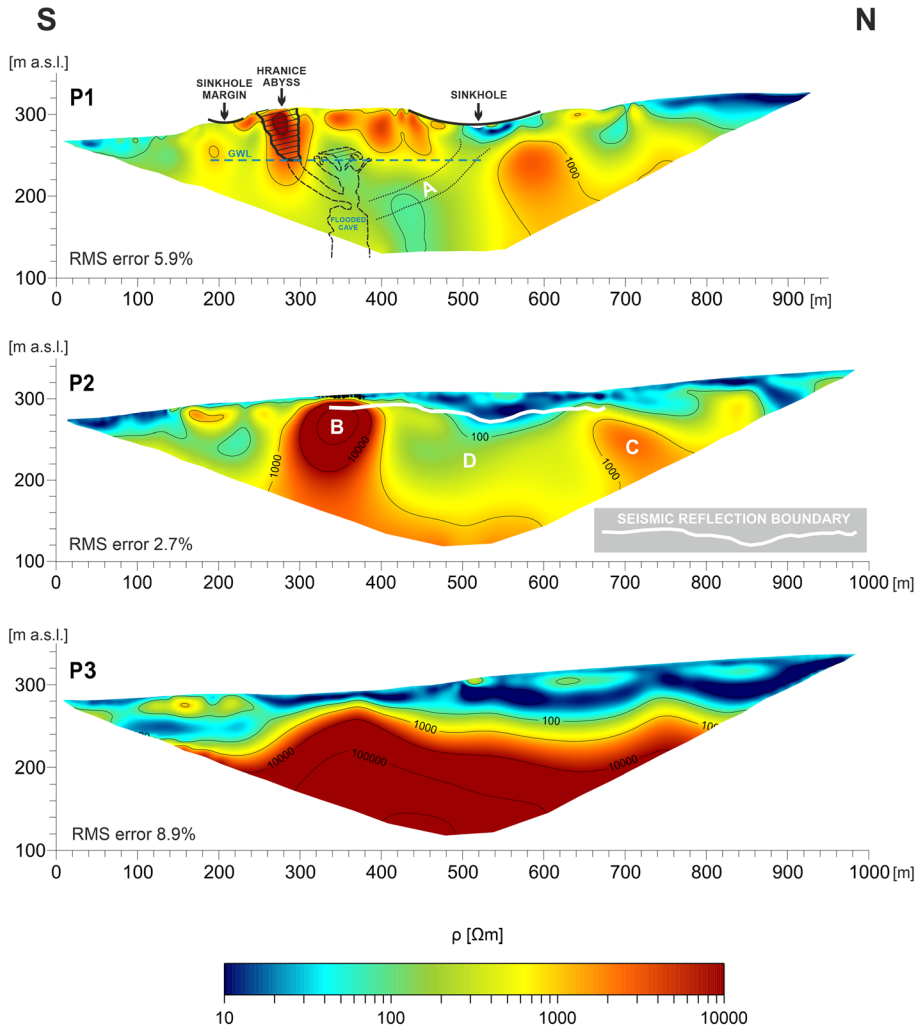


Figure 5. Inversion results for ERT profiles P1 to P3. All three profiles show limestone basement (resistivity > 1,000 Ωm) overlaid by low-resistivity sediments. The most striking feature is the low-resistivity conduit A extending to the surface north of the Hranice Abyss (shape after Guba, 2016). The two high-resistivity units (B and C), together with low-resistivity zone D in the middle of P2, were examined by gravity and seismic surveys.

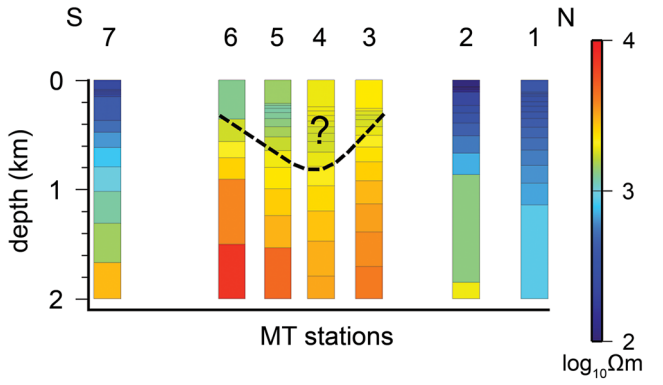


Figure 6. Results of 1-D AMT modeling with marked lower resistivity zone, which could possibly be related to the body of abyss and saturated limestones by mineralized groundwater. The color scale is opposite that of MT standards because it is plotted in the ERT convention.

5.3. AMT

1-D TM (transverse magnetic mode) inversions (Grandis et al., 1999) for each AMT measurement location are shown in Figure 6. The southern extent of the profile is marked by Station 7, which has a near-surface resistivity of ~100 Ωm, increasing to a resistivity of ~1,000 Ωm at a depth of 2 km. The central core of the profile, Stations 3–6, is characterized by near-surface high resistivity (~1,000 Ωm), which extends to ~1 km depth. Below 1 km, the resistivity increases above 10,000 Ωm. The northernmost sites (beyond the HA) are similar to Station 7, again with a low resistivity to ~1 km, underlain by a more resistive (~1,000 Ωm) layer.

5.4. Seismic Measurements

Seismic methods are well suited for distinguishing between the sedimentary rocks which characterize the area of the HA. *P* wave velocities and seismic reflection coefficients vary significantly for the different sedimentary units.

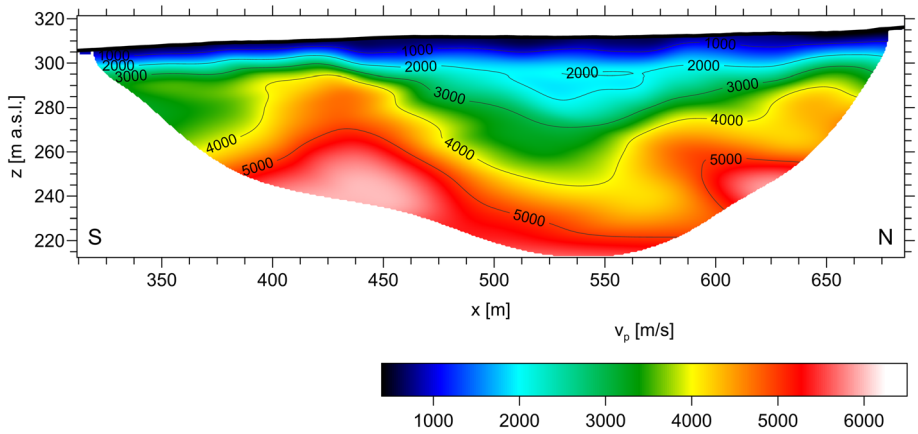


Figure 7. The final tomographical model showing the distribution of *P* wave velocities. The 3,000-m/s contour line could be considered as a boundary between velocity layers (ii) and (iii).

5.4.1. Seismic Refraction

The V_p seismic tomography model (Figure 7) was determined using the Fresnel volumes approach (Watanabe et al., 1999) as implemented in the Rayfract tomography code (Intelligent Resources Inc.) and had an RMS model fit of 1.20. The starting model used for the inversion was a three-layer model obtained using the plus-minus approach (Hagedoorn, 1959). The V_p section (Figure 7) has a large V_p velocity range, although it is characterized by higher velocities with depth. Four units can be identified in the V_p section: (i) a near horizontal slow layer at the surface (<1,800 m/s), (ii) a faster layer (1,800–3,000 m/s) extending to depths of ~250 m in the central part of the profile, (iii) a significantly faster layer (3,000–4,000 m/s) underlying layer (ii) that broadly follows its topographic profile, and (iv) the fastest (>4,000 m/s) V_p layer underlying the sequence representing the "basement" for the seismic tomography.

5.4.2. Seismic Reflection

Seismic reflection processing was carried out with the ReflexW package (Sandmeier Geophysical Research). The unconsolidated sediments at the surface cause the seismic waves to scatter, hindering wave propagation; as such, the resolution depth for the reflection profile is limited (Figure 8). The reflections appear from the near surface to the depth about 20 m, with the exception between 510 and 580 m, where they are forming U-shaped reflector. No significant reflectors are imaged, which would correspond to deeper structure or layer boundaries.

6. Discussion

Epigenic and hypogenic dissolution represent contrasting formation processes that occur under differing tectonic and hydrologic conditions; as such, the ability to determine which of these are the dominant processes can inform the geologic evolution of the region. In accessible dominantly horizontal cave systems with air-filled passages, features indicative of either epigenic and hypogenic (e.g., sedimentary infill, presence of specific karst features on cave walls, and morphology of passages or different cave patterns) can

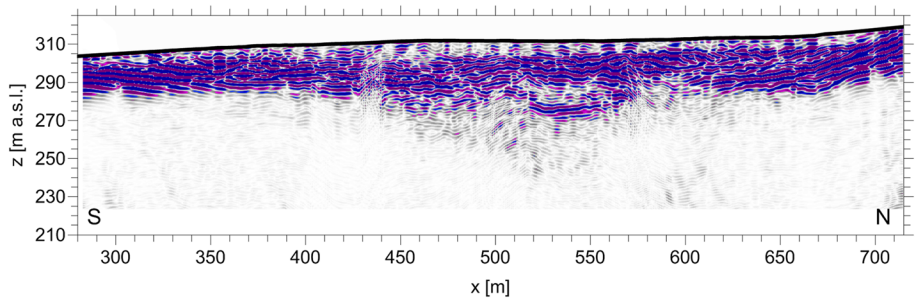


Figure 8. The final stacked and migrated seismic section. The bottommost reflections appear at depths between 20 and 40 m, suggesting a geological boundary.

be found and used to infer formation mechanism (Klimchouk et al., 2016). On the other hand, vertical and subvertical flooded cave systems present a more difficult environment to observe indicative features that reveal the formation mechanism. Historically, indications used to identify formation processes have largely been morphological and relied upon circumstantial evidence such as proximity to faults or basins and the present-day relationship to the surrounding geomorphology and hydrology (Osborne, 2017). Also, determining whether the cave system originated due to hypogenic or epigenic mechanisms is challenging, as descending surface waters may overprint evidence indicative of older hypogenic processes and ascending aggressive late-stage hydrothermal fluids can overprint and erode original structures.

The prevailing consensus for the formation of the HA and similar deep vertical caves elsewhere is hypogenic formation resulting from the presence of deeply sourced CO_2- and H_2S-bearing temperate waters (e.g., Audra & Palmer, 2015; Auler, 2009; Kunský, 1957). This interpretation is, however, based usually only on present-day observations of temperate waters with particular geochemical composition and lacks the required incorporation of the geological and tectonic evolution of the area during the period of cave formation (Sracek et al., 2019). That is also the case of the HA, where the original idea about the hypogenic speleogenesis (Hynie & Kodym, 1936) is followed to present. The newly discovered presence of a former drainage system in the limestone bedrock with a W/NW orientation together with the local geomorphology at the time of cave formation likely representing a large-scale basin based on tectonic reconstructions of the area suggests a reappraisal of the traditional hypogenic model of cave formation and consideration of cave formation via epigenic processes.

6.1. Geophysical Interpretation

Deep seismic velocity results show elevated velocity (>3,000 m/s) typically associated with rigid stronger rock. However, ERT results show a zone of low resistivity corresponding to the zone of elevated seismic velocity; historically, low-resistivity ERT results have been attributed to the presence of fluids or fractures infilled with low-resistivity sediments. Modeling and interpretation of the combined data set must satisfy these seemingly disparate results via the inclusion of constraints from all data types to create a holistic model that fits all data sets to an acceptable level.

The results from different geophysical methods on profile P2 can be interpreted in the framework of a "geophysical stratigraphy." Seismic refraction results are used to define the geophysical "stratigraphy," which will be used when discussing the geophysical results from all methods. The topmost layer is represented by unconsolidated Tertiary and Quaternary sediments (Otava et al., 2016) characterized by seismic velocity <1,800 m/s with varying thicknesses from surface to ~15 m. The base of Layer 1 is identified as the first significant reflector (Figure 8). The ERT identified this layer as a low-resistivity zone with resistivity <50 Ωm.

The second layer consists of marine Miocene sediments (mostly mudstones/sandstones according to borehole evidence) with velocities between 1,800 and 3,000 m/s and varying thickness in depth interval from 10 to 30 m. The basal contact of the layer can be correlated with the second reflection. The ERT did not identify this layer clearly and merged it with the third layer. The gravity modeling based on the seismic and geoelectric results cannot separate the two upper layers and produces a low-density (2,530 kg/m^3) zone that represents the top two layers of the geophysical stratigraphy.

The third layer is characterized by seismic velocities of 3,000–4,000 m/s with varying thicknesses in depth interval between 15 and 45 m. It likely represents weathered or cracked limestone, which in the center of the study area is filled by acidic groundwater (ERT profile position 400–640). Reflectors can be identified in the central portion of the profile (position 510–580). The increased thickness of seismic reflections (Figure 8) is in agreement with the lower density (2,650 kg/m^3) zone (Figure 4), and they have a resistivity of (50 to ~400 Ωm) seen in the ERT as feature "D" (Figure 5).

The lowermost layer corresponds to the rigid limestone basement with velocities exceeding 4,000 m/s and extends to the near-surface in two locations from depth of 20 m to the bottom of the seismic profile (profile position 390–480 and 560–670) marking the two cockpit karst towers. The position of the high-velocity anomalies correlates well with the position of the maxima in the gravity CBA curve and as high resistivity (~400 to thousands of Ωm) ERT features "B" and "C" (Figure 5). The lack of reflectors in the layer suggests that this "basement" layer is massive with little internal structure.

Gravity results are questionable on the southern portion of profile P2, where ERT data is limited at depth and seismic reflection was not collected. Modeling of the southern segment of the profile suggests a sedimentary cover thickness up to ~150 m. It is unlikely that the sedimentary cover is actually this thick. An alternate explanation for the gravity minima is void spaces representing unmapped cave structures. Approximately 200 m to the south is the Na Kučách limestone quarry (Figure 2a), where the recently lost entrance to the Černotín caves was discovered in 1866 (Svozilová, 2009). Currently, the entrance to the cave system and the internal structure of the caves is unknown; it is possible that the cave system was destroyed by limestone mining operations. The presence of the gravity low may be explained by void space of the "lost" Černotín cave system, and as such, their destruction during mining is not certain.

The most interesting features are on profile P1, where the HA zone is saturated by acidic mineral water, and thus the HA zone can be tracked vertically to depth. The channel (feature "A" on Figure 5) with lower resistivity corresponds well with the resistivity of the zone interpreted to be saturated with mineral water (the body of the abyss in Figure 5). The channel structure may represent the main crevice of the sinkhole (at 450–600 m), which has a surface expression characterized by a significant topographic depression partly filled with low-resistivity sediments. Given the proximity of the "sinkhole" and the HA, the sinkhole structure can be considered a part of the HA system and may represent the initial stage in the development of a new abyss.

The HA zone is seen on the AMT profile as a north-dipping low-resistivity (~10^3 Ωm) structure to a depth of ~1 km. The low resistivity is interpreted to represent saturated limestones and coincides with the body of the abyss. The lower resistivity of the AMT section is in agreement with low-resistivity values from ERT, which are unusual for a rigid limestone massif, which would be expected at these depths. The central group of four stations has a common structure, which is interpreted as a single competent block of limestone (or karst tower), in agreement with the interpretation of the ERT results (Figure 5) for this part of the survey area.

In the HA, the water table reaches the void cavity approximately 70 m below the surface, from which the groundwater may be sampled directly. The acidic water sampled in the abyss likely also characterizes the groundwater regime of the karstified and fractured limestones of the survey area (Sracek et al., 2019; Vysoká et al., 2019). The presence of the acidic groundwater is the likely cause for the near-surface low-resistivity zone and its increased depth within the massive limestones on profile P2 (Figure 5, position 400–640).

Cracked or karstified limestones with lower resistivity were also observed by Dleštík and Bábek (2013) and confirmed in nearby boreholes (Fabíková & Peterková, 1963). In both cases, cracks or cavities (caves and caverns) are likely infilled by a significant amount of fine-grained sediments; otherwise, much higher resistivities would be expected if the cracks and cavities were pervasively air-filled voids. However, relatively low resistivity characterizes the limestone bedrock at depths over 100 m (with limestone thickness over 60 m). Intensive karstification to depths of several hundreds of meters is possible (Zajíček, 2017); however, the presence of low-resistivity fine-grain infill at such depths in the massive limestone is questionable.

Figure 9 shows both the present-day (A) surface and the reconstruction of the Devonian limestone basement (B) based on geophysical results. The estimated topology of the reconstructed massive limestone top surface is based on the ERT 1,000 Ωm isoline (and used all three profiles). Comparison of the present and reconstructed limestone surfaces shows that there is significant relief within the limestone bedrock, the topographic highs represent karst towers and the topographic lows dolines.

6.2. New Insight Into the HA Origin

As briefly mentioned above, aside from an older short-lived karstification period in the Late Devonian, significant karst formation in the HK area occurred during the Cretaceous. Large 100 m deep karst sinkhole-like depressions were formed under tropical weathering conditions in the HK, analogous to the Moravian Karst ~75 km SW (see Zajíček, 2017). Relics of these depressions, filled with the Cretaceous Rudice Fm. deposits, were found in the Skalka limestone quarry (Otava et al., 2016). These tropical karst features have been markedly eroded due to Paleogene weathering and denudation processes (Špaček et al., 2015).

The Alpine Orogeny and the nappe thrusting event induced regional compression during the early Miocene at the contact of the Bohemian Massif and Carpathian orogenic belt (Špaček et al., 2015). In the nappe

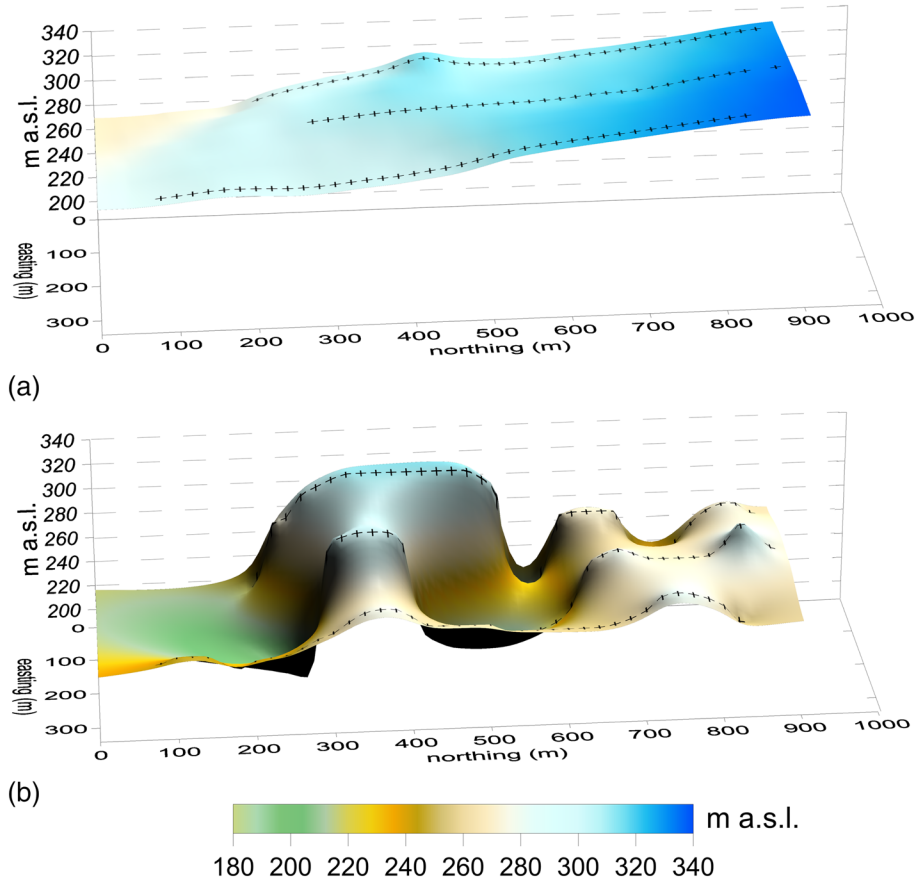


Figure 9. Recent surface (a) compared to a probable rigid limestone surface (b) reconstructed on the 1,000 Ωm contour line from all three ERT profiles. Crosses mark points where the 1,000 Ωm isoline was present.

foreland, a 900-m deep graben opened proximal to the HK (Bubík & Otava, 2016). The canyon-like graben opened in the early Langhian (Otava et al., 2016) from horizontal sinistral strike-slip movement (pull-apart mechanism) along the NE-SW faults induced by the regional compression (Havíř et al., 2004). The horizontal movements and deformations are recorded in the paleomagnetic rotations of early Langhian marine deposits filling the CF graben (Márton et al., 2011). The fast CF opening triggered intense regional erosion leading to the formation of river valleys, pointing to the CF basin and deeply incised the eastern margin of the Bohemian Massif (Dvořák & Slezák, 1953). Borehole logging shows these incised valleys often follow the NW-SE faults and could be up to 300 m deep. One such buried early Miocene valley is located on the opposite side of the CF, approximately 15 km NNW of the HK area (Nehyba et al., 2019). Its hanging position with respect to the 900-m depth of the CF indicates two stages of CF graben opening. During the subsequent early Langhian marine transgression, the CF, together with these hanging valleys, was filled with marine sandstones and claystones (Bubík et al., 2018).

The Prosenice borehole, located 20 km SW of the HA, reached the limestone basement beneath the CF at a depth of 897.2 m below surface (Hufová, 1974)—that is, −682.2 m a.s.l. The 900-m deep CF was a local erosional base for both surface and subsurface waters running across the HK carbonates during the early Miocene. Paleozoic limestone bedding and deformation cleavage dip steeply (up to 40°) to the NW—that is, toward the CF (Havíř et al., 2004). The dip of the limestone beds implies a continuation of the carbonate sequences, underlying the nonkarstic deposits, toward the base of the CF (see Figure 10).

The early Miocene karst surface morphology, reconstructed from borehole data, shows valleys and dolines with E-W and SW-NE orientations, which have been, eroded by westward running surface waters—that is, toward the CF (Otava, 2006). Additionally, running surface waters formed the cockpit-like features, which characterize the karst surface (Kodym, 1960; Tyráček, 1962). The presence of early Langhian

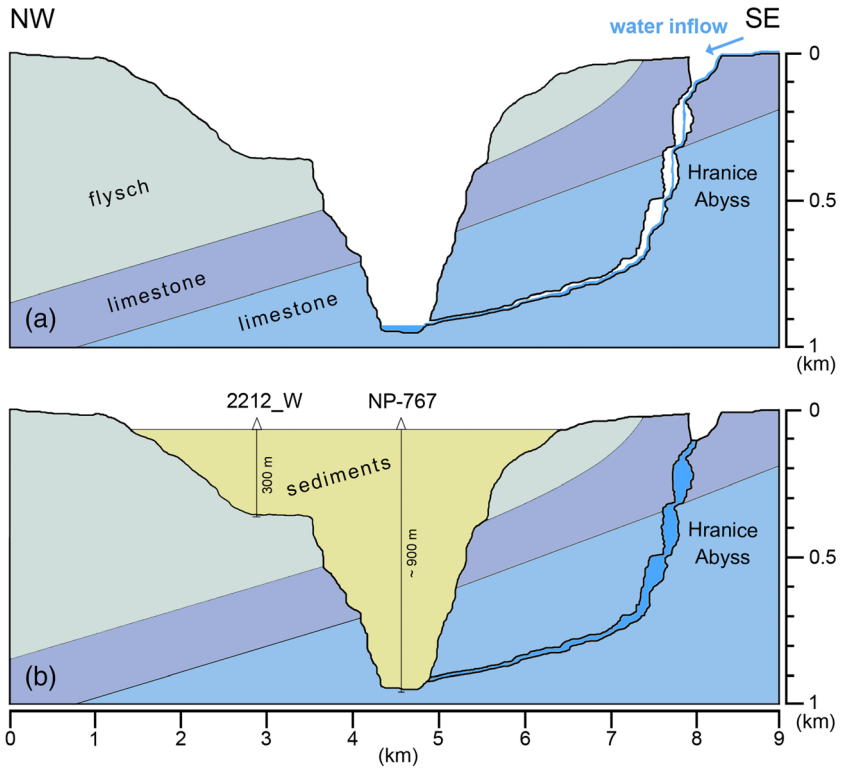


Figure 10. Conceptual geological cross section through the Hranice Abyss and Carpathian Foredeep. Panel (a) shows the situation during early Langhian, when CF was opened and the HA originated, while panel (b) displays current state with known boreholes. 3.5X vertically exaggerated.

marine deposits infilling cavities in the HA walls above the modern water table extent of the cave system (i.e., above the flooded portion) can also be observed in the Zbrašov Aragonite Caves (ZAC) (Otava, 2006, 2016; Sracek et al., 2019), suggesting vertical excavation from descending surface water.

Based on the geological, structural, and geomorphological evidence found in the HK area and its close surroundings, we propose the HA originated by erosion processes of surface waters descending from the karst surface and running underground to the local erosional base, which marks the bottom of the 2–3 km distant CF (Figure 10). The epigenic vadose water circulation regime should dominate during the HA formation. Local structural elements were the dominant control during limestone dissolution and cavity formation. The HA developed at an intersection of dislocation thrusting parallel to cleavage and the subvertical NW-SE faulting (Otava, 2010; Sracek et al., 2019), making the area preferentially susceptible to vertical water circulation. The HA depth is limited by the depth of the local erosional base, that is, by the CF depth ~900 m; as such, the maximum depth of the HA is inferred to be between 800 and 1,000 m, which can be seen in the AMT results (Figure 6).

Following the mid-Miocene marine transgression and widespread deposition of clastic sediments, including the HK, active karst processes were interrupted. The original late–early Miocene cave springs, which originally outflowed at the base of the CF, including the HA spring, were choked by the marine deposits filling the CF graben. The choking or blocking of these springs at the base of the karst zone forced a rise of the water table from pre- to mid-Miocene levels (~800–1,000 m below the surface) to the current level ~70 m below surface. The rise in the water table depth resulted in flooding of much of the extent of the HA, the deeper levels of the ZAC, and causing upwelling in springs at the Bečva River valley bottom (Vysoká et al., 2019). The upwelling waters are CO_2 enriched and use existing "crustal-structural soft zones" in their ascent via faults and tectonic cleavage. A high concentration of ^{226}Ra dissolved in the mineral water indicates that the groundwater is in contact with the crystalline complexes underlying the carbonate sequences (Švajner, 1982). Limestone dissolution by these temperate mineral waters continues to modify the HA resulting in its current extent (Kodym 1960; Kunský, 1957). The HK region, including the early Miocene development

of the HA structure, formed via dominantly epigenic processes (Kodym, 1960; Tyráček, 1962) with later secondary evolution and overprinting of the original cavities by hypogenic processes (see Geršl & Šimečková, 2009).

The novel interpretation of an epigenic formation model for the HA is analogous to that used to explain the formation of the Fountaine de Vaucluse flooded caves (Audra et al., 2004). In both cases, local erosional base deepening and canyon-like depression forming are crucial in the cave's evolution. However, different mechanisms are proposed for canyon formation; the HA canyon-like graben was opened by extensional strike-slip horizontal movement (Havíř et al., 2004), while the Fountaine de Vaucluse canyon was incised due to the Mediterranean Sea low-stand during the Messinian period (Audra et al., 2004). In both cases, the canyon formations were followed by the development of deep epigenic cave systems formed by surface waters, which resurged at the canyon base. Subsequent sediment deposition (via sea-level rise) and infill of these canyons caused spring outflows to become blocked and the cave systems to be flooded with fresh water.

6.3. Implications for the Origin of Other Deep Vertical Caves

The updated model for the formation of the HA demonstrates the benefit of inclusion of new lines of investigation (in this case, multiple geophysical data sets). The inclusion of geophysical results provided new insight into the geological and morphological history of the HA karst. This approach can lead to further understanding of similar karst evolution and formation for deep flooded cave systems elsewhere. Large-scale cave formation is, of course, dependent on water flux; the nature and direction of that water movement are controlled by the tectonic conditions at the time of cave formation which can be inferred from former drainage patterns, groundwater saturated zones, or evidence of variations in local/regional erosional base.

However, the clear evidence for hypogenic cave evolution—for example, unusual groundwater mineralization (Farrant & Harrison, 2017), presence of artesian aquifers and preferably oriented faults (Klimchouk et al., 2017), or the occurrence of characteristic karst features (cupolas and uncommon speleothems) (Gázquez et al., 2017)—is often missing in giant shafts. The lack of detailed information and difficulty in making direct observations in deep flooded cave systems make the inclusion of geophysical surveys a necessity when investigating the processes responsible for large-scale karst cave formation.

Detailed multidisciplinary studies of the world's deepest flooded cave systems and their associated formation mechanisms are rare. A hypogenic origin is suggested for the Pozzo del Merro and Zacatón systems based on the nearby presence of volcanic bodies (Gary, 2017; Gary et al., 2003). The present-day warm mineral waters are also used to infer the hypogenic evolution of the Lagoa Misteriosa cave system in Brasilia (Auler, 2009). Multiple epigenic formation models have been presented for the Red Lake formation in Croatia, variously suggesting that it is a collapsed doline or sinkhole; all of these formation models are based on geologic and hydrologic evidence alone (Andrić & Bonacci, 2014; Bahun, 1991; Petrik, 1960; Williams, 2004). Geophysical imaging of these systems could reveal important new evidence of the geologic evolution and formation processes of these systems.

7. Conclusion

Understanding the evolutional history of deep-flooded caves is difficult given the challenges with making direct observations of these systems. The traditionally accepted hypogenic formation of these systems is largely based on the occurrence of present-day temperate water containing acidic elements originating from a deep source. Based on newly acquired geophysical data sets in the area surrounding the HA, a reappraisal of the accepted hypogenic origin of the system indicates, rather, that epigenic (top-down) processes were dominant during the formation of the large-scale karst system. However, the current secondary evolution of the system is dominated by hydrothermally driven hypogenic (bottom-up) processes. In the preferred top-down formation process, water would have run underground toward the local basal erosional surface—the bottom of the CF—before the mid-Miocene marine transgression event. The ERT results indicate the presence of a "fossil" sediment-filled sinkhole connected to the main vertical shaft of the HA cave system. The connection of the "fossil" sinkhole to the HA indicates a larger spatial extent of the karstified dislocation zone - a first-order control on the origin and morphology of the HA. The inclusion of geophysical results enabled a complete consideration of the formation model by revealing key information about the geological and

morphological evolution of the system, which was then used in conjunction with tectonic and geologic evidence to construct a consistent formation model. This approach is readily applicable to similar flooded cave systems globally.

Data Availability Statement

All geophysical data presented here are available in standard industry formats from https://doi.org/10.17632/fjkpbtb2gd.1.

Acknowledgments

The research was cofunded by the institutional support of the Center for Geosphere Dynamics (UNCE/SCI/006), by the support of the long-term conceptual development research organization RVO: 67985891, and by Operational Program VVV CZ.02.1.01/0.0/0.0/16_013/0001800. Special thanks to Helena Vysoká for help with the preparation of the measurements and accessing the locality. Thanks to Filip Hartvich for help with ERT measurements and Václav Polák with gravity survey.

References

Andrić, I., & Bonacci, O. (2014). Morphological study of Red Lake in Dinaric karst based on terrestrial laser scanning and sonar systems. *Acta Carsologica*, *43*(2–3), 229–239. https://doi.org/10.3986/ac.v43i2.712

Audra, P., Mocochian, L., Camus, H., Gilli, É., Clauzon, G., & Bigot, J.-Y. (2004). The effect of the Messinian Deep Stage on karst development around the Mediterranean Sea. Examples from southern France. *Geodinamica Acta*, *17*(6), 389–400. https://doi.org/10.3166/ga.17.389-400

Audra, P., & Palmer, A. N. (2015). Research frontiers in speleogenesis. Dominant processes, hydrogeological conditions and resulting cave patterns. *Acta Carsologica*, *44*(3), 315–348. https://doi.org/10.3986/ac.v44i3.1960

Auler, A. S. (2009). Styles of hypogene cave development in ancient carbonate areas overlying non-permeable rocks in Brazil and the influence of competing mechanisms and later modifying processes. In A. Klimchouk & D. Ford (Eds.), *Hypogene speleogenesis and karst hydrogeology of artesian basins* (pp. 173–180). Simferopol: Ukranian Institute of Speleology and Karstology.

Bábek, O., & Novotný, R. (1999). The Hněvotín Limestone neostratotype locality revisited: A Conodont biostratigraphy and carbonate microfacies approach, Moravia, Czech Republic. *Acta Univ. Pal. Olom, Fac. Rer. Natural., Geologica*, *36*, 63–68.

Bahun, S. (1991). O postanku Crvenog i Modrog jezera kod Imotskog (Genesis of Red and Blue Lakes near Imotski). *Geoloski Vjesnik*, *44*, 275–280.

Blecha, V., Fischer, T., Tábořík, P., Vilhem, J., Klanica, R., Valenta, J., & Štěpančíková, P. (2018). Geophysical evidence of the eastern marginal fault of the Cheb basin (Czech Republic). *Studia Geophysica et Geodaetica*, *62*(4), 660–680. https://doi.org/10.1007/s11200-017-0452-9

Bubík, M., Břízová, E., Buriánek, D., Gilíková, H., Havíř, J., Janderková, J., et al. (2018). *Explanatory notes to the basic geological map of Czech. Rep., sheet Lipnik nad Bečvou 25-132* (pp. 1–185). Czech Geological Survey Archive (in Czech).

Bubík, M., Otava, J. (2016). Geologický vývoj. In J. Otava, O. Bábek, M. Bubík, D. Buriánek, J. Čurda, J. Franců, et al. (Eds.), *Explanatory notes to the basic geological map of Czech. Rep., sheet Kelč 25-141* (pp. 1–115). Czech Geological Survey (in Czech).

Carmichael, R. S. (1984). *CRC handbook of physical properties of rocks* (Vol. III, p. 354). New York: CRC Press Inc.

Carvalho, J., Matias, H., Torres, L., Manupella, G., Pereira, R., & Mendes-Victor, L. (2005). The structural and sedimentary evolution of the Arruda and Lower Tagus sub-basins, Portugal. *Marine and Petroleum Geology*, *22*(3), 427–453. https://doi.org/10.1016/j.marpetgeo.2004.11.004

CGS (Czech Geological Survey) (2014). Geological map of the Czech Republic 1:500 000. Internet application, available from https://mapy.geology.cz/geocr500/

CUZK (State Administration of Land Surveying and Cadastre) (2017). Digital terrain model of the Czech Republic of the 5th generation (DMR 5G), https://geoportal.cuzk.cz/(S(isdmbslejuke31kelctuwwjj))/Default.aspx?lng=EN&mode=TextMeta&side=vyskopis&metadataID=CZ-CUZK-DMR5G-V&head

Dleštík, P., & Bábek, O. (2013). *Shallow geophysical mapping of buried karst surface near Hranice using electrical resistivity tomography, Geologické výzkumy na Moravě a ve Slezsku, 20* (pp. 1–2) (in Czech). Available at https://journals.muni.cz/gvms/article/view/1568

DuChene, H. R., Palmer, A. N., Palmer, M. V., Queen, J. M., Polyak, V. J., Decker, D. D., et al. (2017). Hypogene speleogenesis in the Guadalupe Mountains, New Mexico and Texas, USA. In A. Klimchouk, A. N. Palmer, J. de Waele, A. S. Auler, & P. Audra (Eds.), *Hypogene karst regions and caves of the world* (pp. 511–530). New York: Springer International Publishing.

Dvořák, J., & Slezák, L. (1953). *Caves in the area of the Hranice devonian. Čs. kras* (Vol. VI, pp. 175–184). Brno (in Czech).

Fabíková & Peterková (1963). Borehole profiles HJ-1/2/3. In *Hydrogeological survey report from Černotín, Czech Geological Survey—Geofond Archive* (in Czech).

Farrant, A. R., & Harrison, T. (2017). Hypogenic caves in UK. In A. Klimchouk, A. N. Palmer, J. de Waele, A. S. Auler, & P. Audra (Eds.), *Hypogene karst regions and caves of the world* (pp. 43–60). New York: Springer International Publishing.

Ford, D. C., & Williams, P. (2007). *Karst hydrogeology and geomorphology* (p. 562). New York: John Wiley & Sons Inc. https://doi.org/10.1002/9781118684986

Friedrichs, B. (2004). *Mapros (Ver. 0.87b freeware)*.

Gamble, T. D., Goubau, W. M., & Clarke, J. (1979). Magnetotellurics with a remote magnetic reference. *Geophysics*, *44*(1), 53–68. https://doi.org/10.1190/1.1440923

Gary, M. O. (2017). Sistema Zacatón: Volcanically controlled hypogenic karst, Tamaulipas, Mexico. In A. Klimchouk, A. N. Palmer, J. de Waele, A. S. Auler, & P. Audra (Eds.), *Hypogene karst regions and caves of the world* (pp. 769–782). New York: Springer International Publishing.

Gary, M. O., Sharp, J. M. Jr, Caramana, G., & Havens, R. H. (2003). *Volcanically influenced speleogenesis: Forming El Sistema Zacatón, Mexico, and Pozzo Merro, Italy, the deepest phreatic sinkholes in the world*. Geological Society of America.

Gázquez, F., Calaforra, J. M., Estrella, T. R., Ros, A., Llamusí, J. L., & Sánchez, J. (2017). Evidence for regional hypogene speleogenesis in Murcia (SE Spain). In A. Klimchouk, A. N. Palmer, J. de Waele, A. S. Auler, & P. Audra (Eds.), *Hypogene karst regions and caves of the world* (pp. 85–98). New York: Springer International Publishing.

Geršl, M., & Šimečková, B. (2009). Zbrašov aragonite caves, Hranice abyss. In J. Hromas, Caves, P. Mackovčin, & M. Sedláček (Eds.), *Protected areas of Czechia, sv. XIV., AOPK Praha* (pp. 363–368).

GM-SYS Modelling (2017). http://www.geosoft.com/products/gm-sys

Grandis, H., Menvielle, M., & Roussignol, M. (1999). Bayesian inversion with Markov chains—I. The magnetotelluric one-dimensional case. *Geophysical Journal International*, *138*(3), 757–768. https://doi.org/10.1046/j.1365-246x.1999.00904.x

Guba, M. (2016). *A press release for the depth survey of the Hranice Abyss and reaching a new maximum depth −404 m* (in Czech). Retrieved from http://www.hranickapropast.cz/

Hagedoorn, J. G. (1959). The plus-minus method of interpreting seismic refraction sections. *Geophysical Prospecting*, *7*(2), 158–182. https://doi.org/10.1111/j.1365-2478.1959.tb01460.x

Havíř, J., Krejčí, O., & Otava, J. (2004). Tektonika. In J. Otava, J. Adámek, M. Adamová, O. Bábek, E. Břízová, M. Bubík, et al. (Eds.), *Explanatory notes to geological map 1:25 000 Hranice 25–123*. Czech Geological Survey (in Czech).

Hill, G. J., Bibby, H. M., Ogawa, Y., Wallin, E. L., Bennie, S. L., Caldwell, T. G., et al. (2015). Structure of the Tongariro volcanic system: Insights from magnetotelluric imaging. *Earth and Planetary Science Letters*, *432*, 115–125. https://doi.org/10.1016/j.epsl.2015.10.003

Holcová, K., Hrabovský, J., Nehyba, S., Hladilová, Š., Doláková, N., & Demény, A. (2015). The Langhian (Middle Badenian) carbonate production event in the Moravian part of the Carpathian Foredeep (central Paratethys): A multiproxy record. *Facies*, *61*(1), 419. https://doi.org/10.1007/s10347-014-0419-z

Hufová, E. (1974). *Radslavice NP 767. Final report* (pp. 1–177). Czech Geological Survey (in Czech).

Hynie, O., & Kodym, O. (1936). *Mineral water springs in the Teplice nad Bečvou Spa: Reconstruction of water abstraction in years 1932–1934* (Vol. 11, pp. 61–117). Sborník SGÚ (in Czech).

Jarvis, A., Reuter, H. I., Nelson, A., & Guevara, E. (2008). Hole-filled SRTM for the globe version 4. In *CGIAR-CSI SRTM 90m database*. Available at http://srtm.csi.cgiar.org

Kalvoda, J., Bábek, O., Fatka, O., Leichmann, J., Melichar, R., Nehyba, S., & Spacek, P. (2008). Brunovistulian terrane (Bohemian Massif, Central Europe) from late Proterozoic to late Paleozoic: A review. *International Journal of Earth Sciences*, *97*(3), 497–518. https://doi.org/10.1007/s00531-007-0183-1

Klimchouk, A., Auler, A. S., Bezerra, F. H. R., Cazarin, C. L., Balsamo, F., & Dublyansky, Y. (2016). Hypogenic origin, geologic controls and functional organization of a giant cave system in Precambrian carbonates, Brazil. *Geomorphology*, *253*, 385–405. http://doi.org/10.1016/j.geomorph.2015.11.002

Klimchouk, A., Palmer, A. N., de Waele, J., Auler, A. S., & Audra, P. (2017). *Hypogene karst regions and caves of the world* (p. 911). New York: Springer International Publishing. https://doi.org/10.1007/978-3-319-53348-3

Kunský, J. (1957). Thermomineral karst and caves of Zbrašov, Northern Moravia. Sbor. Čs. spol.zeměp., sv. 62/1957, 306–351 (in Czech).

Květ, R., & Kačura, G. (1978). *Mineral waters of the northern Moravia region*(pp. 1–173). Praha: Ústř. Úst. Geol.

Loke, M. H., & Barker, R. D. (1996). Rapid least-squares inversion of apparent resistivity pseudosections using a quasi-Newton method. *Geophysical Prospecting*, *44*(1), 131–152. https://doi.org/10.1111/j.1365-2478.1996.tb00142.x

Lukeš, J. (2018). *The Hranice Abyss, schematic map, state at 1.1.2017*. Retrieved from http://hranickapropast.cz/mapy/

Márton, E., Tokarski, A., Krejčí, O., Rauch, M., Olszewska, B., Tomanová Petrová, P., & Wójcik, A. (2011). Non-Europea palaeomagnetic directions from the Carpathian Foredeep at the southern margin of the European plate. *Terra Nova*, *23*, 134–144. https://doi.org/10.1111/j.1365-3121.2011.00993.x

MathWorks (2018). Signal Processing Toolbox: User's Guide (R2018a). https://www.mathworks.com/help/pdf_doc/signal/signal_tb.pdf

Meyberg, M., & Rinne, B. (1995). *Messung des 3He/4He-Isotopenverhaltnisses im Hranicka Propast (Tschechische Republik)* (Vol. 46, No. 1, pp. 5–8). Wien: Die Höhle, Zeitschrift für Karst- und Höhlenkunde.

Nehyba, S., Gilíková, H., Tomanová Petrová, P., Otava, J., & Skácelová, Z. (2019). Evolution of a sedimentary infill of a palaeovalley at a distal margin of the peripheral foreland basin. *Geological Quarterly*, *63*(2), 319–344. https://doi.org/10.7306/gq.1469

Osborne, R. A. L. (2017). Hypogene caves of the Tasmanic Karsts of eastern mainland Australia. In A. Klimchouk, A. N. Palmer, J. de Waele, A. S. Auler, & P. Audra (Eds.), *Hypogene karst regions and caves of the world* (pp. 893–911). New York: Springer International Publishing.

Otava, J. (2006). Current state of knowledge of polyphase karstification of the Hranice Paleozoic. Speleofórum 2006, s. 84-86, Praha (in Czech).

Otava, J. (2010). Geological guide of Hranice area or when the orogenes collides. Česká geologická společnost, 28 s., Praha (in Czech).

Otava, J. (2016): Geologically significant sites. In Otava, J., Bábek, O., Bubík, M., Buriánek, D., Čurda, J., Franců, J. et al. (2016). Explanatory notes to the basic geological map of Czech. Rep., sheet Kelč 25-141. Czech Geological Survey, 115p (in Czech).

Otava, J., Bábek, O., Bubík, M., Buriánek, D., Čurda, J., Franců, J. et al. (2016). Explanatory notes to the basic geological map of Czech. Rep., sheet Kelč 25-141. Czech Geological Survey, 115p (in Czech).

Otava, J., Geršl, M., Havíř, J., Bábek, O., & Kosina, M. (2009). The Hranice Abyss—Through the eyes of geologists, Ochrana přírody, roč. 64, 1, s. 18-22., Praha (in Czech).

Pádua, M. B., Padilha, A. L., & Vitorello, Í. (2002). Disturbances on magnetotelluric data due to DC electrified railway: A case study from southeastern Brazil. *Earth, Planets and Space*, *54*(5), 591–596. https://doi.org/10.1186/BF03353047

Petrik, M. (1960). Hidrografska mjerenja u okolici Imotskog (Hydrographic measurements near Imotski). *Ljetopis JAZU*, *64*, 266–286.

Šmejkal, V., Hladíková, J., Pfeiferová, A., & Melková, J. (1976). Isotopic composion of carbon and oxygen in speleothems from karst caves in northen Moravia. In: J. Čadek & Pačes T (Eds.), Proceedings of International Symposium on Water-Rock Interaction, Czechoslovakia 1974: 363–367. Praha.

Špaček, P., Bábek, O., Štěpáníčková, P., Švancara, J., Pazdírková, J., & Sedláček, J. (2015). The Nysa-Morava zone: An active tectonic domain with Late Cenozoic sedimentary grabens in the Western Carpathians' foreland (NE Bohemian Massif). *International Journal of Earth Sciences*, *104*(4), 963–990. https://doi.org/10.1007/s00531-014-1121-7

Sracek, O., Geršl, M., Faimon, J., & Bábek, O. (2019). The geochemistry and origin of fluids in the carbonate structure of the Hranice Karst with the world's deepest flooded cave of the Hranicka Abyss, Czech Republic. *Applied Geochemistry*, *100*, 203–212. https://doi.org/10.1016/j.apgeochem.2018.11.013

St. Kodym, O. (1960). About the Hranice Karst genesis. Čas. Min. Geol., 5(3), 262–264 (in Czech).

Švajner, L. (1982). *Hydrogeology of mineral waters in Teplice above Bečva R.* (Diploma thesis). Bratislava, Slovakia: Komenský University.

Svozilová, M. (2009). The characteristic of karst processes and landforms in the Hranický Kras Area (Handbook for teachers of geography) (Bachelor thesis). Palacký University Olomouc (in Czech).

Tyráček, J. (1962). Fossil cockpit karst near Hranice na Moravě, Časopis pro Mineral. A Geol., 2, s. 176–185 (in Czech).

Válois, R., Camerlynck, C., Dhemaied, A., Guerin, R., Hovhannissian, G., Plagnes, V., et al. (2011). Assessment of doline geometry using geophysics on the Quercy plateau karst (South France). *Earth Surface Processes and Landforms*, *36*(9), 1183–1192. https://doi.org/10.1002/esp.2144

Vysoká, H., Bruthans, J., Falteisek, L., Žák, K., Rukavičková, L., Holeček, J., et al. (2019). Hydrogeology of the Hranice abyss (Czechia)—The deepest underwater cave in the world. *Hydrogeology Journal*, *27*(7), 2325–2345. https://doi.org/10.1007/s10040-019-01999-w

Watanabe, T., Matsuoka, T., & Ashida ,Y. (1999). Seismic traveltime tomography using Fresnel volume approach. SEG Technical Program Expanded Abstracts 18. https://doi.org/10.1190/1.1820777

Williams, P. (2004). Dolines. In J. Gunn (Ed.), *Encyclopedia of caves and karst science* (pp. 628–642). London, UK: Fitzroy Dearborn.

Wunderman, R. L., Wannamaker, P. E., & Young, C. T. (2018). Architecture of the hidden Penokean terrane suture and midcontinent rift system overprint in eastern Minnesota and western Wisconsin from magnetotelluric profiling. *Lithosphere*, *10*(2), 291–300. https://doi.org/10.1130/L716.1

Zajíček, P. (2017). The Moravin karst in submersible river of time. Academia, 276p (in Czech).

Zajíček, P. (2020). Karst areas of the middle and northern Moravia and Silesia. Academia, 246p (in Czech).

Zhou, W., Beck, F. B., & Adams, A. L. (2002). Effective electrode array in mapping karst hazards in electrical resistivity tomography. *Environmental Geology*, *42*(8), 922–928. https://doi.org/10.1007/s00254-002-0594-z

Příloha 5

Reply to the Comment by Bábek et al. on Hypogenic Versus Epigenic Origin of Deep Underwater Caves Illustrated by the Hranice Abyss (Czech Republic) – The World's Deepest Freshwater Cave: Can the Hranice Abyss, the Deepest Underwater Cave in the World, Really Reach 1 km Depth?

Journal of Geophysical Research: Earth Surface

Kadlec et al. 2021

Kadlec J., Klanica R., Tábořík P., Mrlina J., Valenta J., Kovacikova S., Hill G. J. (2021): Reply to the Comment by Bábek et al. on Hypogenic Versus Epigenic Origin of Deep Underwater Caves Illustrated by the Hranice Abyss (Czech Republic) – The World's Deepest Freshwater Cave: Can the Hranice Abyss, the Deepest Underwater Cave in the World, Really Reach 1 km Depth? Journal of Geophysical Research: Earth Surface 126 (4), Article number e2020JF005952. DOI 10.1029/2020JF005952.

JGR Earth Surface

REPLY

10.1029/2020JF005952

Key Points:

- Geophysical data provide sufficient evidence for the depth of the Hranice Abyss
- Study is not neglecting post-Badenian tectonic movements

Correspondence to:

R. Klanica,
rk@ig.cas.cz

Citation:

Kadlec, J., Klanica, R., Táborík, P., Mrlina, J., Valenta, J., Kováčiková, Sě., & Hill, G. J. (2021). Reply to comment by Bábek et al. on Hypogenic versus epigenic origin of deep underwater caves illustrated by the Hranice Abyss (Czech Republic)—The world's deepest freshwater cave: Can the Hranice Abyss, the deepest underwater cave in the world, really reach 1 km depth? *Journal of Geophysical Research: Earth Surface*, *126*, e2020JF005952. https://doi.org/10.1029/2020JF005952

Received 29 OCT 2020
Accepted 23 DEC 2020

© 2021. American Geophysical Union. All Rights Reserved.

Reply to the Comment by Bábek et al. on Hypogenic Versus Epigenic Origin of Deep Underwater Caves Illustrated by the Hranice Abyss (Czech Republic)—The World's Deepest Freshwater Cave: Can the Hranice Abyss, the Deepest Underwater Cave in the World, Really Reach 1 km Depth?

Jaroslav Kadlec[1], Radek Klanica[1], Petr Táborík[2,3], Jan Mrlina[1], Jan Valenta[2], Světlana Kováčiková[1], and Graham J. Hill[1]

[1]Czech Academy of Sciences, Institute of Geophysics, Prague, Czech Republic, [2]Faculty of Science, Institute of Hydrogeology, Engineering Geology and Applied Geophysics, Charles University, Prague, Czech Republic, [3]Czech Academy of Sciences, Institute of Rock Structure and Mechanics, Prague, Czech Republic

Abstract Comment by Bábek et al. (2020, https://doi.org/10.1029/2020JF005916) is concerning the interpretation of realized geophysical measurements. Since, to our knowledge, Klanica et al. (2020, https://doi.org/10.1029/2020JF005663) conducted the deepest geophysical surveys in the area, a scale of work was probably misunderstood within the interpretation of our results. Second, a large number of objections arise from the comment about the post-Badenian geological development at the eastern margin of the Bohemian Massif. However, evidence for the time when particular geological processes took place is not definite and our conclusions of our study can be related to early Badenian age.

1. Introduction

Our proposed interpretation of the Hranice Abyss (HA) origin, presented in Klanica et al. (2020), is predicated on reconstruction of both geological and tectonic processes which occurred in the study area before the early Badenian (early Langhian) Paratethys marine transgression.

The Hranice Karst (HK), including the HA, developed in a tectonically dynamic region at the contact of two orogenic systems—the Variscan Bohemian Massif and Alpine Carpathian orogenic belt. The succession of geological and tectonic processes can be reconstructed based on information recorded in sedimentary archives located close to the HK area, namely in the Carpathian Foredeep (CF) and the Vienna Basin (VB). The sedimentary sequences in these basins document the early Middle Miocene Paratethys sea-level changes, regional erosional events, and tectonically driven uplift/subsidence periods during the Early and early Middle Miocene. The evolution of the Miocene VB is documented in detail by Kováč et al. (2004) and Hölzel et al. (2010). The conclusions of these studies state a tectonically controlled sea-level rise in the late Karpatian period in the VB followed by global and tectonically controlled sea-level drop between the Lower/Middle Miocene transition and early Badenian (about 16.5 Ma, Kováč et al., 2004).

The sea-level low-stand (in southern Moravian CF segment, the sea-level drop is estimated up to 1,000 m, Jiříček, 1990) is related to the regional erosional hiatus documented in the VB at the Karpatian/Badenian transition (e.g., Hölzel et al., 2010). The fluvial, alluvial, and deltaic processes dominated around and within both the VB and the CF basins (Jiříček, 1990). During this period, an opening within the CF occurred at the Moravian Gate graben (MGG), adjacent to the HK. The graben was formed in two steps. The first triggered by uplift of the areas NW and SE of the MGG, allowing surface water erosion to excavate 300 m deep valleys connected to the MGG (Nehyba et al., 2019). In the second stage, the deeper portion of the MGG was opened by sinistral horizontal strike-slip movement (pull-apart mechanism) (cf., Havíř et al., 2004) resulting in the former erosional valleys becoming hanging valleys leading into the graben. Similar sinistral horizontal strike-slip movements are documented nearby in the VB (Decker et al., 2005). This combination of strike-slip movement and running water erosion (the MGG drained to the SW into the river system running to the VB, cf., Jiříček, 1990) deepened the MGG into a ~1 km deep canyon-like graben (cf., Bubík

& Otava, 2016) with Devonian limestones exposed at the graben floor (cf., Hufová, 1974). This fast graben incision activated large mass wasting on steep slopes (Bubík & Otava, 2016).

Up to 1 km elevation difference between the MGG base and the adjacent HK area resulted in a steep groundwater circulation gradient. Fault systems, rock cleavage, and carbonate bedding plane dips promoted groundwater circulation from the HK into the MGG. The vertical incision of surface water carved vertical karst routes in the carbonate sequence.

The surface water erosion and the Devonian limestone dissolution formed a complex surface and subsurface karst forms within the HK before the early Badenian marine transgression. The epigenic topography of the HK surface is well known based on borehole as well recent and present shallow geophysical surveys. The pre-Badenian matured karst forms together with evolution of adjacent MGG morphology support this interpretation given that the HA origin is closely related to HK pre-Badenian processes. Therefore, our inference is that the HA depth could reach ~900 m representing the elevation difference between the pre-Badenian HK surface and the base of the pre-Badenian MGG. Pre-Badenian karst processes ceased after the early Badenian marine transgression.

2. Response to Comment on Geophysical Measurements Results

In order to appreciate the audio-magnetotelluric (AMT) results, it is necessary to understand basic fundamental principles of the electromagnetic (EM) field as used in the magnetotelluric (MT) method. AMT refers to the period band corresponding roughly to that audible to the human ear (~10,000–1 Hz) suitable for investigations of the near surface to depths of approximately 2 km. The Earth's naturally occurring EM field generates a vertically propagating plane wave orthogonal to the Earth's surface. From measurements of the horizontal surface components of the electric (E) and magnetic (H) fields, a transfer function or impedance tensor Z (Cagniard, 1953; Tikhonov, 1950) is determined in the frequency domain, defined by the relationship $E = ZH$. Similarly, the relationship between the vertical magnetic field H_z and the horizontal magnetic field is expressed in the form of an induction vector (Parkinson, 1962) K so that $-K \cdot H = H_z$. The impedance tensor and the induction vector are complex functions of the Earth's resistivity (ρ or conductivity $\sigma = 1/\rho$), in which period is a proxy for depth where period (t) in seconds and skin depth (δ) in meters are related by $\delta \approx 500\sqrt{\rho t}$. The subsurface distribution of resistivity is determined using inverse modeling (which produces a nonunique solution given the highly underdetermined nature of the problem) of these functions, analogous to seismic tomography. The diffuse nature of EM wave propagation results in resistivity boundaries/interfaces not being resolved as sharp boundaries but as gradients (Kordy et al., 2016a, 2016b), where the resolution of each deeper interface is resolved with less confidence than the overlying interface. Both the impedance tensor and induction vector which contain the observational properties of the MT response are 3D quantities. The "cone of influence" of MT observation implies that with increasing depth (period) the surface MT measurement is sensitive to a larger radial area and should be considered a volumetric response.

Given the 3D dimensional (volumetric) nature of MT data, the N-S oriented profile contains information also (to a lesser lateral extent and resolution) about off profile E-W variations in subsurface electrical structure. The controlling diffusion physics associated with MT means, that sharp boundaries or small-scale subtle resistivity variations are not recoverable and are instead represented as resistivity gradients (Simpson & Bahr, 2005). However, in the near surface complimentary methods such as electrical resistivity tomography (ERT) are better suited to recovering sharp boundaries and identifying subtle small-scale features, and hence can be used to further constrain the geologic structure characterized by the AMT response.

ERT results from the HA indicate the shallow limestones proximal to the Abyss are fractured with these fractures and cracks likely filled with conductive mineral waters—promoting (as a natural electrolyte) a low resistivity signal to be observed in the near surface AMT results. The deeper low resistivity zone identified in the AMT results represents a vertical structure with sharp lateral boundaries (i.e., steep horizontal resistivity gradients are observed). The vertical nature of the "deep" low resistivity feature makes it geologically unlikely to represent a geologic unit such as the siliclastic Culm facies of the Moravice and Hradec-Kyjovice Formation, carbonate mylonites or Brunovistulian crystalline basement suggested by Bábek et al. (2020). All of the suggested alternate sources for the low resistivity signal would reasonably be expected to have a

significant lateral extent far beyond that of the deeper vertical low resistivity zone identified in the AMT results.

Bábek et al. (2020) wisely suggest broad resistivity value ranges for the main geologic units of the study area—the broad overlapping approximately order of magnitude ranges suggested (e.g., 300–1,500 Ωm for karstified limestones and 300–1,000 Ωm for the siliciclastic Moravice and Hradec-Kyjovice Formation) illustrate the difficulty associated with attempting to define a simple mapping between electrical properties and individual lithological units. The order of magnitude range for individual lithological units results from the many factors that contribute to the electrical signature of Earth materials: chemical composition; permeability and porosity; presence and nature of fluids (e.g., fresh water vs. saline brine); etc. Furthermore, resistivity range of studied rocks depends on various geological and geomorphological processes forming the studied landscape, such as intensity and depth of weathering/alteration, intensity of rock fracturing of both tectonics (i.e., crevices, faults) and gravitational origin (i.e., tension cracks), and, in case of carbonates, also karstification (namely dissolving of the rock). Further complicating a simple mapping between electrical properties and lithological units is that there can be significant spatial heterogeneity of electrical properties within a single lithological unit. The complexities associated with 3D structure of the HA and HK region, measurement (instrument) and analysis sensitivity limits, and measurement distortions (from both anthropomorphic and natural noise sources) preclude definition of simple quantitative relationships. Instead, a qualitative interpretation of the geophysical data has been conducted incorporating all geological and geophysical data sets available and tectonic evolution of the region—allowing the construction of a formation model for the HA which satisfies the geological and geophysical observations and places the HA formation into a tectonically consistent evolution model of the region. Given the primary objective of our study was to investigate the maximal depth of the HA, a detailed petrophysical identification of individual lithologic units based on an absolute correlation with modeled resistivity values aside from being difficult and uncertain is not required for the ERT results. A direct comparison of the absolute resistivity values recovered from the AMT and ERT modeling, which while both geoelectrical methods have different governing physics, can be misleading given the differences in both sensitivity and resolution. Nevertheless, the characteristic resistivity suggested by Bábek et al. (2020) and Dleštík and Bábek (2013) for the lithological units of importance for the HK region agrees with the interpretation and results presented by Klanica et al. (2020).

3. Response to Comment on Neglecting Post-Badenian Tectonics at the Eastern Margin of the Bohemian Massif

Timing of the post-Badenian uplift of the HK area as well as the stratigraphic position of the early Badenian detrital shallow-marine deposits, found around and in the surface opening of the HA, is questionable. Bubík et al. (2018) believe that the Maleník unit (including the HK area) was uplifted before early Badenian marine transgression, contradicting the post-Badenian uplift proposed by Bábek et al. (2020). As stated by Bábek et al. (2016), the stratigraphic position of the early Badenian detrital shallow-marine deposits (termed the Černotín sandstone) is problematic and not definitive. These deposits were assumed to be Karpatian to early Badenian in age (Eliáš et al., 2002), late Karpatian (Havíř et al., 2004), or early Badenian (Bábek et al., 2016). As such, it is inappropriate to use the elevation of the Černotín sandstone as an indicator for post-Badenian vertical movement.

Bábek et al. (2020) mention the position of the detrital shallow-marine deposits at the bottom of the MGG documented in the Prosenice borehole log (the total borehole depth is 928 m with the lowermost 879.2–928 m logged as Devonian limestone). However, the marine sandstone (sand) beds or lenses are present in many depth horizons, except the depth interval 480–749 m (cf., Hufová, 1974). The conflicting conclusions of differing researchers discussed herein indicate the position promoted by Bábek et al. (2020) regarding post-Badenian uplift of the HK is not universally accepted.

4. Response to Comment on Epigenic Origin of Deep Water-Filled Caves

By compiling the extent geophysical and geological knowledge of the HA and combining it with the new geophysical data presented by Klanica et al. (2020), an alternate epigenic (rather than the traditional hypogenic-hydrothermal) formation model for the HA is determined to be self-consistent and supported by

the observations. The HK areas, including the structure and morphology of the HA, form dominantly via epigenic processes. The pre-Badenian underground cavities later filled from vertically rising groundwater (cf., Kodym, 1960) enriched in CO_2 from the underlying crust and/or upper mantle. The higher CO_2 concentration characterizing these deep sourced waters results in acceleration of carbonate dissolution leading to overprinting of the original primary epigenic processes by the secondary hypogenic processes. The secondary hypogenic stage is documented by hydrothermal rafted stalagmites found in the HA (e.g., Geršl, 2009).

5. Conclusion

Klanica et al. (2020) offer an alternate epigenic model for the formation of the HA, based on new geophysical data and early Badenian geology within the area. The epigenic formation model is in agreement with accepted views on the geological development on the Eastern margin of the Bohemian Massif in the early Middle Miocene.

Data Availability Statement

All geophysical data used in the original work Klanica et al. (2020) are available in standard industry formats from http://dx.doi.org/10.17632/fjkpbtb2gd.1

Acknowledgments
We dedicate this work to the memory of Jaroslav Kadlec, whose enthusiasm and devotion to the study of karst and cave systems was only possibly surpassed by his eagerness to share this work with others. No additional geophysical data were used in this reply.

References

Bábek, O., Bubík, M., Buriánek, D., Franců, J., Gilíková, H., Havíř, J., et al. (2016). Units geological and petrological characteristics. In J. Otava, et al. (Eds.), *Explanatory notes to the basic geological map of Czech. Rep., sheet Kelč 25-141* (pp. 15–35) (in Czech). Prague: Czech Geological Survey.

Bábek, O., Faimon, J., Geršl, M., & Sracek, O. (2020). Can the Hranice Abyss, the deepest underwater cave in the world, really reach 1 km depth? A Comment on the paper by Klanica et al. (2020). *Journal of Geophysical Research: Earth Surface*, 126, e2020JF005916. https://doi.org/10.1029/2020JF005916

Bubík, M., Břízová, E., Buriánek, D., Gilíková, H., Havíř, J., Janderková, J., et al. (2018). Explanatory notes to the basic geological map of Czech. Rep., sheet Lipník nad Bečvou 25-132 (pp. 1–185) (in Czech). *Czech Geological Survey Archive*. Prague: Czech Geological Survey.

Bubík, M., & Otava, J. (2016). Geologický vývoj. In J. Otava, et al. (Eds.), *Explanatory notes to the basic geological map of Czech. Rep., sheet Kelč 25-141* (pp. 1–115) (in Czech). Prague: Czech Geological Survey.

Cagniard, L. (1953). Basic theory of the magneto-telluric method of geophysical prospecting. *Geophysics*, *18*, 605–635.

Decker, K., Peresson, H., & Hinsch, R. (2005). Active tectonics and Quaternary basin formation along the Vienna Basin Transform fault. *Quaternary Science Reviews*, *24*, 307–322.

Dleštík, P., & Bábek, O. (2013). Shallow geophysical mapping of buried karst surface near Hranice using electrical resistivity tomography (in Czech). *Geologické výzkumy na Moravě a ve Slezsku*, *20*, 174–177.

Eliáš, M., Pálenský, P., & Růžička, M. (2002). Lithostratigraphy of the north Moravian Miocene and its lithostratigraphic correlation with adjacent Polish Miocene (Carpathian Foredeep). *Geological Reports*, *2001*, 22–24.

Geršl, M. (2009). Hranice Abbyss. In P. Mackovčin & M. Sedláček (Eds.), *Protected areas of Czechia, sv. XIV* (pp. 365–368). Brno: AOPK Praha.

Havíř, J., Krejčí, O., & Otava, J. (2004). Tektonika. In J. Otava, et al. (Eds.), *Explanatory notes to geological map 1:25 000 Hranice 25–123*. Prague: Czech Geological Survey (in Czech).

Hölzel, M., Decker, K., Zámolyi, A., Strauss, P., & Wagreich, M. (2010). Lower Miocene structural evolution of the central Vienna Basin (Austria). *Marine and Petroleum Geology*, *27*, 666–681.

Hufová, E. (1974). Radslavice NP 767. Final report (pp. 1–177) (in Czech). *Czech Geological Survey*. Prague: Czech Geological Survey.

Jiříček, R. (1990). Fluvial and deltaic systems of Neogene Paratethys. Sedimentologické problémy Západných Karpát. In *Konferencie-sympózia-semináre* (pp. 79–88). Bratislava: Geologický Úrad Dionýza Štúra.

Klanica, R., Kadlec, J., Táborík, P., Mrlina, J., Valenta, J., Kováčiková, S., & Hill, G. J. (2020). Hypogenic versus epigenic origin of deep underwater caves illustrated by the Hranice Abyss (Czech Republic)—The world's deepest freshwater cave. *Journal of Geophysical Research: Earth Surface*, *125*, e2020JF005663. https://doi.org/10.1029/2020JF005663

Kodym, O. St. (1960). About the Hranice Karst genesis (in Czech). *Časopis pro Mineralogii a Geologii*, *5*(3), 262–264.

Kordy, M., Wannamaker, P., Maris, V., Cherkaev, E., & Hill, G. (2016). 3-D magnetotelluric inversion including topography using deformed hexahedral edge finite elements and direct solvers parallelized on SMP computers—Part I: Forward problem and parameter Jacobians. *Geophysical Journal International*, *204*(1), 74–93.

Kordy, M., Wannamaker, P., Maris, V., Cherkaev, E., & Hill, G. (2016). 3-dimensional magnetotelluric inversion including topography using deformed hexahedral edge finite elements and direct solvers parallelized on symmetric multiprocessor computers—Part II: Direct data-space inverse solution. *Geophysical Journal International*, *204*(1), 94–110.

Kováč, M., Bárath, I., Harzhauser, M., Hlavatý, I., & Hudáčková, N. (2004). Miocene depositional systems and sequence stratigraphy of the Vienna Basin. *Courier Forschungsinstitut Senckenberg*, *246*, 187–212.

Nehyba, S., Gilíková, H., Tomanová Petrová, P., Otava, J., & Skácelová, Z. (2019). Evolution of a sedimentary infill of a palaeovalley at a distal margin of the peripheral foreland basin. *Geological Quarterly*, *63*(2), 319–344.

Parkinson, W. D. (1962). The influence of continents and oceans on geomagnetic variations. *Geophysical Journal of the Royal Astronomical Society*, *6*, 441–449.

Simpson, F., & Bahr, K. (2005). *Practical magnetotellurics*. Cambridge: Cambridge University Press.

Tikhonov, A. N. (1950). On determining electrical characteristics of the deep layers of the Earth's crust. *Doklady Akademii Nauk SSSR*, *73*, 295–297.

Příloha 6

Geophysical anatomy of counter-slope scarps in sedimentary flysch rocks (Outer Western Carpathians)

Geomorphology

Tábořík et al. 2017a

Tábořík P., Lenart J., Blecha V., Vilhelm J., Turský O. (2017a): Geophysical anatomy of counter-slope scarps in sedimentary flysch rocks (Outer Western Carpathians). Geomorphology 276, 59–70. DOI:10.1016/j.geomorph.2016.09.038.

Geomorphology 276 (2017) 59–70

Contents lists available at ScienceDirect

Geomorphology

journal homepage: www.elsevier.com/locate/geomorph

Geophysical anatomy of counter-slope scarps in sedimentary flysch rocks (Outer Western Carpathians)

P. Tábořík [a,b,*], J. Lenart [c], V. Blecha [a], J. Vilhelm [a], O. Turský [c]

[a] Institute of Hydrogeology, Engineering Geology and Applied Geophysics, Faculty of Science, Charles University, Albertov 6, 128 43 Prague 2, Czech Republic
[b] Institute of Rock Structure and Mechanics, Czech Academy of Sciences, V Holešovičkách 94/41, 182 09 Prague 8, Czech Republic
[c] Department of Physical Geography and Geoecology, Faculty of Science, University of Ostrava, Chittussiho 10, Ostrava 710 00, Czech Republic

ARTICLE INFO

Article history:
Received 21 October 2015
Received in revised form 25 September 2016
Accepted 27 September 2016
Available online 28 September 2016

Keywords:
Multidisciplinary geophysical survey
Deep-seated landslide
Integrated interpretation
Counter-slope scarp
Underground discontinuities
Flysch rock

ABSTRACT

A multidisciplinary geophysical survey, consisting of electrical resistivity tomography (ERT), ground penetrating radar (GPR), shallow seismic refraction (SSR) and gravity survey (GS), was used to investigate the counter-slope scarps, one of the typical manifestations of the relaxed zones of rock massifs, and the possible initial stages of deep-seated landslides (DSLs). Two upper parts of the extensive DSLs within the Moravskoslezské Beskydy Mountains (Outer Western Carpathians – OWC) built by the sedimentary flysch rock were chosen as the testing sites. A combined geophysical survey on the flysch rocks was performed on both localities to enhance our present findings. The survey revealed that the ERT is able to reliably detect underground discontinuities, which are manifested at the ground surface by one of the typical landforms (tension cracks, trenches, pseudokarst sinkholes, double-crested ridges and counter-slope scarps). Previous studies suggested that bedrock discontinuities should be depicted by high-resistivity features within ERT surveying. According to SSR and GS, expected zones of weakened rock massif were not confirmed directly underneath the superficial landforms, but they were shifted. Based on the SSR and GS measurements, the depicted high-contrast transitions between high- and low-resistivity domains within the ERT profiles were newly identified as possible manifestation of bedrock discontinuities. The results of GPR measurements give only limited information on the sedimentary flysch rocks, due to shallow penetrating depth and locally strong signal attenuation. The combined results of multidisciplinary geophysical surveying confirmed an importance of employing more than one geophysical technique for integrated interpretations of measured data. Integrated interpretations of the measured geophysical data provided a new insight into massif disintegration and the geomorphic origin of the landforms related to the DSL.

© 2016 Elsevier B.V. All rights reserved.

1. Introduction

Relaxed zones of rock massifs often represent the initial stages of deep-seated landslide (DSL) development (Margielewski and Urban, 2003, 2005). This phenomenon is often connected with ridge disintegration and related slope processes, such as lateral spreading, toppling, sackung and rotational or translational sliding (Nemčok, 1972; Dikau et al., 1996; Agliardi et al., 2001; Nichol et al., 2002; Margielewski, 2006; Esposito et al., 2007; Crosta et al., 2013; Jomard et al., 2014). As a result of a combined effect of these processes, various typical landforms developed, such as exposed rocky headscarps, step-like slopes, back-tilted rock blocks, opened tension cracks, double-crested ridges, parallel trenches, pseudokarst-sinkholes, and crevice-type caves (Lenart et al., 2014). Most of these landforms have distinct geomorphic manifestations; however, they result from the processes that operate under the ground surface, i.e., (i) gravitational widening of joints with formation of crevice-type cave systems, and (ii) subsidence and lateral rotations of rock blocks (Pánek et al., 2010a, 2011a; Lenart et al., 2014). All the processes mentioned above disrupt bedrock and, together with favourable geology they may result in accelerated slope processes (Dikau et al., 1996; Geertsema et al., 2006; Hungr et al., 2001). This is why we often consider these landforms as the initial forms of DSLs (Dikau et al., 1996; Margielewski and Urban, 2003). Investigating these processes helps us to interpret and better understand factors controlling slope development.

Regarding the ages of DSLs, the ^{14}C data of tens of landslides in the Polish, Czech and Slovak Outer Flysch Carpathians mostly reveal the ages of the humid Holocene phases (Margielewski, 2003, 2006; Pánek et al., 2011a, 2013). The ages are mostly obtained from organic material in peat bogs, trench infills or landslide-dammed lakes.

In the present study, we focused on counter-slope (uphill-facing) scarps, which can provide evidence of subsurface gravitational processes within the sedimentary flysch rocks in mid-mountain regions. For the

* Corresponding author at: Institute of Hydrogeology, Engineering Geology and Applied Geophysics, Faculty of Science, Charles University, Albertov 6, 128 43 Prague 2, Czech Republic.
E-mail address: petr.taborik@post.cz (P. Tábořík).

acquisition of the subsurface image of the underground structures, we applied a complex geophysical survey, consisting of DC resistivity imaging (ERT), electromagnetic high-frequency ground penetrating radar (GPR), shallow seismic refraction (SSR) with tomographic data-processing and gravity surveying (GS) (Schrott and Sass, 2008). The obtained geophysical data sets were processed to reveal possible evidence of the above-described processes and the resulting landforms. The results of the individual methods offer models with different information abilities, limited by the character of each investigated geophysical field (sensu Telford et al., 1990; Reynolds, 1997; Milsom, 2003).

We chose two upper parts of an extensive DSL within the Moravskoslezské Beskydy Mountains (Outer Western Carpathians – OWC) as the testing sites, where mass movements entirely dominate the slope development. Disintegration of mountain ridges is controlled by such slope processes, as reported in numerous geomorphological studies from the area of the OWC (Baroň et al., 2004; Lenart et al., 2014; Hradecký and Pánek, 2008; Margielewski, 2001, 2006; Margielewski and Urban, 2003, 2005; Pánek et al., 2007, 2009, 2010a, 2011a). Similar localities were already studied using formal techniques: geomorphological mapping, ERT or even trenching (Lenart et al., 2014; Pánek et al., 2011a). In the present study, we performed, for the first time, the investigation by means of combined multidisciplinary geophysical survey, which offers a better possibility to reveal a massif relaxation and its structure.

The present paper methodically focuses on complex multidisciplinary surveying using four different geophysical techniques. In previous studies, the researchers primarily used the ERT technique as the only method for DSL surveying (Pánek et al., 2007, 2010a,b, 2011a,b, 2014; Šilhán, 2010; Tábořík, 2012; Lenart et al., 2014). There are only few papers concerning the combined geophysical survey of DSLs within the OWC flysch rocks – e.g., Pánek et al. (2011a) performed a complex survey by means of ERT, SSR and symmetric resistivity profiling (symmetric RP). The aim of the present study is, also, to assess the ability of geophysical techniques to reveal the structure and slope development within DSLs in the sedimentary flysch rocks environment.

2. Geological and geomorphological setting

Both of the investigated sites are situated within the western portion of the Carpathian mountain range (OWC, The Moravskoslezské Beskydy Mts.; Fig. 1), which is formed by a flysch of Mesozoic (Late Jurassic) to Paleogene/Neogene (Early Miocene) sedimentary rocks. During the Lower and the Middle Miocene alpine orogeny phases, these sediments were folded and thrusted onto the foredeep in the northern direction, forming several nappes (Menčík et al., 1983). Both of the investigated sites are situated in the culmination portion of the Godula flysch nappe (Fig. 1), which is created by the Godula formation. The sedimentary strata consist of thick-bedded sandstones or conglomerates alternating with very thin-bedded claystones or siltstones with clay mineral content (Menčík et al., 1983; Pánek et al., 2011a). During the Miocene, the rocks were disrupted by joints and faults, trending in the E–W, NW–SE, and NE–SW directions (Menčík et al., 1983; Krejčí et al., 2002; Bubík et al., 2004) as well as the WNW–ESE direction (Menčík et al., 1983; Pánek and Duras, 2002).

Morphologically, the ridges are formed asymmetrically. Because of the inclination of the strata slightly to the south-east, the northern slopes are short but steep, predisposed by the frontal parts of beds, whereas the southern slopes are long and gentle, formed on bedding planes. Such bedrock structure, together with the effects of tectonics (faults, crevices and tension cracks), predispose the mountain ridges to a slope development controlled mainly by the gravitational slope movements (Lenart et al., 2014). Weak and semi-plastic claystones act as shear surfaces for slope movements of more rigid overlying sandstone formations. Lithology and high slope gradient (frequently 30–40°) thus determine the conditions, which cause relatively high vulnerability to DSL development.

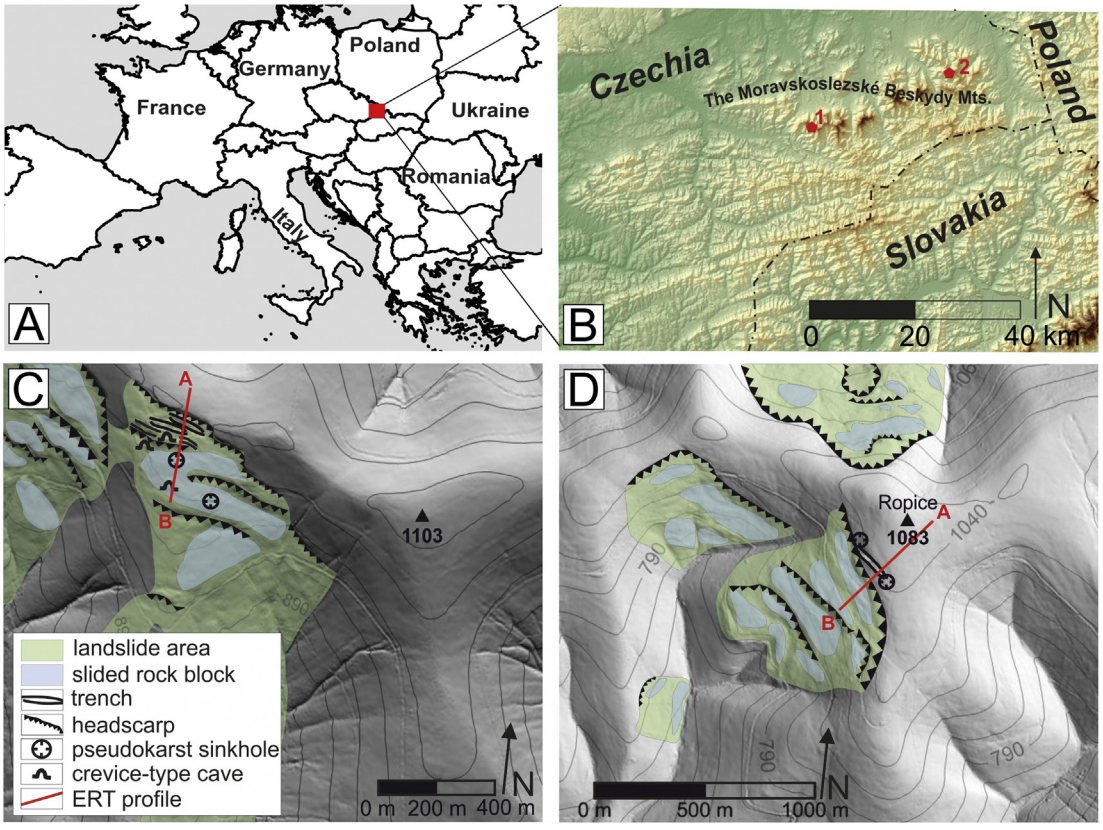


Fig. 1. Studied sites. (A, B) Overall situation. (C) Záryje site with the location of the Záryje 1A geophysical profile. (D) Ropice site with the location of the Ropice 1 geophysical profile.

Both investigated sites are situated more or less within the southern slopes of a main mountain ridge (Fig. 1):

(1) The Záryje site: The DSL Záryje is situated in the upper part of a long, step-like southern slope of a main mountain ridge (The Radhošť ridge, ca. 1100 m a.s.l.; Fig. 1). The DSL involves an overall area of at least 0.5 km^2. The investigated part of the landslide terrain is pronounced by particular rotated slided rock blocks with parallel counter-scarp depressions (up to 10 m deep rocky trenches) between them. Some of the blocks are secondarily disrupted by opened tension cracks, crevices or crevice-type caves with the length of passages of >100 m and an average depth of approximately 12 m. There are other geomorphic features occurring in the area: pseudokarst sinkholes, block fields, exposed rocks cliffs and the accumulations of rockfalls, especially below the headscarp area. The most pronounced is the main headscarp, developed under the main ridge. In the middle part of the area, the landslide decreased the original ridge, when the headscarp line reaches to the ridgeline. There are also initial signs of double-crested ridge development.

(2) The Ropice site: The south-western slopes of the Ropice Mountain (1083 m a.s.l.; Fig. 1) are strongly affected by the DSL, which are manifested mostly in their upper part by the presence of rocky, steep, 20-m high headscarp, with extensive slided rock blocks under it. Above the headscarp, diagonally to its direction, the 10-m deep rocky trench is developed within the slope. In its south-western termination, several shallower trenches, opened tension cracks and pseudokarst sinkholes and crevices are formed. Strong cold air draught within the exposed crevices indicates the presence of a large system of underground gravitationally widened joints or even the crevice-type caves. In the north-east, the main trench is terminated by the debris accumulation and the series of shallow pseudokarst sinkholes of different shapes, developed within the narrow, slightly inclined plateau. North steep slopes are affected by Late Holocene catastrophic slope collapse (Pánek et al., 2009).

3. Methods

3.1. Geomorphic mapping

Both sites were mapped with the accent on landforms strictly related to the DSL formation. In particular, the depression forms (trenches and sinkholes) and counter-scarp ridges were considered to be a result of the subsurface massif relaxation and gravitational extension. The field geomorphic mapping consisted from (i) landform observation with emphasis to the distinctive terrain changes, such as steep scarps, trenches, pseudokarst sinkholes and rock outcrops; and (ii) GPS-based precise localization of the main geomorphic features in order to gain their correct topology. Detailed geomorphic maps of the both studied sites and their close vicinity, with emphasis on the above-mention landforms, were created (Fig. 1). According to the field geomorphological mapping, two particular profiles, one on each studied site, were delimited for a detailed complex multidisciplinary geophysical survey.

3.2. Electrical resistivity tomography

Geoelectrical properties (resistivity $\boldsymbol{\rho}$/conductivity $\boldsymbol{\gamma}$) of the flysch rocks were examined by means of a direct current (DC) multi-electrode resistivity measurement technique, i.e., electrical resistivity tomography (ERT). ERT was chosen as a leading geophysical method for its relatively quick, effective and simple field measurement, especially in hardly accessible areas, and for its previous widespread application in the area of the flysch OWC (Pánek et al., 2007, 2010a,b, 2011a,b, 2014; Šilhán, 2010; Tábořík, 2012; Lenart et al., 2014). Moreover, the method brings satisfactory resolution and rather high depth range (several tens of meters).

ERT is primarily based on measurements using two pairs of electrodes – current ones (C1 and C2) and potential ones (C1 and P2). Current electrodes are used for injecting of direct current (I) to the subsurface, whereas the potential ones measure electric potentials (U). With use of the modified Ohm's Law, we can calculate apparent resistivity (ρ_a) of the measured subsurface lithology:

$$\rho_a = k.\frac{U}{I}, \quad (1)$$

where the geometry of the used electrode array is given by geometric factor (k) (Loke and Barker, 1996). ρ_a may be further inverted to the calculated "real" resistivity (ρ) within the process of the tomographic inversion (Loke, 1997).

Field measurements were realised by means of the multi-electrode system ARES (GF Instruments). A Wenner-Schlumberger electrode array was chosen due to its sufficient penetration depth and satisfactory resolution in both vertical and horizontal directions (Loke, 1997; Zhou et al., 2002; Szalai and Szarka, 2008; Szalai et al., 2009). The electrode spacing varied from 1 to 5 m, depending on the scale of measurement and on the total length of the individual profiles. The location of the ERT profiles is shown in Fig. 1. The obtained data were processed in the Res2Dinv software (Geotomo Software) and depicted as resistivity sections representing a distribution of subsurface resistivity along the measured profile (Fig. 2).

3.3. Ground penetrating radar

Ground penetrating radar (GPR) measurements were performed to reveal the depth and structure of the colluvial cover and to distinguish between the high reflective subsurface structures, i.e., rigid sandstones or dry debris infill, and low reflective features, i.e., fine-grain flysch rocks, water-saturated debris, etc. GPR belongs to the harmonic high-frequency geoelectrical methods. Radar waves are propagated in distinct pulses from a ground surface antenna; reflected off buried objects, bedding contacts or soil units; and detected back at the source by a receiving antenna. As radar pulses are propagating into the depth, their velocity changes, depending on the physical properties of the various materials (Conyers and Goodman, 1997; Conyers, 1999).

Measurements were performed with use of the RAMAC system with X3M control unit (MALÅ Geosciences) with different shielded antennas of specific frequencies of 100, 250 and 500 MHz and using MALÅ GroundVision v. 1.3.4 software. According to the used antenna, the sampling frequencies were 1182 MHz (100 MHz antenna), 2560 MHz (250 MHz ant.) and 6013 MHz (500 MHz ant.) and the trigger intervals were 10 cm (100 and 250 MHz ants.) and 5 cm (500 MHz ant.). Triggering was controlled by the distance wheels.

The measured data were post-processed in the ReflexW v. 6.0.5 software (Sandmeier software). The 2-D data processing was performed in several following steps: dewow filter (subtract mean), static correction/move start-time (alignment of the first arrivals), background removal (noise suppression), amplitude scaling (energy decay), band-pass filtering (in the range 80–180 MHz) and running average filter. The topography of the profile was added in the form of the amplitude time-shift. The GPR sections were displayed in comparison to the ERT resistivity pseudosections (Fig. 3).

3.4. Shallow seismic refraction

The shallow seismic refraction method (SSR) is based on the elastic properties of rocks. Seismic waves travel through different rocks at different velocities, which are further largely influenced by porosity and fluid contents. In this case, a seismic survey was performed to reveal

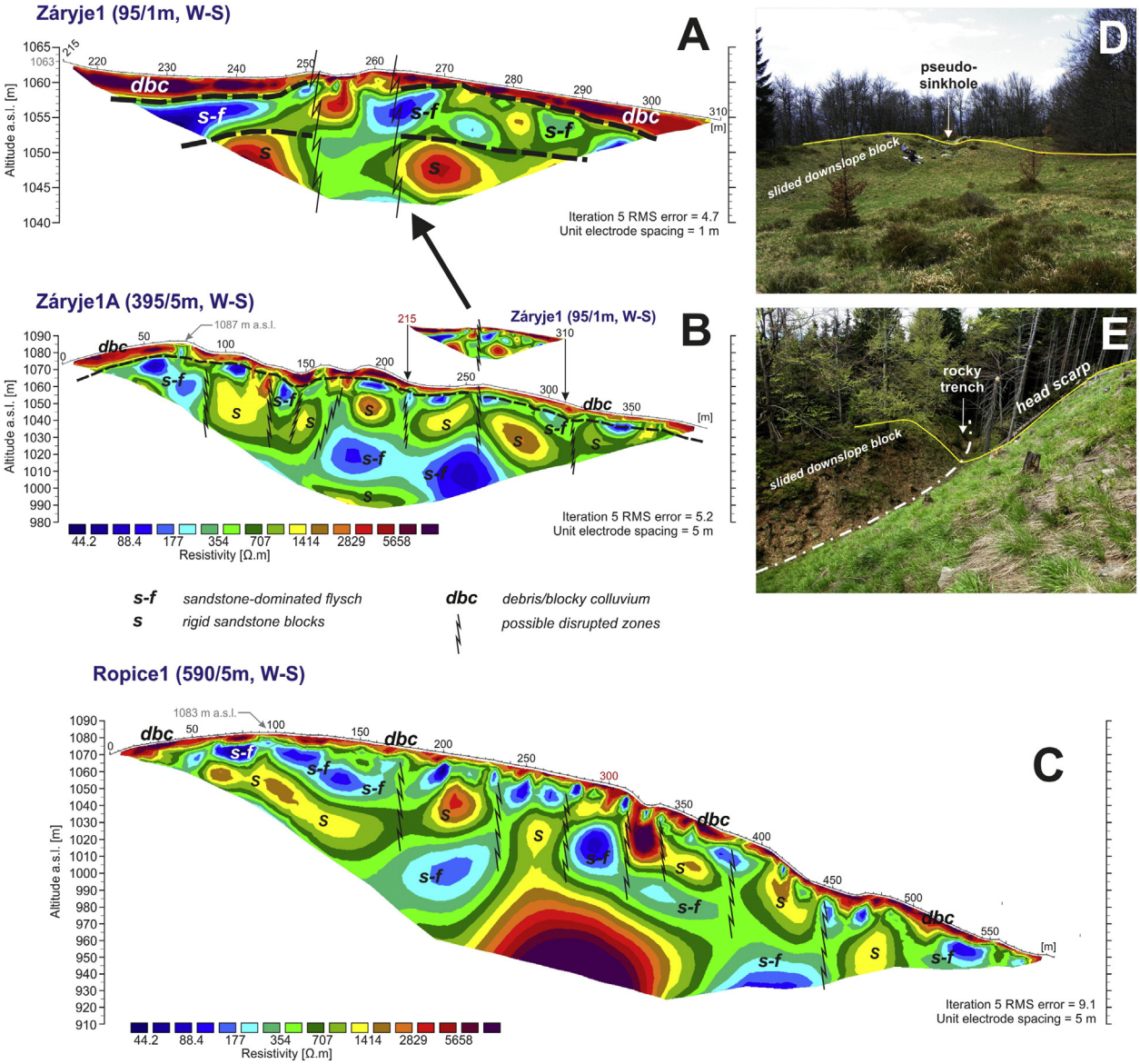


Fig. 2. Elevated inverse resistivity pseudosections (Res2Dinv). (A) Záryje 1 profile (detailed). (B) Záryje 1A profile. (C) Ropice 1 profile. The resistivity scale is unified. (D) Záryje site - downslope rock block with trench on the top of the block (photo: J. Lenart). (E) Ropice site - downslope view on the rocky trench between scarp and toppled block (photo: P. Tábořík).

possible weakening of the bedrock, likely caused by mechanical disruption of the massif.

Measurement is based on the recording of seismograms of the refracted waves using the multi-channel engineering seismograph Geode (Geometrics, USA). As a source of the seismic signal (elastic wave), we used a 7-kg sledge hammer striking a steel plate on the ground. An accelerometer on the hammer handle was used for the triggering of the seismic records. Stacking of up to eight hammer blows at the same shot-point was used for signal enhancement.

The 24-Hz single vertical geophones connected to a 24-channel Geode seismograph were used. We used two 24-geophone spreads, which overlap by one geophone. The total profile length was 92 m, and the geophone interval was 2 m. The seismic sources were placed at a 4-m interval inside the geophone spread and with the offset of up to 100 m outside the geophone layout. Distant shot-points were performed to detect waves refracted from the possible deeper seismic boundaries or to increase the depth range in the case of vertical velocity gradient.

The processing of collected seismograms was based on the first arrivals of the P-waves. The arrival times were picked in the SeisImager–PickWin (OYO) software. Travel-time–distance data sets were processed by means of seismic tomography analysis. The tomographic recursive inversion was performed in the software SeisImager–Plotrefa (OYO Corp.) to obtain the P-wave velocity distribution (Fig. 4).

3.5. Gravity survey

The aim of a gravity survey was to locate gravitationally induced crevice-type caves. Compared to the surrounding rocks, these structures are characterised by a density deficit and, therefore, they are represented by negative anomalies.

We used the gravimeter Scintrex CG-3M with a resolution of 0.001 mGal. Tidal effects and the long-term linear drift were removed by the internal software of the gravimeter. The residual drift and tides were registered by reoccupation of the base station in a time interval of approximately 1 h. 10% of field gravity stations were measured repeatedly at different times. The measurement error was calculated after correction of the residual drift and the tides. The measurement mean square error was 0.006 mGal.

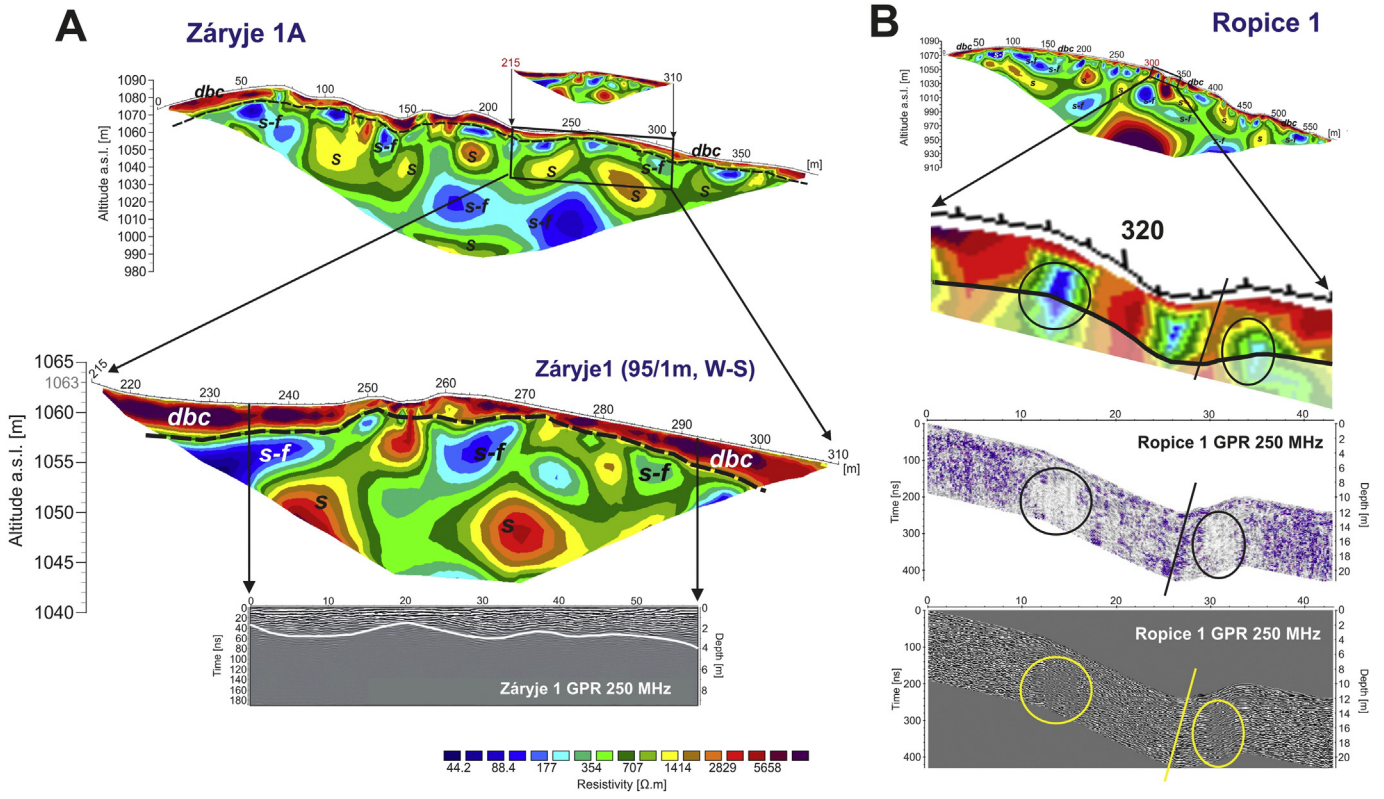


Fig. 3. GPR results compared to ERT pseudosections: (A) Záryje site – GPR revealed thickness of colluvial mantle and surface of the underlying flysch bedrock; (B) Ropice site – strong signal attenuation zones in the GPR profile is in agreement with low resistive zones in ERT section.

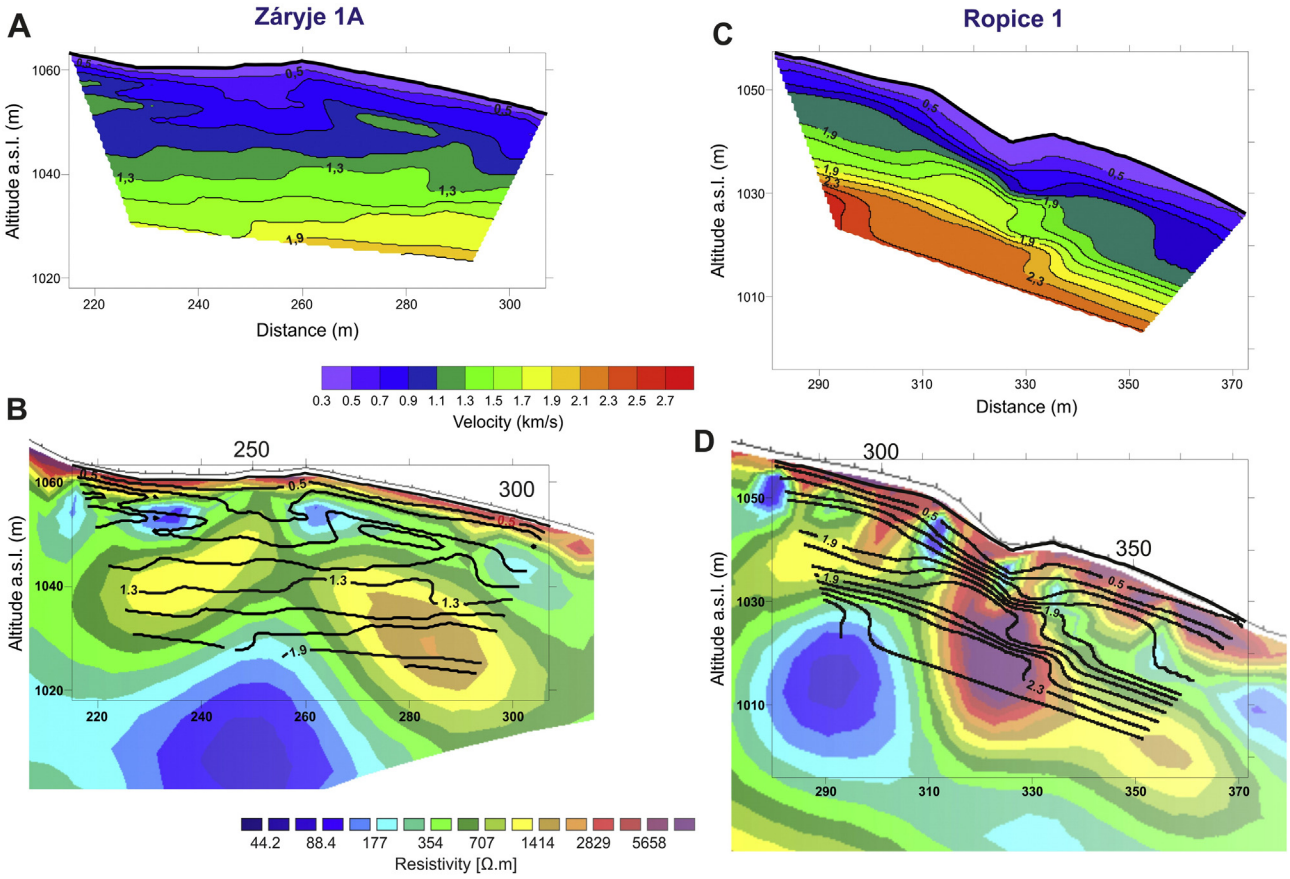


Fig. 4. SSR survey – seismic tomography. (A) Záryje 1 seismic velocity section, (B) Záryje 1 profile – combination of seismic and resistivity tomography, (C) Ropice 1 seismic velocity section and (D) Ropice 1 profile – combination of seismic and resistivity tomography. The resistivity scale given in Fig. 2.

We obtained an 80 m long profile at the Záryje site (stationing 215–295 m). The distance between the gravity stations was 2 m. The profile with length of 40 m was performed at the Ropice site. The gravity stations spacing was not equidistant because of the very rugged topography; the average distance was 3 m. All measuring band distances were converted to horizontal distances, as presented in Figs. 5 and 6.

Bouguer anomalies were calculated according to the following formula:

$$\Delta g = g_{obs} - g_t + 0.3086h - 0.0419\rho h + T - B, \quad (2)$$

where Δg = Bouguer anomaly; g_{obs} = observed gravity; g_t = theoretical gravity (latitude correction); h = height of gravity station; 0.3086 h = free-air correction; ρ = reduction density; 0.0419ρh = Bouguer correction; T = topographic correction; and B = Bullard correction.

Numerical values of the gravity data are given in [mGal] (1 mGal = 10^{-5} m·s^{-2}), h [m] and ρ [g·cm^{-3}] (1 g·cm^{-3} = 1000 kg·m^{-3}). The reduction density is the density of rocks that prevail in the surveyed area (2.51 g·cm^{-3}) (Eliáš and Uhmann, 1968). Topographic corrections were calculated to the distance of 166.7 km from the measured stations. The values of the Bouguer anomalies are given as relative because the value of gravity measured at the base station was not tied to the national gravity network.

Quantitative interpretation of the gravity measurements was performed at both surveyed localities. We used GM-SYS program for forward profile modelling (Geosoft Inc., 2015), in which geological units are visualised as tabular prisms with the axes in their strike directions.

4. Results

Due to a difference of the main physical parameters of each method, we cannot compare the results of the used geophysical techniques directly. However, for the complex image of the subsurface situation, an integrated interpretation of the geophysical data sets was recognised as adequate.

4.1. Záryje site

The positions of all used geophysical measurements (stationing) were adjusted in relation to the ERT profile Záryje 1A (Fig. 2B).

4.1.1. Electrical resistivity tomography

We performed ERT measurements with two different length/electrode spacings: profile Záryje 1 with 95/1 m and profile Záryje 1A with 395/5 m. The results of ERT surveying bring two models of subsurface structure, each differing in the resolution and the depth of penetration.

Profile Záryje 1 (Fig. 2A) was performed directly across the slided rock block with the distinctive elongated pseudokarst sinkhole filled with debris and with the opened tension crack on its top (Fig. 2B). Examining the profile, there is a well-pronounced upper layer of extremely high resistivity (>3000 Ω·m), with the thickness varying from 2 to 10 m. These relatively high resistivity values represent a near-surface debris/blocky colluvial sheet (*dbc*). Beneath this weathered layer, the zones of relatively low resistivity (<300 Ω·m) alternating with relatively higher resistivity structures (~800–3000 Ω·m) represent flysch rocks disrupted by vertical, gravitationally widened joints. The overall image

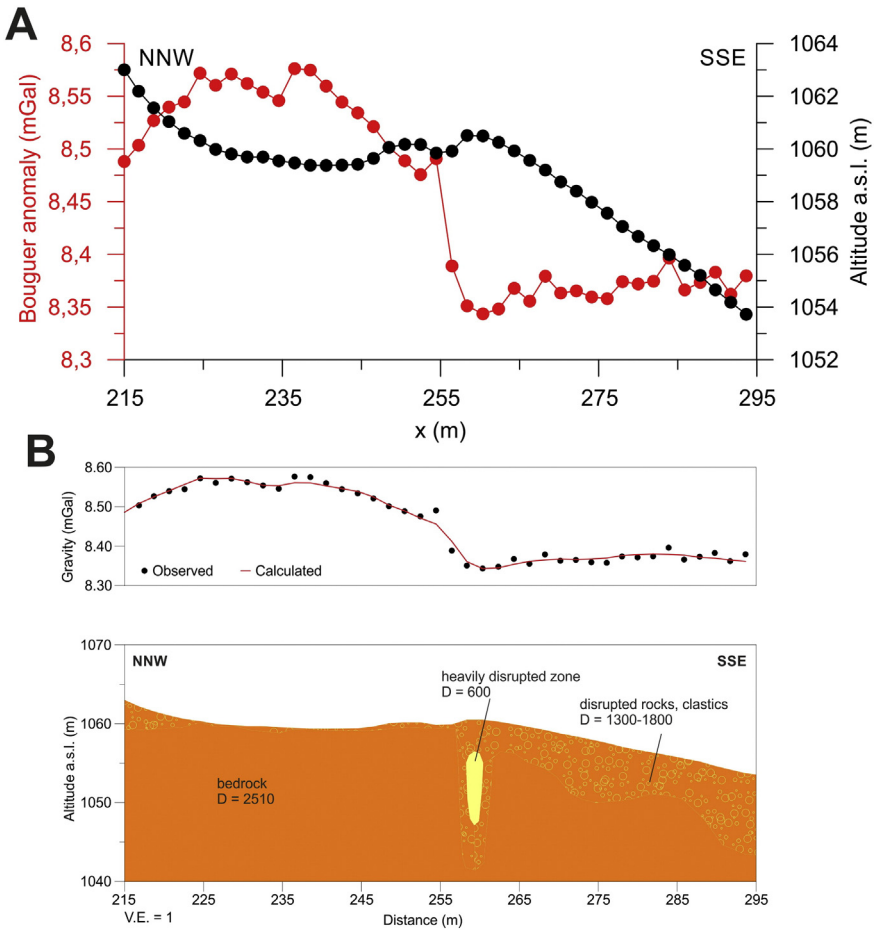


Fig. 5. Gravity survey on the Záryje 1 profile. (A) Results of gravity field measurements: Bouguer anomalies (red dots) and heights of the gravity stations (black dots). (B) Results of gravity modelling. Densities of rocks, *D*, are in kg·m^{-3}. (For interpretation of the references to colour in this figure legend, the reader is referred to the web version of this article.)

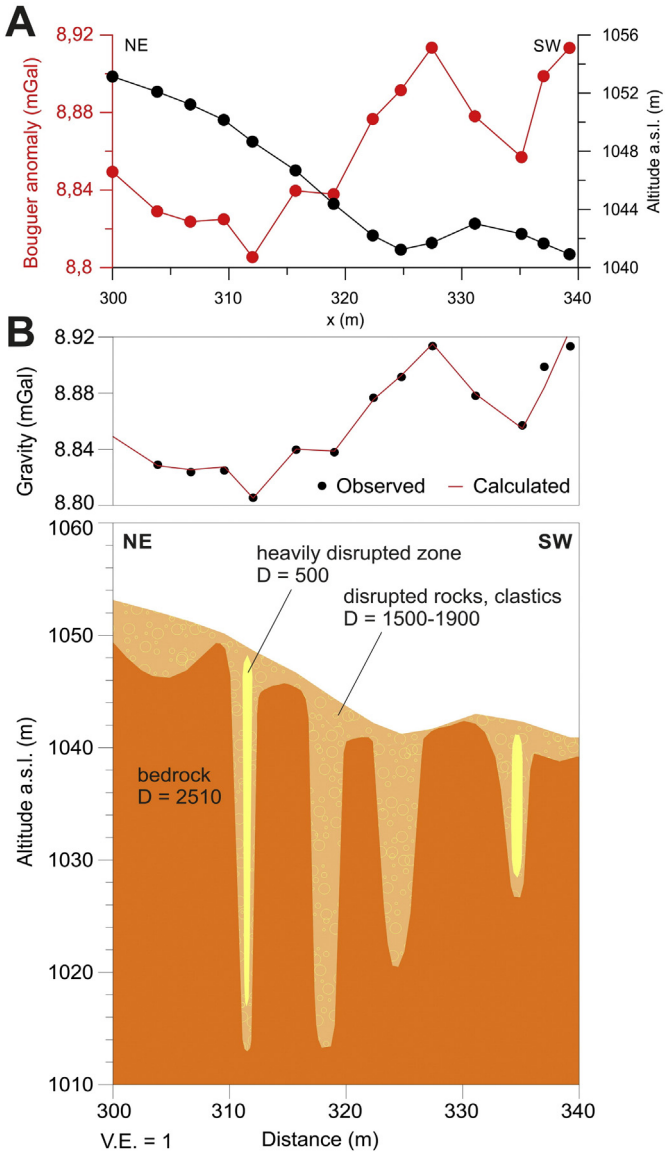


Fig. 6. Gravity survey on the Ropice 1 profile. (A) Results of gravity field measurements: Bouguer anomalies (red dots) and heights of gravity stations (black dots). (B) Results of gravity modelling. Densities of rocks, D, are in $kg \cdot m^{-3}$. (For interpretation of the references to colour in this figure legend, the reader is referred to the web version of this article.)

of the bedrock is therefore fragmented and corresponds to a heterogeneous anisotropic lithology. A significant disrupted zone within the massif is visible underneath the focused rocky trench.

Measurements using a deeper range (maximum of 80 m) and different resolution ability at the Záryje 1A profile (Fig. 2C) were performed to extend the information to a wider area, including the ridge part, and to a greater depth. Because the rock layers are more or less continuous, we can find quite clear evidence of disruption of its course at stationing ~100–170 m of the Záryje 1A profile, with possible subsidence of the sandstone block of several tens of meters. The weakened zone, depicted in the profile Záryje 1 is no longer visible in this profile. This observation might be due to the exceeding electrode spacing related to the limited ability of the discontinuity detection.

4.1.2. Ground penetrating radar

The measurements with three shielded antennas, differing in the frequency used, were carried out. Probably due to the longer wavelength of the EM signal, the resolution of the 100 MHz antenna is rather low. The theoretically deeper range of the 100 MHz antenna was not confirmed by the results. Therefore, we present only the results obtained by the 250 MHz antenna.

The GPR results of the 250 MHz antenna provided only limited information due to the strong signal attenuation. The only usable reflections we recorded within the superficial high reflective and high resistive layer representing the colluvial mantle. The relatively high conductivity of the flysch rock beneath this mantle caused significant attenuation of the EM signal. Therefore, the maximum range of the GPR reflections is up to 4 m, and the deeper structures remained unrevealed by GPR (Fig. 3A). The depth range of the 500 MHz antenna was only several meters; thus, we found the use of this antenna to be insufficient.

4.1.3. Shallow seismic refraction

According to the seismic velocity model (Fig. 4A), there are two main higher-velocity (>1000 $m \cdot s^{-1}$) zones, propagating from the depth towards the surface. In contrast, the low velocity zone (~500 $m \cdot s^{-1}$) is wedged between these two high-velocity zones. From ~ 20 m below the surface, the velocity increases constantly to the depth up to 2000 $m \cdot s^{-1}$. The low velocity zone corresponds to the morphological manifestation of the pseudokarst sinkhole and structures beneath it. Because the high-velocity zones should represent undisturbed rock blocks, the profile probably reveals the subvertical block, subsided into the free space.

4.1.4. Gravity survey

The values of Bouguer anomalies range within the interval of 0.25 mGal (Fig. 5A). The most striking feature on the gravity curve is the steep gradient of Bouguer anomalies at the stationing at approximately 255 m. A gravity low occurs from 260 m to the end of the profile. The density cross section (gravity model) is shown in Fig. 5B. The measurements detected an approximately 20 m deep zone of heavily disturbed rocks on stationing 260 m. The central part of this zone reveals very low density (~500 $kg \cdot m^{-3}$) which could indicate the occurrence of a crevice-type cave. Partly disrupted rocks and rock debris were modelled between ~5–10 m below the surface, from 260 m to the end of the profile.

4.2. Ropice site

The positions of all used geophysical measurements (stationing) were adjusted in relation to the ERT profile Ropice 1.

4.2.1. Electrical resistivity tomography

The ERT section of 590 m/5 m (length/spacing) with the depth range up to 120 m at the Ropice site (Fig. 2D,E) shows the near-surface colluvial layer (*dbc*) of the maximum 10 m thickness. The relatively high-resistivity zone, 10–25 m below the ground surface in the middle section of the profile, is well pronounced. This resistivity demonstrates the gravitationally relaxed rocks below the diagonal rocky trench and might represent the passages of unknown crevice-type cave. In contrast with the Záryje site, the morphological evidence of the block subsidence is not very obvious at the very ridge part, but it is presented at the contiguous slope (~300–550 m of the profile).

4.2.2. Ground penetrating radar

The GPR survey was performed only by 250 MHz antenna for two reasons: (i) previous positive experience with this frequency and (ii) hardly accessible area with extreme slope inclination of ~40°. GPR survey at the Ropice 1 profile shows different results from the Záryje 1 profile. The depth range of the EM signal reaches nearly ~8 m, which is the maximum range of the 250 MHz antenna under optimal conditions (Słowik, 2012). The quality of reflections does not allow a detailed interpretation of the radargram. Nevertheless, two areas with significant signal attenuation are distinctive (Fig. 3B).

4.2.3. Shallow seismic refraction

We acquired similar velocity values as in the case of the Záryje site (Fig. 4C). Two main zones of the higher velocities (>1200 $m \cdot s^{-1}$) are situated underneath the individual blocks, and a wedge-like zone of the lower velocities (<800 $m \cdot s^{-1}$) is situated under the bottom of the trench. The rock block situated downslope appears to be more disturbed according to the rapid changes in measured velocity values.

4.2.4. Gravity survey

The values of the Bouguer gravity anomalies are within the relatively narrow interval of 0.1 mGal. The most intense gravity low on the profile occurs on stationing 312 m. This local anomaly with amplitude of 0.01 mGal was recorded at one measurement station only. This type of "one station–low amplitude" anomaly is usually considered as an outlier. However, the anomaly occurs just at the point of the distinct slope topography change. Thus, we suppose a narrow deep crevice exists at that (Fig. 6B). Other narrow zones of disrupted rocks are visible between the 318 and 335 m. The crevice-type caves might occur inside this zone.

5. Discussion

Geophysical research of slope deformations using various geophysical techniques has been recently used in numerous geomorphological studies (Bláha and Abdullajev, 1993; Godio and Bottino, 2001; Suzuki and Higashi, 2001; Lapenna et al., 2003; Lebourg et al., 2005; Drahor et al., 2006; Friedel et al., 2006; Godio et al., 2006; Lazzari et al., 2006; Jomard et al., 2010; Migoń et al., 2010; Pánek et al., 2010a, 2011a, 2011b, 2014; Chambers et al., 2011). Many of the previous papers focused on the detection of bedrock discontinuities, such as faults, tension cracks or crevice-type caves related to the DSLs (Meric et al., 2005; Pánek et al., 2010b; Pánek et al., 2011a; Lenart et al., 2014). In some papers, a combined geophysical survey of landslides was also used (Sass, 2006; Sass et al., 2008; Naudet et al., 2008; Pánek et al., 2009, 2011a; Heincke et al., 2010; Martínez-Moreno et al., 2013).

However, in the present study, we first used the combination of four different geophysical methods to investigate the DSL structure and development in flysch sedimentary rocks. We chose two morphologically typical testing sites with clear manifestations in terrain: (i) shallow rocky pseudokarst sinkhole at the top of one of the slided rock blocks and (ii) deep rocky trench above the landslide headscarp. We assumed distinct continuation of these slope discontinuities into the deeper structures.

5.1. Combined geophysical surveying

ERT is able to detect the general structure of the investigated DSLs. High resistive bodies (~800–3000 Ω·m) very likely represent rigid sandstone blocks, whereas low resistive structures (<300 Ω·m) represents fine-grain flysch rocks (fine-grain sandstones alternated with siltstone or claystone intercalations). Higher resistivity values (> 3000 Ω·m) denote coherent blocky/debris accumulations of the colluvial sheet, typically reaching the thickness of several metres.

GPR has only limited penetration depth, and anisotropic flysch bedrock is not an ideal environment for its applications due to high intensity of the signal attenuation (Fig. 3A). Nevertheless, in the case of the Záryje site (Fig. 3A), GPR very accurately delimited the boundary between a high resistivity incoherent blocky/debris colluvial mantle and the underlying thick bedded flysch and thus revealed the thickness of colluvial cover, whereas at the Ropice site, GPR detected a different bedrock structure. There were two zones of the strong signal attenuation detected. Compared with the relevant resistivity section (Fig. 3B), the positions of those zones highly match with the low resistive lenses within the surrounding high resistive bedrock. Low resistivity (high conductivity) together with prevailing fine-grain character of the rocks is, however, the most common reason of signal attenuation (sensu Słowik, 2012). We interpret these low resistivity zones as an effect of strong massif disruption, when underground gravitationally widened crevices are gradually filled by high conductivity clay and material saturated with water.

SSR is based on the elastic properties of the rocks. In the case of the Záryje site (Fig. 3B), the clear resemblance between the resistivity and velocity sections is apparent. Higher velocity values propagating to the surface more or less correspond to the higher values of resistivity. Simultaneously, local subvertical decrease of the velocities corresponds to the local drop in resistivity. The subsurface situation at the Ropice site is more complicated (Fig. 3D). The decrease of velocities underneath the headscarp trench appears to be not very significant. The resemblance between the resistivity model and the velocity model is not clear. However, the velocity model shows zones of higher velocities with propagation towards the surface from the depth as well as wedged zones of lower velocities. Generally, the higher velocities correspond to the rigid blocks depicted in the ERT profile by higher resistivity.

Although the modelling of the gravity data can bring several possible solutions, we can interpret the measured gravity values with regard to the results of the other geophysical method as follows:

At the Záryje site (Fig. 5), a relatively well-pronounced gravitational anomaly occurs underneath the elongated pseudokarst sinkhole. The anomaly is heading below the slided block. This observation agrees with the results of SSR and ERT, which both indicate the disrupted zone within the slided block.

At the Ropice site (Fig. 6), the most distinct anomaly occurs at the stationing 312 m of the gravity profile. In the resistivity section, we detected a distinctive vertical resistivity boundary (strong horizontal resistivity gradient) at the very same position of the profile. Another gravity anomaly was measured underneath the slided block, which can be explained by its intensive relaxation. The gravity survey did not confirm the discontinuity directly beneath the trench.

5.2. Are geophysical techniques truly able to detect the DSL structure?

First, we should discuss the applicability of the used geophysical techniques and its combinations. Were they able to well detect the above-described discontinuities in sedimentary flysch rocks? Are the combinations of methods and their integrated interpretations more appropriate than single use of individual method?

Examining the results, the ERT method was able to detect the slope discontinuities described above, with better results at a higher resolution (1 m distance between electrodes). Adequate complementary methods appear to be SSR and GS. Both methods confirmed the existence of the studied discontinuities, although the SSR results are more difficult to interpret. The most problematic and poorly interpretable results are the results of GPR measurements, due to its low penetrating range and sensitivity to water-saturated layers (strong signal attenuation).

The single use of the individual geophysical methods in highly jointed flysch rocks brings only partial information on the subsurface situation. We strongly recommend using the combined geophysical survey and the integrated interpretations of the acquired data. We recommend the use of ERT as a leading geophysical technique, due to its relatively simple manipulation in hardly accessible terrain, sufficient penetrating range and less complicated data processing and interpretation. Considering the terrain conditions, we can combine the ERT measurements with other geophysical techniques.

There is an inherent ambiguity in the interpretation of gravity data, and therefore, these data cannot be interpreted uniquely, even in the case when we achieve a perfect match of the observed and calculated data during modelling. Constraining factors are usually geologic plausibility, knowledge of rock densities at surveyed locality and the results of other geophysical methods. We have only synoptic information regarding the densities of rocks (Eliáš and Uhmann, 1968). However, for sedimentary rocks, even detailed laboratory measurement of rock samples cannot ensure obtaining the correct densities of rocks in

natural conditions and cannot guarantee correct interpretation of the gravity data (Blecha and Mašín, 2013). In our study, important constraining factors of geological interpretation are the measurements of ERT and the refraction seismic measurements at both localities.

The use of the SSR survey is limited by the ability to record usable seismic signal on geophones, especially in incoherent and heterogeneous colluvial mantle. In addition, damping (absorption) of the seismic signal by the colluvial layer strongly affect the penetration depth. However, if we solve these complications (e.g., by using a larger number of stacks), the SSR offers very valuable information on the elastic properties of the bedrock.

Second, we should consider whether some of the supplementary methods are able to upgrade or refine the results measured by ERT. Examining the results from the Záryje site, the short ERT profile clearly revealed the discontinuity under the morphologically distinctive pseudokarst sinkhole, which might indicate the existence of crevice-type caves. One of the possible problems to solve is determining whether these cavities are situated truly just under the sinkhole or not. The GPR waves cannot penetrate under the weathered mantle and, thus, they provide poor information. The ERT profile reveals the high-resistivity domain just under the pseudokarst sinkhole, but the appropriate SSR and GS profiles suggest the most disturbed zone more to the right (downslope), below the top of the slided rock block. Comparing the ERT profile with the SSR and GS results indicates that the searched discontinuity is not displayed by high-resistivity domain, but conversely by the strong contrasting transition (horizontal gradient) between high- and low-resistivity domains.

Similarly, the discontinuity below the rocky trench developed within the Ropice site, proved by the ERT as a very high-resistivity anomaly and originally supposed to be a crevice-type cave just below the trench, is not confirmed by SSR and GS. Both the methods placed the highest anomalies above the trench, upslope from the high-resistivity domain (Figs. 4 and 6). These results lead us to the conclusion that the high-resistivity domains in the ERT profile do not display directly the underground rock discontinuities. On the contrary, the discontinuities are depicted as high-contrast transitions between high- and low-resistivity zones. This behaviour might be supported by the mainly linear subvertical course of such transitions.

5.3. Possible interpretations of contrast transition within the ERT profile

If we intend to discuss the reliability of the above-mentioned conclusions, we should compare it with the results of the previous studies

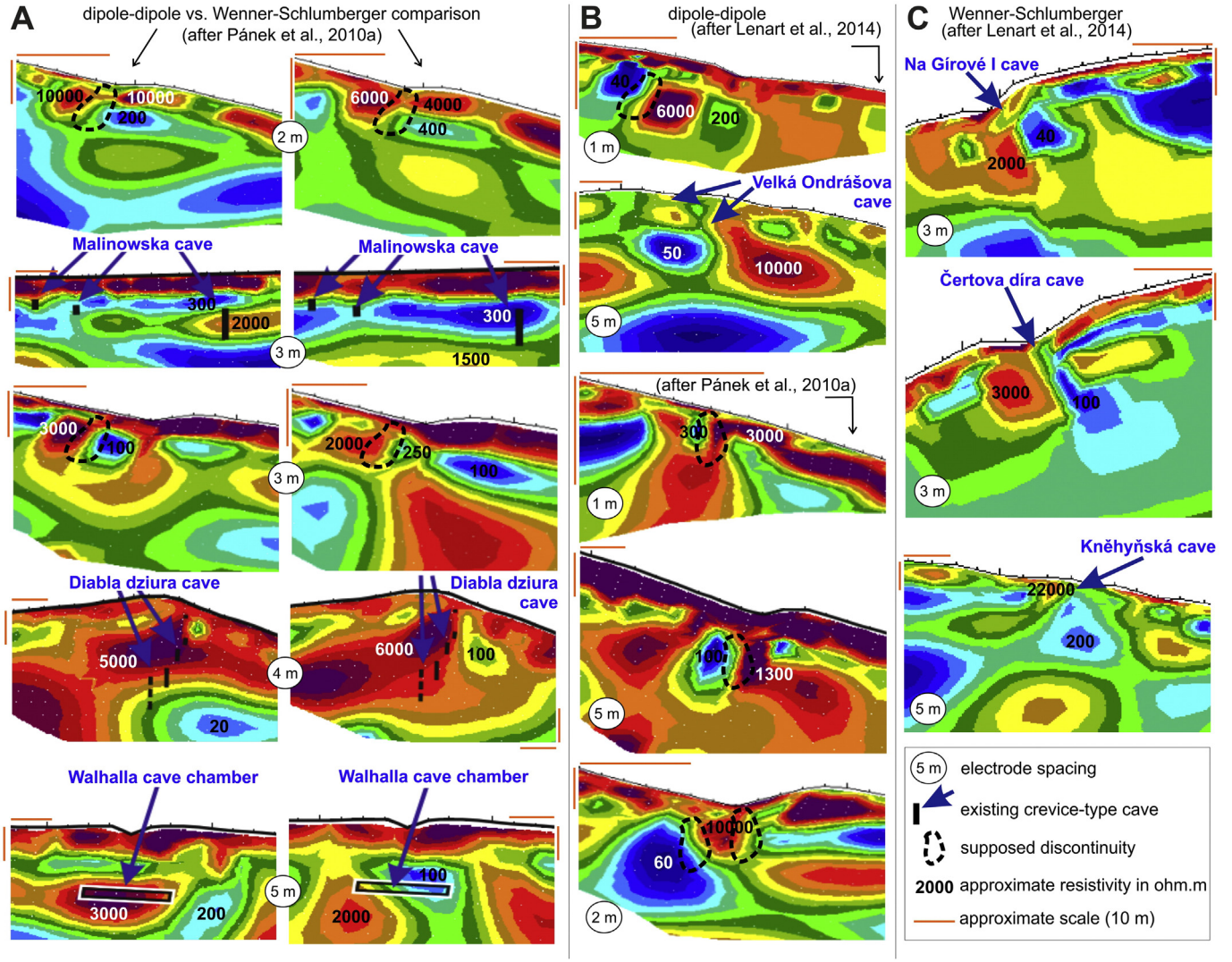


Fig. 7. ERT sections published in previous studies (Pánek et al., 2010a; Lenart et al., 2014) shows resistivity images of the known crevice-type caves. (A) Comparison of Wenner-Schlumberger and dipole-dipole electrode arrays performed on the identical profile. (B) examples of the transition zones and positions of several caves (using dipole-dipole array). (C) examples of the transition zones and positions of several caves (using Wenner-Schlumberger array). Some mapped caves or supposed caves correspond with the transitions between low and high resistivity domains. These phenomena are often repeated within the different profiles. Note the differences between the identical profiles with the use of two different electrode configurations.

realised in the same rock types and similar relief conditions. Fig. 7 shows the segments of the ERT profiles performed by Pánek et al. (2010a) and Lenart et al. (2014). Each segment shows the situation similar to our recent results – high resistivity domain with the low resistivity domain in the close vicinity (in some cases as a mirror image), with a strong contrasting transition of the linear subvertical course, which is unusual within the rest of the profile. Both cited studies considered the relatively high-resistivity domains to be the possible crevice-type caves. However, if we supply the profiles by the precisely located caves detected from the cave maps, the results reveal that the contrast transitions are situated exactly in the areas where the caves are actually formed.

Moreover, some profiles were performed for both dipole-dipole and Wenner-Schlumberger arrays (Pánek et al., 2010a). The dipole-dipole array detected the existing cave quite accurately (as high-resistivity domains), and the Wenner-Schlumberger array depicted the contrasting transition at place where cave should be located. These transitions are very similar to those recently measured in this study. Because we also used the Wenner-Schlumberger array, we believe that these contrast transitions indicate the crevices, i.e., vertical discontinuities in sedimentary flysch rocks.

The discontinuities in the described environment are very often predisposed by faults, which should be depicted in ERT profiles as low-resistivity zones. Same faults very often laterally border the crevice-type caves (Lenart et al., 2014). It follows that the low-resistivity zone (fault, water saturated) passes immediately into the high-resistivity zone (caves, relaxed rock with free air). This contrast alone might be captured within the ERT sections. Another possible explanation of the "contrast feature" is the presence of underground relative low resistivity rock walls (somewhere even water coated) and the extreme high resistivity air filled gravitationally relaxed crevices.

The performed experimental modelling using synthetic data in Res2Dmod v. 3.02.03 software (Loke, Geotomo Software) does not confirm this assumption completely (Fig. 8). The modelled structures are – after application of both forward and inverse modelling – situated at the correct positions. However, in the case of a low resistivity structure modelled directly next to the proposed high resistivity structure (supposed cave), the software provides the model with appearance of the above-mentioned transition zone (Fig. 8G). Nevertheless, there is no reasonable geological explanation of such low resistivity structure. It appears that a simple forward modelling and consequent inversion of the synthetic data (even with inclusion of added random noise to the inversion process) is not able to explain reliably why we experience a discrepancy between the depicted (modelled) positions of the subsurface structures (caves) in inverse resistivity model and the real position verified by precise cave mapping.

The real situation is probably much more complicated by heterogeneity, anisotropy and natural geoelectrical noise. Moreover, the content of water or fine-grain conductive infill together with extremely high resistivity of colluvial mantle or air-filled free space can significantly disturb the electrical field and its behaviour. The real situation is probably further complicated because the modelling software is not able to involve all possible variables; thus, the anomaly is not modelled to be precisely where it should be situated. Furthermore, the presence of the extremely high conductive anomaly just beside the extremely high resistive body is naturally quite unusual and it might be only a response of the modelling program to the rapid change of the resistivity. Therefore, we should perhaps identify the transition zones as probable positions of the traced anomaly.

5.4. Electrode spacing vs. discontinuity detection

The used electrode spacing can considerably affect the final resolution of the ERT model. Shorter electrode spacing will produce a denser measurement grid. Furthermore, smaller distances between the potential electrodes allow us to measure smaller resistivity values – the signal-to-noise ratio is higher (Karous, 1989; Loke, 1997). With higher resolution, the sensitivity to detect smaller anomalies naturally rises. With shorter distances between electrodes, we are able to detect anomalies of smaller scale, such as narrow crevices or gravitationally widened joints.

5.5. Geomorphic significance of the measured results

The results of performed measurements have several new consequences for geomorphology of slopes disturbed by DSLs. During the field mapping, researchers get only limited information on the landslide body, which is usually delimited on the basis of typical superficial landforms. Are these superficial forms direct reflections of underground structure of DSLs, as geomorphic maps usually presume? Generally, yes, because their formation depends on underground structures evolution. But we should not see the superficial forms strictly as direct continuation of underground structures. If we see the trench or tension cracks in the topography, it does not necessarily indicate the continuation of underground discontinuity. According to our results, the topographical manifestation may be shifted downslope, even by several meters. We suppose that it is a common phenomenon at least in incoherent sedimentary flysch rocks.

According to previous studies by various authors (Pánek et al., 2011a, 2013), the slopes are involved by gravitational deformations repeatedly and chronically. The question is, if the evolution of the DSLs has retrograde upslope direction. If we take into account that underground discontinuities are often shifted upslope from their topographical displays, it could support the hypothesis of a retrograde development of the slope deformation. Once the overburden rock layers are hanging over the underground discontinuity, they are prone to further disruption. The underground discontinuities in the headscarp area should be considered as initial forms of the possible future DSLs as well as rockslides or rock avalanches.

The question of a long-term development and age of the studied DSL have not been sufficiently answered yet, namely due to lack of the dateable material. Generally, we have only limited information on the age of the DSLs in the flysch OWC area, only few of them have been dated yet (Margielewski, 2003, 2006; Pánek et al., 2011a, 2013). However, the recent landforms and underground structures are most likely the products of Upper Pleistocene and Holocene processes according to results of dating of peat bogs and buried organic matter within landslides bodies. Unfortunately, we are not able to determine directly the age of particular underground discontinuities reliably.

6. Conclusion

The presented study demonstrated the advantage of the complex geophysical survey, which comprised four different geophysical methods (ERT, GPR, SSR and GS). The combined geophysical survey in sedimentary flysch rocks revealed that the ERT survey is able to reliably detect the existence of the underground discontinuities, which are manifested at the ground surface by one of the typical landforms, such as tension cracks, trenches, pseudokarst sinkholes, double-crested ridges or counter-slope scarps, which may be assigned namely to the processes connected with DSLs development. The previous studies suggested that the discontinuities should be depicted by high-resistivity domains within the ERT profile. However, the SSR and GS measurements revealed that the real underground continuation of such discontinuities may not strictly follow the superficial landforms and may be shifted. Based on the SSR and GS measurements, the discontinuities are depicted by high-contrast transitions between the high- and low-resistivity domains within the ERT profiles, especially with use of a common Wenner-Schlumberger electrode array. These transitions usually have a straight subvertical course. The results of the GPR measurements provide only poorly interpretable information within the sedimentary flysch rocks due to the shallow penetrating depth, and locally due to strong signal attenuation. The results confirmed the importance of

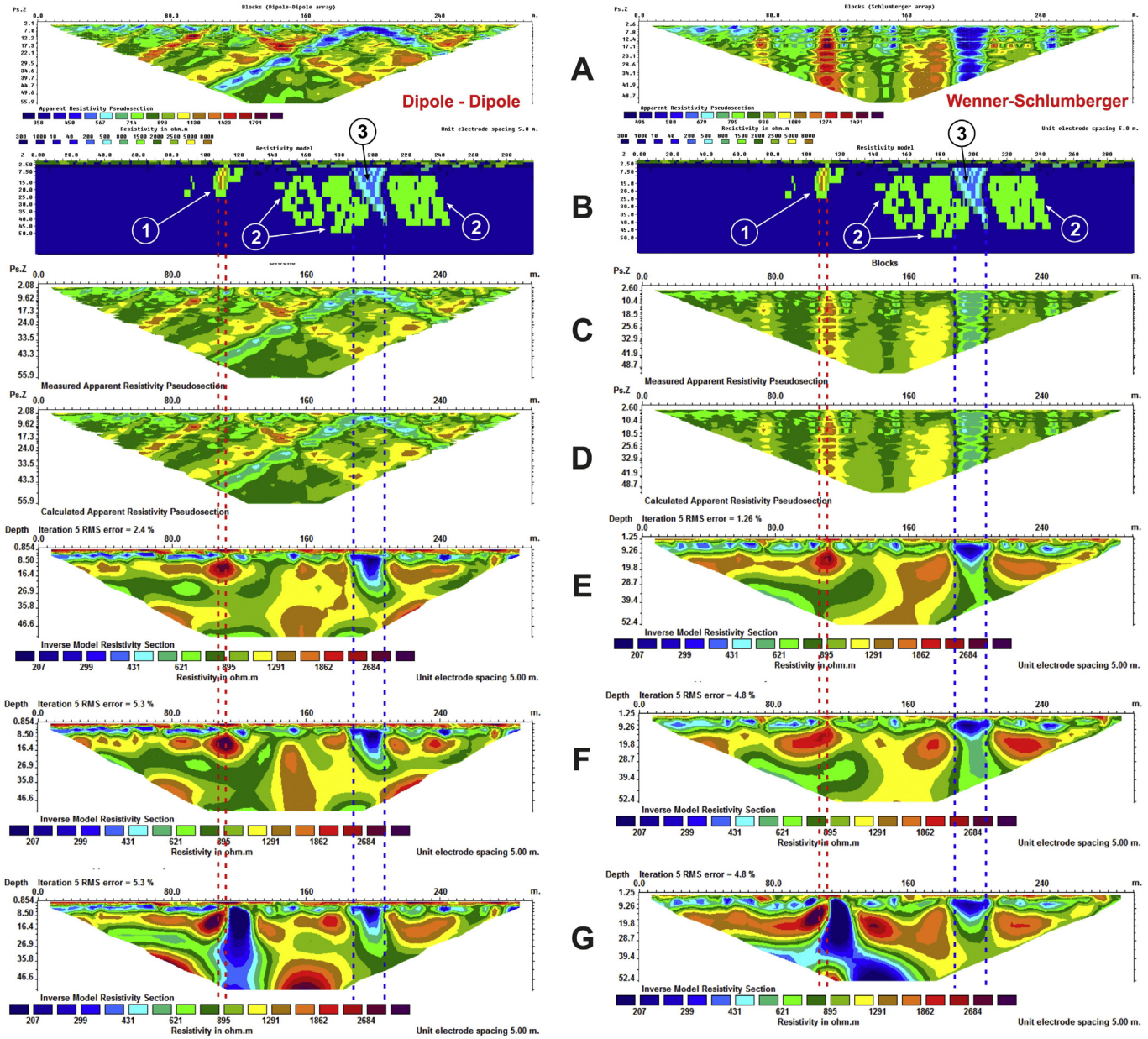


Fig. 8. Forward (Res2Dmod software) and inverse (Res2Dinv software) modelling on synthetic data using dipole-dipole (left) and Wenner-Schlumberger (right) electrode arrays. Res2Dmod: (A) forward model and (B) block model – (1) extremely high resistivity anomaly (e.g., cave), (2) rock block with higher resistivity (e.g., rigid sandstone) and (3) low resistivity zone (e.g., disrupted/weathered rock) wedged between rigid rock blocks. Res2Dinv: (C) measured apparent resistivity pseudosection, (D) calculated apparent resistivity pseudosection, (E) inverse model resistivity section with no additional random noise, (F) inverse model resistivity section with additional random noise (5%), and (G) inverse model resistivity section with modelled transition zone (random noise 5%).

using more than single geophysical technique and of performing integrated interpretations of the measured data. The superficial topography is only indirect reflection of underground discontinuities, which should be considered as initial forms of the possible future deep-seated landslides, rockslides or rock avalanches. Shift of underground discontinuities upslope from the corresponding superficial landform may indicate retrograde evolution of the gravitational deformation.

Acknowledgements

The authors are grateful for the financial support of Grant agency of the Charles University in Prague – project no. GAUK 862213 and for the financial subsidy from the "Support for Science and Research in the Moravian-Silesian Region 2014" program provided by the Moravian-Silesian Region. This work was also carried out thanks to the support of the long-term conceptual development research organisation RVO: 67985891. The authors thank Jitka Hanzelková, Jana Šreinová and Martin Kašing for their technical support during the field works; and, last but not least, the authors thank Tomáš Pánek for the expert opinion and fruitful discussions.

References

Agliardi, F., Crosta, G.B., Zanchi, A., 2001. Structural constrains on deep-seated slope deformations kinematics. Eng. Geol. 59, 83–102.

Baroň, I., Cílek, V., Krejčí, O., Melichar, R., Hubatka, F., 2004. Structure and dynamics of deep-seated slope failures in the Magura Flysch Nappe, Outer Western Carpathians (Czech Republic). Nat. Hazards Earth Syst. Sci. 4, 549–562.

Bláha, P., Abdullajev, Š., 1993. Geofyzikální Metody při výzkumu svahových deformací Geotest Brno, NIS ČR-středisko Geofond; Brno and Praha, in Czech.

Blecha, V., Mašín, D., 2013. Observed and calculated gravity anomalies above a tunnel driven in clays – implication for errors in gravity interpretation. Near Surf. Geophys. 11, 569–578.
Bubík, M., Krejčí, O., Kirchner, K., 2004. Geological Past and Present of Frýdek-Místek Region. Muzeum Frýdek-Místek 54 pp. (in Czech).
Chambers, J.E., Wilkinson, P.B., Kuras, O., Ford, J.R., Gunn, D.A., Meldrum, P.I., Pennington, C.V.L., Weller, A.L., Hobbs, P.R.N., Ogilvy, R.D., 2011. Threedimensional geophysical anatomy of an active landslide in Lias group mudrocks, Cleveland Basin, UK. Geomorphology 125, 472–484.
Conyers, L.B., 1999. Geophysics, ground-penetrating radar and archaeology. Soc. Am. Archaeol. Bull. 17 (4), 26–29.
Conyers, L.B., Goodman, D., 1997. Ground-Penetrating Radar: An Introduction for Archaeologists. AltaMira, Walnut Creek, California.
Crosta, G.B., Frattini, P., Agliardi, F., 2013. Deep seated gravitational slope deformations in the European Alps. Tectonophysics 605, 13–33.
Dikau, R., Brunsden, D., Schrott, D., Ibsen, M.L., 1996. Landslide Recognition: Identification, Movement and Cause. Wiley, Chichester (251 pp.).
Drahor, M.G., Göktürkler, G., Berge, M.A., Kurtulmus, T.Ö., 2006. Application of electrical resistivity tomography technique for investigation of landslides: a case from Turkey. Environ. Geol. 50, 147–155.
Eliáš, M., Uhmann, J., 1968. Synoptic Map of the Density of Rocks in the ČSSR. Ústřední ústav geologický, Prague in Czech.
Esposito, C., Martino, S., Scarascia Mugnoza, G., 2007. Mountain slope deformations along thrust fronts in jointed limestone: an equivalent continuum modelling approach. Geomorphology 90, 55–72.
Friedel, S., Thielen, A., Springman, S.M., 2006. Investigation of a slope endangered by rainfall-induced landslides using 3D resistivity tomography and geotechnical testing. J. Appl. Geophys. 60, 100–114.
Geertsema, M., Clague, J.J., Schwab, J.W., Evans, S.G., 2006. An overview of recent large catastrophic landslides in northern British Columbia, Canada. Eng. Geol. 83, 120–143.
Geosoft Inc., 2015. GM-SYS modelling, advanced software for potential fields. Accessed on January 20, 2015, at http://www.geosoft.com/products/gm-sys.
Godio, A., Bottino, G., 2001. Electrical and electromagnetic investigation for landslide characterisation. Phys. Chem. Earth 26, 705–710.
Godio, A., Strobbia, C., De Bacco, G., 2006. Geophysical characterisation of a rockslide in an alpine region. Eng. Geol. 83, 273–286.
Heincke, B., Günther, T., Dalsegg, E., Rønning, J.S., Ganerød, G.V., Elvebakk, H., 2010. Combined three-dimensional electric and seismic tomography study on the Åknes rockslide in western Norway. J. Appl. Geophys. 70, 292–306.
Hradecký, J., Pánek, T., 2008. Deep-seated gravitational slope deformations and their influence on consequent mass movements (case studies from the highest part of the Czech Carpathians). Nat. Hazards 45, 235–253.
Hungr, O., Evans, S.G., Bovis, M.J., Hutchinson, J.N., 2001. A review of the classification of landslides of the flow type. Environ. Eng. Geosci. 7, 221–238.
Jomard, H., Lebourg, T., Guglielmi, Y., Tric, E., 2010. Electrical imaging of sliding geometry and fluids associated with a deep seated landslide (La Clapière, France). Earth Surf. Process. Landf. 35, 588–599.
Jomard, H., Lebourg, T., Guglielmi, Y., 2014. Morphological analysis of deep-seated gravitational slope deformation (DSGSD) in the western part of the Argentera massif. A morphotectonic control? Landslides 11 (1), 107–117.
Karous, M., 1989. Geoelektrické Metody průzkumu. SNTL/Alfa, Praha 1989 424 pp (in Czech).
Krejčí, O., Baroň, I., Bíl, M., Hubatka, F., Jurová, Z., Kirchner, K., 2002. Slope movements in the flysch Carpathians of eastern Czech Republic triggered by extreme rainfalls in 1997: a case study. Phys. Chem. Earth 27, 1567–1576.
Lapenna, V., Lorenzo, P., Perrone, A., Piscitelli, S., Sdao, F., Rizzo, E., 2003. High resolution geoelectrical tomographies in the study of Giarrossa landslide (southern Italy). Bull. Eng. Geol. Environ. 62, 259–268.
Lazzari, M., Geraldi, E., Lapenna, V., Loperte, A., 2006. Natural hazards vs. human impact: an integrated methodological approach in geomorphological risk assessment on the Tursi historical site, southern Italy. Landslides 3, 275–287.
Lebourg, T., Binet, S., Tric, E., Jomard, H., El Bedoui, S., 2005. Geophysical survey to estimate the 3D sliding surface and the 4D evolution of the water pressure on part of a deep seated landslide. Terra Nova 17, 399–406.
Lenart, J., Pánek, T., Dušek, R., 2014. Genesis, types and evolution of crevice-type caves in the Flysch Belt of the Western Carpathians (Czech republic). Geomorphology 204, 459–476.
Loke, M.H., 1997. Electrical imaging surveys for environmental and engineering studies. A practical guide to 2-D and 3-D surveys. Geotomo software. Accessed on January 31, 2015 at http://www.geotomosoft.com.
Loke, M.H., Barker, R.D., 1996. Rapid least-squares inversion of apparent resistivity pseudose ctions by a quasi-Newton method. Geophys. Prospect. 44, 131–152.
Margielewski, W., 2001. O strukturalnych uwarunkowaniach rozwoju głembokich osuwisk – implikacje dla Krapat fliszowych. Przegl. Geol. 49 (6), 515–524 in Polish.
Margielewski, W., 2003. Late Glacial-Holocene palaeoenvironmental changes in the Western Carpathians: case studies of landslide forms and deposits. Folia Quaternaria 74, 1–97.
Margielewski, W., 2006. Structural control and types of movements of rock mass in anisotropic rocks: case studies in the Polish Flysch Carpathians. Geomorphology 77, 47–68.
Margielewski, W., Urban, J., 2003. Crevice-type caves as initial forms of rock landslide development in the Flysch Carpathians. Geomorphology 54, 325–338.
Margielewski, W., Urban, J., 2005. Pre-Existing Tectonic Discontinuities in the Rocky Massifs as Initial Forms of Deep-Seated Mass Movements Development: Case Studies of Selected deep Crevice-Type Caves in the Polish Flysch Carpathians. In: Senneset, K., Flaate, K., Larsen, J.O. (Eds.), Landslides and Avalanches ICFL 2005 Norway. Balkema. Taylor and Francis, London, pp. 249–256.
Martínez-Moreno, F.J., Pedrera, A., Ruano, P., Galindo-Zaldívar, J., Martos-Rosillo, S., González-Castillo, L., Sánchez-Úbeda, J.P., Marín-Lechado, C., 2013. Combined microgravity, electrical resistivity tomography and induced polarization to detect deeply buried caves: Algaidilla cave (southern Spain). Eng. Geol. 162, 67–78.
Menčík, E., Adamová, M., Dvořák, J., Dudek, A., Jetel, J., Jurková, A., Hanzlíková, E., Houša, V., Peslová, H., Rybářová, L., Šmíd, B., Šebesta, J., Tyráček, J., Vašíček, Z., 1983. Geologie Moravskoslezských Beskyd a Podbeskydské Pahorkatiny. Ústřední Ústav Geologický, Praha 304 pp. (in Czech).
Meric, O., Garambois, S., Jongmans, D., Wathelet, M., Chatelain, J.L., Vengeon, J.M., 2005. Application of geophysical methods for the investigation of the large gravitational mass movement of Séchilienne, France. Can. Geotech. J. 42, 1105–1115.
Migoń, P., Pánek, T., Malik, I., Hradecký, J., Owczarek, P., Šilhán, K., 2010. Complex landslide terrain in the Kamienne Mountains, Middle Sudetes, SW Poland. Geomorphology 124, 200–214.
Milsom, J., 2003. Field Geophysics, the Geological Field Guide Series. 3rd ed. Wiley, Chichester (232 pp.).
Naudet, V., Lazzari, M., Perrone, A., Loperte, A., Piscitelli, S., Lapenna, V., 2008. Integrated geophysical and geomorphological approach to investigate the snowmelttriggered landslide of Bosco Piccolo village (Basilicata, southern Italy). Eng. Geol. 98, 156–167.
Nemčok, A., 1972. Gravitational Slope Deformation in High Mountains. Proceedings of the 24th International Geological Congress vol. 13. International Geological Congress, Montreal, pp. 132–141.
Nichol, S.L., Hungr, O., Evans, S.G., 2002. Large-scale brittle and ductile toppling of rock slopes. Can. Geotech. J. 39, 773–788.
Pánek, T., Duras, R., 2002. The morphotectonics of the eastern marginal slope of the Ropice-range (the Moravskoslezské Beskydy Mts.). Moravian Geogr. Rep. 10, 20–27.
Pánek, T., Tábořík, P., Hradecký, J., 2007. Gravitační rozpad hřbetu Čertova Mlýna (Moravskoslezké Beskydy). Geol. Výzkumy Morav. Slezsku Roce 2006 (14), 124–129.
Pánek, T., Hradecký, J., Minár, J., Hungr, O., Dušek, R., 2009. Late Holocene catastrophic slope collapse affected by deep-seated gravitational deformation in flysch: Ropice Mountain, Czech Republic. Geomorphology 103, 414–429.
Pánek, T., Margielewski, W., Tábořík, P., Urban, J., Hradecký, J., Szura, C., 2010a. Gravitationally induced caves and other discontinuities detected by 2D electrical resistivity tomography: Case studies from the Polish Flysch Carpathians. Geomorphology 123, 165–180.
Pánek, T., Hradecký, J., Smolková, V., Šilhán, K., Minár, J., Zernitskaya, V., 2010b. The largest prehistoric landslide in northwestern Slovakia: chronological constraints of the Kykula long-runout landslide and related dammed lakes. Geomorphology 120, 233–247.
Pánek, T., Tábořík, P., Klimeš, J., Komárková, V., Hradecký, J., Šťastný, M., 2011a. Deep-seated gravitational slope deformations in the highest parts of the Czech Flysch Carpathians: Evolutionary model based on kinematic analysis, electrical imaging and trenching. Geomorphology 129, 92–112.
Pánek, T., Šilhán, K., Tábořík, P., Hradecký, J., Smolková, V., Lenart, J., Brázdil, R., Kašičková, L., Pazdur, A., 2011b. Catastrophic slope failure and its origins: Case of the May 2010 Girová Mountain long-runout rockslide (Czech Republic). Geomorphology 130, 352–364.
Pánek, T., Smolková, V., Hradecký, J., Baroň, I., Šilhán, K., 2013. Holocene reactivations of catastrophic complex flow-like landslides in the flysch Carpathians (Czech Republic/Slovakia). Quat. Res. 80, 33–46.
Pánek, T., Hartvich, F., Jankovská, V., Klimeš, J., Tábořík, P., Bubík, M., Smolková, V., Hradecký, J., 2014. Large Late Pleistocene landslides from the marginal slope of the Flysch Carpathians. Landslides 11 (6), 981–992.
Reynolds, J.M., 1997. An Introduction to Applied and Environmental Geophysics. John Wiley & Sons, Chichester (796 pp.).
Sass, O., 2006. Determination of the internal structure of alpine talus deposits using different geophysical methods (Lechtaler Alps, Austria). Geomorphology 80, 45–58.
Sass, O., Bell, R., Glade, T., 2008. Comparison of GPR, 2D-resistivity and traditional techniques for the subsurface exploration of the Öschingen landslide, Schwabian Alb (Germany). Geomorphology 93, 89–103.
Schrott, L., Sass, O., 2008. Application of field geophysics in geomorphology: advances and limitations exemplified by case studies. Geomorphology 93, 55–73.
Šilhán, K., 2010. Geoelektrické vlastnosti blokovobahenních proudů. Zprávy Geol. Výzkumech Roce 2009, 122–124 in Czech.
Słowik, M., 2012. Influence of measurement conditions on depth range and resolution of GPR images: the example of lowland valley alluvial fill (the Obra River, Poland). J. Appl. Geophys. 85, 1–14.
Suzuki, K., Higashi, S., 2001. Groundwater flow after heavy rain in landslide–slope area from 2-D inversion of resistivity monitoring data. Geophysics 66, 733–743.
Szalai, S., Szarka, L., 2008. Parameter sensitivity maps of surface geoelectric arrays. Part 1: linear arrays. Acta Geod. Geophys. Hung. 43, 419–437.
Szalai, S., Novák, A., Szarka, L., 2009. Depth of investigation and vertical resolution of surface geoelectric arrays. J. Environ. Eng. Geophys. 14, 15–23.
Tábořík, P., 2012. Use of Electrical Resistivity Tomography in the Research of Mountain Relief (Ph.D. Thesis. Ostrava (in Czech)).
Telford, W.M., Geldart, L.P., Sheriff, R.E., 1990. Applied Geophysics. 2nd edition. Cambridge University Press (792 pp.).
Zhou, W., Beck, B.F., Adams, A.L., 2002. Effective electrode array in mapping karst hazards in electrical resistivity tomography. Environ. Geol. 42, 922–928.

Příloha 7

Applicability of near-surface geophysics for the characterisation of block accumulations

Earth Surface Processes and Landforms

Duffek et al. under review

Duffek V., Táborík P., Stacke V., Mentlík P. (under review): Applicability of near-surface geophysics for the characterisation of block accumulations. Earth Surface Processes and Landforms, Manuscript ID ESP-21-0109.

Earth Surface Processes and Landforms

Applicability of near-surface geophysics for the characterisation of block accumulations

Journal:	*Earth Surface Processes and Landforms*
Manuscript ID	ESP-21-0109
Wiley - Manuscript type:	Research Article
Keywords:	Electrical resistivity tomography, Ground penetrating radar, Seismic refraction, Electromagnetic induction, Integrated interpretation, Block accumulation
Abstract:	Understanding the internal structure of specific landforms is a crucial prerequisite for determining their origin and evolution. Near-surface geophysics represents a non-invasive way of subsurface investigation, and it can be used to describe subsurface conditions, especially in protected areas. We evaluated the applicability of four different geophysical methods: electrical resistivity tomography (ERT), shallow seismic refraction (SSR), ground penetrating radar (GPR), and electromagnetic induction (EMI) to determine the internal architecture and thickness of block accumulations in the Central European Uplands. Our results indicate that SSR is probably the most applicable method for determining the thickness of block accumulation. However, this method is not highly efficient in determining the internal structure of block accumulations. ERT is conditionally suitable for such investigations because it provides information on both thickness and internal architecture of the block accumulations. On the other hand, GPR and EMI yield poor results with lower explanatory power, and, therefore, they have limited applications. Based on the integrated interpretation, we (i) estimated the thicknesses of block accumulation to be approximately 8–10 m, (ii) partially described its internal structure, and (iii) outlined the most probable genesis of block accumulations in two investigated sites. Our investigation proved that the surface manifestations of block accumulations mostly correspond to the sub-surface geophysical conditions.

SCHOLARONE™
Manuscripts

Applicability of near-surface geophysics for the characterisation of block accumulations

Václav Duffek[a,b], Petr Tábořík[c,d], Václav Stacke[b], Pavel Mentlík[b]

[a] University of Ostrava, Department of Physical Geography and Geoecology, Chittussiho 10, 710 00 Ostrava, Czech Republic

[b] University of West Bohemia, Centre of Biology, Geoscience and Environmental Education, Klatovská 51, 30619 Plzeň, Czech Republic

[c] Charles University, Institute of Hydrogeology, Engineering Geology and Applied Geophysics, Albertov 6, 128 43 Prague 2, Czech Republic

[d] Czech Academy of Sciences, Institute of Rock Structure and Mechanics, V Holešovičkách 94/41, 182 09 Prague 8, Czech Republic

Abstract

Understanding the internal structure of specific landforms is a crucial prerequisite for determining their origin and evolution. Near-surface geophysics represents a non-invasive way of subsurface investigation, and it can be used to describe subsurface conditions, especially in protected areas. We evaluated the applicability of four different geophysical methods: electrical resistivity tomography (ERT), shallow seismic refraction (SSR), ground penetrating radar (GPR), and electromagnetic induction (EMI) to determine the internal architecture and thickness of block accumulations in the Central European Uplands. Our results indicate that SSR is probably the most applicable method for determining the thickness of block accumulation. However, this method is not highly efficient in determining the internal structure of block accumulations. ERT is conditionally suitable for such investigations because it provides information on both thickness and internal architecture of the block accumulations. On the other hand, GPR and EMI yield poor results with lower explanatory power, and, therefore, they have limited applications. Based on the integrated interpretation, we (i) estimated the thicknesses of block accumulation to be approximately 8–10 m, (ii) partially described its internal

structure, and (iii) outlined the most probable genesis of block accumulations in two investigated sites. Our investigation proved that the surface manifestations of block accumulations mostly correspond to the sub-surface geophysical conditions.

Graphical abstract

Applicability of near surface geophysics in the reconstruction of internal structure and thickness of block accumulations.

Geophysical task	ERT	SSR	EMI	GPR
detection of thickness	+	++	-	+
determination of internal structure	+	+/-	+/-	+/-
How demanding the method is				
in man-power	+/-	-	+/-	-
in survey speed	-	-	+/-	+
in data processing	+	-	++	+/-
in interpretation	+	+	+/-	-

Key:
Geophysical task: ++ suitable, + suitable but with limitations, +/- suitable but with significant limitations, or modification necessary, - unsuitable
How demanding the method is: ++ undemanding, + undemanding with exceptions, +/- demanding, - very demanding

Keywords: Electrical resistivity tomography, Ground penetrating radar, Seismic refraction, Electromagnetic induction, Integrated interpretation, Block accumulation

Applicability of near-surface geophysics for the characterisation of block accumulations

Abstract

Understanding the internal structure of specific landforms is a crucial prerequisite for determining their origin and evolution. Near-surface geophysics represents a non-invasive way of subsurface investigation, and it can be used to describe subsurface conditions, especially in protected areas. We evaluated the applicability of four different geophysical methods: electrical resistivity tomography (ERT), shallow seismic refraction (SSR), ground penetrating radar (GPR), and electromagnetic induction (EMI) to determine the internal architecture and thickness of block accumulations in the Central European Uplands. Our results indicate that SSR is probably the most applicable method for determining the thickness of block accumulation. However, this method is not highly efficient in determining the internal structure of block accumulations. ERT is conditionally suitable for such investigations because it provides information on both thickness and internal architecture of the block accumulations. On the other hand, GPR and EMI yield poor results with lower explanatory power, and, therefore, they have limited applications. Based on the integrated interpretation, we (i) estimated the thicknesses of block accumulation to be approximately 8–10 m, (ii) partially described its internal structure, and (iii) outlined the most probable genesis of block accumulations in two investigated sites. Our investigation proved that the surface manifestations of block accumulations mostly correspond to the sub-surface geophysical conditions.

Graphical abstract

For Peer Review

Applicability of near surface geophysics in the reconstruction of internal structure and thickness of block accumulations.

Geophysical task	ERT	SSR	EMI	GPR
detection of thickness	+	++	-	+
determination of internal structure	+	+/-	+/-	+/-
How demanding the method is				
in man-power	+/-	-	+/-	-
in survey speed	-	-	+/-	+
in data processing	+	-	++	+/-
in interpretation	+	+	+/-	-

Key:
Geophysical task: ++ suitable, + suitable but with limitations, +/- suitable but with significant limitations, or modification necessary, - unsuitable
How demanding the method is: ++ undemanding, + undemanding with exceptions, +/- demanding, - very demanding

Keywords: Electrical resistivity tomography, Ground penetrating radar, Seismic refraction, Electromagnetic induction, Integrated interpretation, Block accumulation

1. Introduction

Block accumulations formed by rock fragments of various sizes and genesis are a significant part of mountain and periglacial geosystems. In their relict forms that usually occurs in temperate mountain regions, accumulations occur with different degrees of infilling. The study of such accumulations is important for understanding the genesis of the surveyed area. This research has significant importance for practical applications in those areas where information on the extent and thickness of the accumulations are crucial for land use.

Practically, the only non-invasive approach (in cases where drilling and digging are not possible) to investigate the above-mentioned characteristics is the use of geophysical methods. The suitability of these methods has been widely demonstrated in many geomorphological studies (e.g. Evans et al., 2000; Völkel et al., 2001; Musil et al., 2002; Gabriel et al., 2003; Otto and Sass, 2006; Kasprzak, 2015;

Hartvich et al., 2017). The general advantages and limitations of some of these methods have been summarised by Loke (2000), Musset and Khan (2000), Pelton (2005), Neal (2004), Schrott and Sass (2008), Milsom and Eriksen (2011), Słowik (2012), Tábořík et al. (2017), and Blecha et al. (2018). However, relatively few studies (Sass, 2006, 2007; Otto and Sass, 2006; Hauck and Kneisel, 2008; Schrott and Sass, 2008; and Uxa et al., 2019) have evaluated the potential of the commonly used geophysical methods for studying block accumulations. This is because both non-compact and heterogeneous structure (Rea, 2007) and the presence of a large number of air-filled voids (Schrott and Sass, 2008) limit the possible applicability of geophysics.

This study aims to evaluate the strengths and limitations of the use of selected geophysical methods in the investigation of block accumulations, including a comparison of geophysical results with the outcomes of geomorphological mapping of block accumulations based on Żurawek et al. (2005). In addition, it provides new information on the characteristics of periglacial landforms that were formed during the cold periods of the Pleistocene epoch.

Besides the very complicated conditions for undertaking geophysical surveying (such as problematic accessibility of the block accumulations due to rough terrain, impenetrable vegetation, or extreme weather conditions), there are limitations due to some inherent properties of the geophysical methods themselves (i.e. the output power of the resistivity system, power of GPR antenna, type and intensity of the seismic source, and sensitivity and resolution of the systems used).

2. Regional settings

The present study was carried out in two localities (Skalka site and Slunečná site, respectively) of the Bohemian Forest, which is a typical Central European crystalline metamorphic mountain range (Fig. 1). The Bohemian Forest stretches 125 km along the state border of Czechia and Germany. During Pleistocene, several glacial cirques and small glacial troughs were formed across the Bohemian Forest and most of the slopes were modified by glacial or periglacial processes (Hauner et al., 2019). These phenomena generated numerous scattered blocks, boulders, and block accumulations with different

For Peer Review

degrees of infilling. Such structures are commonly observed in the Bohemian Forest (Mentlík, 2016). The block accumulations observed in the studied localities differ in their (i) surface structures (infilled in Slunečná vs. open blocky surface (OBS) type in Skalka. In the latter case, the inter-block spaces are not filled with matrix), (ii) topography (lower altitude and gentler slope in Slunečná vs. higher altitude with a steeper slope in Skalka), (iii) geological composition (medium-grained porphyric biotite granite in Slunečná vs. two mica-paragneiss in Skalka), and (iv) vegetation cover (fully forested in Slunečná vs. virtually non-forested area in Skalka). The basic characteristics of the two localities are provided in Table 1 and plotted in Fig. 1. Both localities have a subarctic climate (Dfc) as defined according to the Köppen climate classification (Tolasz et al., 2007).

Mentlík (2011) performed pioneering research and geophysical investigations of block accumulations in the study area. This research introduced the first insights into the thickness of block accumulation in the Bohemian Forest using the ERT method.

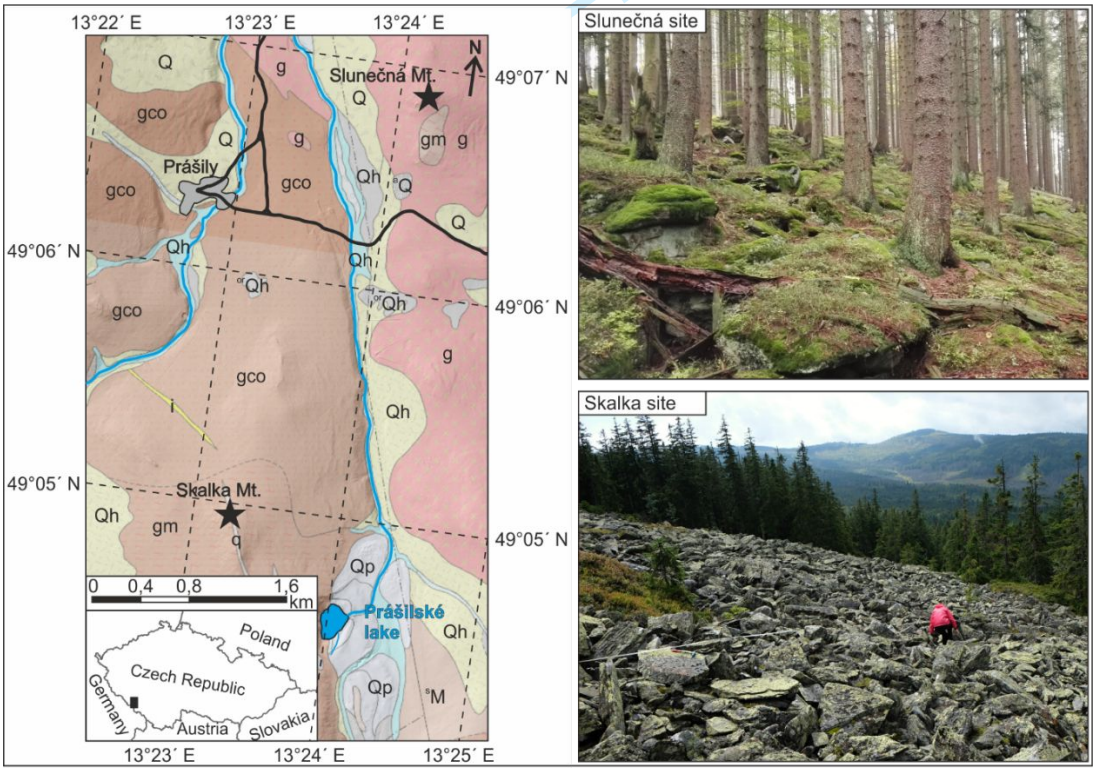


Figure 1: Location of the investigated areas and geological conditions. The key to the geological map has been simplified for the purpose of this research: Q = Sediment (Q colluvial, Qh fluvial, °ʳQh organic, °Q anthropogenic, Qp glaciogenic), gm = Paragneiss, gco = Paragneiss with garnet, g = Granite, q = Quartzite, ˢM = Biotitic migmatite, i = Aplite. Data source: Pelc and Šebesta, 1994.

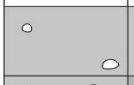
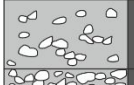
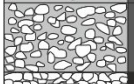
Table 1: Basic characteristics of the localities. The total area of Slunečná is the sum of the partial areas of the surveyed block accumulations.

	Characteristics					
Locality	Altitude [m a.s.l.]	Area [m^2]	Aspect	Slope [°]	Rock	Open blocky surface
Slunečná	915–935	7645.5	West	11–21	Granite	No
Skalka	1192–1218	2215	West	17–25	Paragneiss	Yes

3. Methodology

In the preparatory phase of our survey, we performed geomorphological mapping of the extent and the surficial manifestations of block accumulations using the adopted methodology by Żurawek et al. (2005). In addition to the boundaries of block accumulations, we determined the concentration of blocks as a ratio of the area covered with visible blocks to the area covered by fine-grained and/or organic debris matrix. We also investigated the clast size (given by the length of the longest axis) and the degree of filling of inter-block spaces. The individual types of block accumulations observed in the study area are summarised in Table 2.

Table 2: Types of block accumulation with a graphical representation of the block concentration per unit of surface area, colour symbology (the same as in Figs. 3, 4, 5, 6, and 7), and description of the detailed characteristics of block cover. The schematic is based on Żurawek et al. (2005).

Block concentration	Category with colour symbology	Description
	B1	Scarce blocks on slope
	B2	Scattered blocks (between blocks is 10x larger space than block diameter)
	B3	Loose block cover (between blocks is several times larger space than block diameter)
	B4	Transitional type (sometimes blocks touch each other)
	B5	Dense block cover (most blocks contact each other; vegetation still grow)
	B6	Blockfield senso stricto (blocks form open-work matrix, vegetation cannot grow)

Electrical resistivity tomography (ERT), shallow seismic refraction (SSR), ground penetrating radar (GPR), and electromagnetic induction measurement (EMI) were applied to the mapped block accumulations. Considering the spatial distribution of the blocks and/or the observed transitions between block accumulations of different characteristics, various profile orientations in the two localities were chosen to capture the most representative accumulations. The central block

For Peer Review

accumulation in Skalka was investigated along the longitudinal profile (i.e. in the direction of the greatest slope angle), and the cluster of block accumulations in Slunečná was examined along the transverse profile (i.e. along the contour line).

We employed four different geophysical techniques to obtain as much geophysical information as possible. The survey results were used to evaluate the applicability of individual methods and as input information to provide a combined interpretation based on all the methods used. These complex interpretations include (a) cross-validation of the results obtained from different methods (if possible, considering the different natures of various geophysical fields); (b) combined interpretation of the main subsurface structures of the block accumulations, which could be compared with the surficial manifestation of the accumulations; and (c) reinterpretation of previous results (Mentlík 2011) based on the combined geophysical interpretation.

The combined interpretation and subsequent evaluation of the applied methods focused on changes and contrasts in the variations of the observed physical quantities (e.g. resistivity) and their distribution. Such contrasts (especially step-like variations) could be interpreted as a manifestation of changes in the subsurface conditions. The basic parameters of the geophysical instruments and of the measurements used in this study are provided in Table 3.

*Table 3: Selected measurement parameters of the used geophysical methods. Note that the profiles of both the sites do not start or end at the same position. *Always placed at half distance between two neighbouring geophones (i.e. positions 127.5 - 133.5 - 139.5 m at Slunečná and 92.5 - 102.5 - 112.5 m at Skalka).*

		Slunečná	Skalka
ERT	Device	Automatic resistivity system - ARES	Automatic resistivity system - ARES
	Start [m]	0	0
	End [m]	315	315
	Spacing [m]	5	5
	Array	WS and Wα	WS
SSR	Device	Geode Seismic Recorder	Geode Seismic Recorder
	Start [m]	126	90
	End [m]	264	205
	Spacing [m]	3	5
	Shot-points [m]	6*	10*

For Peer Review

GPR	Device	Malå Ramac system X3M CU 100 MHz and 250 MHz	Malå Ramac system X3M CU 100 MHz and 250 MHz
	Start [m]	126	106
	End [m]	267	178
	Sampling [m]	0,2 (manual trigger)	0,2 (manual trigger)
EMI	Device	CMD-Explorer (Hi/Lo) CMD MiniExplorer (Hi/Lo)	CMD-Explorer (Hi/Lo)
	Start [m]	126	106
	End [m]	267	178
	Sampling [m], [s]	1 m (manual mode), 0.2 s (continual mode)	1 m (manual mode)

3.1 Electrical resistivity tomography (ERT)

The multi-electrode resistivity method of measurement and subsequent processing by ERT were selected as the main exploration technique in both sites. This method was especially selected because of the following reasons: (i) it has been widely used in previous studies of block accumulations with different genesis (Kneisel and Hauck, 2008; Pánek et al., 2009; Lenart et al., 2014; Raška et al., 2014; Kasprzak, 2015, Kasprzak et al., 2017; Engel et al., 2017; Stemberk et al., 2017, Strzelecki et al., 2017), (ii) it has a high resolution (Rizzo et al., 2004; Maillet et al., 2005)and (iii) large depth range (Nguyen et al., 2009; Blecha et al., 2018; Chalupa et al., 2018), as well as (iv) it processes data relatively faster (Loke and Barker, 1996; Loke, 2000). High-quality grounding is crucial to acquire reliable data (sensu Dahlin and Zhou, 2004). Therefore, in Skalka, the electrodes were grounded using sponges saturated in electrolyte (hypersaline solution) (Fig. 2A) to ensure sufficient conductive contact with the surface. This approach has been previously verified by Otto and Sass (2006) and Tábořík (2012). The ERT measurements in Skalka were carried out in 2009, and the first results were reported by Mentlík (2011), which marked the initial stage of the block accumulation research. In our study, we used the original data from 2009 and reprocessed them using a more advanced approach (i.e. using a newer version of processing Res2Dinv software and advanced data interpretation skills). The Wenner–Schlumberger (WS) electrode array was used in both sites since it gives sufficient resolution, depth range, and sensitivity to both horizontal and vertical structures. It is also robust toward geoelectrical noise (Loke, 2000; Zhou et al., 2002; Szalai and Szarka, 2008; Szalai et al., 2009.). In Slunečná, we also used the Wenner alpha (Wα) electrode configuration, which, due to its lower sensitivity, possess higher

For Peer Review

136 robustness to noise (Loke, 2000; Zhou et al., 2002). Stacking and standard deviation were applied to
137 improve data quality. Basic information on the measurement geometry is summarised in Table 3.

138 The data measured in both localities were processed using Res2Dinv tomographic inversion software,
139 and topographic corrections were applied. Data from both arrays (WS and Wα) were inverted, and a
140 joint inversion model was used. We applied both standard (L2 norm) and robust (L1 norm) inversions
141 (Loke, 2019). However, models using robust blocks did not deliver satisfactory explanatory power.
142 Therefore, we further interpreted the standard inversion models. Damping factor values (Sasaki, 1992;
143 Loke et al., 2015a, 2015b; Chalupa et al., 2018) were optimised to suppress the effect of the
144 heterogeneity of the block fields within inverse resistivity models.

145 **3.2 Shallow seismic refraction (SSR)**
146 SSR measurements are generally used to evaluate the elastic properties of block accumulations
147 (Gabriel et al., 2003; Schrott et al., 2003; Schrott and Hoffmann, 2008; Schrott and Sass, 2008; Valenta
148 and Dohnal, 2007). In this study, geophones with a frequency of 10 Hz were used to measure the SSR.
149 The source of the seismic signal was an 8 kg sledge hammer (Fig. 2G) and a metal pad, which were
150 used to determine the initial time t_0. Distant shotpoints and signal summing were used in both
151 locations to acquire better quality data. Data were processed using the plus–minus method
152 (Hagedoorn, 1959) and seismic tomography (Nolet, 2008; Valenta and Dohnal, 2007). The picking of
153 the first arrival times (OYO Pickwin) was further adjusted by a reciprocal time check (OYO Plotrefa).
154 Seismic tomography (ST) in the Rayfract program was used to create a layered and a gradient model.
155 However, both models yielded similar results. As determining the thickness of block accumulations
156 was one of the main goals of the study, we preferred layered models. Topography corrections were
157 introduced in all models.

158 **3.3 Ground penetrating radar (GPR)**
159 GPR was employed as the wave method, and electromagnetic signals were used to reveal the possible
160 depth and internal structures of the block accumulation (Davis and Annan, 1989; Neal, 2004; Sass and
161 Wollny, 2001; Berthling and Melvold, 2008; Sass O., 2008; Słowik, 2012, Campbell et al., 2018). In both

For Peer Review

locations, measurements were performed using the Malå Ramac system geological radar with X3M control unit and shielded antennas of 250 and 100 MHz. The use of shielded antennas was important in Slunečná, which is forested. The trigger wheel or time-mode trigger could not have been used owing to the extreme conditions of block accumulations, which caused continuous motion with constant velocity impossible. Therefore, a 20 cm manual trigger was used in all cases (Figs. 2C and 2D). The measured data from both locations were processed using ReflexW 6.0 software (Sandmeier software). The topography of the environment was introduced into all GPR sections. The EM wave propagation velocity of 0.09 $m*ns^{-1}$ was used based on the assumption of non-homogeneous unsaturated stacking of loose blocks with predominantly air-filled inter-block voids (van Overmeeren 1998; Völkel, 2001; Neal, 2004). The radargrams were processed using the following processing sequence: (1) Resorting – X-Flip Profile (due to extremely difficult operation with antennas and to save time, some profiles were measured in a reversed way), (2) Static corrections – move start-time (first arrival time adjustment), (3) 1-D Filter – subtract mean (dewow), (4) 2-D filter – background removal; (5a) Gain – energy decay and (5b) Gain – Y-manual gain (in a vertical direction), (6) 2-D filter – running average, and (7) Topographic migrations. In some cases, topographic migrations provide more continuous reflections and, thus, its interpretations are mostly unambiguous (Neal, 2004).

3.4 Electromagnetic induction (EMI)

EMI measurements were carried out to obtain information on the conductive and/or resistive properties of block accumulations (Evans et al., 2000; Hauck et al., 2001; Gabriel et al. 2003; Hördt and Hauck, 2008; Dobinski et al., 2008). In contrast to the ERT, EMI measurements do not require coupling with the subsurface using metal electrodes. The device uses contactless measurements based on the principle of EM induction (McNeill, 1980; Andrade and Fischer, 2018). We utilised a CMD Explorer conductivity meter (GF Instruments, Brno), which allowed us to take measurements in two different regimes, i.e. both vertical and horizontal orientations of the measuring dipole coil axes with different calibrated penetration depths (measuring position “Hi” refers to vertical orientation and a full depth range and “Lo” refers to horizontal orientation and a half depth range). In Slunečná, we also used a

For Peer Review

different conductivity probe CMD MiniExplorer (GF Instruments, Brno), which is designed for more detailed survey. Owing to the heterogeneity of the examined environment and the expected high variance of the measured values, manual data collection (sampled at 1 m intervals) was used in both localities (Figs. 2E and 2F) to obtain more accurate results with direct control on data quality based on the measured standard deviation (σ) of up to 5%. Owing to the more accessible nature of the terrain, continuous data collection was also applied at the Slunečná site for experiments. The apparent resistivity values were measured at the following depth levels (Explorer – Hi: -2.2, -4.2, and -6.7 m, Lo: -1.1, -2.1, and -3.3 m; MiniExplorer – Hi: -0.5, -1.0, and -1.8 m, Lo: -0.25, -0.5, and -0.9 m) calibrated by the manufacturer. The resultant apparent resistivity curves for individual coil dipoles with both horizontal and vertical orientations of the coil axes were graphically processed using Grapher 9 (Golden Software).

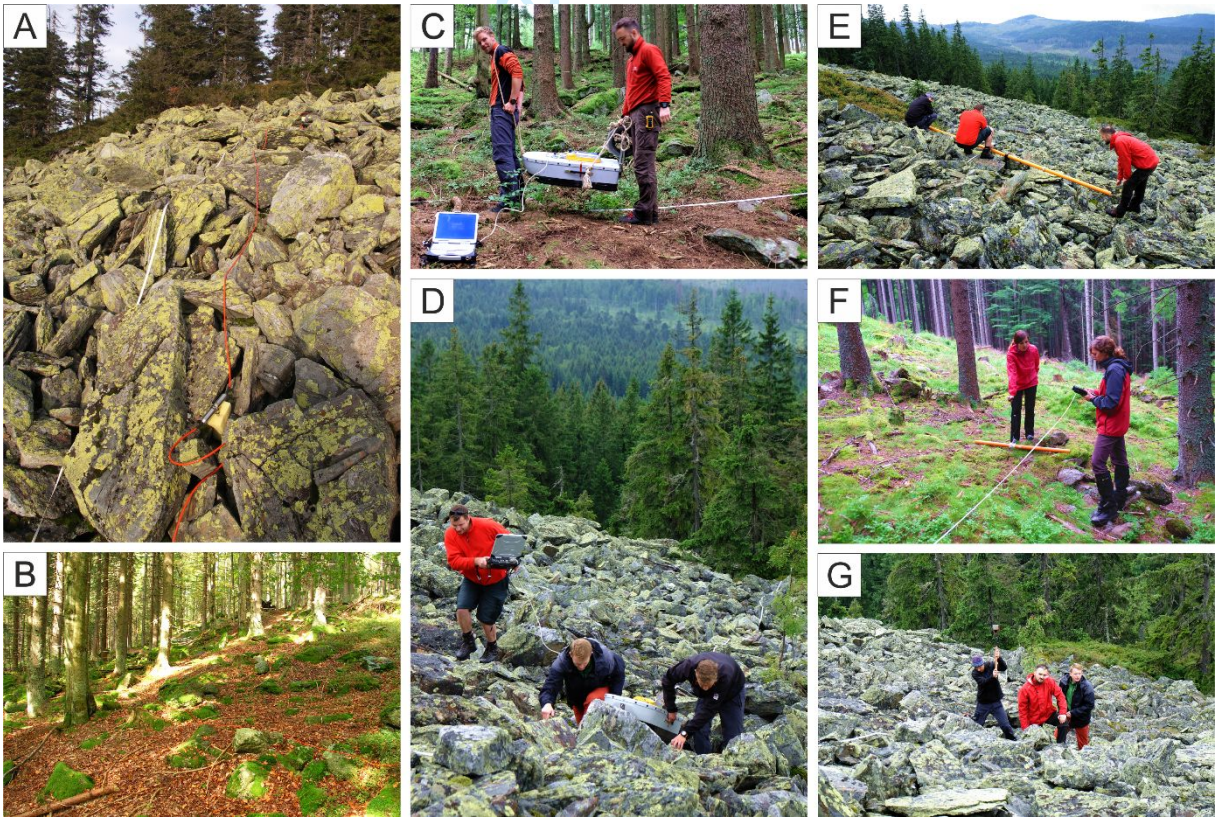


Figure 2: Various geophysical methods ERT (A, B), GPR (C, D), EMI (E, F), and SSR (G) used for studying the central block accumulation in Skalka (A, D, E, G) and block accumulations in Slunečná (B, C, F).

4. Results and interpretations

4.1 Slunečná locality

Block accumulations with different characteristics were delineated through geomorphological mapping of the block accumulation clusters in the Slunečná locality (Fig. 3). Most of the accumulations were less dense (type B1, B2, and B3, where blocks were not in a visible contact with each other), except for a single dense accumulation (situated in 228–265 m, Fig. 4A), where blocks were in contact with each other – type B5 (sensu Żurawek et al., 2005). All accumulations were mostly composed of blocks with the longest axis of up to 1 m, with sparsely incorporated larger and smaller blocks. The spaces between the blocks were all filled with finer matrix.

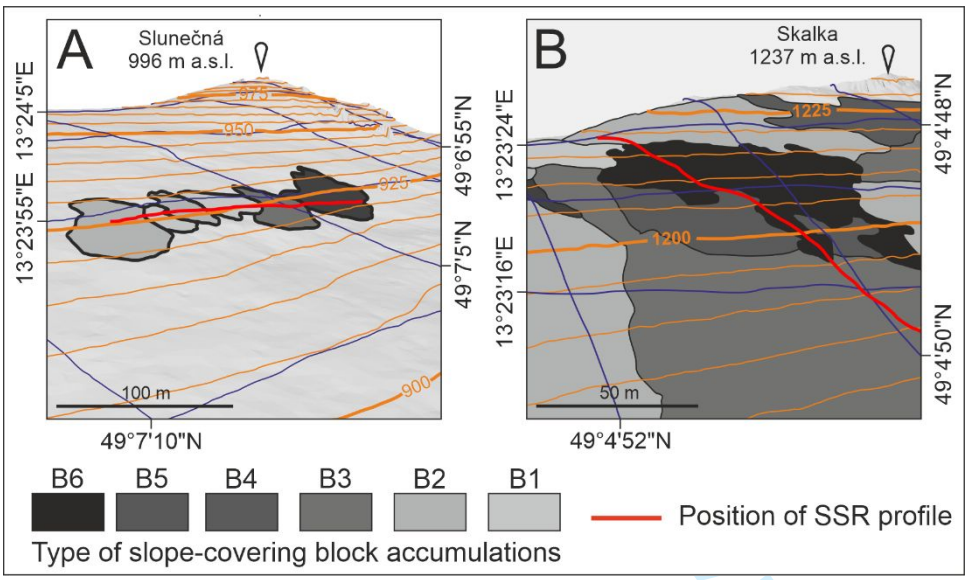


Figure 3: Location of block accumulations at the Slunečná (A) and Skalka (B) sites. The types of block accumulations and position of the geophysical profile are shown. For block accumulation types description, see Table 2. The surroundings of the mapped block accumulations at the Slunečná site are formed of a mixture of scattered islets of B1 and B2 block accumulation types.

The integration of the WS and Wα electrode configurations in the ERT resulted in a high-definition model of the subsurface resistivity distribution (Fig. 4B). This model shows an increase in the thickness of high-resistive bodies (resistivity from 6 to 28 kΩ m), with the thickness in the first half of the profile (0–195 m) reaching a maximum of 7 m. The maximum thickness in the second half (195–270 m) of the profile was 9 m. This pattern was interrupted several times in the uppermost layer (at 200–205, 245–250, and 270 m) with significantly lower resistivity (varying from 5 to 6 kΩ m). The greater thickness of high-resistive bodies in the second half of the ERT profile most likely reflects an increase in the thickness of the block accumulations. Similarly, bodies with very high resistivities (over 20 kΩ m) may indicate areas with higher block concentrations (accumulations with air-filled inter-block spaces, i.e.

225 B5 category) compared to the bodies with lower resistivities (ca. 6–20 kΩ m). The later likely represent
226 block accumulations with smaller blocks whose inter-block spaces are filled with fine-grained matrix.
227 At a depth of ca. 7 m lies conductive band, which is characterised by low resistivities (< 6 kΩ m); the
228 minimum resistivity is < 1 kΩ m) at a depth of ca. 12 m. At a position of approximately 200 m, there is
229 a zone of relatively higher resistivities (ranging from 3 to 4 kΩ m) that interrupts the low resistive
230 environment of the second layer. An environment with the lowest resistivities (< 6 kΩ m) underlying
231 the layer of higher-resistivity bodies probably corresponds to the disrupted (likely weathered) parent
232 rocks (sensu Ballantyne, 1998). The relatively higher resistivity (3–10 kΩ m) at a depth of approximately
233 15 m, which forms the third layer, most likely corresponds to intact rock.

234 The seismic model consists of three layers. The solid white lines in Fig. 4C represent two subsurface
235 refraction boundaries detected by the SSR plus–minus method (Hagedoorn, 1959). The first interface
236 within the inverse seismic velocity model is partially copied by an isoline of 2000 $m.s^{-1}$ at an average
237 depth of 7 m. The second interface is partially copied with isolines of 5000 $m.s^{-1}$. In parts of the profile
238 between 150 and 220 m, and between 180 and 250 m, the 2000 $m.s^{-1}$ and 5000 $m.s^{-1}$ isolines drop to
239 greater depths. This shift in isolines to varying depth may be caused by the selective weathering of
240 bedrock in these zones (sensu Bustin and Mathews, 1979; Pye, 1985; Hill, 1996). The first (uppermost)
241 layer with a constant thickness was delineated by isolines of approximately 2000 $m.s^{-1}$. The second
242 layer was delineated by isolines of 2000 and 5000 $m.s^{-1}$. The thickness of the second (middle) layer was
243 found to change along the profile when the isolines of 5000 $m.s^{-1}$ drops to a depth of 180 and 250 m.
244 The third (bottom) layer was bounded by an isoline of 5000 $m.s^{-1}$, which corresponds to the seismic
245 wave propagation velocity in intact granites (Telford et al., 1990; Barton, 2007; Whiteley and Stewart,
246 2008; Albers, 2011; or Reynolds, 2011).

247 Two depth profiles of the subsurface environment were measured by GPR using antennas with f = 100
248 MHz and 250 MHz, respectively. The 100 MHz antenna exhibited a higher penetration depth with
249 almost the same resolution as the 250 MHz antenna. Therefore, we have reported data obtained only

For Peer Review

from the aforementioned antenna. We achieved a penetration depth of approximately 6–9 m, with a modal value of 7 m, which corresponds to the assumed overall thickness of the block accumulation (Fig. 4D). In the resulting radargrams, it was relatively difficult to detect any unequivocal interface or significant changes in the subsurface environment, except for a structure that could be related to the infilled shallow depression (at approximately 215 m). In some places, the reflections reached deeper, i.e. at depths of 195, 220, and 255 m, which might indicate pockets of thicker debris (Fig. 4D). The absence of interpretable reflection boundaries (but not a lack of reflections) is further discussed in the following sections.

We used EMI measurements to construct the apparent resistivity curves. The curves were scattered, and the measured values were highly variable (ranging from 200 to 1100 Ω m). The variations in values obtained using CMD Mini Explorer conductivity meter were even more pronounced, and the measured values often dropped to negative values. The best quality results were obtained by CMD Explorer conductivity meter with vertical coil setting (Hi position) in the manual measurement mode (Fig. 4E). Measurements in continuous mode did not yield better results, and the data obtained were mostly scattered with significantly lower explanatory power. Despite that EMI measurements offered significantly low interpretation ability, the dataset obtained by CMD Explorer using the Hi/manual measurement mode provided limited information on block accumulations. The curves in Fig. 4E represent the calibrated depth values of apparent resistivity. The rapid changes in the trend of curve with a prominent change in the scattered value were observed at the positions 200 and 205 m (with depth of -2.2 m and 6.7 m, respectively). They were smoother in the 120–200 (205) m section and were more variable in the second half of the profile. This is likely caused by the rapidly changing thickness of the block accumulation. Consequently, this increase in thickness can be observed as an abrupt change in the scatter of the EMI curve.

For Peer Review

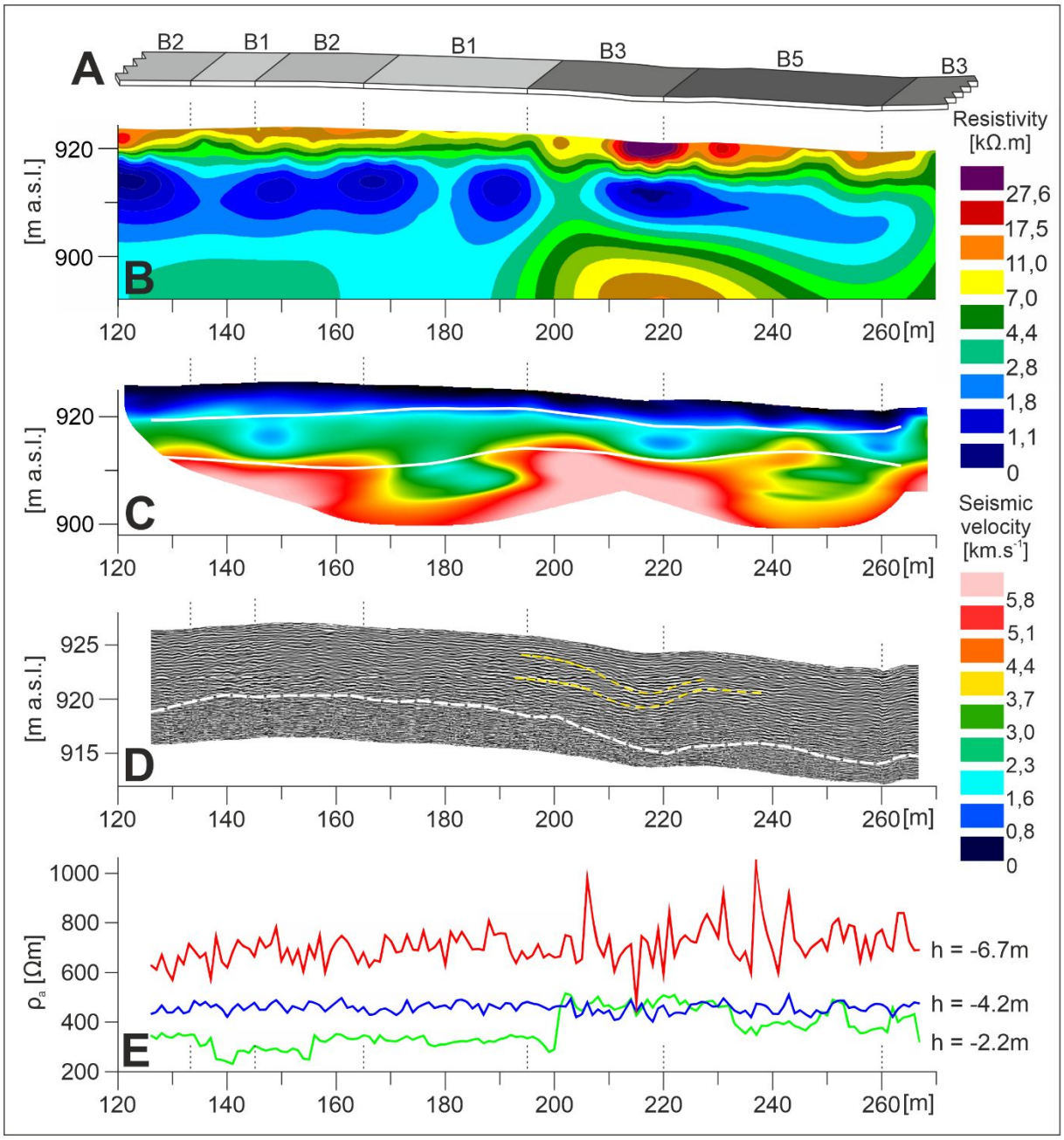


Figure 4: Results of the survey in the Slunečná locality. A) Types of block accumulation (modified after Żurawek et al. 2005) along the geophysical profile, black dashed lines in ERT and SSR models, radargram and EMI curves denote the boundary between different types of block accumulation. B) ERT subsurface resistivity distribution model (5th iteration standard inversion, RMS error 2.1). C) Subsurface contour model of seismic velocities with first and second interfaces derived from Hagedoorn's plus–minus method (solid white lines). D) Radargram (vertical exaggeration: two times) obtained by GPR (f = 100 MHz) with a significant reflector (yellow dashed line) and maximum effective penetration depth (white dashed line). E) Apparent resistivity depth curves obtained by EMI (CMD Explorer, Hi).

4.2 Skalka locality

In Skalka, the surficial characteristics of the clusters of block accumulations were determined by geomorphological mapping (Figs. 3 and 5A). Block concentration of the central accumulation was found to be very high when the blocks were in contact with each other (i.e. category B6 (Żurawek et al. 2005)) and the inter-block voids were not filled with the matrix (Fig. 2). We found blocks with the

longest axis of ~1 m, sparsely distributed smaller blocks (tens of centimetres), and/or larger blocks (up to 2 m) on the surface of the central accumulation.

The results of ERT measurements in Skalka demonstrate the presence of several extremely high-resistive bodies (resistivity varying from 75 to 102 kΩ m) on the surface and in the uppermost layer of the profile (below the surface) (Fig. 5B). Their occurrences are mainly linked to the upslope parts of the profile. Along the downslope part of the profile, the resistivity of the uppermost layer generally decreases. However, approximately in the third quarter of the profile (i.e. at 165 m), there is another extremely high-resistive body (from 75 to 102 kΩ m). There is a relatively lower resistivity environment (from 5 to 30 kΩ m) under the layer of these bodies (approximately 20 m deep). The high-resistivity bodies in the resistivity model (at approximately 100, 115, 130, and 165 m) most likely correspond to the stacking of blocks with large air-filled voids. The occurrence of lower resistivities at depths of up to 5 m (at approximately 120 m and from 140 m to 160 m) most likely correspond to areas where the inter-block spaces are filled with a fine-grained matrix. A sudden increase in subsurface resistivity at 95 m probably indicates the upslope limit of block accumulation, whereas the sharp reduction in resistivity at 175 m marks its downslope limit.

The seismic velocity isolines shown in the tomographic inverse section (Fig. 5C) follow the slope topography, except for the upper half of the profile where they fall to greater depths. Based on the plus–minus method (Hagedoorn, 1959), a single interface was found that copies the slope topography along the entire profile at depths of 8–10 m. This observation points to very low variability in the thickness of block accumulation and a double-layered environment. This refraction boundary follows an isoline of 2500 $m.s^{-1}$, which does not correspond to higher propagation velocity (> 4500 $m.s^{-1}$) of seismic waves in intact gneisses (Telford et al., 1990; Barton, 2007; Whiteley and Stewart, 2008; Albers, 2011; or Reynolds, 2011). Therefore, we can infer that this interface at a depth of 8–10 m marks the base of block accumulation that overlies the layer of disrupted bedrock with relatively lower seismic velocity values. It is noted that the interface does not mark direct contact of the block accumulation

For Peer Review

311 with an intact rock. The total thickness of the accumulation and disruption zone were delineated by an
312 isoline of 4500 $m.s^{-1}$, which corresponds to the velocity of propagation in the intact gneiss (Barton,
313 2007). This thickness varies greatly over the course of the profile, exceeding 15 m at the deepest point
314 in the first half of the profile. In this position, we identified a probable interjacent layer of disrupted
315 (e.g. by tectonics and frost shattering) and likely weathered parent rock, which is represented by lower
316 seismic velocities in the seismic tomography model.

317 Similar to the Slunečná site, we have presented the GPR results of Skalka sites that were obtained by
318 100 MHz antenna (note that the 250 MHz antenna did not reach a sufficient depth). Our results (Fig.
319 5D) indicated similar depths with a narrow range between 6–9 m. However, the depth was
320 approximately 7 m in majority of the profile. This is in accordance with the commonly accepted values
321 of the effective depth range for a 100 MHz antenna, i.e. 6–7 m (e.g. Słowik, 2012). Furthermore, the
322 reflections completely disappeared at greater depths, probably due to the loss of energy. As we
323 reached the limits of the used antenna, we can only presume that we have reached the lower margin
324 of the investigated block field. No major reflecting interfaces, indicating the presence of a possible
325 internal architecture (e.g. layering), were not found in the sections. We found areas with stronger and
326 weaker reflections in the radargram attained by the 100 MHz antenna after processing raw data (at
327 approximately 140 and 160 m for the former, and at approximately 120 m for the latter).

328 The apparent resistivity curves for the two coil orientations and for all depth ranges were constructed
329 based on the EMI measurements. Despite the chosen approach of measurement (i.e. manual data
330 acquisition), the measured values were highly variable (ranging from 400 to 1600 Ω m). The CMD
331 Explorer conductivity meter provides the best quality data, and a common trend could be interpreted
332 from the curves acquired from its vertical coil orientation setting (Hi position). The curves acquired
333 from similar depths using two different coil orientations (i.e. Lo (black) and Hi (green) in Fig. 5E) did
334 not show similar values of the apparent resistivities when mutually compared. An interpretation of the

For Peer Review

variable EMI curves, including a comparison with the results of other methods, is further discussed in the subsequent section.

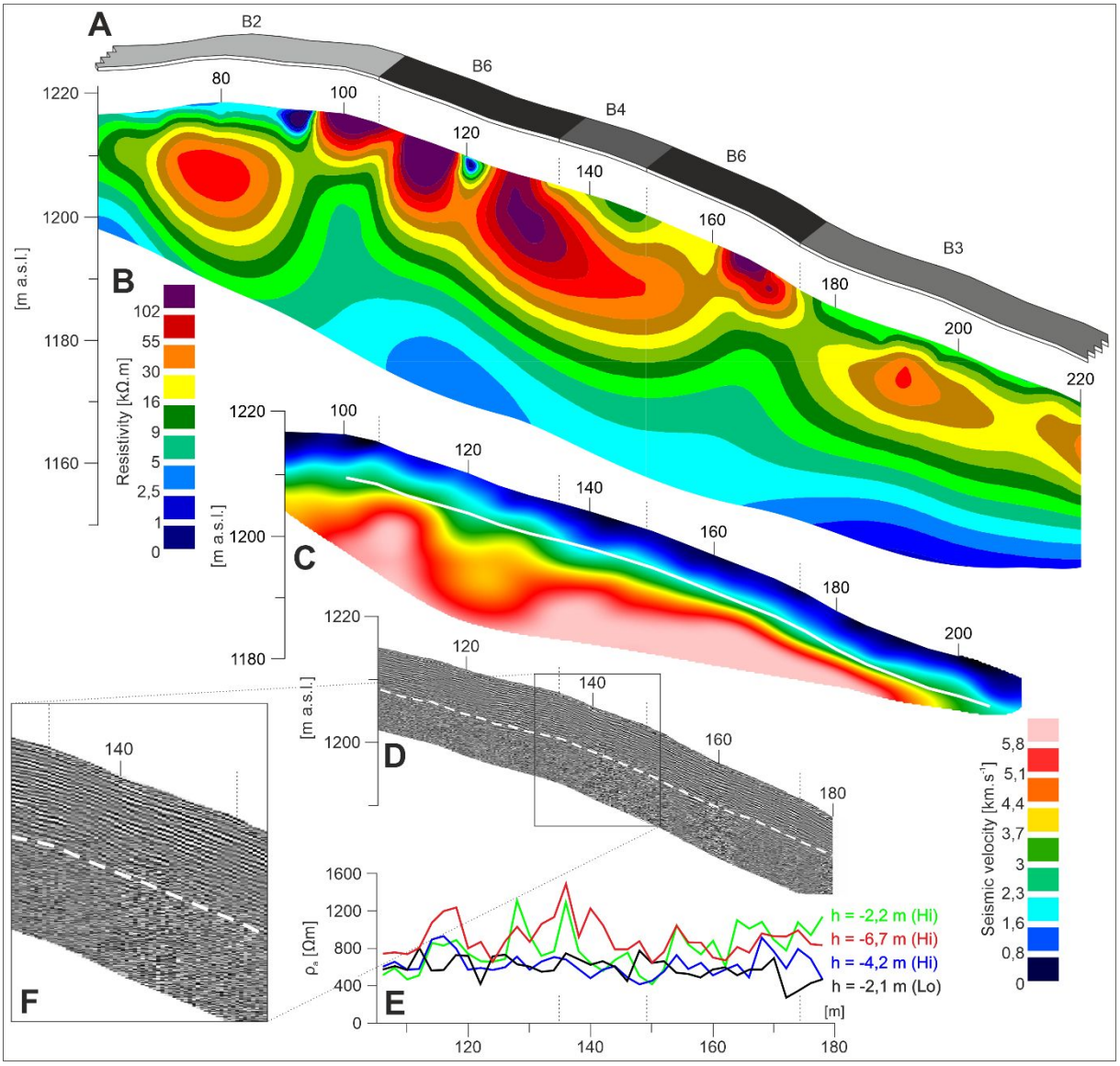


Figure 5: Results of survey in the Skalka area. A) Different types of block accumulation (Żurawek et al. 2005) along the geophysical profile, black dashed lines in ERT and SSR models radargrams and EMI curves denote the boundary between different types of block accumulation. B) Model of subsurface distribution of the resistivity obtained by ERT (5th iteration standard inversion, RMS error 5.8). C) Contour model of seismic velocities below the surface with the first interface from plus–minus method (solid white line). D) Radargram obtained using GPR (f = 100 MHz) with maximum effective penetration depth (white dashed line). E) Depth curves of apparent resistivity obtained by EMI (CMD Explorer Lo – black curve and Hi – remaining curves). Note that the curves of nearly identical depths do not follow the same trend and tend to go against each other. F) Detailed segment of radargram where B6 block accumulation changes into B4 and vice versa.

5. Discussion

5.1 Architecture and genesis of block accumulations

We reconstructed the internal structure and accumulation thickness in the two studied localities mostly on the basis of the data obtained from the SSR and ERT surveys. This is because the EMI and

GPR methods provided ambiguous results possibly due to insufficient penetration depth of GPR and sometimes extremely scattered EMI curves. The EMI results only confirmed some of the outputs of the ERT model. The thickness of the block accumulations ranged from 7 to 9 m. In the integrated geological model (Figs. 6 and 7) obtained by the synthesis of ERT and SSR interpretations, the surface of unweathered parent rock was determined as the second velocity boundary as derived from the Hagedoorn's plus–minus method (Hagedoorn, 1959; van Overmeeren, 2001) at Slunečná and the isoline of 4500 $m.s^{-1}$ in the seismic velocity model of Skalka. This approach suggests that the overall depth of the block accumulations with the eluvium ranged from 10 to 15 m in Slunečná and from 8 to 20 m in Skalka. The individual types of block accumulation (Żurawek et al. 2005) were interpreted in a vertical section, and the internal architecture of the block accumulation was outlined based solely on the ERT results.

The integrated geological model of the Slunečná site (Fig. 6) shows that the results of the geophysical survey agrees well with the results of geomorphological mapping, except for the area from 240 to 260 m, where a discrepancy between the mapped surficial accumulations of B5 and relatively lower resistivity subsurface bodies can be observed.

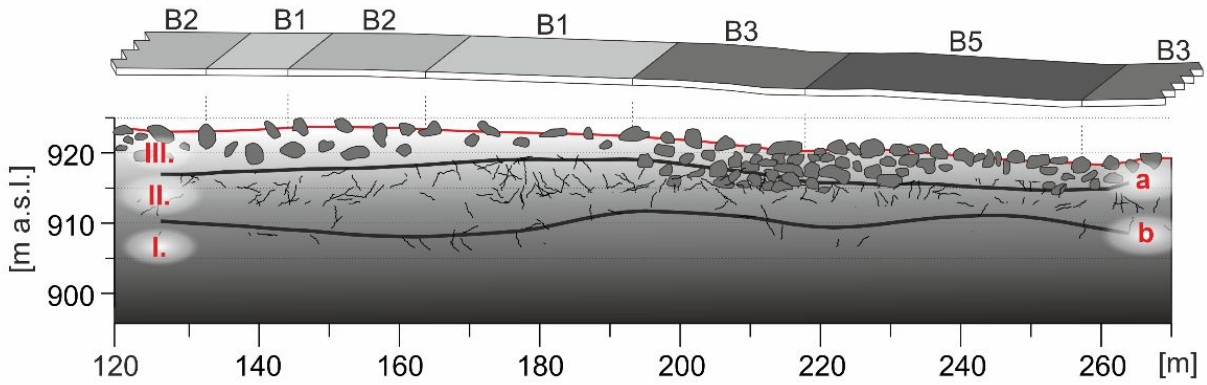


Figure 6: Integrated geological model of the Slunečná site interpreting the subsurface conditions and particular types of block accumulations along the geophysical profile. Red indexes reflect the following: I. = body of parent rock; II. = the most probable body of the disturbed parent rock; III. = body of block accumulation; a, b – seismic refraction boundaries derived from the plus–minus method (Hagedoorn, 1959). Results obtained by processing our data collected in 2017.

The integrated geological model reconstructed for Skalka (Fig. 7) shows that the sub-surficial extent of the block accumulation determined by the geophysical survey does not fully correspond to its surficial manifestation found by geomorphological mapping. The accumulation emerges at 106 m in the profile

and submerges at 176 m. The geophysical survey indicated the presence of a block accumulation at 95 m. The discrepancy in these results indicated the presence of a well-developed block accumulation covered by soil, with no surficial manifestation. Such outcomes confirm the importance of integrated interpretations and cross-validation of geophysical and geomorphological methods.

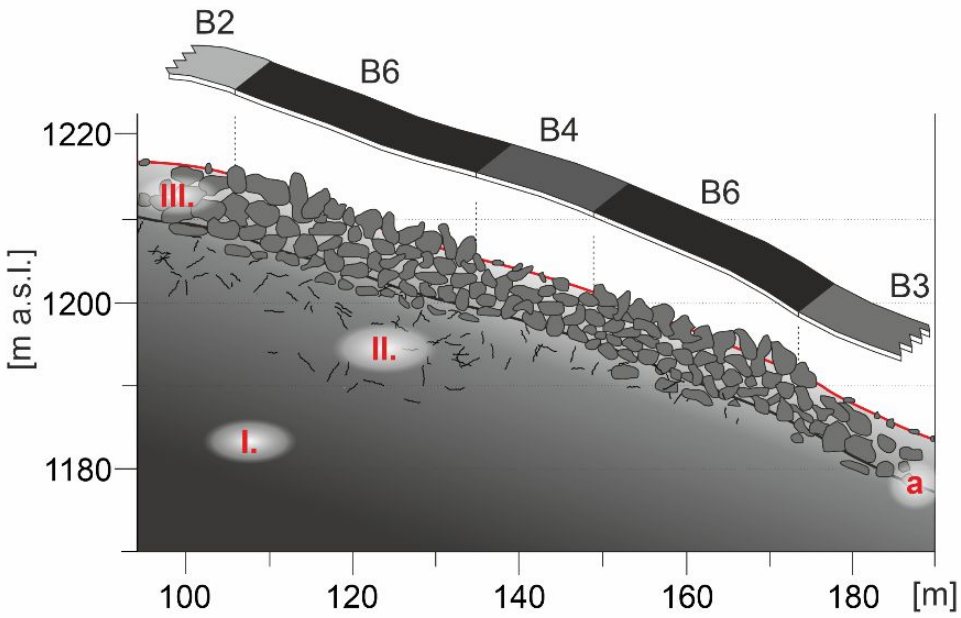


Figure 7: Integrated geological model of the Skalka site interpreting the subsurface conditions and particular types of block accumulations along the geophysical profile. Red indexes show the following: I. = body of parent rock; II. = the most probable body of disturbed parent rock; III. = body of block accumulation; a – seismic refraction boundary derived from the plus–minus method (Hagedoorn, 1959). Results obtained by processing our own data collected in 2017.

In both sites, we detected low resistivity zones (i.e. the entire middle layer in Slunečná and multiple low resistivity zones in Skalka) under the investigated high resistivity block accumulations (bodies of disrupted parent rock in Figs. 6 and 7). The low resistivity bodies in both localities do not completely match the upper or middle layers with respect to periglacial cover beds (Völkel et al., 1995; Semmel and Terhorst, 2010). According to this concept, the uppermost and middle layers were sedimented in periglacial conditions during the late glacial period (Hülle et al., 2009) and consisted of fine-grained allochthonous materials such as loess and silt (Völkel et al., 2002). If the low resistivity layer represents one of the layers of cover bed, the origin of the uppermost block accumulations (visible as surficial block concentrations and represented by high resistivity bodies in the ERT section) has to be explained by different processes (e.g. large mass movements). Such accumulations had to be of relatively younger age and had moved fast to cover the entire area during the Holocene. However,

393 geomorphological mapping did not detect any evidence of such processes in both localities. Moreover,
394 the occurrence of large and fast mass movements is very unlikely in the Bohemian Forest Mts. during
395 Holocene climatic conditions.

396 Although part of the Bohemian Massif was glaciated during the last ice age, we do not favour the
397 hypothesis of glaciogenic sediment occurrence (sensu Engel et al., 2017) because the site is located far
398 from the hypothetical extent of the nearest paleoglaciers (Mentlík et al., 2011; Hauner et al., 2019).
399 The lower resistivities might be also caused by stagnant seepage water (Mentlík et al., 2010;
400 Colombero et al., 2014). Considering the position of the block accumulations at approximately 70 m
401 above the valley floor on the Slunečná slope, and its position almost on a high plateau without any
402 peat bog and a high slope angle (reaching 25°) in Skalka, we do not favour such an interpretation.

403 The refraction boundaries modelled by the plus–minus method point to a three-layered environment
404 for the Slunečná site and predominantly two-layered environment for the Skalka site, respectively, was
405 found to be in accordance with the ERT models. Considering that the seismic velocities represent the
406 middle layer (especially in Slunečná), we rather declined the above-mentioned hypotheses on
407 periglacial cover beds or glaciogenic sediment occurrence from a geophysical perspective. The
408 measured velocities in both sites (over 2500 $m.s^{-1}$) do not match either with the velocities of 300–600
409 $m.s^{-1}$ (Rinaldi et al., 1998; Reynolds, 2011; Wang et al., 2012) anticipated for fine-grained aeolian
410 sediments (e.g. silt, loess, and aeolian sand) or with the typical velocities of glaciogenic sediments (i.e.
411 till) with < 2500 $m.s^{-1}$ (Sheriff and Geldard, 1995; Sharma, 1997; Barton, 2007; Reynolds, 2011). These
412 values are significantly lower than the measured velocities in both the studied localities.

413 In summary, we do not consider the theories on periglacial cover beds or glaciogenic sediment
414 occurrence relevant for the interpretation of genesis of the study site in terms of the regional
415 geological and climatic conditions during the Holocene. Furthermore, the results of the geophysical
416 (seismic) survey deny such theories. Thus, we consider an autochthonous periglacial explanation of

For Peer Review

block accumulations origin (Ballantyne, 1998) with possible solifluction remodelling the uppermost metres only.

5.2 Evaluation of the applicability of geophysical methods

Analysis of the results showed that the applied methods generated data with variable quality. During the evaluation of their applicability, we considered the quality of the obtained data and considered the main difficulties of their acquisition, i.e. geophone and electrode placement, extremely difficult motion, and manipulation with the EMI probe or GPR antennas. Based on our outputs, we can state that i) the SSR method is suitable for block accumulation research (similar to Schrott and Sass, 2008), ii) the usage of ERT method is "conditional" depending on the quality of electrode grounding, and iii) contactless EMI can be conditionally utilised but with considerable limitations. We recommend that EMI should be used as a complementary method. Finally, the GPR method would be the most suitable to determine the thickness of block accumulation; when uses low frequency (e.g. 20–30 MHz) antennas to achieve a greater maximum penetration depth (Sass, 2008).

ERT

In both sites, ERT measurements indicated the probable thickness of the block accumulations as well as some interfaces among them. The penetration depth reported by Loke (2000) was achieved in both sites. However, the ERT method is not fully suitable for determining the exact thickness of the block accumulation separately as exemplified by investigation of Mentlík (2011) who provided interpretations based solely on the ERT. Such inaccurate interpretations are most likely a result of overestimated thickness of the superficial layer caused by decreasing resolution and sensitivity at larger depths and associated interpolations (Otto and Sass, 2006; Kiflu et al.; 2016, Loke, 2019). This confirms that the comprehensive approach presented by Sass (2007) and Schrott and Sass (2008) provided results with lesser uncertainty. We confirmed the difficulty of good grounding of the electrodes on the OBS type of block accumulation, as previously mentioned by Tábořík (2012). A mere preparation for geophysical profiling, especially ensuring sufficient grounding of the electrodes required 5 hours in Skalka. A similar time was reported by Otto and Sass (2006) when applied to a talus

For Peer Review

443 cone. We can also confirm that on the sparser block accumulations with inter-block spaces filled with
444 more conductive material, the method better determined the depth, as proposed by Schrott and Sass
445 (2008). The authors are aware that a shorter electrode step would result in a more detail output with
446 higher resolution, and the resulting model and its interpretation could be more accurate (as advised
447 by e.g. Schrott and Sass, 2008).

448 **SSR**
449 The SSR method supplemented and adjusted the interpretations of resistivity tomography in both
450 sites, especially for the correction of the subsurface interface depth. In Slunečná, the thickness of the
451 block accumulations determined based on the plus–minus method was approximately 7 m, which is
452 slightly lesser than the thickness value determined by ERT. Otto and Sass (2006) and Sass (2007) also
453 reported that the SSR method can accurately detect the first interface at a shallower depth compared
454 to ERT.

455 In Skalka, the maximum thickness of the highly resistive bodies was previously estimated to be 20 m,
456 which was interpreted as block accumulation layer (Mentlík, 2011). However, this thickness was
457 subsequently reduced to only 8 m based on our SSR results, specifically from the first refraction
458 boundary captured by the plus–minus method (Hagedoorn, 1959). This refraction boundary is
459 approximately followed by the 2500 $m.s^{-1}$ isoline. However, such seismic velocity does not correspond
460 to the velocity of the intact parent rock. We assumed that the intact rock surface might be
461 characterised by 4500 $m.s^{-1}$ isoline (Telford et al., 1990; Barton, 2007; Whiteley and Stewart, 2008;
462 Reynolds, 2011), and the interjacent layer could likely represent the form of a heavily disrupted parent
463 rock. The applied correction was based on the ability to detect changes in the elastic parameters of
464 the bedrock in SSR compared to ERT (Barton, 2007).

465 In Slunečná, the thickness of surface layer modelled by the plus–minus method was found to roughly
466 correspond to the thickness of block accumulations reconstructed by the ERT method. Similarly, the
467 second interface modelled by the plus–minus method corresponded to a certain increase in the

For Peer Review

resistivity of the subsurface environment compared to the interjacent middle layer, which could be characterised by an intact rock (e.g. Beauvais et al., 2003; Chambers et al., 2012).

Paradoxically, we achieved better results in Skalka, which is formed of larger loose blocks. In the vegetated sparse block accumulation with a loamy matrix in Slunečná, the seismic waves in the substrate appeared to be poorly transmitted, and the energy induced by the seismic hammer was attenuated since the beginning (sensu Pelton, 2005). In the shallow refraction seismic method, it is necessary to repeat the impulse at individual spots several times, which requires long measurement time and demanding manpower (as reported by Schrott and Sass, 2008; Otto and Sass, 2006).

GPR

GPR did not provide any easily interpretable data on the internal architecture of the studied block accumulations. Even though we could observe strong reflections in the radargram, the investigated environment was too heterogeneous, and the inner structure (formed of loose blocks) was rather highly disordered (chaotic) for any anticipation of continuous reflecting interfaces (its graphical interpretation is provided in Fig. 8). Therefore, it was not possible to accurately identify the assumed interfaces between the block accumulations and the underlying bedrock, as confirmed by other methods. Furthermore, the probable energy loss and attenuation of the residual signal at the depth of the assumed bedrock surface played a significant role in not allowing the reliable determination of accumulation thickness (Słowik, 2012; Mustasaar, 2012). Similar problems were noted by Bruno and Martillier (2000) in a landslide environment. Nevertheless, we could find areas with noticeably stronger (at ca. 140 and 160 m) and weaker reflections (at ca. 120 m) in the GPR section of Skalka. The zone of weaker reflections was found to correspond with the sharply delineated low resistivity anomaly in the ERT section, as well as with a rapid drop in the apparent resistivity on the EMI curves of the same stationing. In summary, the determination of the internal structure of block accumulation using GPR was rather unfeasible (sensu Sass, 2008).

For Peer Review

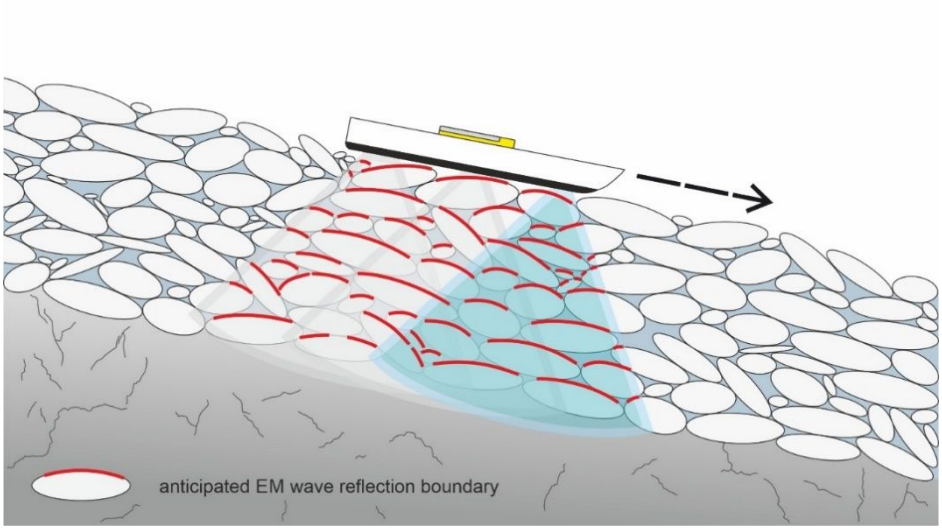


Figure 8: Schematic interpretation of the propagating EM waves, and the anticipated discontinuous GPR reflection boundaries on discrete blocks forming accumulations with an irregular architecture. Inter-block space is either air-filled (Skalka site) or partially filled with a fine-grained matrix (Slunečná site).

For both GPR antennas, the maximum depth range reported by Słowik (2012) was achieved in both sites. In particular, the 100 MHz antenna reached a maximum depth of 8–9 m, which slightly exceeded the effective penetration depth of 6–7 m (Słowik, 2012). Even if we agree that block accumulations can provide suitable conditions for reaching the maximum penetration depth of the GPR method (sensu Saas, 2007; Cassidy, 2009), we could not assert with absolute certainty that the obtained penetration depth exceeded the thickness of the investigated block accumulations as we had probably reached the method limitations. Meanwhile, the sudden disappearance of reflection might be caused by a strong signal attenuation in the relatively more conductive environment composed mostly of disrupted, weathered, and water-saturated parent rocks. We can conclude that the overall thickness assumed for the studied block layer approximately matched the GPR penetration depth.

The use of lower-frequency antennas with a greater penetration depth could be a solution for the above-mentioned problem. Sass (2006) reached a depth of over 50 m on a talus cone using a frequency of 25 MHz. Otto and Sass (2006) reached a depth of 40 m using the same antenna. These depths could be sufficient to detect the surface of the parent rock in the both locations. However, the use of low-frequency antennas has several limitations. Although the low-frequency GPR antenna (e.g. 20 or 30 MHz) delivers sufficient penetration depth, the resolution of such measurement and the ability to distinguish geological structures are rather low due to its long wavelength (Conyers, 1999; Cassidy,

2009). In addition, such antennas are not shielded, and, therefore, they are highly sensitive to geoelectric noise and unwanted reflections from trees and operators (Neal, 2004). Schrott and Sass (2008) considered the use of unshielded antennas in wooden terrains to be almost impossible. The lower-frequency antennas also have larger size. Even the transportation of a 100 MHz antenna with the size of approximately 1 m^2 to the survey site was extremely difficult. The measurement itself was very demanding and sometimes even dangerous. In accordance to Schrott and Sass (2008), due to the difficult terrain, we experienced a significantly longer measurement time.

EMI

All the measured EMI data were highly variable, and the apparent resistivity curves were scattered. The most reliable data were obtained in both sites using CMD Explorer with vertical coil axis orientation and manual gain measurement mode. Note that acquiring data with direct quality control demands large amount of time. Although the apparent resistivity curves were scattered, we could observe and further interpret specific trends in the curves, which agree with ERT resistivity models. However, the interpretation of EMI without any other supporting data is questionable. There are several reasons for the poor EMI results with low interpretation ability, such as (i) the natural heterogeneity of block accumulations, (ii) discontinuous measurement mode with a discrete induced EM field at every single point, and (iii) extremely high sensitivity of EM to noise (sensu McNeill, 1980).

In Slunečná, EMI data were found to roughly correspond to the results of ERT, SSR, and geomorphological mapping, especially for the indication of transitions to different subsurface conditions. For example, the change in the apparent resistivity distribution along the EMI profile agrees with the ERT resistivity section, where the described change matches with the increasing thickness of the uppermost highly resistive body from 200 m to the end of the profile. Similarly, we observed a progradation of higher seismic velocities toward the surface, causing the interpreted refraction boundary (plus–minus method) to shift upward. The minimum thickness of the interpreted block accumulation occurred exactly at the position of changing resistivities.

For Peer Review

Even though the EMI data measured in Skalka were highly scattered, a certain concordance of the EMI curves (especially those in −2.2 and −6.7 m) with the ERT section could be observed. There is a local maximum between 110 and 120 m in the profile that matches the extreme resistivity zone in the ERT section, followed by the above-mentioned low resistivity anomaly at ca. 120–125 m. Furthermore, a segment with highly scattered curves and with several peaks in the apparent resistivity was observed between 125 and 140 m, which roughly corresponded to a distinct high-resistivity body in the ERT model. The decrease in the apparent resistivity between 140 and 160 m (evident in a general curve trend) represents the area with sparse vegetation, and it matches the zone of relatively lower ERT resistivities (10–30 kΩ m). Finally, the increase in resistivities from 160 to 178 m most likely represents another high-resistivity body depicted in the ERT section.

The two geoelectrical methods used in this study yielded similar results, and they partially described the variable properties of the subsurface environment in both sites, despite that the operation of ERT and EMI are based on significantly different geophysical and technical principles. Measurements using direct current electric field and closed circuit with grounded electrodes for ERT were compared with contactless induction measurement of electromagnetic field for EMI (McNeill, 1980; Reynolds, 2011; Loke, 2019).

The present study confirmed the importance of using a multidisciplinary geophysical survey. Subsequent integrated interpretations of the used geophysical methods, including cross-validation between various methods and geomorphological mapping, are crucial for understanding the geological and geomorphological properties and for the compilation of the conceptual geological models for both investigated sites. Table 4 provides a clear comparison of the applicability of the methods for the investigation of block accumulations and the associated difficulties. Using this table, it is possible to clearly determine the advantages and disadvantages of the selected geophysical methods.

Table 4: Comparison of the applicability of the selected geophysical methods for the exploration of block accumulations according to certain characteristics. Individual characteristics of geophysical task are provided using the following symbols: ++ suitable; + suitable but with limitation; +/- suitable but with significant limitations or modification necessary; - unsuitable.

For Peer Review

Characteristics of the difficulty of the method are given by the following symbols: ++ undemanding; + undemanding with exceptions; +/- demanding; - very demanding.

Applicability of near surface geophysics in the reconstruction of internal structure and thickness of block accumulations.				
Geophysical task	ERT	SSR	EMI	GPR
detection of thickness	+	++	-	+
detection of internal structure	+	+/-	+/-	+/-
How demanding the method is				
in man-power	+/-	-	+/-	-
in time measurement	-	-	+/-	+
in data processing	+	-	++	+/-
in interpretation	+	+	+/-	-

6. Conclusion

The combined use of geophysical methods provided us an opportunity to acquire new information on the characteristics of block accumulations. The accumulations were simultaneously mapped and classified based on block concentrations per unit surface area. Geophysical research estimated that the thickness of block accumulations can reach approximately 7–9 m at both investigated sites. The ascertained depth of the unweathered parent rock surface ranged from 8 to 20 m. We interpreted the interjacent middle layer (if present) as an intensively disrupted and weathered parent rock, and we preferred the concept of periglacial origin of the autochthonous block accumulations. The exploration demonstrated that the surface manifestations of block accumulations correspond to the sub-surface geophysical image, with only a few exceptions with different surface block occurrences.

It can be concluded that SSR is probably the most suitable technique for exploring the thickness of block accumulation. However, it does not provide abundant information on the internal structure due to insufficient resolution while using a sledge hammer as a seismic source. ERT was applicable for determining the thickness of the block accumulation as well as the changes in subsurface conditions. GPR delivered less information on the internal structure than expected, probably because of the erratic characters of block accumulations. Although the achieved penetration depth was reasonable, it was insufficient for the determination of the accumulation thickness. The use of EMI measurements is suitable only with significant limitations. The EMI method might provide results on horizontal changes of the subsurface conditions similar to ERT in a specific measurement setting.

For Peer Review

591 An integrated interpretation of all results proved to be very useful for creating a conceptual geological
592 model. It furthermore provided a means to (i) cross-validate the individual methods, (ii) cross-validate
593 the geophysical results and geomorphological mapping, and (iii) mutually compare the applicability of
594 individual method.

595 **Acknowledgement**

596 This work was carried out with the support of the long-term conceptual development of the research
597 organisation RVO: 67985891. It was co-funded by the institutional support of the Centre for Geosphere
598 Dynamics (UNCE/SCI/006) and by Faculty of Education at the University of West Bohemia. Finally, we
599 are very thankful to Wiley Editing Services for the English style revision.

For Peer Review

References

Albers, B., 2011. Linear elastic wave propagation in unsaturated sands, silts, loams and clays. Transport in Porous Media 86, 537-557.

Andrade, F.C.M., Fischer, T., 2018. Generalised relative and cumulative response functions for electromagnetic induction conductivity meters operating at low induction numbers. Geophysical Prospecting 66(3), 595-602.

Ballantyne, C. K., 1998. Age and significance of mountain-topdetritus. Permafrost and Periglacial Processes 9, 327–345.

Barton N., 2007. Rock Quality, Seismic Velocity, Attenuation and Anisotropy. Taylor & Francis e-Library, 2007, 756 p.

Beauvais, A., Ritz, M., Parisot, J.-C., Bantsimba, C., 2003. Testing etching hypothesis for the shaping of granite dome structures beneath lateritic weathering landsurfaces using ERT method. Earth Surf. Process. Landforms 28, 1071–1080.

Berthling, I., Melvold K., 2008. Ground-penetrating radar. In: Hauck, C., Kneisel, C. (Eds.), Applied Geophysics in Periglacial Environments. Cambridge University Press, Cambridge, pp. 81–97.

Blecha, V., Fischer, T., Táborík, P., Vilhem, J., Klanica, R., Valenta, J., Štěpančíková, P., 2018. Geophysical evidence of the eastern marginal fault of the Cheb basin (Czech Republic). Stud. Geophys. Geod. 62/4, 660-680.

Bruno, F., Martillier, F., 2000. Test of High-Resolution Seismic Reflection and other Geophysical Techniques on the Boup Landslide in The Swiss Alps. Surveys in geophysics 21, 335-350.

Bustin, R. M., Mathews, W. H., 1979. Selective weathering of granitic clasts. Canadian Journal of Earth Sciences 16(2), 215–223.

For Peer Review

622 Campbell, S., Affleck, R.T., Sinclair, S., 2018. Ground-penetrating radar studies of permafrost,
623 periglacial, and near-surface geology at McMurdo Station, Antarctica. Cold Regions Science and
624 Technology 148, 38-49.

625 Cassidy, N.J., 2009. Electrical and magnetic properties of rocks, soils and fluids. In: Jol, H.M. (Ed.),
626 Ground Penetrating Radar: Theory and Applications. Elsevier B.V., Amsterdam, Netherlands, 41-72.

627 Chalupa, V., Pánek, T., Tábořík, P., Klimeš, J., Hartvich, F., Grygar, R., 2018. Deep-seated gravitational
628 slope deformations controlled by the structure of flysch nappe outliers: Insights from large-scale
629 electrical resistivity tomography survey and LiDAR mapping. Geomorphology 321, 174-187.

630 Chambers, J.E., Wilkinson, P.B., Wardrop, D., Hameed, A., Hill, I., Jeffrey, C., Loke, M.H., Meldrum, P.I.,
631 Kuras, O., Cave, M., Gunn, D.A., 2012. Bedrock detection beneath river terrace deposits using three-
632 dimensional electrical resistivity tomography. Geomorphology 177–178, 17–25.

633 Colombero, Ch., Comina, C., Gianotti, F., Sambuelli, L. 2014. Waterborne and on-land electrical
634 surveys to suggest the geological evolution of a glacial lake in NWItaly. Journal of Applied Geophysics
635 105, 191–202

636 Conyers, L.B., 1999. Geophysics, ground-penetrating radar and archaeology. Soc. Am. Archaeol. Bull.
637 17 (4), 26-29.

638 Dahlin, T., Zhou, B., 2004. A numerical comparison of 2D resistivity imaging with ten electrode arrays.
639 Geophys. Prospect. 52 (5), 379–398.

640 Davis, J.L., Annan, A.P., 1989. Ground-penetrating radar for high-resolution mapping of soil and rock
641 stratigraphy. Geophys. Prospect. 37, 531-551.

642 Dobinski, W., Zogala, B., Wzietek, K., Litwin, L., 2008. Results of geophysical surveys on Kasprowy
643 Wierch, the Tatra Mountains, Poland.In: Hauck, C., Kneisel, C. (Eds.), Applied Geophysics in Periglacial
644 Environments. Cambridge University Press, Cambridge, pp.126–136.

For Peer Review

645 Engel, Z., Křížek, M., Kasprzak, M., Traczyk, A., Hložek, M., Krbcová, K., 2017. Geomorphological and
646 sedimentary evidence of probable glaciation in the Jizerské hory Mountains, Central Europe.
647 Geomorphology 280, 39-50.

648 Evans, R. L., Law, L.K., Louis, B.St., Cheesman, S., 2000. Buried paleo-channels on the New Jersey
649 continental margin: channel porosity structures from electromagnetic surveying. Marine Geology 170
650 (3-4), 381-394.

651 Gabriel, G., Kirsch, R., Siemon, B., Wiederhold, H., 2003. Geophysical investigation of buried
652 Pleistocene subglacial valleys in Northern Germany. Journal of Applied Geophysics 53, 159-180.

653 Hagedoorn, J. G., 1959. The plus-minus method of interpreting seismic refraction sections. Geophysical
654 Prospecting 7, 158-181.

655 Hartvich, F., Blahůt, J., Stemberk, J., 2017. Rock avalanche and rock glacier: a compound landform
656 study from Hornsund, Svalbard. Geomorphology 276, 244-256.

657 Hauck, C., Guglielmin, M., Isaksen, K., Vonder Mühll, D., 2001. Applicability of frequency-domain and
658 time-domain electromagnetic methods for mountain permafrost studies. Permafrost and Periglacial
659 Processes 12, 39-52.

660 Hauck, C., Kneisel, C. (Eds.), 2008. Applied Geophysics in Periglacial Environments. Cambridge
661 University Press, Cambridge, 256 p.

662 Hauner, U., Lehrberger, G., Brugger, M. Der Naturraum Bayerischer Wald – Šumava In den Eiszeiten.
663 Nationalparkverwaltung Bayerischer Wald Freyunger Straße 2. 2019.

664 Hill, S.M., 1996. The differential weathering of granitic rocks in Victoria, Australia. AGSO Journal of
665 Australian Geology & Geophysics 16 (3), 271-276.

666 Hördt, A., Hauck, C., 2008. Electromagnetic methods. In: Hauck, C., Kneisel, C. (Eds.), Applied
667 Geophysics in Periglacial Environments. Cambridge University Press, Cambridge, pp. 28–56.

For Peer Review

668 Hülle, D., Hilgers, A., Kühn, P., Radtke, U., 2009. The potential of optical stimulated luminescence for
669 dating periglacial slope deposits – a case study from the Taunus area, Germany. Geomorphology 109,
670 66-78.

671 Mustasaar, M., Plado, J., Jõeleht, A., 2012. Determination of Electromagnetic Wave Velocity in
672 Horizontally Layered Sedimentary Target: A Ground-Penetrating Radar Study from Silurian Limestones,
673 Estonia. Acta Geophysica 60(2), 357-370.

674 Nguyen, F., Kemna, A., Antonsson, A., Engesgaard, P., Kuras, O., Ogilvy, R., Gisbert, J., Jorreto, S.,
675 Pulido-Bosch, A., 2009. Characterization of seawater intrusion using 2D electrical imaging. Near Surf.
676 Geophys. 7, 377–390.

677 Kasprzak, M., 2015. High-resolution electrical resistivity tomography applied to patterned ground,
678 (Wedel Jarlsberg Land, south-west Spitsbergen). Polar Research 34, 25678.
679 http://dx.doi.org/10.3402/polar.v34.25678.

680 Kasprzak, M., Strzelecki, M. C., Traczyk, A., Kondracka, M., Lim, M., Migała, K. 2017. On the potential
681 for a bottom active layer below coastal permafrost: the impact of seawater on permafrost degradation
682 imaged by electrical resistivity tomography (Hornsund, SW Spitsbergen). Geomorphology 293, 347–
683 359. doi:10.1016/j.geomorph.2016.06.013

684 Kiflu, H., Kruse, S., Loke, M. H., Wilkinson, P. B., & Harro, D., 2016. Improving resistivity survey
685 resolution at sites with limited spatial extent using buried electrode arrays. Journal of Applied
686 Geophysics, 135, 338–355. doi:10.1016/j.jappgeo.2016.10.011

687 Kneisel, C., Hauck, C., 2008. Electrical methods. In: Hauck, C., Kneisel, C. (Eds.), Applied Geophysics in
688 Periglacial Environments. Cambridge University Press, Cambridge, pp. 3–27.

689 Lenart, J., Pánek, T., Dušek, R., 2014. Genesis, types and evolution of crevice-type caves in the flysch
690 belt of the Western Carpathians (Czech Republic). Geomorphology 204, 459–476.

For Peer Review

691 Loke, M.H., 2000. Electrical imaging surveys for environmental and engineering studies. A practical
692 guide to 2-D and 3-D surveys, Geotomo software (1997-2000), 67 p. Accessed on April 30, 2020 at
693 http://www.geotomosoft.com.

694 Loke, M.H., 2019. Tutorial: 2-D and 3-D Electrical Imaging Surveys. User's Manual. Accessed 21
695 February 2021 at www.geotomosoft.com

696 Loke, M.H., Barker R.D., 1996. Rapid least-squares inversion of apparent resistivity pseudosections
697 using a quasi-Newton method. Geophysical Prospecting 44, 131-152.

698 Loke, M.H., Kiflu, H., Wilkinson, P.B., Harro, D., Kruse, S., 2015a. Optimized arrays for 2D resistivity
699 surveys with combined surface and buried arrays. Near Surf. Geophys. 13 (2096), 505–517.

700 Loke, M.H., Wilkinson, P.B., Chambers, J.E., Uhlemann, S.S., Sorensen, J.P.R., 2015b. Optimized arrays
701 for 2-D resistivity survey lines with a large number of electrodes. J. Appl. Geophys. 112, 136–146.

702 Maillet, G.M., Rizzo, E., Revil, A., Vella, C., 2005. High Resolution Electrical Resistivity Tomography (ERT)
703 in a Transition Zone Environment: Application for Detailed Internal Architecture and Infilling Processes
704 Study of a Rhône River Paleo-channel. Marine Geophysical Researches 26, 317-328.

705 McNeill, J.D., 1980. Electromagnetic terrain conductivity measurement at low induction numbers.
706 Geonics Limited Technical Note TN-6, Ontario. Available at
707 http://www.geonics.com/pdfs/technicalnotes/tn6.pdf.

708 Mentlík, P., 2011. Development of summit parts in the SW part of Šumava Mts. – research by
709 innovative methods] [Výzkum vývoje reliéfu vrcholových partií SZ Šumavy prostřednictvím inovativních
710 výzkumných metod]. Pilsen, 178 p. Comenius University in Bratislava, Faculty of Natural Sciences.
711 (Habilitation Thesis (in Czech))

712 Mentlík, P., Minár, J., Břízová, E., Lisá, L., Tábořík, P., Stacke, V. 2010. Glaciation in the surroundings of
713 Prášilské Lake (Bohemian Forest, Czech Republic). Geomorphology 117, 181–194.

For Peer Review

714 Mentlík, P., 2016. Bohemian Forest: Landscape and People on the Frontier. In: Pánek, T., Hradecký, J.
715 (Eds.), Landscapes and Landforms of the Czech Republic. Springer International Publishing, Switzerlan,
716 pp. 87–100.

717 Milsom, J., Eriksen, A., 2011. Field Geophysics. Fourth Edition. London: Wiley and Sons, 304 p.

718 Musset, A. E., Khan, A. M., 2000. Looking into the Earth. An Introduction to Geological Geophysics.
719 London: Cambridge University Press, 492 p.

720 Musil, M., Maurer, H.R., Green, A.G., Horstmeyer, H., Nietsche, F.O., Vonder Mühll, D., Springman, S.,
721 2002. Shallow seismic surveying of an Alpine rock glacier. Geophysics 67 (6), 1701-1710.

722 Neal, A., 2004. Ground-penetrating radar and its use in sedimentology: principles, problems and
723 progress. Earth-Science Reviews 66 (3), 261-330.

724 Nolet, G. 2008. A Breviary of Seismic Tomography: Imaging the Interior of the Earth and Sun.
725 Cambridge, UK: Cambridge University Press, 360 p.

726 Otto, J. C., Sass, O., 2006. Comparing geophysical methods for talus slope investigation in the Turmann
727 valley (Swiss Alps). Geomorphology 76, 257-272.

728 Pánek, T., Hradecký, J., Minár, J., Hungr, O., Dušek, R., 2009. Late Holocene catastrophic slope collapse
729 affected by deep-seated gravitational deformation in flysch: Ropice Mountain, Czech Republic.
730 Geomorphology 103, 414–429. https://doi.org/10.1016/j.geomorph.2008.07.012.

731 Pelc, Z., Šebesta, J., 1994. Geological map of the Czech Republic [Geologická mapa ČR. List 22–33
732 Kašperské Hory, 1:50 000]. Praha. Czech Geological Survey.

733 Pelton, J. R., 2005. Near-Surface Seismology: Surface-Based Methods. In: Butler, D. K. et al. Near-
734 Surface Geophysics. USA, Tulsa: Society of Exploration Geophysics, 219–264.

735 Pye, K., 1985. Granular disintegration of gneiss and migmatites. Catena 12, 191-199.

For Peer Review

736 Raška, P., Hartvich, F., Cajz, V., Adamovič, J., 2014. Structural setting of the Čertovka landslide (Ústí
737 nad Labem, Czech Republic): morphostructural analysis and electrical resistivity tomography.
738 Geological Quaterly 58 (1), 85-98

739 Rea, B. R., 2007. Periglacial landforms, rock forms: Blockfields (Felsenmeer). In: Elias, S. A., Mock, C. J.
740 (Eds.), Encyclopedia of Quaternary Science. Elsevier, pp. 2225-2236.

741 Reynolds, J.M., 2011. An Introduction to Applied and Environmental Geophysics, 2nd Edition. Wiley.
742 720 p. ISBN: 978-0-471-48535-3

743 Rinaldi, V. A., Redolfi, E. R., Santamarina, J. C., 1998. Characterization of collapsible soils with combined
744 geophysical and penetration testing. In Robertson, P. K., Mayne, P. W. (Eds.): Geotechnical site
745 characterization: volume 1. Proceedings of the First International Conference on Site Characterization
746 – ISC'98, Atlanta, Georgia, USA, 19-22 April 1998. 1998 pp.581-588.

747 Rizzo, E., Colella, A., Lapenna, V., Piscitelli, S., 2004. High-resolution images of the fault controlled High
748 Agri Valley basin (Southern Italy) with deep and shallow Electrical Resistivity Tomographies, Phys.
749 Chem. Earth 29, 321–327.

750 Sasaki, Y., 1992. Resolution of resistivity tomography inferred from numerical simulation. Geophys.
751 Prospect. 40 (4), 453–463

752 Sass, O., 2006. Determination of the internal structure of alpine talus using different geophysical
753 methods (Lechtaler Alps, Austria). Geomorphology 80, 45-58.

754 Sass, O., 2007. Bedrock detection and talus thickness assessment in the European Alps using
755 geophysical methods. Journal of Applied geophysics 62, 254-269.

756 Sass O., 2008. The use of GPR in determining talus thickness and talus structure. In: Hauck, C., Kneisel,
757 C. (Eds.), Applied Geophysics in Periglacial Environments. Cambridge University Press, Cambridge, pp.
758 165–171.

For Peer Review

759 Sass, O., Wollny, K., 2001. Investigations regarding alpine talus slopes using ground penetrating radar
760 (GPR) in the Bavarian Alps, Germany. Earth Surface Processes and Landforms 26, 1071-1086.

761 Semmel, A. and Terhorst, B. 2010. The concept of the Pleistocene periglacial cover beds in central
762 Europe: A review. Quaternary International. 222, 120-128.

763 Schrott, L., Hoffmann, T., 2008. Refraction seismics. In: Hauck, C., Kneisel, C. (Eds.), Applied Geophysics
764 in Periglacial Environments. Cambridge University Press, Cambridge, pp. 57–80.

765 Schrott, L., Hufschmidt, G., Hankammer, M., Hoffmann, T., Dikau, R., 2003. Spatial distribution of
766 sediment storage types and quantification of valley fill deposits in an alpine basin, Reintal, Bavarian
767 Alps, Germany. Geomorphology 55, 45–63.

768 Schrott, L., Sass, O., 2008. Application of field geophysics in geomorphology: advances and limitations
769 exemplified by case studies. Geomorphology 93, 55-73.

770 Sharma, P.V., 1997. Environmental and Engineering Geophysics. Cambridge University Press,
771 Cambridge, 1-475.

772 Sheriff R. E., Geldart L. P. 1995. Exploration Seismology. 2nd edition. Cambridge University Press. 628
773 p. https://doi.org/10.1017/CBO9781139168359

774 Słowik, M., 2012. Influence of measurement conditions on depth range and resolution of GPR images:
775 The example of lowland valley alluvial fill (the Obra River, Poland). Journal of Applied Geophysics 85,
776 1-14.

777 Stemberk, J., Hartvich, F., Blahut, J., Rybář, J., and Krejčí, O., 2017. Tectonic strain changes affecting
778 the development of deep seated gravitational slope deformations in the Bohemian Massif and Outer
779 Western Carpathians. Geomorphology 289, 3-17.

For Peer Review

780 Strzelecki, M. C., Kasprzak, M., Lim, M., Swirad, Z. M., Jaskólski, M., Pawłowski, Ł., & Modzel, P., 2017.
781 Cryo-conditioned rocky coast systems: A case study from Wilczekodden, Svalbard. Science of The Total
782 Environment 607-608, 443–453. doi:10.1016/j.scitotenv.2017.07.009.

783 Szalai, S., Szarka, L., 2008. Parameter sensitivity maps of surface geoelectric arrays. Part 1: linear arrays.
784 Acta Geod. Geophys. Hung. 43, 419–437.

785 Szalai, S., Novák, A., Szarka, L., 2009. Depth of investigation and vertical resolution of surface
786 geoelectric arrays. J. Environ. Eng. Geophys. 14, 15–23.

787 Tábořík, P., 2012. Use of Electrical Resistivity Tomography in the Research of Mountain Relief (Ph.D.
788 Thesis. Ostrava (in Czech)).

789 Tábořík, P., Lenart, J., Blecha, V., Vilhelm J., Turský, O., 2017. Geophysical anatomy of counter-slope
790 scarps in sedimentary flysch rocks (Outer Western Carpathians). Geomorphology 276, 59-70.

791 Telford, W.M., Geldart, L.P., Sheriff, R.E., 1990. Applied Geophysics. Cambridge University Press; Jones,
792 E.J.W., 1999. Marine Geophysics. John Wiley.

793 Tolasz, r. et al. 2007. Climate atlas of Czechia. Czech Hydrometeorological Institute, Praha; Palacký
794 University

795 Uxa, T., Křížek, M., Krause, D., Hartvich, F., Tábořík, P., Kasprzak, M., 2019. Comment on 'Geophysical
796 approach to the study of a periglacial blockfield in a mountain area (Ztracené kameny, Eastern Sudetes,
797 Czech Republic)' by Stan et al. (2017). Geomorphology 328, 231-237.

798 Valenta, J., Dohnal, J., 2007. 3D seismic travel time surveying a comparison of the time–term method
799 and tomography (an example from an archaeological site). Journal of Applied Geophysics 63, 46–58.

800 van Overmeeren, R.A., 1998. Radar facies of unconsolidated sediments in The Netherlands: a radar
801 stratigraphy interpretation method for hydrogeology. J. Appl. Geophys. 40, 1 –18.

For Peer Review

802 van Overmeeren, R.A., 2001. Hagedoorn's plus-minus method: the beauty of simplicity. Geophysical
803 Prospecting 49, 687-696.

804 Völkel, J., Leopold, M., Roberts M.C., 2001. The radar signatures and age of periglacial slope deposits,
805 Central Highlands of Germany. Permafrost and Periglacial Processes 12, 379-387.

806 Völkel, J., Zepp, H., Kleber, A. 2002. Periglaziale Deckschichten in Mittelgebirgen – ein offenes
807 Forschungsfeld. BERICHTE ZUR DEUTSCHEN LANDESKUNDE. 76, 101-114. Available online:
808 https://www.deutsche-landeskunde.de/download/665/bd-76-heft-2-3/997/bgl_bd_76_heft_02-
809 03_2002_01_voelkel_zepp_kleber.pdf. [accessed on 17. 2. 2021]

810 Völkel, J. 1995. Periglaziale Deckschichten und Böden im Bayerischen Wald und seinen Randgebieten:
811 als geogene Grundlagen landschaftsökologischer Forschung im Bereich naturnaher Waldstandorte.
812 Gebrüder Borntraeger, Germany.

813 Wang, P., Wang, L. M., Wang, Q., & Wang, J., 2012. Study on Critical Shear Wave Velocity of Saturated
814 Loess Foundation Soil Liquefaction under Different Seismic Magnitudes Action. Advanced Materials
815 Research, 594-597, 1720–1726.

816 Whiteley R.J., Stewart S.B., 2008. Case studies of shallow marine investigations in Australia with
817 advanced underwater seismic refraction (USR). Exploration Geophysics 39, 34-40.

818 Zhou, W., Beck, B.F., Adams, A.L., 2002. Effective electrode array in mapping karst hazards in electrical
819 resistivity tomography. Environ. Geol. 42, 922–928.

820 Żurawek, R., Żyszkowski, E., Górecki, A., 2005. Topographic Control of Periglacial Slope Covers, Ślęża
821 Massif, Southwest Poland: A Statistical Approach. Permafrost and Periglacial Processes 16, 241-248.

For Peer Review

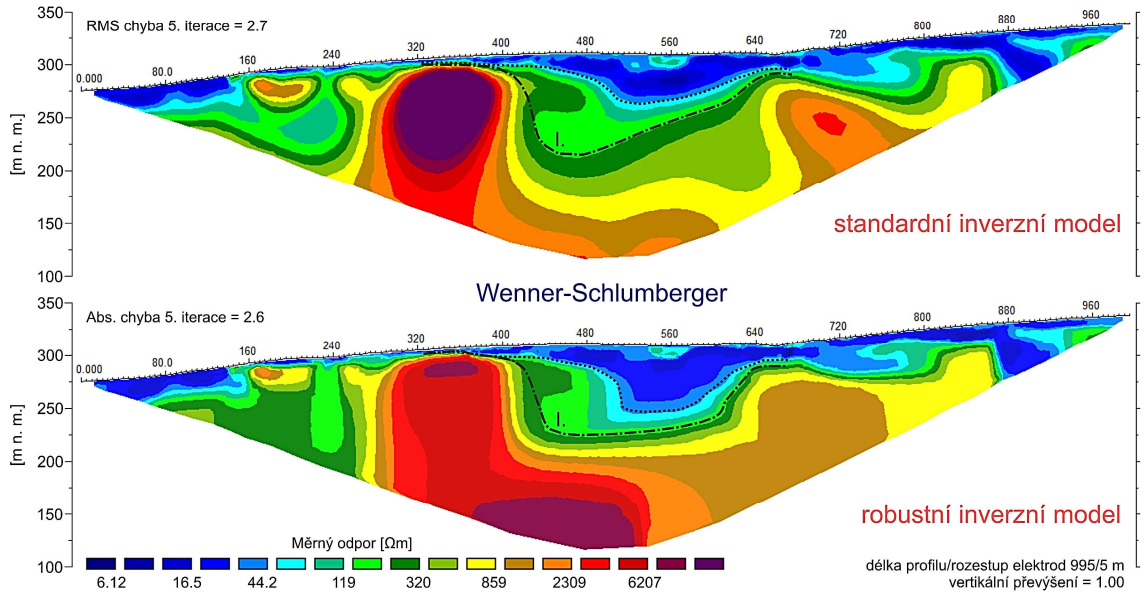
Příloha 8

Obr. 32 (vyšší rozlišení)

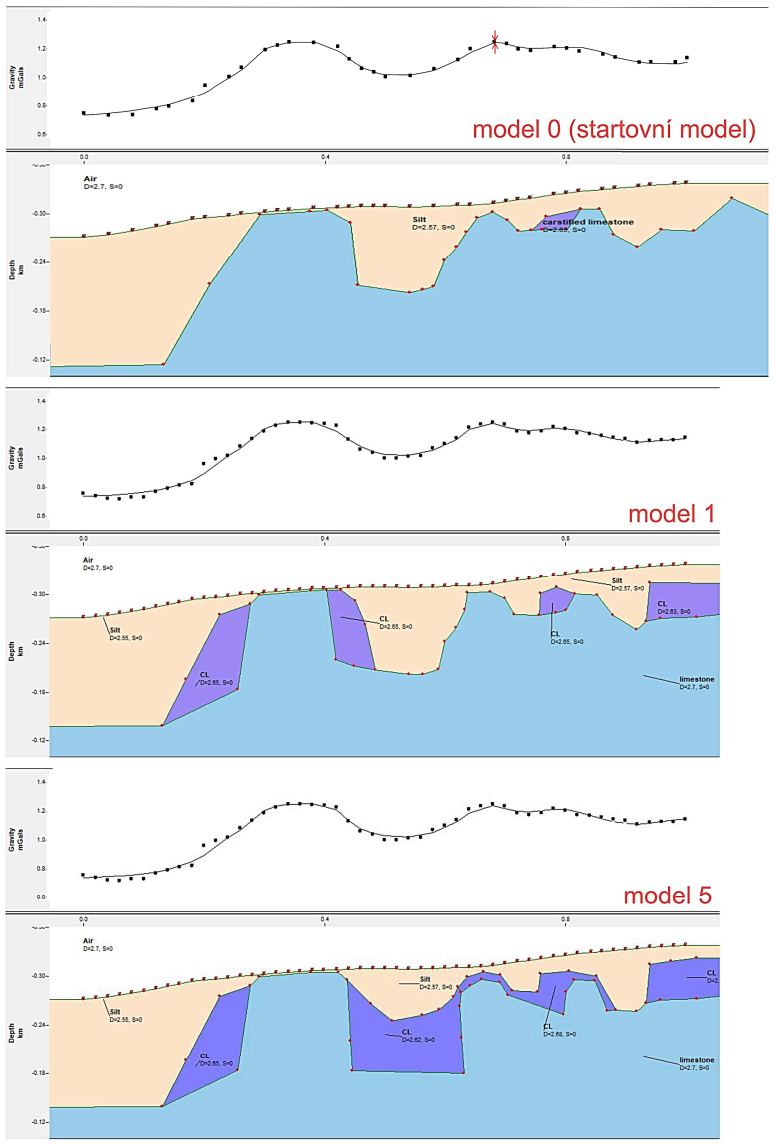
Obr. 32: Sdružená interpretace výsledků na lokalitě Hranická propast – profil P2: reinterpretace gravimetrického modelu a ERT odporového řezu na základě seismického průzkumu: (A) ERT – původní interpretace geologických rozhraní na odporovém řezu; (B) GM – původní přímý gravimetrický model na základě ERT a interpretovaných rozhraní; (C) seismický průzkum – zpracovaný reflexní řez a tomografický řez s rychlostmi šíření P-vln (MRS); (D) seismický průzkum – interpretace rozhraní na základě refrakční seismiky podle metody t_0 a izolinie seismických rychlostí 3000 $m.s^{-1}$; (E) GM – reinterpretovaný gravimetrický model na základě seismického průzkumu, (F) ERT – reinterpretace invertovaného odporového řezu na základě seismického průzkumu.

PŮVODNÍ INTERPRETACE

A

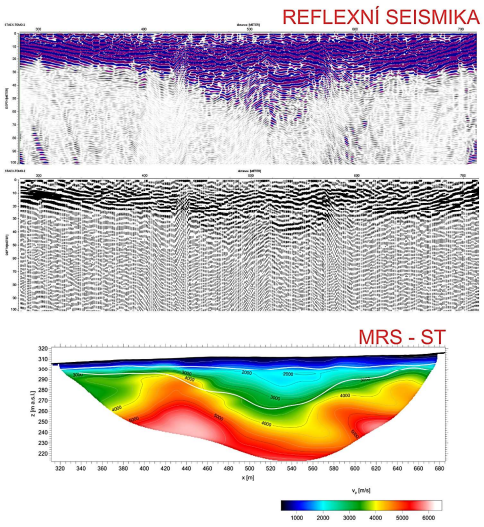


B

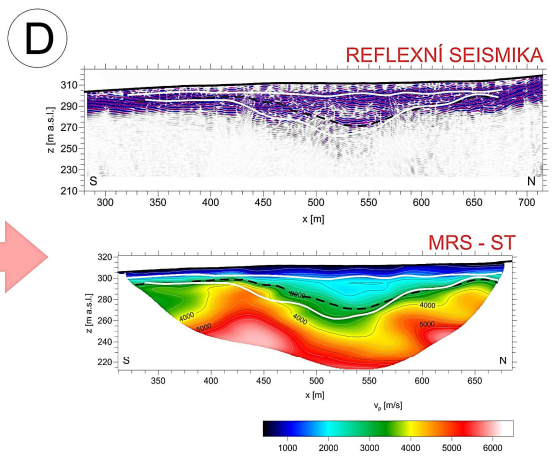


REINTERPRETACE na základě SEISMICKÉHO MĚŘENÍ

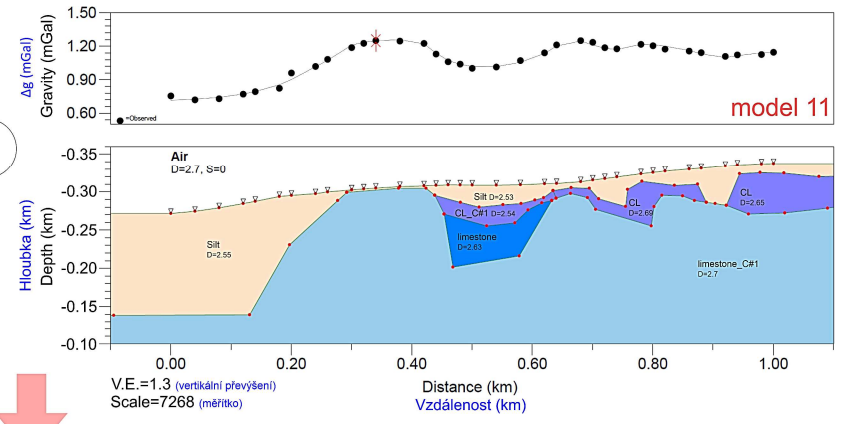
C



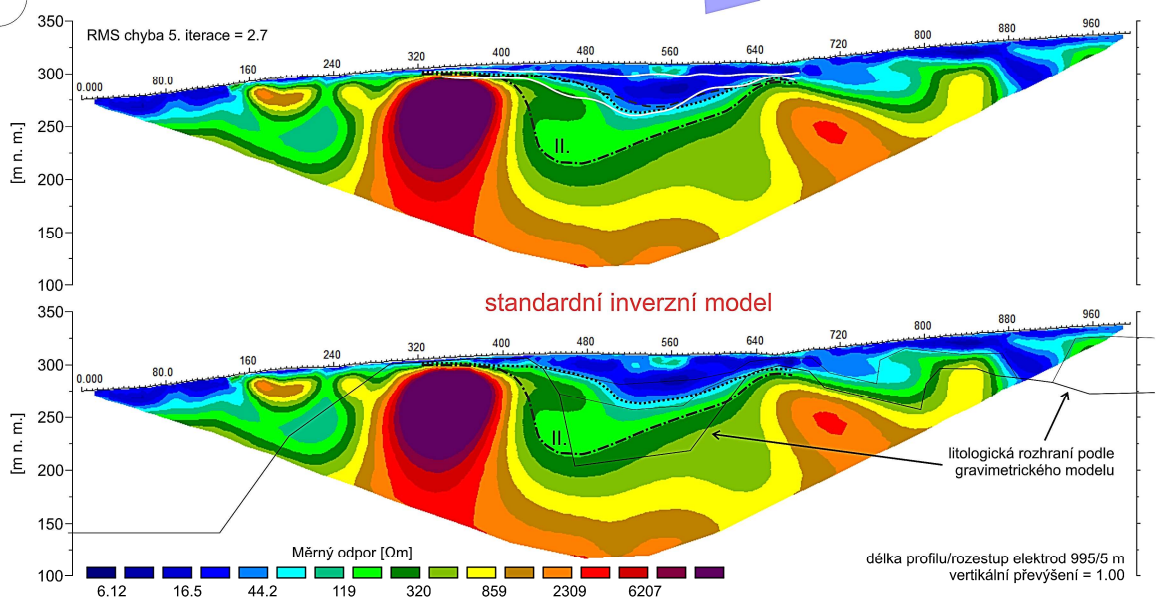
D

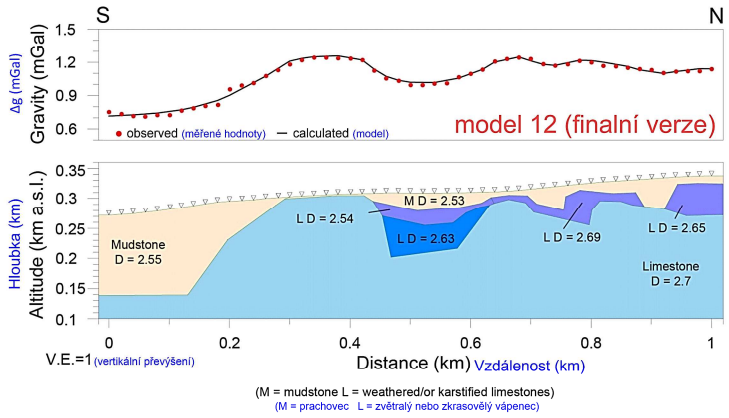


E



F





šipka indikuje postup zpracování a interpretace dat (na základě původní interpretace ERT měření byl vytvořen přímý gravimetrický model, který byl následně reinterpretován na základě výsledků seismiky)

šipka indikuje vzájemné porovnání výsledných interpretací strukturně-litologických rozhraní v rámci sdružené interpretace různých geofyzikálních metod použitých v rámci výzkumu

(I. původní intepretace / II. reinterpretace)

rozhraní podle „metody t_0"

izolinie 3000 m/s

I. jílovitý / hrubozrnněší neogén
II. neogén / vápence podle ERT

I. neogén / zvětralé vápence podle ERT ?
II. zvětralé / zdravé vápence podle ERT ?